INVESTIGATING FLOW BEHAVIORS OF COLLOIDAL MATERIALS AT THE SINGLE-PARTICLE SCALE

A Dissertation

Presented to the Faculty of the Graduate School

of Cornell University

in Partial Fulfillment of the Requirements for the Degree of

Doctor of Philosophy

by

Yen-Chih Lin

January 2017

INVESTIGATING FLOW BEHAVIORS OF COLLOIDAL MATERIALS AT THE SINGLE-PARTICLE SCALE

Yen-Chih Lin, Ph.D.

Cornell University 2017

My thesis work focuses on the nonlinear mechanical behaviors of colloidal suspensions at the particle-level. This work covers both quiescent and strongly sheared suspensions. For quiescent suspensions, we image their 3D structures with confocal microscopy, and implement Stress Assessment from Local Structural Anisotropy (SALSA) to visualize the stress fields in them. Unlike traditional numerical methods, SALSA takes a statistical approach converting the probability of hard-sphere Brownian collisions to stresses. This direct stress measurement allows us to quantify the particle-level stresses surrounding vacancies, dislocations, and grain boundaries in crystalline materials. To drive the suspensions away from equilibrium, we develop a confocal-rheoscope, which is able to shear and image colloidal materials simultaneously. Using this device, we investigate the nonlinear flow behavior governed by Brownian motion, shear induced diffusion, and advection, and more importantly, disentangle them. We also study particle assembly and its corresponding rheological properties under confinement. Finally, we study even more strongly sheared suspensions, in which particle dynamics are too fast to be imaged by a confocal microscope. Here, we use flow reversal rheometry to reveal the underlying mechanism of suspension shear thickening where the viscosity increases with shear rate. We show that the thickening behavior of a suspension arises from the particle contact forces rather than hydrodynamic interactions. Such findings then lead us to design a biaxial shear protocol that can tune the suspension vis-

cosity on demand. This viscosity tuning capability is a foundational step toward using dense suspensions in 3D printing, energy storage, and robotics.

BIOGRAPHICAL SKETCH

Neil was born and raised in Hsinchu city, Taiwan until he finished his bachelor degree in Physics at National Tsing-Hua University. He served in the Republic of China Army as an artillery soldier-gunner for the following year, then came to Cornell University pursuing his PhD study in Physics. Neil has one sibling: Yen-wei Lin. In addition to his academia pursuits, Neil has a broad recreational interests including hiking, sailing, as well as playing piano and violin.

This thesis is dedicated to Christine Wang

– my beloved wife and great helper in my life.

ACKNOWLEDGEMENTS

During my time at Cornell, I have been privileged to collaborate with many experts in soft-condensed matter. I owe a great debt of gratitude to my advisor, Itai Cohen. Itai has taught me how to be a scientist who is always curious about everything, and turn those questions into creative scientific researches. In addition to typical scientific trainings, he has also spent countless hours on teaching me how to write, present, and even communicate. I am also tremendously grateful to my peers from Cohen group. They have generously taught me valuable experimental skills and scientific knowledges. I have included project-specific acknowledgments at the end of each chapter. Furthermore, I would like to thank my parents, grandmother, brother, and wife. Their love and unconditional supports play a major role in my PhD life. Finally, I thank my God, for His grace and mercy never ends.

TABLE OF CONTENTS

CHAPTER 1

INTRODUCTION

While suspensions are simple as particles mixed with liquid, understanding how they flow remains one of the main challenges in the fields of fundamental and engineering sciences. When the suspended particles have a size $\sim$ 1 μm ($\approx$1/100 of the diameter of a hair), they become *colloidal* and undergo Brownian motion. These Brownian particles interact with one another through thermal collisions and hydrodynamic forces mediated by the background liquid. Colloidal suspensions, such as toothpastes, paints, and milk, are common in daily life and understanding how they flow is crucial for many industrial processes. For instance, the flow properties of printer inks – one of the most expensive liquids ($8,800 USD/gallon four times more expensive than 1985 Krug champagne) – directly determines the speed, resolution, and reliability of inkjet printers. In addition to their technological applications, colloidal suspensions have also been widely employed as a model system to study many fundamental material behaviors. For example, mechanisms that cannot be studied at the atomic level including crystal melting, growth, and yielding as well as liquid-glass transitions, can be investigated at the particle-level in colloidal suspensions. Colloidal suspensions are a great model system since colloids are small enough to demonstrate random motion, preserving a true thermodynamic ensemble, while still large enough to be optically imaged.

In the first part of this thesis (Chapters 2-5), we describe how we image the 3D structures of hard-sphere suspensions with confocal microscopy and use the confocal images to determine the suspensions' internal stresses. This non-invasive approach allows us to measure mechanical responses at the single-particle level. In Chapter 2 we introduce a method "Stress Assessment from Local Structural

Anisotropy" (SALSA) that measures the Brownian stress at the single-particle scale. By implementing this method, we effectively transform a confocal microscope into a local pressure gauge probing 3D stress fields in colloidal materials. In particular, we use this method to measure the stresses surrounding three canonical crystalline defects – vacancies, dislocations, and grain boundaries. In Chapter 3, we design an multi-axial confocal rheoscope that can drive the suspension out-of-equilibrium while also measuring the suspension microstructure and bulk response simultaneously. In Chapter 4, we use this rheoscope to investigate the nonlinear response of a far-from-equilibrium suspension. By imaging the structure of suspensions under oscillatory shear and locating individual particle positions, we directly separate the nonlinear Brownian contribution to the stress from the hydrodynamic term. We also use this rheoscope to study shear-induced particle assemblies and report their corresponding flow behaviors in Chapter 5.

In the second part (Chapters 6 and 7), we focus on a fascinating suspension flow behavior – shear thickening – in which the viscosity increases with shear rate. Since the shear rate is high in the thickening regime, the particles move too fast and thus cannot be imaged using currently available confocal microscopes. Therefore, we design strategic shear protocols to explore the particle-level mechanism that underlies suspension thickening. In Chapter 6, we show that by performing flow reversal measurements, we separate the contact force and hydrodynamic contributions to the thickening viscosity. We conclude that the contact contribution dominates over the hydrodynamic term in thickening suspensions, settling long-standing debates in the field of suspension rheology. Finally, in Chapter 7, we harness our knowledge of the particle-level flow mechanism to design a biaxial shear protocol that can tune the suspension viscosity over two orders of magnitude.

CHAPTER 2

MEASURING NONLINEAR STRESSES GENERATED BY DEFECTS IN 3D COLLOIDAL CRYSTALS[1]

2.1 Abstract

The mechanical, structural, and functional properties of crystals are determined by their defects [54, 45, 2, 27], and the distribution of stresses surrounding these defects has broad implications for the understanding of transport phenomena. When the defect density rises to levels routinely found in real-world materials, transport is governed by local stresses that are predominantly nonlinear [54, 55, 38, 10, 33]. Such stress fields however, cannot be measured using conventional bulk and local measurement techniques. Here, we report direct and spatially resolved experimental measurements of the nonlinear stresses surrounding colloidal crystalline defect cores, and show that the stresses at vacancy cores generate attractive interactions between them. We also directly visualize the softening of crystalline regions surrounding dislocation cores, and find that stress fluctuations in quiescent polycrystals are uniformly distributed rather than localized at grain boundaries, as is the case in strained atomic polycrystals. Nonlinear stress measurements have important implications for strain hardening [9], yield [54, 55], and fatigue [59].

[1] Neil Lin, Matthew Bierbaum, Peter Schall, James Sethna, Itai Cohen. "Measuring Nonlinear Stresses Generated by Defects in 3D Colloidal Crystals" Nature materials (2016) in press.

2.2 Introduction

Bulk measurements of the nonlinear materials response have shown that fascinating mechanical behaviors emerge when crystals are plastically deformed [27]. Such measurements however, average over the rich spatial heterogeneity in structure and stress distributions. This averaging makes it difficult to determine how microscopic mechanisms collude to determine a crystal's bulk behavior. Pioneering measurements of local crystalline strains have done much to elucidate the heterogeneity in the linear stress response of crystals [26, 69, 3, 29, 30, 37]. Despite these advances however, applying such techniques to measure the nonlinear stress distributions in crystals with defects has remained prohibitive since it is impossible to *a priori* determine how the nonlinear modulus varies with strain or even define a strain when the structure is highly distorted. Consequently, it has been difficult to experimentally determine even the qualitative interactions between defects that give rise to these fascinating mechanical behaviors under large deformations.

2.3 Experiment

Here, building on the technological advances offered by high-speed confocal microscopy, we use Stress Assessment from Local Structural Anisotropy (SALSA) to directly measure the complete stress tensor down to the single particle-scale in a 3D colloidal crystal. Hard-sphere colloidal crystals have been widely employed as a model system to investigate many fundamental and important processes including defect nucleation [69], crystal melting [2, 45], and crystal growth [65]. In Brownian hard-sphere systems, the force with which particles collide can be related to the thermal energy k_BT. Therefore, using a time series of featured particle positions

[15, 14], we determine the thermal collision probability, and directly report the stress arising from these Brownian collisions. Our derivation (see Supplemental Information) shows the stress tensor $\sigma_{ij}^{\alpha} = \sigma_{ij}(\mathbf{x}^{\alpha})$ at particle α can be approximated by

$$\sigma_{ij}^{\alpha} = \frac{k_B T}{\Omega^{\alpha}} \left(\frac{a}{\Delta}\right) \langle \psi_{ij}^{\alpha}(\Delta) \rangle \tag{2.1}$$

where $k_B T$ is the thermal energy, Ω^{α} is the volume occupied by the particle, a is the particle radius, and Δ is the cutoff distance from contact (SI and SI video). Here $\langle \psi_{ij}^{\alpha}(\Delta) \rangle$ is the time-averaged *local structural anisotropy* or fabric tensor for the particle, $\langle \psi_{ij}^{\alpha}(\Delta) \rangle = \langle \sum_{\beta \in nn} \hat{r}_i^{\alpha\beta} \hat{r}_j^{\alpha\beta} \rangle$, where nn is the set of particles that lie within a distance $2a + \Delta$ from particle α, ij are spatial indices, and $\hat{r}^{\alpha\beta}$ is the unit vector between particle α and particle β. In the *local structural anisotropy* calculation, the trace $\hat{r}_i^{\alpha\beta} \hat{r}_i^{\alpha\beta}$ is the total number of neighbors while the remaining components captures the anisotropy of the collisions [3]. The time averaged fabric tensor of each particle accurately captures the probability of thermally induced collisions arising from the spatial distribution of its neighbors (Fig. 2.1). Scaling the probability by the energy density per collision $k_B T/\Omega^{\alpha}$, we then determine the Cauchy stress at the selected particle's position. This capability enables us to measure the local stress distributions surrounding crystalline defects such as vacancies (0D), dislocations (1D), and grain boundaries (2D).

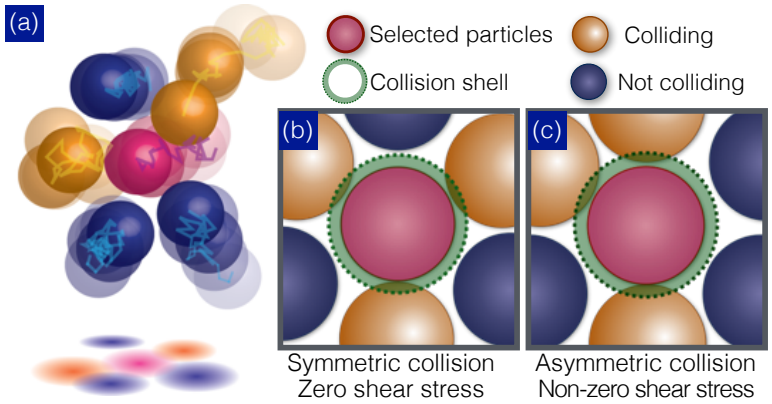

Figure 2.1: **Algorithm of particle-level stress measurements (SALSA).**(a) Particles exhibit Brownian motions (trajectories segments) and exert stresses on the selected particle (red sphere) when the neighboring particles collide with it. The energy density (stress) per collision is k_BT/Ω^α. (b) Schematic illustrating the SALSA algorithm for hard spheres. A thin shell (Δ=106 nm) is constructed to identify colliding particles (yellow spheres), which lie within distance $2a + \Delta$ from the selected particle. The shear stress is zero when the colliding particles' configuration is symmetric. When the collisions are asymmetric, the shear stress is non-zero. The schematics here are two dimensional, but all presented calculations are fully three dimensional.

2.4 Results

2.4.1 Vacancies

Vacancies dominate mass transport in crystals by playing key roles in electromigration growth of voids in integrated circuit interconnects, impurity diffusion, and dislocation creep and climb. These processes are governed by the vacancy interaction arising from the stress field. Whether the stress field surrounding the core is linear or nonlinear directly determines the qualitative interaction between vacancies and influences our understandings of those processes. To measure the stress field using SALSA, we create a crystal of $2a$ =1.3 μm diameter silica particles via sedimentation in an index matched water-glycerol mixture. We image the 3D

microstructure of isolated vacancies (Fig. 2.2 (a)) and determine their stress fields.

The mean pressure of our crystal sample is $\sim$ 24 mPa (green line in Fig 2.2((b))), which is consistent with previous numerical predictions (orange curve) [1] and our Brownian dynamics simulations (blue dots) for hard-sphere crystals at $\phi \sim 0.59$ (purple line). The top row of images in Fig 2.2(c) show the vacancy 3D stress isosurfaces predicted by linear elasticity. The six independent stress components determined by SALSA are shown in the next row of Fig 2.2(c). For simplicity we show 2D cuts of each stress component along the (111) or x–y plane (green planes) centered at the vacancy core in the upper images. We also conduct Brownian dynamics simulations (see SI) and directly calculate particle stresses (second to last row of Fig 2.2(c)). The simulation results give quantitatively similar features for all stress components. For example, as shown in the first column of Fig 2.2(c), σ_{xy} exhibits a quadrupole distribution, which arises from the asymmetric collisions due to the absence of a particle at the vacancy core (blue and red arrows in Fig 2.2(a)).

The vacancy stresses also show non-trivial trends in the radial pressure distribution as shown in Fig 2.2(d) that are not captured by isotropic linear elasticity. In particular, while linear elasticity predicts a constant pressure outside the vacancy core, here we observe a pressure bump at $r \sim 3a$ that results from a $\approx 50\%$ reduction in particle surface separation near the core (double arrows in Fig 2.2(e)). In hard sphere systems this reduced separation, hence increased local collision rate, leads to an enhancement of the local modulus.

To account for this changing modulus, we develop an isotropic elastic model including all terms up to third-order with finite strain. Using the volume change ($\Delta V = 8.4\%$) estimated in experiments and literature values of the bulk ($K =$

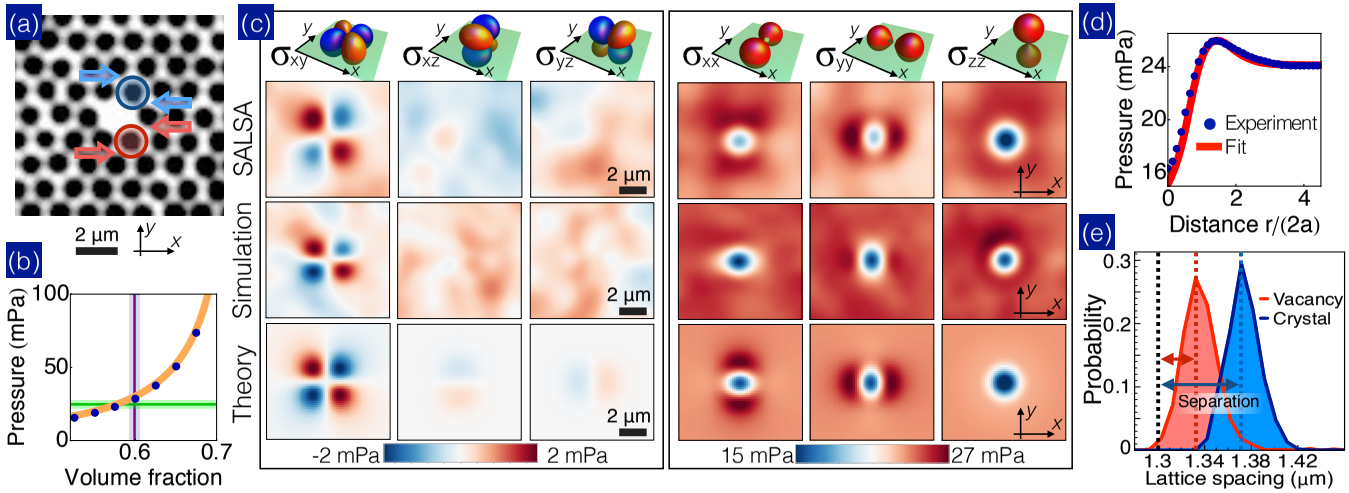

Figure 2.2: **Stress around a vacancy.**(a) Confocal image of a crystal with an isolated vacancy defect with no other defects within five lattice spacings in the plane, or in the adjacent layers along the (111) direction. The hard-sphere interparticle potential, large particle size, and high volume fraction slow down vacancy diffusion, which allows for time averaging. To account for particle polydispersity (SI) and the background stress we imaged 20 independent defects. Each vacancy is imaged for 20 seconds at a scan rate of 2 stacks per second, yielding a total of 800 snapshots for averaging. The absence of a particle at the defect core results in asymmetric collisions on the particles surrounding the vacancy. The upper right (blue) and lower right (red) particles are under positive and negative shear σ_{xy}. (b) SALSA accurately reports the mean pressure of the tested colloidal crystal with volume fraction 0.59 (purple line). Green line is the SALSA value. The blue dots are our hard sphere simulation results, and orange curve is the prediction from the literature. The shades of green and purple lines are the standard deviations. (c) All stress components around a vacancy determined using SALSA (upper row), simulation (middle row), and nonlinear elasticity (lower row). In contrast to the significant feature in σ_{xy}, we find that the small fluctuations in σ_{xz} and σ_{yz} are less than 20% of the variation in σ_{xy}. These measurements are consistent with the fact that both σ_{xz} and σ_{yz} exhibit nodes along the x-y plane. Additionally, we find that the normal stresses σ_{xx} and σ_{yy} demonstrate elastic dipoles that align horizontally and vertically, respectively.(d) Pressure is plotted as a function of distance d from the vacancy core. Both experimental (Blue) and theory (Red) results show clear stress enhancements at $d \sim 3a$. (e) Histograms of the particle separations near (red) and far away from (blue) the vacancy. The observed 50% change in surface-surface spacing would correspond to a $\sim 8.3\%$ local volume change in a defect free crystal.

93 mPa) and shear ($\mu = 92$ mPa) moduli for our system's volume fraction [49], we fit the pressure distribution by adjusting the three third-order isotropic elastic constants. We find the predicted stress distributions quantitatively reproduce all stress components (last row of Fig 2.2(c)) as well as the radial pressure distribution (red line Fig. 2.2(e)). Furthermore, the local modulus at the pressure ring region can be determined from the fitting. We find that the bulk modulus at that region more than doubles to 213 mPa. This drastically increased modulus is consistent with the value from numerical studies of bulk hard spheres [49, 1] at the local interparticle spacing of the pressure ring region. Overall, the strongly enhanced local modulus indicates a significant hardening near the defect core.

While linear isotropic theory predicts no interaction between vacancies, our findings indicate vacancies attract within the length scale associated with the pressure bump, as was predicted by numerical studies [5, 15, 33]. This attraction can be understood by noting that the volume change ΔV due to one vacancy is negative and so the $P\Delta V$ term in the elastic energy leads to a force that attracts that vacancy to the pressure ring of the other (see SI). Therefore, we estimate the elastic energy of the attraction $\sim 2.6\ k_B T$ at $r \sim 4a$. Since this attraction is several times larger than the thermal energy, it will significantly accelerate the aggregation of vacancies. In an atomic crystal, this large vacancy aggregate will form a void. For hard sphere crystals without attractive interactions, void formation is inhibited by large configurational entropies found at very low equilibrium defect density. At the vacancy densities in many experimental systems, however, voids form in equilibrium [5] and neighboring particles surrounding a void will 'evaporate' into the void, filling it with liquid-state particles in local equilibrium with the surrounding crystal.

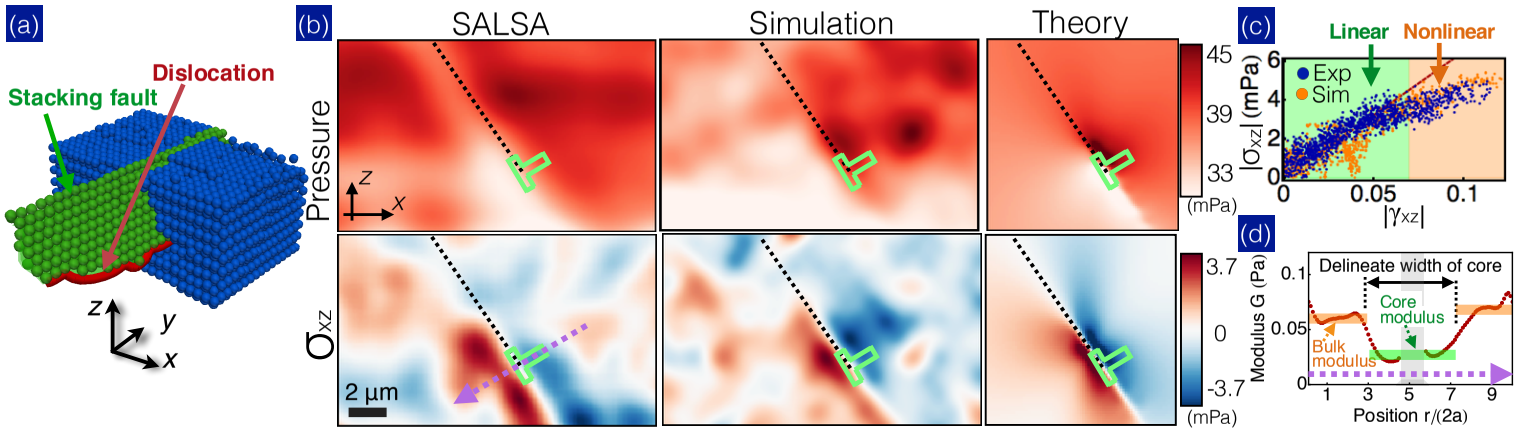

Figure 2.3: **Stress around a dislocation.**(a) 3D reconstruction of a partial dislocation (red line) and the associated stacking fault plane (blue) analyzed using the Dislocation Extraction Algorithm. (b) Pressure and shear stress, σ_{xz}, around a dislocation determined using SALSA (left column), simulation (middle column), and linear elasticity (right column). The experimental and simulation data are depth-averaged. In simulation, the experimental particle positions are used to determine appropriate initial and boundary conditions. The system is relaxed prior to recording the stresses to avoid particle overlaps due to featuring uncertainties. For the theory calculation, we use the observed Burgers vector and orientation of the partial dislocation to calculate the corresponding stress fields. (c) Both experimental and simulation stress-strain relations show softening behaviors at strains $|\gamma| \geq 0.08$ (orange region). (d) Shear modulus versus position for fields within 2μm of the purple line in (b). The modulus decreases by $\sim 50\%$ at the defect core, which is approximately four particles wide. Since the modulus value fluctuates in the gray area due to the sign changes in stress and strain, the corresponding points are removed for clarity.

2.4.2 Dislocations

Dislocations are one-dimensional topological defects whose collective interactions determine macroscale plasticity including work hardening, yield stress, and fatigue. At the high defect densities involved in such processes however, interactions are significantly altered by nonlinear stress fields surrounding these defects. One critical conjecture that has been widely employed in the dislocation simulation literature is that the modulus softens at the dislocation core [10, 23]. This conjecture however, has never been validated.

To study the dislocation stress field using SALSA, we grow a crystal on a patterned template with a lattice spacing 1.5% larger than the equilibrium crystal lattice. A 3D reconstruction of the particle configuration is shown in Fig. 2.3(a). The dislocation (red) delineates the lower bound of a stacking fault (green) embedded in a crystalline region (blue) which has been clipped for visual clarity. The dislocation is slightly curved (variation$\sim 2a$) and aligned along the y-axis corresponding to the $(1\bar{1}0)$ direction of the fcc lattice. The dislocation core is highlighted with a ($\perp$) and has a Burgers vector $1/6(\bar{1}\bar{1}2)$, which corresponds to a Shockley partial, the most prominent dislocation in fcc metals.

Using SALSA we measure the stresses near the dislocation and show the pressure (upper row) and shear stress, σ_{xz} (lower row) in Fig. 2.3. The stress field is averaged along the dislocation line to eliminate the effects of polydispersity. To confirm SALSA accurately extracts the stress features in this more complicated defect structure, we compare to stresses calculated by direct Brownian dynamics simulations that are seeded by the experiment data (middle column Fig. 2.3) (SI). Both experimental and simulation results show comparable features. Overall, we observe a pressure gradient across the stacking fault, and a shear stress

dipole centered at the defect core. These general trends are consistent with predictions of linear isotropic elastic theory (right column Fig. 2.3) indicating that dislocation curvature does not qualitatively alter the stress distribution. However, both SALSA (blue) and the simulation (orange) results show a non-linear strain softening in highly strained regions near the defect core (Fig. 2.3 (c)). This local modulus drop allows us to visualize the precise location and size of the dislocation core. To do so, we focus on the cross-section region denoted by the dashed line in Fig. 2.3(b), and plot nonlinear shear modulus ($d\sigma_{xz}/d\gamma_{xz}$) versus position ($r/2a$) in Fig. 2.3(d) (SI). The modulus decreases by $\sim 50\%$ on both sides of the dislocation core, which is about four particles in width. Overall, our measured modulus profile shows a softening consistent with the non-singular continuum assumption widely employed in dislocation theories and simulations [10, 23], in which the divergence in the stress at the dislocation core is cut off. Moreover, this modulus softening regularizes the interactions between dislocations and dramatically influences the dislocation creep behavior in crystals.

2.4.3 Grain boundaries

Grain boundaries are 2D structures important for crystal growth [21], melting kinetics [2, 45], transport properties [22], and can substantially harden materials through internal stress variation [50, 30, 37]. While X-ray microbeam experiments have been used to reveal *strain* fluctuations at the scale of 100 nm [37], measuring *stress* remains challenging at these scales, especially at the grain boundaries where particles are highly disordered.

To visualize such stresses using SALSA, we grow polycrystals using the same method described in the vacancy section (see Fig. 2.4 (a) for a confocal image). We

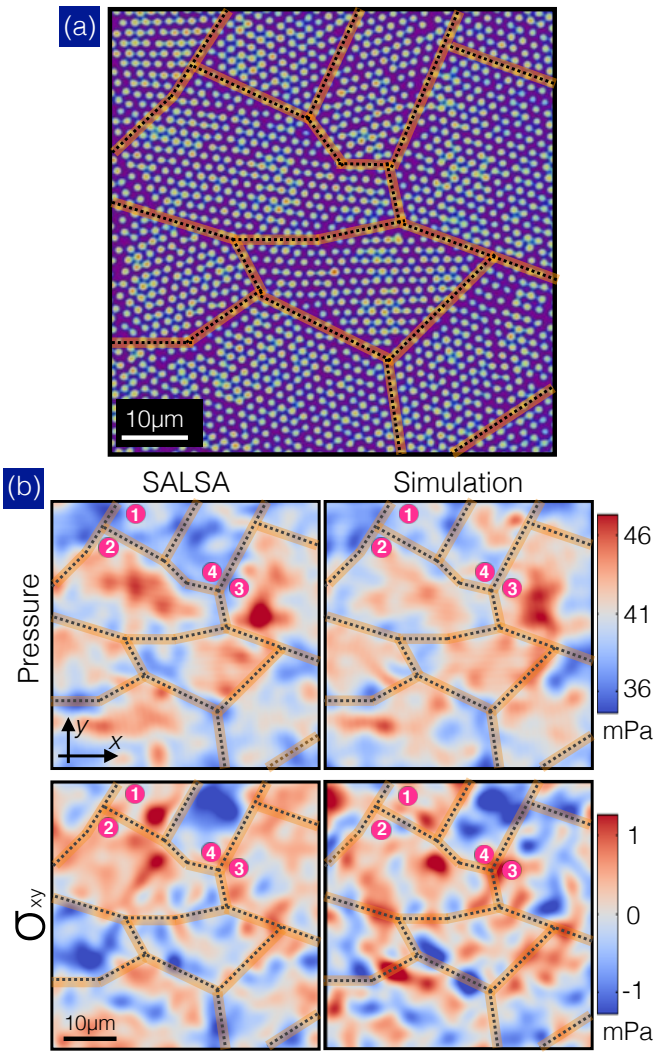

Figure 2.4: **Stress near grain boundaries.**(a) One confocal image slice of a time series consisting of fifty 3D stacks. (b) Pressure (upper) and σ_{xy} (lower) fields of the polycrystal. Both experimental (left) and simulation (right) results show qualitatively similar stress distribution features. The grain boundaries are indicated with dashed lines.

plot the measured pressure and shear stress σ_{xy} in the left column of Fig. 2.4(b). Just as for the dislocation simulation, we employ the featured particle positions as initial configurations, and simulate stresses in the polycrystal. The simulation results (right column in Fig. 2.4(b)) show similar features to the SALSA stress distributions in both pressure and shear components.

The spatial fluctuations in both pressure and shear stress seen in Fig. 2.4 (b) are significant compared to relevant stress scales. The standard deviation in pressure ($\approx$ 6 mPa) is about 15% of the mean pressure whereas the shear stress fluctuation ($\approx$ 0.7 mPa). To provide intuition, this stress level is about 30% of the stress magnitude one lattice constant from a dislocation core, the principle component of a tilt grain boundary. Moreover, we find that both pressure and shear stresses fluctuate between and within grains. For example, the mean pressure difference between grain 1 and 2 is 5 mPa (25%) whereas grain 3 shows an *intragrain* fluctuation of $\approx$10% the mean pressure. Similar trends can be seen in the shear stress difference between grains 1 and 4, and the fluctuations within grain 3.

2.5 Conclusion

Overall, our observation of the stress fluctuations in the polycrystal is consistent with previous simulations [54], and X-ray microbeam measurements [30, 37], where neighboring grains consisting of millions of atoms were found to have substantially different strains. The SALSA measurements indicate such stress fluctuations also arise *within* grains consisting of only hundreds of particles. These small crystallites are reminiscent of the nano-scale grains in atomic crystals. Previous atomistic simulations have predicted the stress fluctuations in a strained nanocrystal are

predominately localized to the grain boundaries [54]. In our colloidal crystal grains however, the stress fluctuations are spread roughly evenly throughout the grains (See SI for direct comparison). Our sample however has not been subject to shear. We conjecture that condensation of stress under plastic strain arises from trapping of dislocations at grain boundaries, grain boundary slip [54], or an as of yet unidentified mechanism.

In conclusion, we measure, for the first time, the microscale stress fields of crystalline defect cores that determine fundamental mechanisms governing processes ranging from local defect interactions to macroscale yielding. The ability to measure local stresses beyond the linear response regime opens the door to investigating systems driven further out of equilibrium by applied strains, and directly determine the stress precursors that generate material failure. More broadly, since SALSA can extract stresses without a reference lattice, this technique becomes particularly advantageous as the suspensions become even more disordered, as is the case in melting crystals, colloidal alloys, and glasses.

2.6 Acknowledgements

The authors thank F. Spaepen, J. Schiøtz, T. Lubensky, and the Cohen lab for useful discussions. J.S. and M.B. acknowledge funding from Department of Energy DOE-BES DE-FG02-07ER46393. P.S. acknowledges support by a VICI grant from the Netherlands Organization for Scientific Research (NWO). I.C. and N.L. were supported by NSF DMR-CMP Award No. 1507607.

2.7 Supplementary Information

2.7.1 Derivation of the SALSA method

Derivation

For a hard-sphere colloidal system, its bulk pairwise Brownian stress can be calculated by an integral over the three-dimensional pair correlation function $g(\vec{r})$ [18, 24, 32, 19].

$$\sigma_{ij}^{B} = nk_BTa \int_{S_2} \hat{r}_i \hat{r}_j n g(\vec{r}) dS_2 + nk_BT\delta_{ij} \tag{2.2}$$

Here, n is the number density of particles, k_BT is the thermal energy, a is the particle radius, and i, j are the indices of the stress tensor. The second term is the ideal gas stress contribution arising from the kinetic energy. The off-diagonal components of the first term, which usually dominate at high volume fractions, simply capture the anisotropy of $g(\vec{r})$ at contact surface S_2. To determine the stresses at the particle-level, we write the pair correlation function, $g(\vec{r})$, as an ensemble average of delta functions.

$$\begin{aligned} \sigma_{ij}^{B} &= \left\langle \frac{k_BTa}{\Omega} \int_{S_2} \hat{r}_i \hat{r}_j \frac{N}{V} \frac{V}{N^2} \sum_{\alpha} \sum_{\beta \neq \alpha} \delta(\vec{r} - \vec{r}^{\alpha\beta}) dS_2 \right\rangle + nk_BT\delta_{ij} \\ &= \left\langle \frac{1}{N} \sum_{\alpha} \frac{k_BTa}{\Omega} \int_{S_2} \hat{r}_i \hat{r}_j \sum_{\beta \neq \alpha} \delta(\vec{r} - \vec{r}^{\alpha\beta}) dS_2 \right\rangle + nk_BT\delta_{ij} \end{aligned} \tag{2.3}$$

where V, N, Ω are system volume, particle number, and particle volume, respectively. The bracket $\langle ... \rangle$ denotes an average over configurations and can be replaced with a time average in our system. In Eq. 2.3 we identify the outer sum as being an average over the particles in the sample, so we obtain an individual stress tensor

for each,

$$\begin{aligned}\sigma_{ij}^{\alpha} &= \frac{k_B T a}{\Omega^{\alpha}} \left\langle \int_{S_2} \hat{r}_i \hat{r}_j \sum_{\beta \neq \alpha} \delta(\vec{r} - \vec{r}^{\alpha\beta}) dS_2 \right\rangle + n k_B T \delta_{ij} \\ &= \frac{k_B T a}{\Omega^{\alpha}} \bar{\Psi}_{ij}^{\alpha} + n k_B T \delta_{ij} \end{aligned} \tag{2.4}$$

The elements of the sum $\bar{\Psi}_{ij}^{\alpha}$ can be identified as the fabric tensor linear density of particle α as the units work out to be $[1/L]$. This fabric tensor density directly reports the angular distribution of neighbors in contact with a particle while the magnitude of its trace is related to the total number of neighbors. To calculate $\bar{\Psi}_{ij}^{\alpha}$ in simulation and experiment, it is necessary to perform an average over a narrow interval $\Delta \ll 1$

$$\begin{aligned}\bar{\Psi}_{ij}^{\alpha} &= \left\langle \int_{S_2} \sum_{\beta \neq \alpha} \hat{r}_i \hat{r}_j \delta(\vec{r} - \vec{r}^{\alpha\beta}) dS_2 \right\rangle \\ &\approx \left\langle \frac{1}{\Delta} \int_{S_2} \int_{a}^{a+\Delta} \sum_{\beta \neq \alpha} \hat{r}_i \hat{r}_j \delta(\vec{r} - \vec{r}^{\alpha\beta}) dS_2 dr \right\rangle \\ &= \frac{1}{\Delta} \left\langle \sum_{\beta \in \Delta} \hat{r}_i^{\alpha\beta} \hat{r}_j^{\alpha\beta} \right\rangle \end{aligned} \tag{2.5}$$

where Δ is the thickness of the measurement shell and $\hat{r}^{\alpha\beta}$ is the unit vector connecting the centers of particles α and β. Using this particular form, the SALSA formula reads

$$\begin{aligned}\sigma_{ij}^{\alpha} &= \frac{k_B T}{\Omega^{\alpha}} \left(\frac{a}{\Delta}\right) \left\langle \sum_{\beta \in \Delta} \hat{r}_i^{\alpha\beta} \hat{r}_j^{\alpha\beta} \right\rangle + n k_B T \delta_{ij} \\ &= \frac{k_B T}{\Omega^{\alpha}} \left(\frac{a}{\Delta}\right) \Psi_{ij}^{\alpha}(\Delta) + n k_B T \delta_{ij} \end{aligned} \tag{2.6}$$

where Ψ_{ij}^{α} can now be identified as the fabric tensor of particle α. In general, the shell thickness $\Delta \ll 1$ should be small enough that the measurement result σ_{ij}^{α} becomes independent of the particular choice of Δ. In the calibration section,

we perform experiments and simulations to confirm this independence. The details concerning the particle volume Ω^α and converting the pointwise stresses to continuum fields are discussed in later sections.

Finally, it is possible to extend our particle-level stress calculations to other finite potentials including the depletion force [47, 51, 64], paramagnetic [68] and electrostatic [66] interactions, and soft particles [44, 11]. While similar calculations have been performed at the bulk scale [68], extending our method to these systems would allow us to further investigate their heterogeneous elastic properties.

Local structural anisotropy tensor

The local structural anisotropy tensor reports the instantaneous arrangement of colliding neighbors. The trace of this tensor, $\hat{r}_i\hat{r}_i$, is the total number of neighbors while the remaining terms capture the anisotropy of the collisions. As an illustration, we consider a two-dimensional case. Assuming one particle is at the origin and in contact with one other particle at an angle θ with respect to the x-axis then the fabric tensor can be written as

$$r_i r_j = \begin{bmatrix} \hat{r}_x\hat{r}_x & \hat{r}_x\hat{r}_y \\ \hat{r}_y\hat{r}_x & \hat{r}_y\hat{r}_y \end{bmatrix} = \begin{bmatrix} \cos^2\theta & \sin\theta\cos\theta \\ \sin\theta\cos\theta & \sin^2\theta \end{bmatrix}.$$

Here, the trace $\sin^2\theta + \cos^2\theta$ is always 1 and a maximum shear is achieved at four locations, $\theta = \pm\ 45°$ and $\pm\ 135°$. These directions correspond to the maximal compression and extension axes. For instance, if θ is 30°, then the trace is $(\sin^2 30°) + (\cos^2 30°) = 1$, and the shear component is $\hat{x}\hat{y} = \hat{y}\hat{x} = (\sin 30°)(\cos 30°) = \sqrt{3}/4$. Similarly, if θ is 90°, while the trace remains unity,

the shear component becomes $\hat{x}\hat{y} = \hat{y}\hat{x} = (\sin 90°)(\cos 90°) = 0$.

From pointwise functions to continuum fields

In the literature of molecular dynamics simulation, the virial

$$s_{ij}^{\alpha} = \frac{1}{2}\sum_{\beta \neq \alpha} \frac{\partial V(r)}{\partial r}\frac{r_i r_j}{r} + m v_i v_j \tag{2.7}$$

has been widely used to report stresses at the atomic level [16, 35, 54]. In particular, this quantity has been used to measure many interesting phenomena including the stress correlation length in liquid metals [35] and stress fluctuations near grain boundaries [54]. While the sum of the virials s_{ij} divided by system volume V yields the bulk stress of the system, there are multiple choices that can be made as to how to incorporate local volume variation and how to smooth the pointwise stress into a continuum field. Similar to the Irving-Kirkwood-Noll procedure, which constructs continuum fields from the underlying discrete distribution with phase averaging, we perform a spatial average to obtain a macroscopic measurement at the particle-level [61]. The final continuum stress field $\sigma_{ij}^{cont}(\vec{x};t)$ is given by

$$\sigma_{ij}^{cont}(\vec{x};t) = \int_{\vec{y}\in R} w(\vec{y}-\vec{x})\sigma_{ij}^{pt}(\vec{x};t)d\vec{y} \tag{2.8}$$

where $w(\vec{r})$ is a weighting kernel function, and $\sigma_{ij}^{pt}(\vec{x};t)$ is the pointwise function. Here, the weighting function w must be normalized so that the total energy is conserved during spatial averaging. We use a normalized Gaussian function that weights values closer to $\vec{x}$ more strongly than other points that are further away:

$$w(r) = \pi^{-3/2} r_w^{-3} e^{-\frac{r^2}{2r_w^2}} \tag{2.9}$$

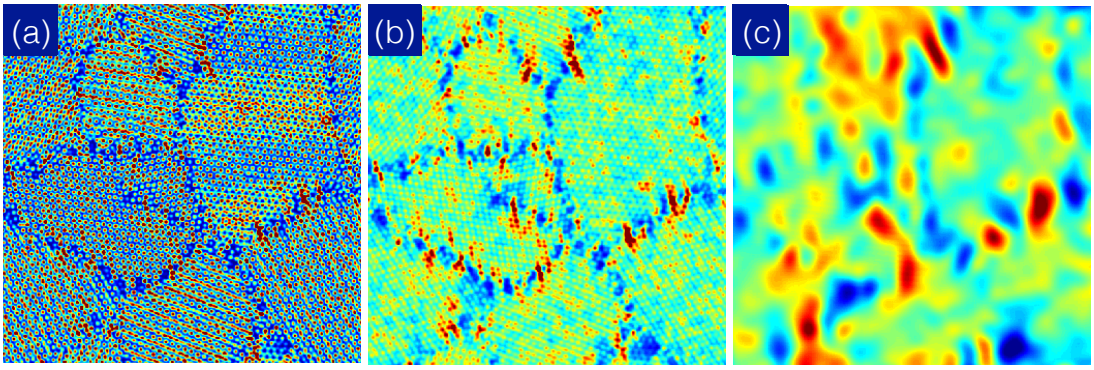

Figure 2.5: **Spatially smoothed stress fields of a simulated polycrystal**We plot the smoothed stressed field of a polycrystal as a function of filter size $r_w/2a$ at (a) 0.2 (b) 0.3 and (c) 1. For small $r_w/2a$, only the points containing particle centers with assigned stresses have nonzero values. As the value of $r_w/2a$ increases, the stress field becomes smoother and more continuous. Note that since the weighting Gaussian function is normalized, the overall stress of the system is the same for all different $r_w/2a$. The color scale is adjusted for each sub figure to emphasize the stress variation features. In all calculations, we use the value $r_w/2a = 1$, where the features of individual particles are no longer distinguishable.

where $r = \|\vec{r}\|$, and the filter size r_w is chosen to emphasize the length scale of the continuum fields of interest [61]. Similar smoothing algorithms have been implemented in previous literature [43, 42, 25, 4].

In our experiments and simulations, we set $r_w/2a = 1$ so that we remove stress features on length scales smaller than a particle. The pointwise stress is constructed by first assigning calculated particle virial, $\sigma_{ij}^{\alpha}\Omega^{\alpha}$ to their corresponding grid boxes, then dividing their values by the box volume. This pointwise function shows singularities at particle centers and zero elsewhere. Finally, we smooth the field using the Gaussian kernel, Eq. 2.9. We show the spatial averaged continuum fields of a simulated polycrystal for three different filter sizes r_w in Fig. 2.5.

In this spatial averaging procedure, the influence of local volume variation on

the stress distribution is already incorporated. In particular, as the occupied volume of a particle increases, the stress is proportionally reduced due to the increased effective averaging volume. Furthermore, the final fields are nearly independent of the grid size and the mean stresses are constant at all values of r_w.

To explore how the filter size r_w affects our final SALSA stress fields, we show the experimental vacancy stress field, σ_{xy} for five different values of r_w in Fig. 2.6(a). We find that the feature of the stress quadrupole [2] remains discernible up to $r_w = 2.7(2a)$. Note in Fig. 2.6(a), while the quadrupole distribution theoretically diverges as $1/r^3$, it is cut off by the lattice and smoothed over the distance r_w, squelching the stress features near the vacancy core. Similarly in Fig. 2.6(b), we find that the near field of the pressure is strongly affected by the filter, but the long-range nonlinear pressure ring at $r_w = 1(2a)$ and $1.3(2a)$ match each other. Indeed, the long-range stresses from all defects have correspondingly slow variations, and hence will be invariant to the choice of r_w. The filter size choice is a balance – hiding noise at lengths $r < r_w$ to enhance features of size $r > r_w$.

In terms of elastic theory, the filter size can be thought of a regularization for the theory, renormalizing higher order terms in the elastic free energy. To see how smoothing affects these terms, consider how smoothing changes a linear elastic free

[2] There is a nomenclature problem when describing the stress and strain around a point defect. Some describe them as quadrupolar fields, reflecting the similar $\cos 2\theta$ angular dependence with electrical quadrupoles. This angular dependence is special, however, to isotropic elastic theory; also, the displacement field has a 'monopolar' isotropic component $\Delta V/(4\pi r^2)$ with no angular dependence. (However, as noted in Fig. 2.7, the off-diagonal stresses for an isotropic vacancy still look like quadrupoles.) Some describe them as elastic dipoles, reflecting both the common $1/r^3$ force law with electric dipoles and their origins as 'force dipoles' (two opposite forces acting on nearby points in the elastic medium.) Finally, others (particularly studying elasticity in amorphous systems) name the field after Eshelby – thus bypassing the choice by using an uninformative label. Here, we use the term quadrupole, mostly because the 'strength' of a point defect is quantified by a 3x3 symmetric matrix (either the strain quadrupole Q_{ij} described here, or the corresponding stress quadrupole / force dipole.) We must note, however, that in the present case of vacancies in a cubic environment, $Q_{ij} = \Delta V \delta_{ij}$ has no correspondence to electric quadrupoles, which are traceless.

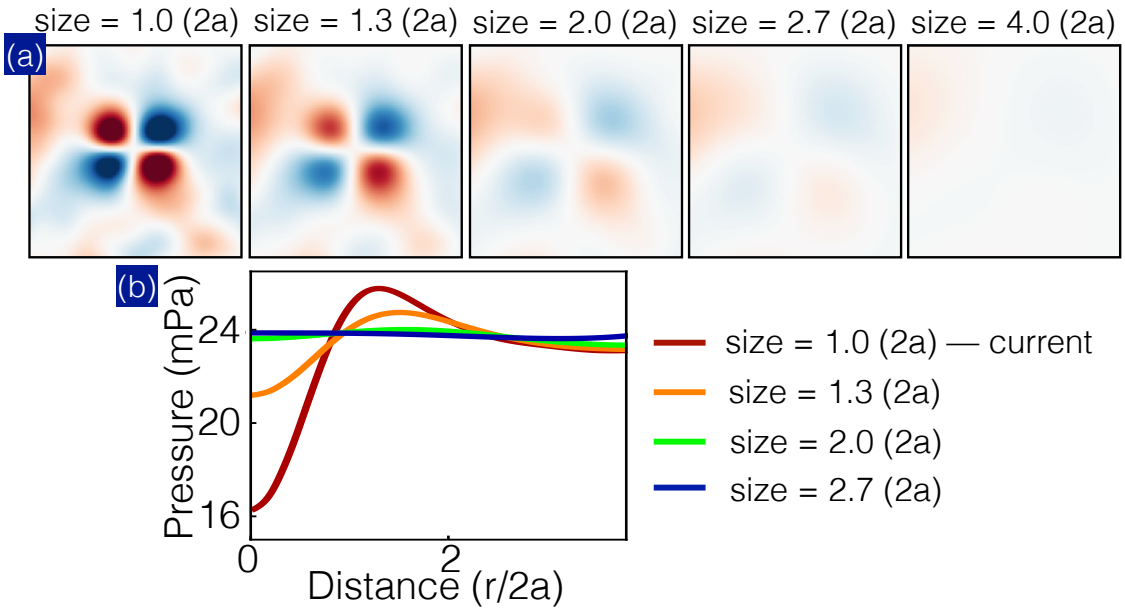

Figure 2.6: **Spatially smoothed stress fields of a vacancy.**(a)The values of smoothing length scale r_w from left to right are 1.0×2a, 1.3×2a, 2.0×2a, 2.7×2a and 4.0×2a, respectively. (b) The radial distribution of pressure for different r_w.

energy

$$\mathcal{F}_0 = \int d^3r \, S_{ijkl} \, \sigma_{ij} \, \sigma_{kl} \tag{2.10}$$

where S_{ijkl} is the elastic compliance tensor and σ_{ij} is the stress tensor. If we smooth the stress tensor using a Gaussian kernel of size r_w this linear elastic theory changes to

$$\begin{aligned}
\mathcal{F}' &= \int d^3r \, d^3k \, d^3k' \;\; S_{ijkl}[\sigma_{ij}(\vec{k})e^{-k^2r_w^2/2}e^{i\vec{k}\cdot\vec{r}}][\sigma_{kl}(\vec{k}')e^{-k'^2r_w^2/2}e^{i\vec{k}'\cdot\vec{r}}] \\
&= \int d^3k \;\; S_{ijkl} \, \sigma_{ij}(\vec{k}) \, \sigma_{kl}(-\vec{k}) \, e^{-k^2r_w^2} \\
&\approx S_{ijkl} \int d^3k \;\; (1 - k^2r_w^2) \, \sigma_{ij}(\vec{k}) \, \sigma_{kl}(-\vec{k}) \\
&= \int d^3k \;\; S_{ijkl} \, \sigma_{ij}(\vec{k}) \, \sigma_{kl}(-\vec{k}) - \int d^3k \;\; S_{ijkl} \, k^2r_w^2 \sigma_{ij}(\vec{k})\sigma_{kl}(-\vec{k}) \\
&= \mathcal{F}_0 - r_w^2 \int d^3k \;\; S_{ijkl}(k_m\sigma_{ij}(\vec{k}))(k_m\sigma_{kl}(-\vec{k}))
\end{aligned}$$

What new terms must we add to $\mathcal{F}'$ to cancel the second term? Since each factor

of k introduces a gradient, we can check that a stress gradient term $S_{ijkl}\partial_m\partial_m\sigma_{ij}\sigma_{kl}$ has the correct form.

$$\begin{aligned} S_{ijkl}\int d^3r\ \partial_m\partial_m(\sigma_{ij}\,\sigma_{kl}) &= S_{ijkl}\,\partial_m\partial_m\int d^3r\,d^3k\,d^3k'\ e^{-i\vec{k}\cdot\vec{r}}\sigma_{ij}(\vec{k})\,e^{-i\vec{k}'\cdot\vec{r}}\sigma_{kl}(\vec{k}') \\ &= -2S_{ijkl}\int d^3r\,d^3k\,d^3k'\ k_m k'_m e^{-i\vec{k}\cdot\vec{r}}\sigma_{ij}(\vec{k})\,e^{-i\vec{k}'\cdot\vec{r}}\sigma_{kl}(\vec{k}') \\ &= -2S_{ijkl}\int d^3k\ k_m k_m\sigma_{ij}(\vec{k})\sigma_{kl}(-\vec{k}) \end{aligned}$$

Indeed, the energy regularized by smoothing by r_w is the original free energy plus a filter size-dependent term times a stress gradient energy:

$$\mathcal{F}' \approx \mathcal{F}_0 + \frac{r_w^2}{2}S_{ijkl}\int d^3r\ \partial_m\partial_m(\sigma_{ij}\,\sigma_{kl}) \tag{2.11}$$

Similarly, nonlinear and other terms in the energy will produce regularization-dependent counter terms. We will now demonstrate that these gradient terms contribute less to the free energy than other nonlinear terms in the case of hard sphere crystals.

Let us consider the long and short wavelength behavior of the first nonlinear and gradient terms of the elastic free energy to see which dominates the behavior both close and far from a defect. For isotropic elasticity, the allowed terms that arise in the free energy density are

$$\mathcal{F} = C_{ijkl}\epsilon_{ij}\epsilon_{kl} + D_{ijklmn}\epsilon_{ij}\epsilon_{kl}\epsilon_{mn} + E_{ijklmn}\partial_i\partial_j\epsilon_{kl}\epsilon_{mn} \tag{2.12}$$

where the allowed elements of the elastic constant tensors C, D, and E are determined by the symmetries of the system being studied. In the case of isotropic materials, these tensors must be built using terms that are formed by δ_{ij} and Δ_{ijkl} and $\mathcal{D}_{ijklmn}$, the Kronecker delta and the four and six index equivalents of the

Kronecker delta. That is, the parts of the free energy may be written

$$\mathcal{F}_C = c_0\,\epsilon_{ii}\epsilon_{jj} + c_1\,\epsilon_{ij}\epsilon_{ij}$$

$$\mathcal{F}_D = d_0\,\epsilon_{ii}\epsilon_{jj}\epsilon_{kk} + d_1\,\epsilon_{ij}\epsilon_{ij}\epsilon_{kk} + d_2\,\epsilon_{ij}\epsilon_{jk}\epsilon_{ki}$$

$$\mathcal{F}_E = e_0\,\partial_i\partial_i\epsilon_{jj}\epsilon_{kk} + e_1\,\partial_i\partial_j\epsilon_{ij}\epsilon_{kk} + \cdots$$

Which terms should we keep to describe the elastic fields? We consider their contributions in the case of the elastic field of a vacancy defect – since the displacement field for linear theory goes as $u(r) \sim \Delta V/r^2$, the strain field goes as $\epsilon \sim \Delta V/r^3$. The quadratic term then has energy density which scales as r^{-6}, while the nonlinear cubic term (ϵ^3) scales as r^{-9} and the gradient term as $r^{-1}r^{-1}r^{-3}r^{-3} = r^{-8}$. For short range behavior, the nonlinear contributions are nearly equal, with the cubic term contributing more for $r \ll 1$. However, we also need to consider the magnitude and scaling of the coefficients for each term. In the case of the cubic elastic constants, we know from the equation of state that the pressure diverges at maximal packing as $P \sim (\phi_c - \phi)^{-1}$, implying that e.g. the bulk modulus diverges as $K = \phi\frac{\partial P}{\partial \phi} \sim (\phi_c - \phi)^{-2}$ [46]. If we write the scaling in terms of the two length scales in the problem, the lattice constant a and the surface to surface distance Δ, we find that the cubic term in the free energy goes as $(a/\Delta)^{-2}r^{-9}$ and the first gradient term as a^2r^{-8}. In the case $(a/\Delta) \ll 1$, we find that the cubic terms dominates the gradient contributions. It is for this reason as well as the fact that gradient terms are not unique in our smoothing scheme that we only consider nonlinear elasticity without gradient terms.

2.7.2 Calibration of the SALSA method

To validate our SALSA measurements, it is crucial to calibrate the method and evaluate its performance and dependence on input parameters. We divide the calibration section into three parts: A) comparison with simulation stresses, B) contact criteria dependence, and C) force balance in a smoothed field. We show that the SALSA method accurately captures the stress fields as calculated by Brownian dynamics very well. The stress field determined by using SALSA is not significantly sensitive to the particle contact criteria e.g. the shell thickness Δ. Finally, we discuss a systematic residual force within the vacancy core in the continuum stress field due to the smoothing process and compare the elastic fields to similarly smoothed continuum calculations.

Calibration: SALSA versus actual stress

To evaluate how well SALSA is able to report the correct stress field of a complex system, we use Brownian dynamics (BD) to generate a vacancy in a simulated crystal, whose orientation is matched to that found in our experiments. We use SALSA to determine all six independent stress components and compare their values with the BD stress calculation using the same set of position data (see Fig. 2.7). The continuum stress field from BD is constructed by spatially averaging pointwise virials $F_i x_j$. We see that the BD and SALSA stresses exhibit a good match. We also find that SALSA stresses become more quantitatively similar to the actual stress fields as a longer time-average is performed (not shown).

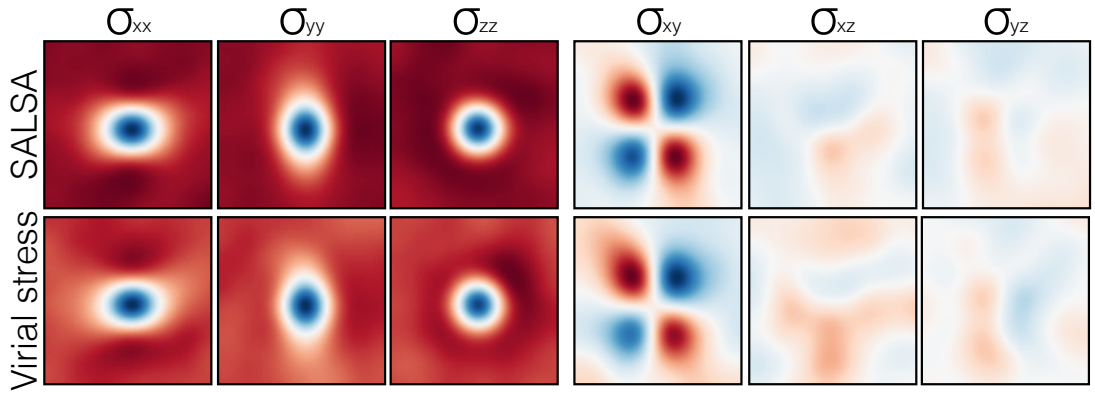

Figure 2.7: **SALSA and actual stresses comparison.**Stresses determined through the SALSA method (top row) are compared with the stresses directly calculated in simulation (bottom row) using the same dataset.

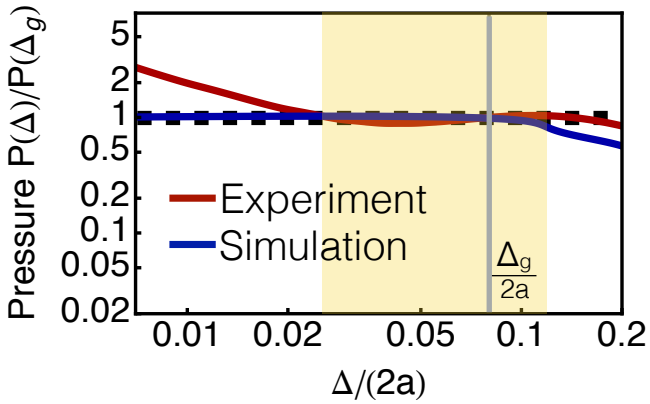

Figure 2.8: **SALSA pressure versus Δ in experiment and simulation**. Pressure measured using different shell thickness Δ is plotted as a function of Δ. The pressures values $P(\Delta)$ are normalized by $P(\Delta_g)$ where $\Delta_g + 2a$ is the position of the $g(r)$ first peak, which is denoted by the gray line. The vacancy experimental data (red curve) shows that SALSA method generates quantitatively consistent results in a wide range of shell thickness $0.03(2a) \leq \Delta \leq 0.15(2a)$ (shaded area). The corresponding length scale of this thickness range is 40 nm $\leq \Delta \leq$ 230 nm. The simulation data (blue curve) demonstrate an even wider pressure plateau that extends beyond $\Delta \sim 10^{-4}(2a)$. The diverging trend of the experimental pressure at small Δ occurs due to slight particle overlaps arising from featuring uncertainties.

Calibration: Contact criteria dependence

There is another parameter in the SALSA method, which is the shell thickness Δ used to identify particles in contact. This shell thickness directly determines the number of particles that are included in the stress calculation, larger Δ allowing for shorter time averages. However, at large Δ, the radial distribution of particles $g(r)$ will vary through out the thickness of the shell, leading to systematic errors in stress. We test for the optimum by calculating the pressure of a system versus $\Delta/2a$. Fig. 2.8 shows the SALSA pressure $P(\Delta)/P(\Delta_g)$ versus $\Delta/2a$ for both experimental and simulation data. Here, $\Delta_g/2a$ (gray line in Fig. 2.8) is the cutoff thickness used throughout our analysis of the experiments, where $2a + \Delta_g$ roughly coincides with the first peak of $g(r)$. We find that the measured pressure has negligible dependence on $\Delta/2a$ for $\Delta/2a \leq 0.12$. In the experiment the normalized pressure deviates from 1 when Δ is smaller than $\sim 3\%$ of the particle size, corresponding to $\approx 1/4$ of a pixel (~ 35 nm). This trend arises due to particle overlaps from featuring uncertainties. Overall, as shown in Fig. 2.8, both the experimental and simulation results indicate an insignificant correlation between the SALSA pressure and shell thickness Δ in the range of 35 nm $\leq \Delta \leq$ 230 nm (yellow shaded area).

Finally, we also investigate how the shell thickness Δ affects the spatial distribution of stresses. We show the experimental pressure and σ_{xy} fields near a vacancy for four different Δ in Fig. 2.9. Again, we find that the stress fields for all Δ demonstrate qualitatively similar trends, where the pressure exhibits an enhancement surrounding the defect core and σ_{xy} shows a quadrupole distribution. This weak Δ dependence is consistent with the previous experimental studies [12, 52] where the authors have found that different contact criterion consistently generate

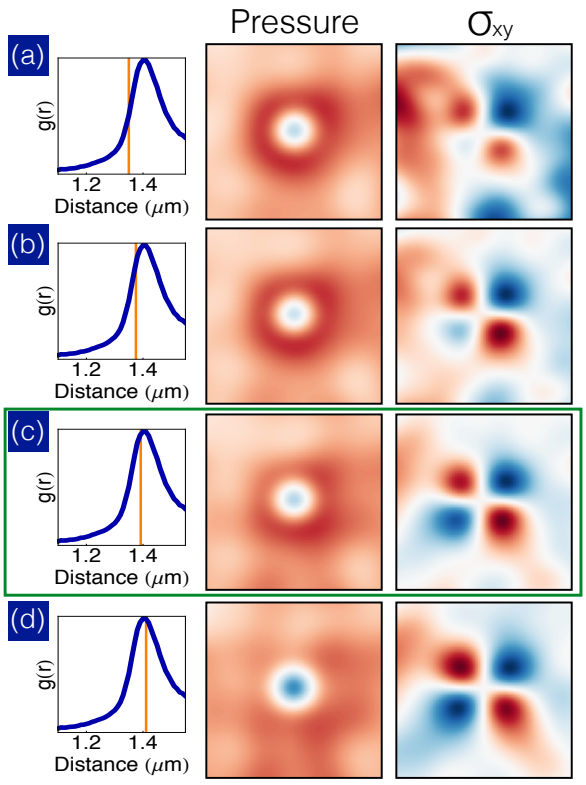

Figure 2.9: **Pressure and σ_{xy} fields for different** ΔPressure (middle row) and shear stress σ_{xy} (right row) distributions for four different values of shell thicknesses. (c) The contact criteria used throughout our experiments. The pair correlation functions $g(r)$ (left row) are plotted to illustrate the differences between the shell thickness Δ choices (orange lines).

similar bulk Brownian stresses. Here, we provide a similar calibration but at the particle level. As shown in Fig. 2.9, it is remarkable that SALSA is able to produce consistent results with a wide range of shell thickness 35 nm $\leq \Delta \leq$ 150 nm. This wide window of Δ choice promises robust stress measurements in the typical colloidal experiments with 3D imaging, where the particle positions can be precisely determined with a sub-pixel resolution ($\leq$ 50 nm) using standard featuring algorithms.

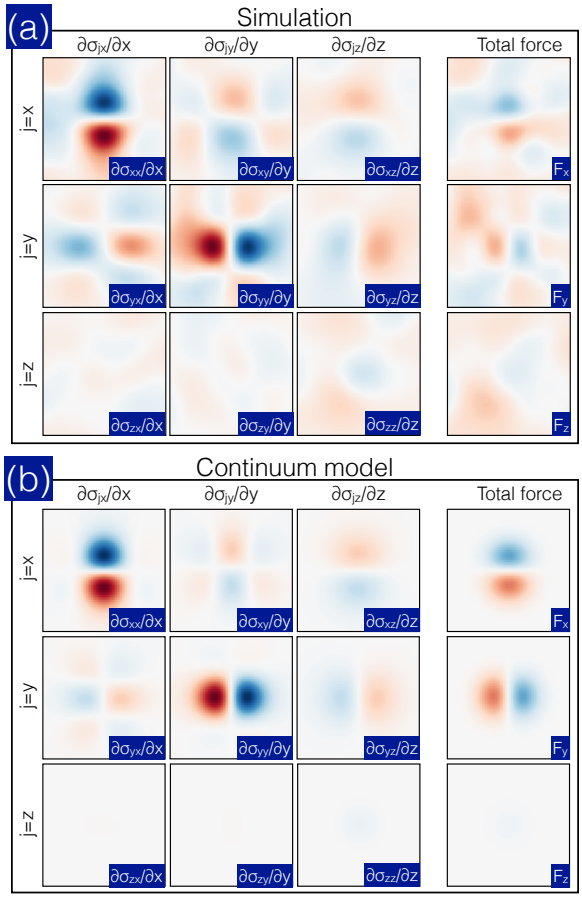

Figure 2.10: **Force balance of vacancy.**The right-most frames show the divergence of the stress fields from simulation (a) and continuum theory (b). In the group of nine panels in each of these subfigures, we show the components of the divergence of the stress. Summing along each row, we find the total force as the sum of the gradients. Both the BD simulation and continuum elastic fields show systematic force dipoles in their center indicating that the small residual forces are produced not from the SALSA method but from the choices made in creating a continuum field.

Calibration: Mechanical equilibrium of a smoothed field

In principal, it is possible to further determine the continuous force field by calculating the divergence of the smoothed stress distribution. In our experiments, where all the studied regions are stationary, the calculated force field should be zero implying a mechanical equilibrium. It has recently been shown that this mechanical equilibrium of the microscopic stress closely depends on the details of the stress definition at particle-level [63]; it is important to check it for SALSA. To investigate this issue, we calculate the divergences of the vacancy SALSA stresses in simulation (Fig. 2.10 (a)). We find that the force fields are consistent with zero everywhere except the region of the defect core, where the force shows a dipole distribution in all components. Since there is no particle in the region that violates mechanical equilibrium, it is unclear whether this force imbalance leads to a particle drift or not. Nevertheless, to confirm that this is only a result of the smoothing procedure, we perform a similar analysis on calculated continuum elastic fields. In doing so, we mimic the SALSA measurements by introducing a pressure hole in the center, and smooth the stress fields with the same kernel used in the simulation. As shown in Fig. 2.10 (b), the force fields from continuum theory also display force dipoles consistent with SALSA and BD stress fields. This consistency clearly indicates that the force imbalance mostly arises from the pressure drop and smoothing algorithm rather than the SALSA calculation.

To further characterize the magnitude of the force imbalance, we perform a similar mechanical equilibrium calibration in a simulated polycrystal. In particular, we construct a three dimensional box enclosing a grain boundary. Then we determine the net force acting on this box by calculating the tractions from stresses. We find that the forces correspond to the shear and normal tractions approximately

cancel each other, indicating a good mechanical equilibrium. The residual force can then be related to a drift arising from this force imbalance given that the system is over-damped. Finally, we find that the drift, which is independent of the box size, is less than 5% of the particle diameter over the entire simulation.

2.7.3 Vacancy Stress Fields

Experimental details

We create a colloidal crystal consisting of 1.3 μm diameter silica particles via sedimentation in a sealed sample cell. The particles are suspended in a water-glycerol mixture with a refractive index matching the silica particles. This matched refractive index allows us to acquire confocal images of the sample. Vacancy defects form spontaneously during sedimentation (along with stacking faults and grain boundaries), and are imaged directly using a high-speed confocal microscope. In the measurements, we select isolated vacancies that contain no other defects within five lattice spacings in the plane or in either of the adjacent layers perpendicular to the plane.

Since the system is thermal, it is important to perform a time average to correctly determine the equilibrium stress field. Therefore, we record, analyze, and average the stress fields over 60 snapshots (20 seconds). We further average the stress field over 20 vacancies to reduce the effects of polydispersity and the local vacancy environment. In Fig. 2.11, we show the confocal images of all measured vacancies in the experiment (the horizontal slices of full 3D confocal image stacks) to illustrate the vacancy morphology. As shown in Fig. 2.11, the independent vacancies have random orientations with respect to the microscope and must be

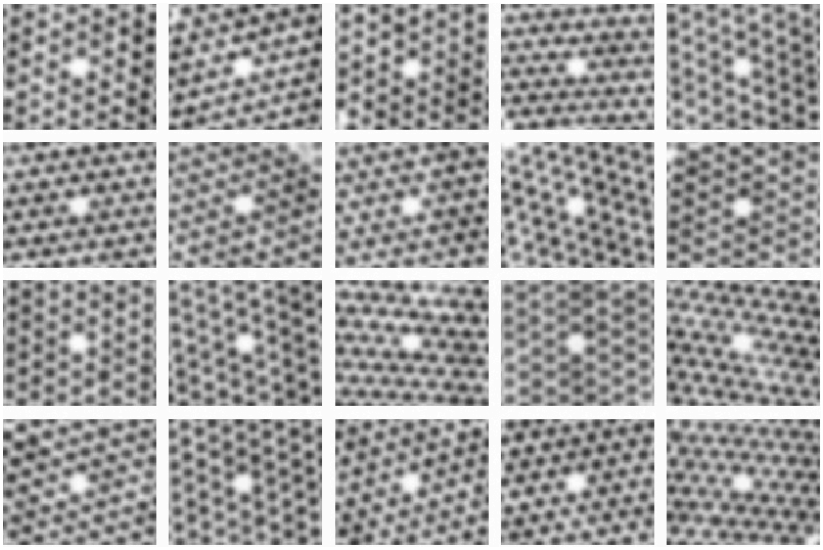

Figure 2.11: **Confocal images of 20 isolated vacancies**

aligned before averaging. With all images aligned in the same orientation, we then calculate the stress field of each sample and average over 20 seconds. This time interval is sufficiently long for the colloids to explore the local phase space as the time required to diffuse one particle separation (100 nm) in the absence of obstructing neighbors is about 0.35 s. Finally, we average the per-vacancy stress field over all 20 samples.

Since SALSA solely relies on the particle positions to determine the stress field, the correctness of final measurements directly depends on the accuracy of particle featuring and noise in the experiment. We employ both time and sample averages to remove noise and improve such measurement accuracies. Uncorrelated noise such as the current noise in the electronics, can be effectively reduced by using a time average. On the other hand, there is correlated noise that result in a persistent featuring bias in time, including spherical aberration in the optics [58, 57, 62], the microscope point-spread-function [6, 27, 56], and particle polydispersity [41]. In the vacancy experiment, we minimize the effects of spherical aberration and

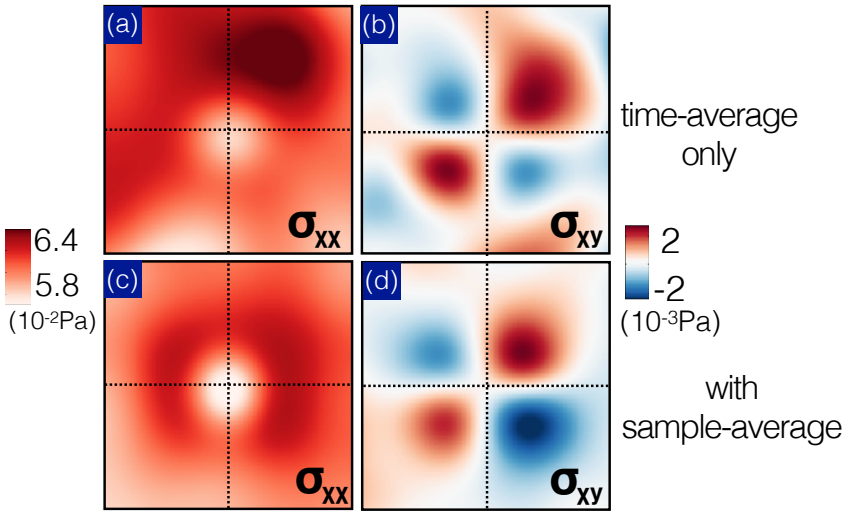

Figure 2.12: **Effects of sample average**.
Comparison of time average and sample average on a normal component σ_{xx} (a,c) and shear component σ_{xy} (b,d). We see that sample average improves the measurement of the normal component more than the shear components due to the effects of polydispersity.

point-spread-function by index-matching the sample within 0.1% and confining the imaging field to a few particles away from the coverslip. Polydispersity also affects our ability to determine which particles are in contact. For instance, when two larger particles are touching, the SALSA method may identify them as not in contact because their center-to-center distance is larger than $2\langle a\rangle + \Delta$, the mean distance between particles plus the shell thickness. The polydispersity ($\approx$ 35 nm for our silica colloids) is about 30% of the shell thickness Δ = 106 nm used in our experiment. In the vacancy experiment, by averaging the stress field over 20 different samples, the collision uncertainty due to polydispersity is further reduced by a factor of $\sqrt{20} = 4.5$.

Furthermore, we find that the polydispersity has different effects on the pressure and shear stress measurements. We show two representative stress components σ_{xx} and σ_{xy}, first time averaged, Fig. 2.12 (a) and (b), and then with an additional

sample average, Fig. 2.12 (c) and (d). We find that the pressure does not fully capture the enhanced stress ring around the vacancy defect if only a time average is applied. However, the shear component of the same time-averaged data already shows a clear quadrupole structure that is very similar to the one with additional sample averaging. This finding implies that while the pressure measurement may rely on a more precise identification of touching particles, the shear measurement is relatively robust and insensitive to the noise. In contrast to the normal stresses that are strongly associated with the collision (touching) probability of surrounding particles, the shear components are more related to the angular anisotropy of the neighboring particle configurations. Finally, it is also possible to avoid the effects of polydispersity by determining the individual particle size and taking the size variation into account [31].

Simulated vacancy stresses

We confirm the experimental findings by simulating the stress of a vacancy in a colloidal crystal using nearly hard-sphere Brownian dynamics. Here, we numerically simulate the Langevin dynamics of N particles interacting through a very sharp radial potential $V(r)$. We do so using cell neighbor lists calculated on an NVIDIA GPU integrating with the velocity Verlet algorithm. The virials of each particle, calculated through Eq. 2.7, are used to compare directly to the stresses calculated with the SALSA method.

Based on previous literature [52], we have tried several interparticle potentials including the Yukawa potential, pure power law, and smoothed power law. Here we use the smoothed power law to ensure continuity in derivatives:

$$V(r) = \mathcal{E}\left(\frac{r}{r_0} - 1\right)^2 \left(\frac{r_0}{r}\right)^{24} \tag{2.13}$$

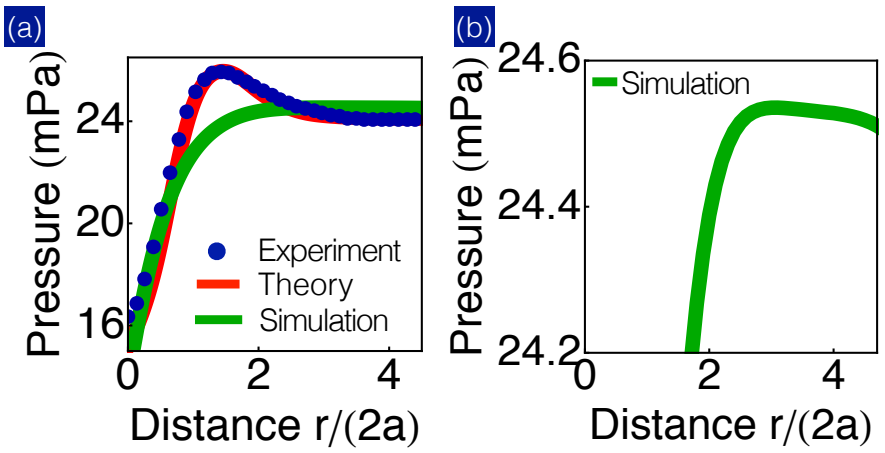

Figure 2.13: **Vacancy pressure distribution.**Comparison of experimental (blue dots in (a)), theoretical (red line in (a)), and simulation (green line in (b)) pressure. Despite its relatively insignificant feature, the simulated vacancy pressure also exhibits a pressure enhancement at $r \sim 4a$. All individual stress components in experiment, theory, and simulation show qualitatively similar results.

To simulate the vacancy, we begin with a periodic cell of a fcc crystal with the same physical parameters as the experimental setup. We create a periodic cell containing $2^{14} = 16384$ particles at a packing fraction of $\phi = 0.59$, temperature $T = 300\, k_B T$ and viscosity $\eta = 10^3$. We remove the center particle and simulate for 2500 snapshots where each snapshot is separated by $t = 10\tau$ diffusion times. The stress of these particle configurations is calculated using both the simulation virial and SALSA and averaged over the entire simulation time. A direct comparison of these stress fields can be found in Fig. 2.7. We do find some quantitative differences between the experiment and simulation. For example, the pressure of the simulated vacancy is plotted as a function of distance from the defect core in Fig. 2.13. While the morphology in each individual stress component is very close to that seen in experiments, we do not find as strong of a pressure enhancement around the simulated vacancy. This softening is most likely due to the softened core of the potential we use. Overall, however, all the qualitative features are reproduced in each of experiment, simulation, and theory.

Linear elasticity

To further measure the performance of SALSA, we also compare the stress fields calculated in simulation and experiment to the corresponding continuum elastic theory. In linear isotropic elastic theory, a vacancy's displacement field can be described by a radial function determined entirely by the local volume change $u_i(r) = \Delta V/r^2\ \hat{r}_i$. This can be seen by looking at the elastic free energy which can be written

$$\mathcal{F}_{\text{linear}} = \frac{1}{2}K\epsilon_{ii}^2 + \mu(\epsilon_{ij} - 1/3\ \delta_{ij}\epsilon_{ll})^2 \tag{2.14}$$

where K is the bulk modulus, μ is the shear modulus and ϵ_{ij} the strain tensor, the symmetrized Jacobian of the displacement field u, $\epsilon_{ij} = 1/2(\partial_i u_j + \partial_j u_i)$. Since the material is isotropic, we make u a radial function such that $u_i(\vec{r}) = u(r)\hat{r}_i$. We then minimize the free energy with respect to this displacement field through the Euler-Langrange equations $\frac{\partial F}{\partial u_i} - \frac{\partial}{\partial x_i}\frac{\partial F}{\partial \partial u_i} = 0$, giving a differential equation for the displacement $r^2u'' + 2ru' - 2u = 0$ whose solution is given by

$$u(r) = \frac{\Delta V}{4\pi r^2} + \frac{P_\infty}{3K}r \tag{2.15}$$

Here, ΔV is the local volume change, P_∞ is the pressure at long length scales due to boundary conditions and K is again the bulk modulus. This displacement field leads to a strain and stress field in linear elasticity that has the form

$$\begin{aligned}
\epsilon_{ij} &= \frac{1}{2}(\partial_i u_j + \partial_j u_i) \\
&= \frac{u}{r}\left(\delta_{ij} - \frac{r_i r_j}{r^2}\right) + u'\frac{r_i r_j}{r^2} \\
\sigma_{ij} &= K\epsilon_{ll}\delta_{ij} + 2\mu(\epsilon_{ij} - 1/3\delta_{ij}\epsilon_{kk}) \\
&= K\left(2\frac{u}{r} + u'\right)\delta_{ij} + 2\mu\left(\frac{u}{r} - u'\right)\left(\frac{1}{3}\delta_{ij} - \frac{r_i r_j}{r^2}\right)
\end{aligned}$$

Using this stress field, we find the pressure field is a constant

$$P = \sigma_{ii}/3 = K\left(2\frac{u}{r} + u'\right) = P_\infty \tag{2.16}$$

Geometric nonlinearity

However, both the simulation and experimental data show a pressure ring that suggests we need to move to higher order elasticity to accurately describe the stress field of the colloidal vacancy. The first natural attempt to capture this ring can be done by including the geometric nonlinearity (also known as finite strain), an extra term in the strain field that makes it rotationally invariant but is higher order in displacement. Doing so, we find that

$$\begin{aligned}\epsilon_{ij} &= \frac{1}{2}(\partial_i u_j + \partial_j u_i + \partial_i u_k \partial_j u_k) \\ &= \frac{u}{r}\left(\delta_{ij} - \frac{r_i r_j}{r^2}\right) + u'\frac{r_i r_j}{r^2} + \frac{1}{2}\left[\left(\frac{u}{r}\right)^2\left(\delta_{ij} - \frac{r_i r_j}{r^2}\right) + u'^2\frac{r_i r_j}{r^2}\right] \\ &= \bar{U}\left(\delta_{ij} - \frac{r_i r_j}{r^2}\right) + \bar{U}'\frac{r_i r_j}{r^2}\end{aligned}$$

where we can define $\bar{U} = u/r + 1/2(u/r)^2$ and $\bar{U}' = u' + 1/2u'^2$. We then calculate the stress which is linear in the strain, arriving at the same answer as previously, except with these variables substituted. Lastly, we find the differential equation for the radial displacement field via the Euler-Lagrange equations, yielding a long nonlinear ODE, which we omit for brevity. Fitting the experimental data using this form yields a small pressure enhancement which cannot be tuned to quantitatively match the experimental data without resorting to unphysical values for the bulk and shear modulus.

Nonlinear elasticity Motivated by arguments made in Section II, we next calculate the stress field incorporating the leading terms in nonlinear isotropic elastic theory. In particular, we modify the free energy such that

$$\mathcal{F}' = \mathcal{F}_{\text{linear}} + \frac{\alpha}{3}\epsilon_{ii}\epsilon_{jj}\epsilon_{kk} + \frac{\beta}{6}\epsilon_{ij}\epsilon_{jk}\epsilon_{ki} + \frac{\gamma}{4}\epsilon_{ii}\epsilon_{jk}\epsilon_{jk} \tag{2.17}$$

We insert the definition of finite strain into the new free energy to arrive at another differential equation for the displacement field as a function $u(r)$.

$$
\begin{aligned}
&r^5(24r(\lambda+2\mu)u''(r)+6(\alpha+\beta+\gamma)u'(r)^5\\
&+4u'(r)^3(2(8\alpha+3(4\beta+2\gamma+\lambda+2\mu))+15r(\alpha+\beta+\gamma)u''(r))\\
&+4u'(r)^2(8\alpha+6(2\beta+\gamma+4\lambda+6\mu)+9ru''(r)(2\alpha+2\beta+2\gamma+\lambda+2\mu))\\
&+24u'(r)(2(\lambda+2\mu)+ru''(r)(\alpha+\beta+\gamma+3\lambda+6\mu))\\
&+3u'(r)^4(2(6\alpha+8\beta+5\gamma)+5r(\alpha+\beta+\gamma)u''(r)))+2r^4u(r)(8(r(\alpha+3(\beta+\lambda))u''(r)\\
&-3(\lambda+2\mu))+3(\alpha+3\beta)u'(r)^4+12(\alpha+3\beta)u'(r)^3+4u'(r)^2(5\alpha+3(6\beta+\lambda)+3r(\alpha+3\beta)u''(r))\\
&+8u'(r)(\alpha+3(\beta+\lambda)+3r(\alpha+3\beta)u''(r)))+4r^3u(r)^2(2(r(2\alpha+9\beta+3\lambda)u''(r)\\
&-3(2\alpha+4\beta+\gamma+6\lambda+6\mu))+3u'(r)^2(\alpha+6\beta+r(\alpha+3\beta)u''(r))+6r(\alpha+3\beta)u'(r)u''(r))\\
&+4r^2u(r)^3(2(-13\alpha-6(5\beta+\gamma+\lambda+\mu)+r(\alpha+6\beta)u''(r))+(\alpha+6\beta)u'(r)^2-2(\alpha+6\beta)u'(r))\\
&+2ru(r)^4(-32\alpha-72\beta-15\gamma+r(\alpha+6\beta)u''(r)-2(\alpha+6\beta)u'(r))-6u(r)^5(2\alpha+4\beta+\gamma)=0
\end{aligned}
$$

We use this nonlinear ODE to fit the pressure profile found in the experimental data using only the purely compressional third-order elastic constant $\alpha = 3.6$ Pa, leaving $\beta = \gamma = 0$. In this same fit, we set the other elastic constants $K = 0.093$ Pa and $\mu = 0.092$ Pa based on studies of hard sphere elastic constants [49]. We also set the volume change $\Delta V = -0.083$ to be the same as the experimental value. In this fit, we are able to reproduce the experimental pressure ring with one third-order elastic constant and one initial condition (u' far from the vacancy).

The value of α we find from our fit of the pressure ring is consistent with the variation of bulk modulus with packing fraction as calculated by hard sphere simulations. We can directly compare these values using the equation of state. Given the pressure of a hard sphere system as a function of packing fraction, $P(\phi)$, we can expand the elastic constants as $K(\phi_0) + K'(\phi_0)(\phi - \phi_0) + \frac{1}{2}K''(\phi_0)(\phi -$

$\phi_0)^2 + \cdots$ giving $\alpha = K'(\phi_0) = \partial_\phi(\phi\partial_\phi P)|_{\phi_0}$. Using the functional form for $P(\phi)$ we get that $\alpha(0.59) \approx 3.0$ Pa in agreement with our fit $\alpha = 3.6$ to experimental stresses using nonlinear elasticity.

Vacancy interaction The overall sign of the interaction between vacancies must be negative as vacancies are in general attracted to areas of higher pressure just as interstitials are attracted to areas of lower relative pressure. In the case of two vacancies, the local increase in pressure around one vacancy acts as a higher pressure region for the second, causing them to mutually attract. Physically speaking, the collapse of particles towards the core of one vacancy causes particles to collide more frequently which is relieved by the negative volume change given by the second vacancy.

The above argument gives the dominant nonlinear term (the linear field of one vacancy coupling to the nonlinear pressure around another). Higher order effects can be repulsive but are smaller than this leading order term. Specifically, to calculate the attraction or repulsion of vacancies, we look at the elastic free energy, which strictly speaking is entirely entropic. In this treatment, we will be calling all entropic contributions aside from the configurational entropy the elastic energy E_{elastic}, giving us a free energy density $\mathcal{F} = E_{\text{elastic}} - TS_{\text{conf}}$. To first order, the elastic energy density is $E_{\text{elastic}} = \sigma_{ij}\epsilon_{ij}$ where σ is stress and ϵ is strain. We consider the perturbative view of the elastic free energy in the case of the interaction of two vacancies A and B, which can be expanded into three primary terms, $E_{\text{elastic}} = \sigma_{ij}^{A,\text{L}}\epsilon_{ij}^{B,\text{L}} + 2\sigma_{ij}^{A,\text{N}}\epsilon_{ij}^{B,\text{L}} + \sigma_{ij}^{A,\text{N}}\epsilon_{ij}^{B,\text{N}}$ where L indicates a linear contribution and N indications a nonlinear one. In isotropic linear elastic theory, vacancies do not interact making the first term independent of vacancy separation and leaving us with the second and third terms of the expansion. The

second term is the linear part vacancy B's quadrupole strain field sitting in the nonlinear (pressure bump) stress field of vacancy A. In this simple case, we know that the energy can be given by the vacancy quadrupole $E = \sigma_{ij}^{\text{ext}} Q_{ij}^{B}$, where the strain quadrupole for a vacancy is diagonal $Q_{ij}^{B} = \Delta V^{B} \delta_{ij}$ and $\sigma^{\text{ext}} = \sigma^{A,\text{N}}$ is an external stress field given by vacancy A. Therefore, the energy can be written $E = \sigma_{ii}^{\text{ext}} \Delta V^{B} = \sigma_{ii}^{A,\text{N}} \Delta V^{B} = P^{A,\text{N}} \Delta V^{B}$. Since $\Delta V \leq 0$ for vacancy defects, this term is negative, leading to an overall attraction, consistent with previous literature [33, 34, 13, 5]. This calculation will have higher-order corrections due to the nonlinear elastic overlap of the nonlinear pressure rings $\propto P^{A,\text{N}} P^{B,\text{N}}$ as well as nonlinear corrections to the pressure bump itself due to the presence of a second vacancy, but the qualitative behavior remains unchanged.

2.7.4 Dislocation Stress and Strain Fields

Experimental details

The dislocation is produced by templating the [100] axis on a glass coverslip at a registry 1.5% larger than the equilibrium lattice constant [68]. Particles are sedimented onto the substrate forming a single face-centered cubic crystal. As the crystal thickness reaches about 31 μm, a significant number of dislocations spontaneously nucleate and grow. We then image the three dimensional microstructure of an isolated dislocation using a confocal microscope. A schematic of these dislocations is found in the main text.

Simulated dislocation stresses

To closely simulate the particular dislocation studied in the experiment, we import the experimentally measured particle positions into the Brownian dynamics simulation. Prior to recording the stress, we relax the system to remove overlaps using a soft Hertzian potential and a large damping factor to ensure very little rearrangement. We then freeze the border particles as labeled in red in Fig. 2.14 to ensure that the topologically constrained dislocation does not migrate. After performing a time average, we find that the calculated stress field, both through virial calculation and SALSA method, are in excellent agreement with the experiment, providing a confirmation to the SALSA measurements. Importantly, since this simulation procedure only requires a single snapshot of data for the initial condition, this technique can be particularly useful in determining stresses in the experimental cases where time average is challenging. For instance, it is difficult to perform a time average in a system where the fluorescent dye photobleaches significantly or the dynamic time-scale is comparable to the time between acquisition of successive image stacks.

Continuum elastic theory

To compare against isotropic linear elasticity, we again calculate the stress field of the dislocation. The stress field of a dislocation in coordinates where z is along

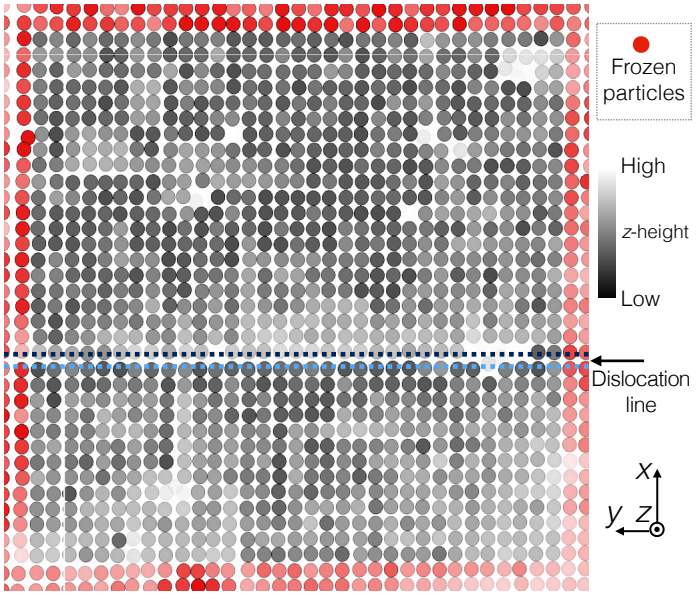

Figure 2.14: **Frozen particle border (dislocation).**A screen-shot of our Brownian dynamics simulation of the experimental fcc crystal. In shades of gray are active hard sphere particles while in red are the frozen boundary particles. Luminance in this picture roughly indicates the position in the z direction with only a thin slice of the entire simulation shown and darker colors indicating being deeper into the page. The dislocation line is visible 1/3 from the bottom of the image running left to right as indicated by the discontinuity in particle shade between adjacent rows.

the dislocation line, is given by [28]

$$\sigma_{xx} = -y\frac{3x^2+y^2}{(x^2+y^2)^2}$$
$$\sigma_{yy} = y\frac{x^2-y^2}{(x^2+y^2)^2}$$
$$\sigma_{xy} = x\frac{x^2-y^2}{(x^2+y^2)^2}$$
$$\sigma_{zz} = \nu(\sigma_{xx}+\sigma_{yy})$$

Using the method known as Dislocation Extraction Algorithm (DXA), we extract the line dislocation for our partial dislocation [60]. We rotate and translate

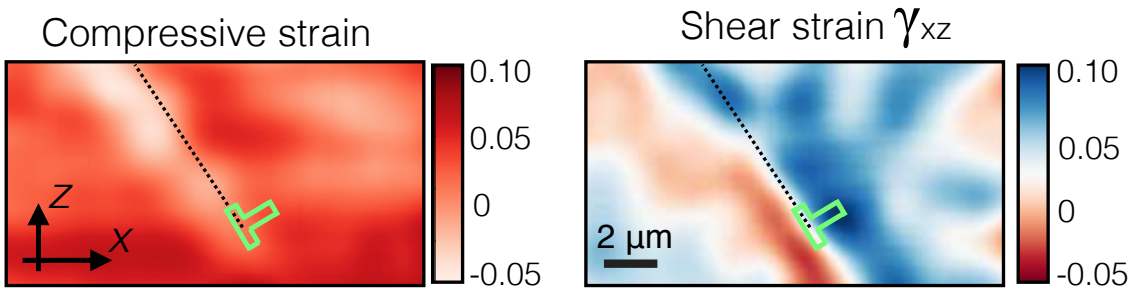

Figure 2.15: **Strain fields of a dislocation.** Experimental measurements of strain using the technique of Falk *et al.* [18] showing both compressive (left) and shear (right) strain distributions near a dislocation defect. The approximate location of the dislocation core is labeled with a (⊥). Notice that while the trend is very similar to that of the dislocation stress field (as in linear elasticity), there is a stronger divergence towards the core which is highlighted in the main text in Fig. 3.

the theoretical stress field for a single dislocation, integrating along the length of the dislocation as done in the experiment and simulation. Doing so, we find an excellent agreement with the other methods as shown in the main text Fig 3.

Strain fields

To investigate the relation between stress and strain, we determine the strain field near the dislocation. Following a previously developed algorithm [18], we measure the particle-level strain by quantifying the local affine deformation of individual particles. The compressive and shear strain (γ_{xz}) fields are shown in Fig. 2.15. We find that the strain fields show qualitatively similar features found in the stress distributions. However, as illustrated in Fig. 3(c) of the main paper, the stress-strain curve deviates from linearity near defects where strains are large.

Elastic moduli

Using the strain measurement, we analyze other experimentally accessible cubic moduli as done in the main manuscript. To that end, we compute the compressive C_{33} and shear C_{13} modulus profiles and discuss their behaviors below. We focus on the moduli associated with the strain component γ_{zz}, which shows a larger response than γ_{xx} and γ_{yy} in our experiment. For this analysis we rotate our stress and strain tensors so that the x and y axes align with the (100) and (010) axes of the cubic system. In this frame, the moduli for an cubic crystal have the following symmetries: $C_{33} = C_{22} = C_{11}$, and $C_{23} = C_{13} = C_{12}$.

To compute the compressive modulus near the dislocation core, we first determine the compressive stress σ_{zz} and strain γ_{zz}. Here, we determine the uniform background strain (due to the overall pressure arising from confinement and gravity) by matching the measured modulus to the corresponding theoretical value [20]. We then perform the same analysis used in the shear modulus calculation, and plot the compressive modulus C_{33} as a function of position $r/2a$ in Fig. 2.16(a). The region of the dislocation core is at $r/2a \approx 5.5$ (gray shade). We find that C_{33} is higher on the side with an additional half plane of particles. Similarly, we also observe a reduction in C_{33} on the other side due to the missing half plane of particles. We also find that the trend of the shear modulus C_{23} is similar to the compressive modulus C_{33} (Fig. 2.16(b)), which shows an enhancement on the left side and a reduction on the right.

The moduli we report are only calculated along a line perpendicular to the glide plane of the dislocation. The other two natural directions along the glide plane are excluded due to experimental limitations. Along the burgers vector we are limited by the noise in the stress and strain fields. Since the modulus is the

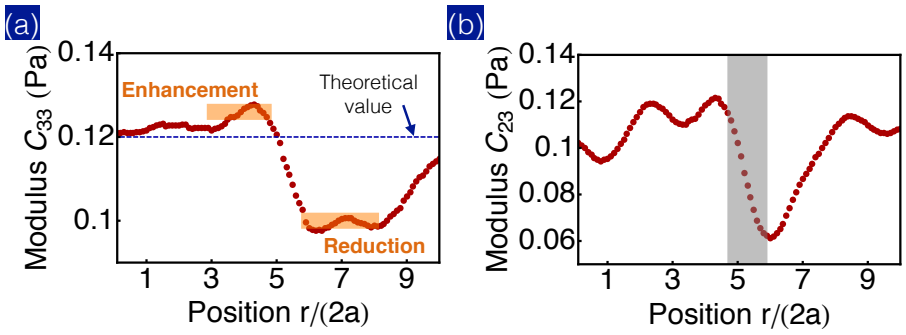

Figure 2.16: **Profile of the cubic moduli C_{33} and C_{23}.**(a) Compressive modulus C_{33} versus position perpendicular to the glide plane of the dislocation. (b) Shear modulus C_{23} measured along the same direction. Both moduli are calculated using the protocol described in the main manuscript.

ratio of the two, zeros remain problematic, similar to issues in deconvolution, and a new method of inference must be applied to the moduli in these regions. Along the dislocation line, we have already collapsed the data by averaging the stress and strain fields in this direction in order to reduce noise in the x-z plane. This averaging makes it infeasible to calculate the modulus variation in this direction. Due to symmetry, this direction should display a constant modulus. In the future, with a full time series of dislocation images, we can begin to look at the modulus variation near kinks and jogs along the dislocation line.

2.7.5 Polycrystal Stress Fields

Experimental details

We show a confocal image of the polycrystal we use in our experimental analysis in Fig. 2.17(a). The shown field of view is the same as the one of the stress field reported in the main manuscript. We show only a slice in the x-y plane of a complete 3D image stack. The z-interval between adjacent scan slices is 0.135 μm ~ 0.1 times the particle diameter. By matching the refractive indices of the water-glycerol mixture and silica particles, we minimize effects from the point spread function and z-axis spherical aberration, thus optimizing the image quality. We show the featured particle position with green circles in Fig. 2.17 (a). The data are visually overlaid to ensure there are no missing or repeated features.

To investigate the featuring accuracy, we plot the 1D $g(r)$ of the suspension in Fig. 2.17(b). As indicated by the sharpness of the first peak of $g(r)$, limiting our field of view to the first ten layers from the coverslip (in the optical z direction) enables us to accurately feature the particle positions. The spread of this peak arises from three contributions: featuring errors, polydispersity, and the thermal fluctuation of the equilibrium separation between particles. The location of the peak is primarily influenced by particle featuring errors and the packing fraction of the sample. While the polydispersity of this sample is $\sigma_a^2 \sim 5\%\langle a\rangle = 50$ nm, this variation in size will not shift the peak of $g(r)$ from the mean particle diameter (Fig. 2.17) unless there are spatial correlations of particle size. Therefore, at most, the averaging featuring errors should correspond to this peak shift of 50 nm.

Furthermore, we show a SEM micrograph to illustrate the roundness of the colloidal particles and the smoothness of their surfaces, see Fig. 2.17(c). As shown

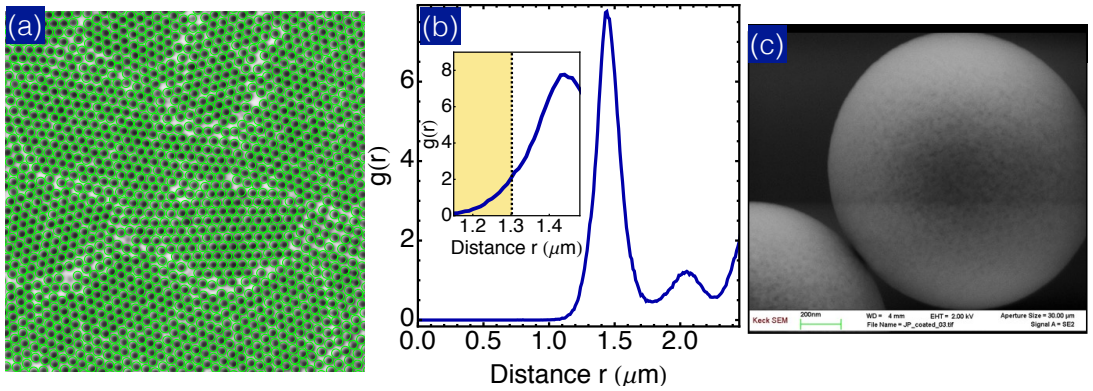

Figure 2.17: **Colloidal polycrystal sample.**(a) A representative slice of a 3D confocal image stack. Green circles illustrate the featured particle positions. This overlaid image shows that all particle positions are correctly identified without any missing particles. (b) The pair correlation function $g(r)$ calculated using featured particle positions. In the inset we show that the amount of particle overlap (yellow region) is negligible. (c) A SEM micrograph of two particles showing how the true particle size was determined in the sample.

in the SEM image, the surface roughness is less than the SEM resolution $\sim$ 5 nm. We also use the SEM image to measure the polydispersity of the silica colloids. We find that the polydispersity of the sample is less than 3% of the particle size, consistent with the specification provided by the manufacturer.

In the stress measurement of the polycrystal, we average the calculated stress field over 50 stacks of images. The structure of the polycrystal remains unchanged within the acquisition time ($\sim$ 30 s). While we expect to observe short-time stress fluctuations arising from particle Brownian motion within the acquisition time, we do not find any significant stress fluctuations on longer time scales.

Simulated polycrystal stresses

As with the dislocation stresses, we verified that the experimental stresses are accurate using a simulation-experiment hybrid. Again we use the experimentally

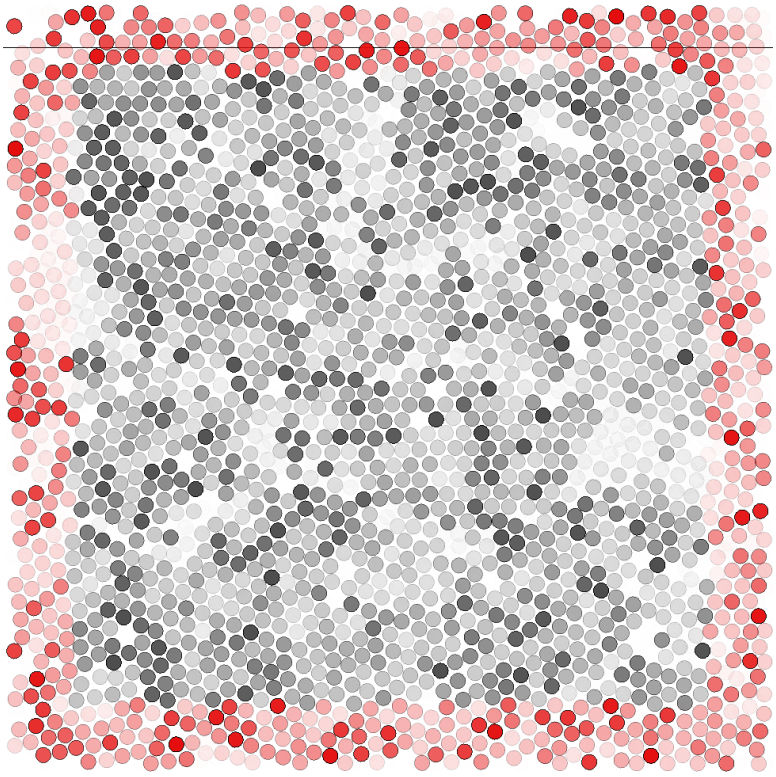

Figure 2.18: **Frozen particle border (polycrystal).**A screen-shot of our Brownian dynamics simulation of the experimental polycrystal. In shades of gray are active hard sphere particles while in red are the frozen boundary particles. Luminance in this picture roughly indicates the position in the z direction with only a thin slice of the entire simulation shown.

featured particle positions as initial conditions for our hard sphere Brownian dynamics simulation. For each experimental snapshot, we remove overlaps and freeze boundary particles as before, then evolve the system, measuring stresses using both the true virial measurements as well as SALSA. By averaging over the various snapshots, we arrive at a stress field very similar to that found by the experimental SALSA calculation.

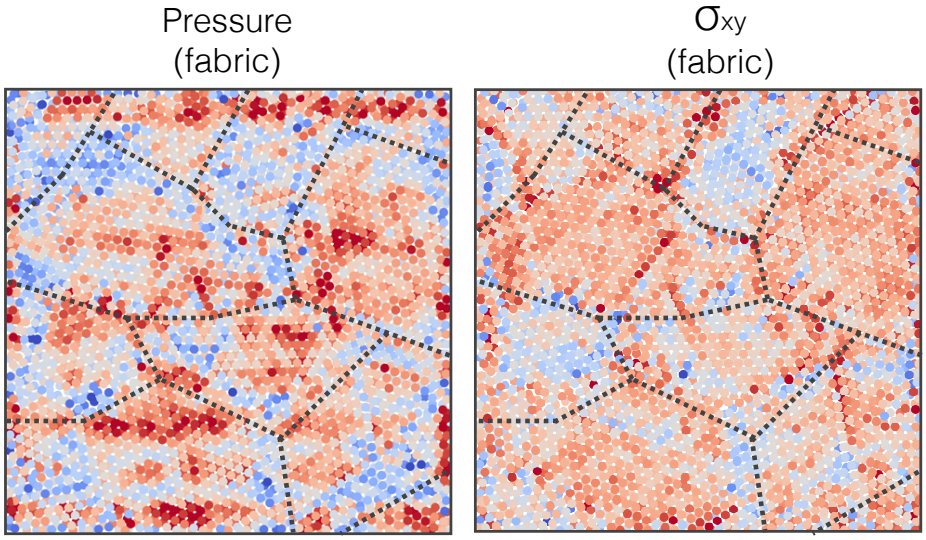

Figure 2.19: **Per-particle virials**The experimental polycrystal with particles colored by the magnitude of the fabric tensor (directly proportional to particle virial). While we see large scale correlations of fabric tensor trace with grain interiors and variation of off-diagonal components between grains, the magnitude of variation is much smaller than that found in previous numerical studies of stress distributions in strained polycrystals [54]

Virial stresses

In simulation literature, the atomic-level stress has been referred to as the virial of an individual atom either normalized or un-normalized by the system volume [54, 36, 41, 67]. Here, the virial $F_i x_j$ can be considered to be a stress that does not account for the local variation of atomic (particle) free volume. To compare our experimental results with the previous simulation findings (which do not correct for local particle density fluctuations), we plot (Fig. 2.19) the un-smoothed fabric tensor (local structural anisotropy) that is calculated using SALSA. For detailed information of the fabric tensor calculation, see the section of SALSA derivation. As shown in Fig. 2.19, we find that both the pressure and shear stress fluctuations are evenly distributed throughout the polycrystal. This is in sharp contrast to

simulation results of sheared atomic polycrystals [54], which showed much stronger virial fluctuations at grain boundaries than in grain interiors.

REFERENCES

[1] BJ Alder, WG Hoover, and DA Young. Studies in molecular dynamics. v. high-density equation of state and entropy for hard disks and spheres. *The Journal of Chemical Physics*, 49(8):3688–3696, 1968.

[2] Ahmed M Alsayed, Mohammad F Islam, J Zhang, Peter J Collings, and Arjun G Yodh. Premelting at defects within bulk colloidal crystals. *Science*, 309(5738):1207–1210, 2005.

[3] AR Bausch, MJ Bowick, A Cacciuto, AD Dinsmore, MF Hsu, DR Nelson, MG Nikolaides, A Travesset, and DA Weitz. Grain boundary scars and spherical crystallography. *Science*, 299(5613):1716–1718, 2003.

[4] Ted Belytschko, Yury Krongauz, Daniel Organ, Mark Fleming, and Petr Krysl. Meshless methods: an overview and recent developments. *Computer methods in applied mechanics and engineering*, 139(1):3–47, 1996.

[5] CH Bennett and BJ Alder. Studies in molecular dynamics. ix. vacancies in hard sphere crystals. *The Journal of Chemical Physics*, 54(11):4796–4808, 1971.

[6] Thijs Herman Besseling, Jissy Jose, and A BLAADEREN. Methods to calibrate and scale axial distances in confocal microscopy as a function of refractive index. *Journal of microscopy*, 257(2):142–150, 2015.

[7] Dapeng Bi, Jie Zhang, Bulbul Chakraborty, and RP Behringer. Jamming by shear. *Nature*, 480(7377):355–358, 2011.

[8] John F Brady. The rheological behavior of concentrated colloidal dispersions. *J. Chem. Phys.*, 99(July):567–581, 1993.

[9] Vasily V Bulatov, Luke L Hsiung, Meijie Tang, Athanasios Arsenlis, Maria C Bartelt, Wei Cai, Jeff N Florando, Masato Hiratani, Moon Rhee, Gregg Hommes, et al. Dislocation multi-junctions and strain hardening. 2006.

[10] Wei Cai, Athanasios Arsenlis, Christopher R Weinberger, and Vasily V Bulatov. A non-singular continuum theory of dislocations. *Journal of the Mechanics and Physics of Solids*, 54(3):561–587, 2006.

[11] Ke Chen, Wouter G Ellenbroek, Zexin Zhang, Daniel TN Chen, Peter J Yunker, Silke Henkes, Carolina Brito, Olivier Dauchot, Wim Van Saarloos,

Andrea J Liu, et al. Low-frequency vibrations of soft colloidal glasses. *Physical review letters*, 105(2):025501, 2010.

[12] Xiang Cheng, Jonathan H McCoy, Jacob N Israelachvili, and Itai Cohen. Imaging the microscopic structure of shear thinning and thickening colloidal suspensions. *Science*, 333(6047):1276–9, September 2011.

[13] Fabio Cinti, Tommaso Macrì, Wolfgang Lechner, Guido Pupillo, and Thomas Pohl. Defect-induced supersolidity with soft-core bosons. *Nature communications*, 5, 2014.

[14] John C Crocker and David G Grier. Methods of digital video microscopy for colloidal studies. *Journal of colloid and interface science*, 179(1):298–310, 1996.

[15] LC DaSilva, L Cândido, L da F Costa, and Osvaldo N Oliveira Jr. Formation energy and interaction of point defects in two-dimensional colloidal crystals. *Physical Review B*, 76(3):035441, 2007.

[16] TJ Delph. Local stresses and elastic constants at the atomic scale. *Proceedings of the Royal Society A: Mathematical, Physical and Engineering Science*, 461(2058):1869–1888, 2005.

[17] Anthony D Dinsmore, Eric R Weeks, Vikram Prasad, Andrew C Levitt, and David A Weitz. Three-dimensional confocal microscopy of colloids. *Applied Optics*, 40(24):4152–4159, 2001.

[18] ML Falk and JS Langer. Dynamics of viscoplastic deformation in amorphous solids. *Physical Review E*, 57(6):7192, 1998.

[19] David R Foss and John F Brady. Brownian dynamics simulation of hard-sphere colloidal dispersions. *Journal of Rheology (1978-present)*, 44(3):629–651, 2000.

[20] Daan Frenkel and Anthony JC Ladd. Elastic constants of hard-sphere crystals. *Physical review letters*, 59(10):1169, 1987.

[21] C Friesen and CV Thompson. Reversible stress relaxation during precoalescence interruptions of volmer-weber thin film growth. *Physical review letters*, 89(12):126103, 2002.

[22] Shreyas Gokhale, K Hima Nagamanasa, V Santhosh, AK Sood, and Rajesh

Ganapathy. Directional grain growth from anisotropic kinetic roughening of grain boundaries in sheared colloidal crystals. *Proceedings of the National Academy of Sciences*, 109(50):20314–20319, 2012.

[23] Robert Gracie, Jay Oswald, and Ted Belytschko. On a new extended finite element method for dislocations: core enrichment and nonlinear formulation. *Journal of the Mechanics and Physics of Solids*, 56(1):200–214, 2008.

[24] Jean-Pierre Hansen and Ian R McDonald. *Theory of simple liquids*. Elsevier, 1990.

[25] Robert J Hardy. Formulas for determining local properties in molecular-dynamics simulations: Shock waves. *The Journal of Chemical Physics*, 76(1):622–628, 1982.

[26] Pinshane Y Huang, Simon Kurasch, Jonathan S Alden, Ashivni Shekhawat, Alexander A Alemi, Paul L McEuen, James P Sethna, Ute Kaiser, and David A Muller. Imaging atomic rearrangements in two-dimensional silica glass: Watching silica's dance. *science*, 342(6155):224–227, 2013.

[27] Derek Hull and David J Bacon. *Introduction to dislocations*, volume 257. Pergamon Press Oxford, 1984.

[28] Derek Hull and David J Bacon. *Introduction to dislocations*, volume 37. Elsevier, 2011.

[29] William TM Irvine, Vincenzo Vitelli, and Paul M Chaikin. Pleats in crystals on curved surfaces. *Nature*, 468(7326):947–951, 2010.

[30] Andrew King, G Johnson, D Engelberg, W Ludwig, and J Marrow. Observations of intergranular stress corrosion cracking in a grain-mapped polycrystal. *Science*, 321(5887):382–385, 2008.

[31] Rei Kurita, David B Ruffner, and Eric R Weeks. Measuring the size of individual particles from three-dimensional imaging experiments. *Nature communications*, 3:1127, 2012.

[32] Erik Lange, Jose B Caballero, Antonio M Puertas, and Matthias Fuchs. Comparison of structure and transport properties of concentrated hard and soft sphere fluids. *The Journal of chemical physics*, 130(17):174903, 2009.

[33] Wolfgang Lechner and Christoph Dellago. Defect interactions in two-dimensional colloidal crystals: vacancy and interstitial strings. *Soft Matter*, 5(14):2752–2758, 2009.

[34] Wolfgang Lechner and Christoph Dellago. Point defects in two-dimensional colloidal crystals: simulation vs. elasticity theory. *Soft Matter*, 5(3):646–659, 2009.

[35] V. a. Levashov, J. R. Morris, and T. Egami. Viscosity, Shear Waves, and Atomic-Level Stress-Stress Correlations. *Phys. Rev. Lett.*, 106(11):115703, March 2011.

[36] Valentin A Levashov, James R Morris, and Takeshi Egami. Viscosity, shear waves, and atomic-level stress-stress correlations. *Physical review letters*, 106(11):115703, 2011.

[37] Lyle E Levine, Bennett C Larson, Wenge Yang, Michael E Kassner, Jonathan Z Tischler, Michael A Delos-Reyes, Richard J Fields, and Wenjun Liu. X-ray microbeam measurements of individual dislocation cell elastic strains in deformed single-crystal copper. *Nature materials*, 5(8):619–622, 2006.

[38] Ju Li, Krystyn J Van Vliet, Ting Zhu, Sidney Yip, and Subra Suresh. Atomistic mechanisms governing elastic limit and incipient plasticity in crystals. *Nature*, 418(6895):307–310, 2002.

[39] Neil YC Lin, Sushmit Goyal, Xiang Cheng, Roseanna N Zia, Fernando A Escobedo, and Itai Cohen. Far-from-equilibrium sheared colloidal liquids: Disentangling relaxation, advection, and shear-induced diffusion. *Physical Review E*, 88(6):062309, 2013.

[40] Neil YC Lin, Jonathan H McCoy, Xiang Cheng, Brian Leahy, Jacob N Israelachvili, and Itai Cohen. A multi-axis confocal rheoscope for studying shear flow of structured fluids. *Review of Scientific Instruments*, 85(3):033905, 2014.

[41] C Mottet, G Rossi, F Baletto, and R Ferrando. Single impurity effect on the melting of nanoclusters. *Physical review letters*, 95(3):035501, 2005.

[42] A Ian Murdoch. A critique of atomistic definitions of the stress tensor. *Journal of Elasticity*, 88(2):113–140, 2007.

[43] AI Murdoch and D Bedeaux. Continuum equations of balance via weighted

averages of microscopic quantities. *Proceedings of the Royal Society of London A: Mathematical, Physical and Engineering Sciences*, 445(1923):157–179, 1994.

[44] Kerstin N Nordstrom, E Verneuil, PE Arratia, Anindita Basu, Zheng Zhang, Arjun G Yodh, Jerry P Gollub, and Douglas J Durian. Microfluidic rheology of soft colloids above and below jamming. *Physical review letters*, 105(17):175701, 2010.

[45] Yi Peng, Ziren Wang, Ahmed M Alsayed, Arjun G Yodh, and Yilong Han. Melting of colloidal crystal films. *Physical review letters*, 104(20):205703, 2010.

[46] See-Eng Phan, William B Russel, Zhengdong Cheng, Jixiang Zhu, Paul M Chaikin, John H Dunsmuir, and Ronald H Ottewill. Phase transition, equation of state, and limiting shear viscosities of hard sphere dispersions. *Physical Review E*, 54(6):6633, 1996.

[47] WCK Poon. The physics of a model colloid–polymer mixture. *Journal of Physics: Condensed Matter*, 14(33):R859, 2002.

[48] Wilson CK Poon, Eric R Weeks, and C Patrick Royall. On measuring colloidal volume fractions. *Soft Matter*, 8(1):21–30, 2012.

[49] Sander Pronk and Daan Frenkel. Large difference in the elastic properties of fcc and hcp hard-sphere crystals. *Physical review letters*, 90(25):255501, 2003.

[50] Ian Robinson and Ross Harder. Coherent x-ray diffraction imaging of strain at the nanoscale. *Nature materials*, 8(4):291–298, 2009.

[51] D Rosenbaum, PC Zamora, and CF Zukoski. Phase behavior of small attractive colloidal particles. *Physical review letters*, 76(1):150, 1996.

[52] Peter Schall, Itai Cohen, David A Weitz, and Frans Spaepen. Visualization of dislocation dynamics in colloidal crystals. *Science*, 305(5692):1944–1948, 2004.

[53] Peter Schall, Itai Cohen, David A Weitz, and Frans Spaepen. Visualizing dislocation nucleation by indenting colloidal crystals. *Nature*, 440(7082):319–323, 2006.

[54] Jakob Schiøtz, Francesco D Di Tolla, and Karsten W Jacobsen. Softening of

nanocrystalline metals at very small grain sizes. *Nature*, 391(6667):561–563, 1998.

[55] Jakob Schiøtz and Karsten W Jacobsen. A maximum in the strength of nanocrystalline copper. *Science*, 301(5638):1357–1359, 2003.

[56] Peter J Shaw and David J Rawlins. The point-spread function of a confocal microscope: its measurement and use in deconvolution of 3-d data. *Journal of Microscopy*, 163(2):151–165, 1991.

[57] Colin JR Sheppard and Min Gu. Aberration compensation in confocal microscopy. *Applied optics*, 30(25):3563–3568, 1991.

[58] Colin JR Sheppard, Min Gu, Keith Brain, and Hao Zhou. Influence of spherical aberration on axial imaging of confocal reflection microscopy. *Applied optics*, 33(4):616–624, 1994.

[59] Ralph I Stephens, Ali Fatemi, Robert R Stephens, and Henry O Fuchs. *Metal fatigue in engineering*. John Wiley & Sons, 2000.

[60] Alexander Stukowski and Karsten Albe. Extracting dislocations and non-dislocation crystal defects from atomistic simulation data. *Modelling and Simulation in Materials Science and Engineering*, 18(8):085001, 2010.

[61] Ellad B Tadmor and Ronald E Miller. *Modeling materials: continuum, atomistic and multiscale techniques*. Cambridge University Press, 2011.

[62] P Török, SJ Hewlett, and P Varga. The role of specimen-induced spherical aberration in confocal microscopy. *Journal of microscopy*, 188(2):158–172, 1997.

[63] Alejandro Torres-Sánchez, Juan M Vanegas, and Marino Arroyo. Examining the mechanical equilibrium of microscopic stresses in molecular simulations. *Physical review letters*, 114(25):258102, 2015.

[64] VERONIQUE Trappe, V Prasad, Luca Cipelletti, PN Segre, and DAVID A Weitz. Jamming phase diagram for attractive particles. *Nature*, 411(6839):772–775, 2001.

[65] Alfons Van Blaaderen, Rene Ruel, and Pierre Wiltzius. Template-directed colloidal crystallization. *Nature*, 385(6614):321–324, 1997.

[66] Anand Yethiraj and Alfons van Blaaderen. A colloidal model system with an interaction tunable from hard sphere to soft and dipolar. *Nature*, 421(6922):513–517, 2003.

[67] Kenji Yoshimoto, Tushar S Jain, Kevin Van Workum, Paul F Nealey, and Juan J de Pablo. Mechanical heterogeneities in model polymer glasses at small length scales. *Physical review letters*, 93(17):175501, 2004.

[68] Klaus Zahn, Axel Wille, Georg Maret, Surajit Sengupta, and Peter Nielaba. Elastic properties of 2d colloidal crystals from video microscopy. *Physical review letters*, 90(15):155506, 2003.

CHAPTER 3

A MULTI-AXIS CONFOCAL RHEOSCOPE FOR STUDYING SHEAR FLOW OF STRUCTURED FLUIDS[1]

3.1 Abstract

We present a new design for a confocal rheoscope that enables uniform uniaxial or biaxial shear. The design consists of two precisely-positioned parallel plates with a gap that can be adjusted down to 2 ± 0.1 μm, allowing for the exploration of confinement effects. By using our shear cell in conjunction with a biaxial force measurement device and a high-speed confocal microscope, we are able to measure the real-time biaxial stress while simultaneously imaging the material 3D structure. We illustrate the importance of the instrument capabilities by discussing the applications of this instrument in current and future research topics in colloidal suspensions.

3.2 Introduction

In many systems driven far from thermodynamic equilibrium, deformation plays a decisive role. Structured fluids in particular exhibit a rich array of non-equilibrium flow phenomena that impact natural and industrial processes alike [87, 46]. Structured fluids have microscopic components, such as suspended particles, polymers, or micelles, whose distribution and dynamics can strongly affect bulk properties

[1]Neil Y.C. Lin, Jonathan H. McCoy, Xiang Cheng, Brian Leahy, Jacob N. Israelachvili, and Itai Cohen. "A multi-axis confocal rheoscope for studying shear flow of structured fluids." Review of Scientific Instruments 85, no. 3 (2014): 033905.

such as viscosity. Thus, changes in microstructure arising from imposed flow conditions can have significant consequences. Understanding the cooperative dynamics of entangled polymers is important for the processing of thermoplastics [23], for example, and the interplay between platelet aggregation and blood flow is important in blood clotting [12]. Likewise, the non-Newtonian rheology of structured fluids can be exploited in the design of useful materials, such as the shear-thinning properties of paint or toothpaste or the possible use of shear-thickening to engineer flexible body armor [50, 37]. The microscopic underpinnings of such phenomena and the range of microscopic behaviors observed in structured fluids more generally have been the subject of considerable discussion. The multi-scale, many-body character of these problems continues to challenge our physical understanding of systems far from equilibrium.

Imposing flow conditions in which the velocity gradient tensor takes a relatively simple form is a classic strategy for investigating structured fluids [46, 40]. A strain-controlled measurement performed on a commercial rheometer, for example, provides precise data on how shear stress varies with applied shear rates. Alternatively, these instruments are capable of stress-controlled measurements and oscillatory measurements, as well as impulsive measurements in which transients can be explored. These bulk rheological techniques can be used to characterize viscous and elastic responses, including nonlinear behaviors such as shear thinning and thickening, thixotropy, and yielding commonly observed in structured fluids [46, 40, 37]. In addition, by modifying the motor of a commercial rheometer and using a cylindrical Couette geometry, it is possible to superimpose a small-amplitude oscillatory motion orthogonal to a primary shear flow [80, 49, 86, 29]. This modification enables biaxial flow measurements and can be used to probe force signatures arising from anisotropies in flow-induced structures.

While rheology does supply a great deal of useful information, deeper understanding generally requires *in situ* measurement techniques that provide access to the fluid's microscopic degrees of freedom, *e.g.*, polymer orientation, flow velocity field, or particle positions. Scattering techniques provide powerful tools for probing microscopic structures. Small angle x-ray and neutron scattering (SAXS and SANS), for example, are able to resolve the nanoscale structures and dynamics associated with polymeric systems. Dynamic light scattering (DLS) and other light scattering techniques [78, 44, 34, 79], by comparison, are less expensive, and easier to incorporate into a table-top experiment but are limited to structures no smaller than the wavelengths associated with visible light. When combined with conventional rheology these techniques offer valuable insights into the microscopic origins of observed flow behaviors in a variety of systems [7, 61, 71, 75]. However, the structural information provided by scattering techniques is averaged over a large volume of sample, so point defects [69, 68], grain boundaries [57], shear bands [19, 56, 4], and other heterogeneities [42] can be difficult to resolve. Moreover, real-space structures can only be extracted from scattering data through Fourier analysis and, due to missing phase information, this process is not always straightforward.

Such limitations can be overcome by a variety of real space imaging techniques[57, 59, 62]. More recently, for samples with structures larger than the wavelength of light, confocal microscopy has been used to measure a material's microstructure under shear. Using this technique, individual structures of interest can be followed in real time or, by scanning through the sample, the full three-dimensional structure can be mapped out, allowing for accurate reconstruction of flow profiles using particle velocimetry and detailed measurements of a material's dynamic microstructure [10, 67, 60, 24, 88, 31].

Two types of experimental designs combining confocal microscopy with precise flow control have been reported. The major distinction between these two types is the geometry of the flow. The first group of designs uses counter-rotating surfaces to drive torsional flows with circular streamlines [24, 25, 3, 9, 4, 70, 67]. Often, one of these surfaces is fixed in the laboratory frame. Independently rotating both surfaces, while more difficult, allows the zero-velocity plane to be moved away from the sample boundaries [24, 25]. This, in turn, allows particle tracking in bulk, even under very rapid shear conditions. An alternate approach for torsional flows requires mounting a commercial rheometer on a confocal microscope [3, 9, 4, 70]. To achieve a uniform shear rate, commercial rheometers use a cone and plate geometry in which the sample thickness increases linearly with distance from the rotation axis. Measurements of confined suspensions, however, require a parallel plate geometry in which the sample thickness is uniform but the shear rate is not. Thus, while this approach allows a great variety of bulk measurements to be paired with simultaneous visualization of sheared microstructures, confined systems under uniform shear cannot be explored using this apparatus.

The second group of experimental designs use flat, counter-translating surfaces to drive planar Couette flows with straight, parallel streamlines [36, 37, 60, 20, 19, 74, 10, 73, 88, 89]. Again, the simplest designs have one surface fixed in the laboratory frame, though independently moving both is possible and has the same advantages as in the analogous rotational design [88, 89]. In these planar designs, with careful alignment of the boundaries, sample thicknesses of just a few particle diameters become possible, allowing exploration of thin film flow behaviors associated with confinement [20, 33, 39]. However, force measurement is a significant challenge in this flow geometry. To achieve a high degree of parallelism, shear cell designs tend to use much smaller surfaces than those found in commercial rheome-

ters. With weak stresses acting on these areas, the resulting shear forces can be on the order of micro-Newtons even when working with fairly viscous suspensions. For this reason, these planar, uniaxial designs have traditionally been used to study questions concerning particle configuration and dynamics rather than rheological phenomena.

Here, we discuss a new translating, parallel-plate design incorporating both fast confocal microscopy and force measurement [13]. This instrument offers precision control of uniform shear flow. The plates can be brought within two microns of each other and, with lateral displacements of hundreds of microns possible, very large strains and strain rates can be achieved in strongly confined samples. Our custom-built, high precision force measurement devices (FMDs) allow *in situ* rheological measurements to be combined with simultaneous visualization of sheared microstructures in this flow geometry. These devices are sensitive enough to detect shear stresses on the order of tenths of a Pascal. Moreover, our instrument is capable of performing biaxial shear experiments in which oscillatory shear flows in two orthogonal directions are superimposed. By adjusting the relative amplitude and phase of these orthogonal components, uniaxial flows in different directions can be explored, as well as perturbations to uniaxial flows and even elliptical flows. This multi-axial instrument is therefore capable of probing anisotropic structure and dynamics in a variety of systems and, unlike currently available commercial instruments, allows direct visualization of sheared microstructures.

This paper is organized as follows. In Section II, we discuss design challenges and our solutions to them, focusing on geometric and kinematic aspects of the design. In Section III, we discuss the force measurement problem in detail and present designs for both uniaxial and biaxial FMDs. Section IV discusses the use

of confocal microscopy in connection with our shear cell design. Finally, in Section V, we outline the application of our shear cell to the study of some representative experimental systems.

3.3 Parallel Plate Shearing Apparatus

3.3.1 Control of shear cell alignment and spacing

The first design challenge is ensuring that the two plates are extremely parallel with a given separation. In our shear flow apparatus, two large mounting plates are used to control the alignment and spacing of the shear cell boundaries. The lower boundary is attached (via a piezoelectric translation stage) to the lower mounting plate. The upper boundary is attached via a force measurement device and rotational stage to the upper mounting plate. This arrangement is shown in Fig. 3.1 and 3.2. To control the spacing and ensure the mounting plates are parallel, we use a constrained system of three adjustment screws, placed at the vertices of an equilateral triangle. Each screw passes through a tight, threaded bushing in the upper mounting plate and has a ball bearing at its tip, which rests on a post attached to the lower mounting plate. One of these posts has a conical hole in its upper surface, which prevents any lateral motion of its screw. Another post has a linear groove, which allows lateral motion of its screw but only in one direction. The last post has a flat surface, allowing its screw to move freely in two directions. Holding the plates together with stiff springs prevents the plates from moving about during shear, keeping the plate separation fixed. The plates are sufficiently thick that the springs cause no observable warping when in place.

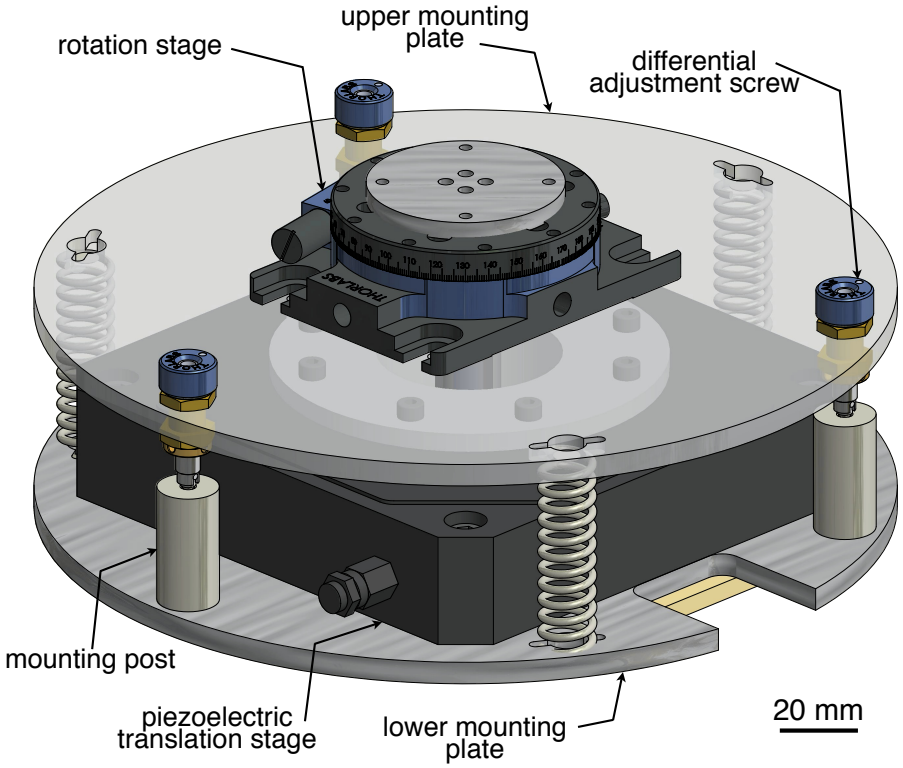

Figure 3.1: Schematic representation of the shear flow apparatus, with semi-transparent rendering of upper mounting plate (angled top view). The three differential adjustment screws allow us to accurately position the plates in a parallel geometry. The black piezoelectric translation stage drives the bottom plate of the shear cell back and forth, and the top plate of the shear cell and Force Measurement Device are mounted to the top mounting plate. Figures. 3.2 and 3.3 show a close-up of the mounting setup and shear cell chamber.

This kinematic mount design exploits the rigid body degrees of freedom of the upper mounting plate. In free space, the plate has exactly three translational degrees of freedom and three rotational degrees of freedom. All three translational degrees of freedom are lost when one of the screw tips engages the conical hole. Two of the rotational degrees of freedom are lost if another screw tip engages the linear groove. The last rotational degree of freedom is lost when the remaining screw tip engages the flat post. Thus, for each setting of the adjustment screws, there is a unique configuration of screw tip positions that immobilizes the upper mounting

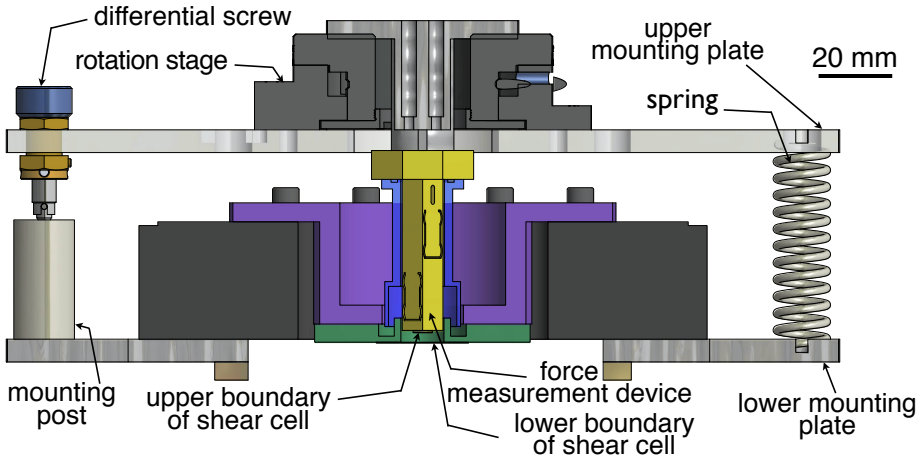

Figure 3.2: Schematic representation of the shear flow apparatus (side view, cut). See Fig. 3.3 for an enlarged view of the shear cell.

plate. As the screws are independently rotated, small cooperative motions of the screw tips along the grooved and flat posts allow the mount to freely explore different orientations without building up mechanical stress in either the screws or the plates. In this way, microscopic misalignments due to the mechanics of the mount are minimized.

The adjustment screws and springs are evenly spaced around a circle 200 mm in diameter, visible in the angled view of Fig. 3.1. Each screw (ThorLabs, DAS110) has an outer thread for course adjustments and a differential inner mechanism for fine adjustments. The coarse thread advances the screw 0.3175 mm per rotation. Thus, one full rotation of any one of the adjustment screws corresponds to an angular change of only 2.12×10^{-3} radians in the relative orientation of mounting plates. The more precise differential adjustment mechanism advances the screw 0.025 mm per rotation. Thus, one full rotation of this mechanism in any one screw corresponds to an angular change of only 1.67×10^{-4} radians in the relative orientation of the mounting plates. Since the upper and lower shear cell boundaries are independently fixed to the upper and lower mounting plates, as described

above, these adjustments allow precise control of the shear cell geometry. We find that small cooperative motions using the coarse threads alone are usually enough to align the cell boundaries parallel to within roughly 5×10^{-5} radians or, equivalently, to within roughly 0.2 μm across the entire shear zone.

The use of three precision adjustment screws not only allows us to level the plates, but it also allows us to adjust their gap over a wide range. With careful alignment of the three screws, the cell boundaries can be brought very close together (*e.g.*, 2 μm), enabling study of samples containing only a few particle layers. Moreover, due to their large adjustable range, the screws can be adjusted to increase the plate separations to more than 1 mm.

3.3.2 The shear cell

To prevent evaporation and contamination of the sample, the sample loading region is isolated via a solvent trap, as shown in Fig. 3.3. The lower mounting plate is attached to a solvent trap plate with an annular groove; this groove is filled with 300 μL of mineral oil before beginning an experiment. The top plate has a metal or polycarbonate tube attached to it, via the base of the FMD. This tube provides the lateral sidewalls of the solvent trap. As the top plate is brought down into the sample from above, the bottom rim of this tube lines up with an annular groove in the solvent trap plate. The 300 μL pool of mineral oil forms an airtight seal between these two pieces of the solvent trap. In this way, sample evaporation and exposure to air can be minimized. Since there is no direct mechanical contact between the FMD and the moving pieces of the shear cell, the solvent trap disturbs neither the shear experiment nor the force measurements.

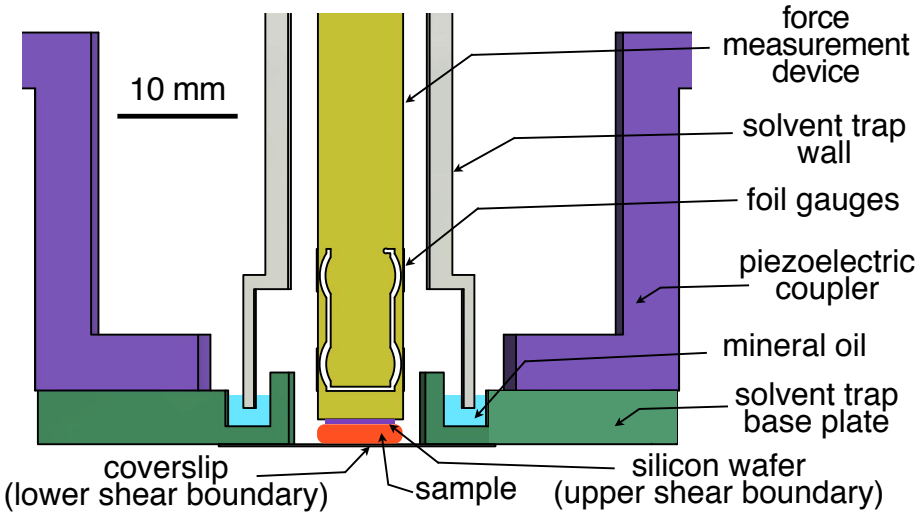

Figure 3.3: Schematic representation showing major components of the shear cell in greater detail (side view, cut). Note that the aspect ratio of the sample pool is exaggerated here to make it visible from the side. In practice, the gap is much smaller relative to the width, as discussed in later sections. The sample volume can also extend beyond the shear zone, forming a reservoir that is not shown here.

Our shear apparatus needs a transparent bottom plate to allow confocal imaging, and it needs smooth top and bottom plates to avoid a spatially varying plate separation due to surface roughness. We use a standard No. 1.5 microscope cover slip (Warner Instruments CS-25R15, approximately 170 μm thick) as the lower boundary of the shear cell. In addition to granting us the ability to image with a confocal microscope, a glass cover slip allows us to treat the surface, *e.g.* by base-washing to clean the surface and to make it hydrophilic, or by silanization to make it hydrophobic. The glass cover slips are both smooth and fairly planar, allowing for a uniform shear profile across the sample. The cover slip is glued to the bottom of the solvent trap plate using ultraviolet-cured optical adhesive (Norland NOA89), as shown in Fig. 3.3. A half-inch diameter circular hole in the center of the solvent trap plate provides access to the cover slip from above, both for sample loading and for placement of the top plate. Samples are loaded into the

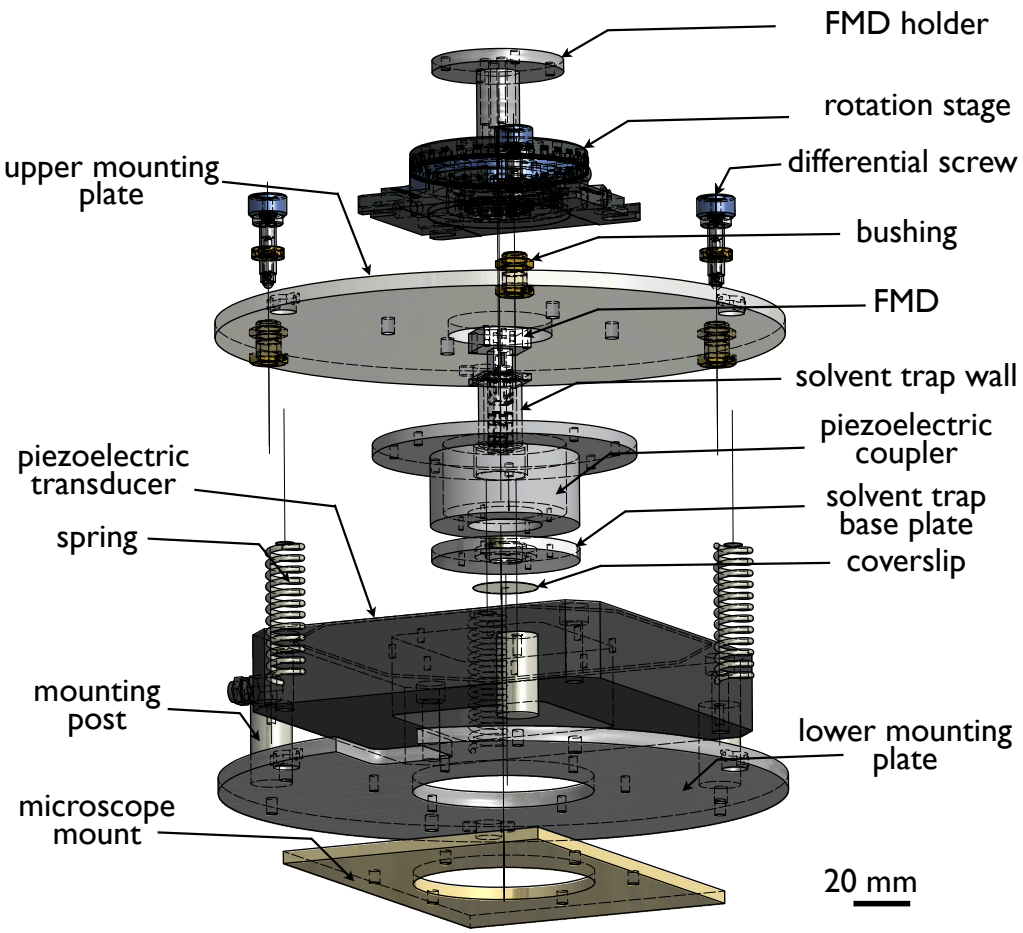

Figure 3.4: Exploded view drawing of the confocal rheoscope.

center of the cylindrical space defined by the walls of this hole. This plate is in turn connected to the lower mounting plate, via a rigid adapter connection to the piezoelectric translation stage. For the upper boundary of the shear cell, we use a 4 mm $\times$ 4 mm silicon wafer, which is atomically smooth. This wafer is attached to the upper mounting plate via the tip of the force measurement device (FMD). The relationship and order of assembly of the confocal rheoscope parts are illustrated in the exploded view drawing, as shown in Fig. 3.4.

3.3.3 Control of shear cell motion

Finally, our apparatus requires a drive that can operate precisely over a large range of strain amplitudes and shear frequencies. Drives such as linear actuators or stepper motors provide the ability to access large strain amplitudes, but the precision for typical actuators is around 1 μm and their frequency range is often limited. For the small plate separations and shear rates we are interested in accessing these limitations are problematic. Thus, for the most recent versions of our apparatus, we selected as our drive a three-axis piezoelectric device with an open central aperture (Physik Instrumente, P-563.3CD). This particular device has a square hole in the center, which allows for access from above for sample loading and for flow visualization from below. Our piezoelectric device is capable of close-loop travel of up to 300 μm laterally. For oscillatory shear flow, this translates to a maximum displacement amplitude u_0 of roughly 150 μm. For small gaps, such as $d = 5$ μm, the maximum strain amplitude $\gamma_0 = u_0/d$ can reach 30 and the maximum strain rate amplitude $\dot{\gamma}_0 = \omega\gamma_0$ can reach 2.1×10^4. This value of $\dot{\gamma}_0$ is obtained for an oscillation frequency $\omega/(2\pi)$ of 110 Hz, which can be achieved without approaching the resonant frequencies of the device. Another important motivation for choosing a piezoelectric controller is the precision. Our piezoelectric controller has a displacement resolution of 2 nm. Moreover, the piezo displacement is almost perfectly proportional to applied voltage, with a deviation from linearity of 3×10^{-4}. Because the piezoelectric transducer design is standard, as newer products come on line these capabilities can be further improved.

This piezoelectric strategy offers flexibility as well as high precision. Applying a triangular waveform to a single axis of the device, for example, results in steady unidirectional shear with periodic reversals of direction. A sinusoidal waveform, on

the other hand, results in an oscillatory shear flow. Thus, the device is capable of many of the controlled motions necessary for standard rheological measurements, including amplitude sweeps, frequency sweeps, and step strains or strain rates, as well as steady shear at constant strains or strain rates. Moreover, the three-axis capability of our device allows us to select the direction of shear and to shear in multiple directions.

The superposition of two time-dependent shear flows can be written as:

$$\boldsymbol{\gamma}_{\text{tot}}(t) = \boldsymbol{\gamma}_1(t) + \boldsymbol{\gamma}_2(t) \quad , \tag{3.1}$$

where the subscript 1 or 2 indicates the primary or secondary flow and $\boldsymbol{\gamma}$ is the tensorial time-dependent shear strain. By imposing different types of shear, we can perform a mixture of creep (square waveform), oscillatory (sine waveform), and continuous (triangular waveform) measurements. If we consider as a special case, a superposition of two oscillatory shear flows, we can write $\boldsymbol{\gamma}_1(t) = \tilde{\boldsymbol{\gamma}}_1 \sin(\omega_1 t)$ and $\tilde{\boldsymbol{\gamma}}_2 \sin(\omega_2 t + \delta)$. Here $\tilde{\boldsymbol{\gamma}}_1$ and $\tilde{\boldsymbol{\gamma}}_2$ are the tensorial strain amplitudes of primary and secondary flows respectively, ω is the shear frequency, and δ is a phase difference. If $\delta = 0$ and $\omega_1 = \omega_2$, then the flow is a uniaxial shear with strain amplitude $\boldsymbol{\gamma}_{\text{tot}} = \tilde{\boldsymbol{\gamma}}_1 + \tilde{\boldsymbol{\gamma}}_2$. However if either $\delta \neq 0$ or $\omega_1 \neq \omega_2$, then the applied shear is not uniaxial. For instance, if $\omega_1 = \omega_2$ but $\delta \neq 0$, the shear flow is elliptically polarized. Alternatively, by using a strong primary flow $\boldsymbol{\gamma}_1$ to drive the system away from equilibrium and a weak secondary flow $\boldsymbol{\gamma}_2$ to probe the system, a biaxial superposition spectroscopy measurement can be performed. These possibilities open up new avenues of inquiry for investigating the flow behavior of anisotropic materials, including liquid crystals [86, 83], colloidal suspensions [58], polymers [83], and biolgical tissues [32, 34] in which the viscoelastic modulus generally varies with the direction of shear.

It is crucial to ensure that the piezoelectric device is aligned with the top and bottom shear cell plates. As discussed above, the relative alignment and spacing of the shear cell's top and bottom plates are determined through adjustments made to the kinematic mount. In principle, once the cell geometry is set, the motion of the lower boundary of the cell can be computer controlled through the piezoelectric device without any further manipulation of the mount. This is only possible, however, if the axis of travel initiated by the piezoelectric device has no component perpendicular to the cell boundaries. Any misalignment of this axis will cause the distance d between the cell boundaries to vary as the lower boundary is moved. We find that, with sufficiently careful machining of our apparatus components, this problem can be avoided and, in practice, d remains constant to within 0.1 μm across the device's full range of motion. This small change in d is barely measurable with a confocal microscope, due to intrinsic resolution limits set by the optics.

Finally, due to mismatch in the thermal expansion coefficients of the various shear cell components we find that with moderate temperature control of a few °C gap stability is on the order of 1 μm over a period of one day. With better implementation of temperature control of about 1°C we find that any drift in the gap height remains below 0.1 μm, which is the imaging resolution of the microscope along the vertical direction.

3.4 Force Measurement

The main challenge in designing a force measurement device (FMD) is obtaining high sensitivities without sacrificing reliability and repeatability and without disturbing the applied shear flow. For instance, to measure the viscosity of glycerol

at a strain amplitude of 1 and strain frequency of 1 Hz the FMD needs to be sensitive to stresses on the order of 6 Pa. However, for a 4 mm $\times$ 4 mm wafer, this corresponds to forces on the order of 0.1 mN. To measure the viscosity of water requires the FMD to resolve forces as small as 0.1 μN. Thus, *in situ* measurements using our shear cell require extremely sensitive devices.

3.4.1 Uniaxial force measurement devices

Our FMDs operate by converting laterally-oriented shear stresses into small but measurable deflections in a system of cantilevers. Our uniaxial device consists of a thin, horizontal plate suspended from a pair of parallel cantilevers oriented vertically, as shown in Fig. 3.3. The entire device is machined from a single block of aluminum. The silicon wafer forming the upper boundary of the shear cell is anchored to the tip of the device. Laterally-oriented shear stresses deflect the wafer horizontally, creating a characteristic sigmoidal distortion in the cantilevers, which is shown schematically in Fig. 3.5a. The vertical deflection associated with these distortions is negligible, ensuring that the alignment and spacing of the shear cell boundaries are preserved under shear.

The deflection of the cantilevers tells us the force exerted on the top plate. We measure this deflection in the double cantilevers using a system of strain gauge resistors, which are typically foil or semiconductor gauges. The resistance of these strain gauges increases when the strain gauge is stretched; the change in resistance is proportional to the strain in the resistor. Two of these strain gauges are placed on the outer surface of each cantilever, as shown in Fig. 3.5a. When a cantilever is deflected, the inward curvature of one of the strain gauges causes its resistance to increase, while the outward curvature of the other strain gauge causes its resistance

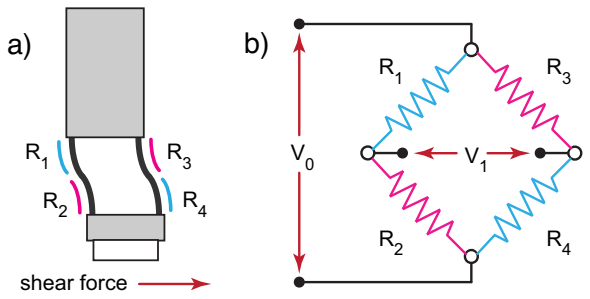

Figure 3.5: (a) Schematic representation of force measurement device under shear (side view), showing exaggerated deformation of the cantilevers and placement of the strain gauges. Note that for this deformation pattern R_1 and R_4 experience inward curvature, while R_2 and R_3 experience outward curvature. (b) Wheatstone bridge circuit configuration.

to decrease.

Wiring all four strain gauges in a standard Wheatstone bridge configuration provides a sensitive method for measuring these changes [15]. This circuit, shown in Fig. 3.5b, requires a excitation voltage V_0 across the bridge in one direction. For small changes in resistance and four strain gauges of equal resistance R in equilibrium, the voltage V_1 measured across the bridge in the other direction has the approximate form

$$V_1 \approx \frac{V_0}{4}\left(\frac{\Delta R_1}{R} - \frac{\Delta R_2}{R} - \frac{\Delta R_3}{R} + \frac{\Delta R_4}{R}\right) \quad .$$

The circuit is wired so that all four gauges make complementary contributions to the measured voltage V_1. In particular, for the distortion pattern shown schematically in Fig. 3.5a, the two strain gauges colored cyan have the same effect: both experience a positive ΔR and, by assigning these to positions 1 and 4 in the bridge circuit, both make a positive contribution to V_1. Likewise, the two strain gauges colored magenta both experience a negative ΔR and, by assigning these to positions 2 and 3 in the bridge circuit, both make positive contributions to V_1 as well. Assuming a symmetric distortion pattern, these contributions are all equal

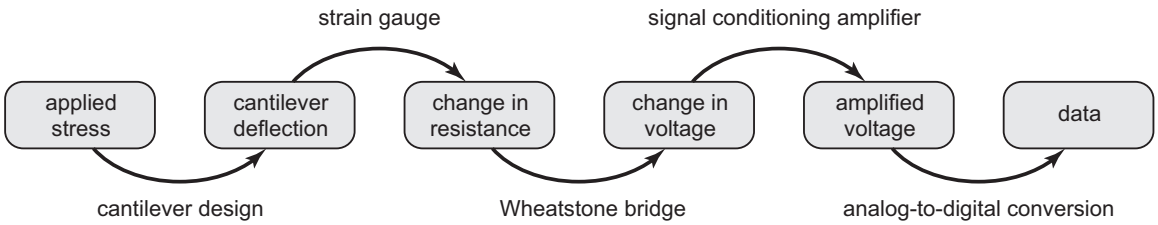

Figure 3.6: Data flow in our force measurement device. Shear flow in the sample exerts a stress on the end of the FMD, resulting in a lateral deflection of the cantilevers. Curvature associated with this deflection changes the resistance of four strain gauges mounted on the cantilevers. Using a Wheatstone bridge circuit, these resistance changes are converted to a change in voltage. However, due to the small magnitude of the strains involved, we must amplify the corresponding voltage change by using a signal conditioning amplifier. Finally, the amplified voltage is output to a computer using an analog-to-digital converter.

in magnitude, $|\Delta R_j| = \Delta R$, and the above equation reduces to

$$V_1 \approx V_0 \frac{\Delta R}{R} \quad . \tag{3.2}$$

Thus by measuring the voltage V_1 across the bridge, we can determine the deflection of the strain gauges and thus the deflection in the FMD. We amplify V_1 using a Vishay 2310 signal conditioning amplifier with a gain of 10^4. To avoid distortions in the output signal we refrain from any filtering of the signal. This conversion of applied stresses into measurable signals is summarized schematically in Fig. 7, noting the experimental component or process responsible for each step.

3.4.2 Uniaxial calibration and sensitivity measurements

As discussed above, we expect that the measured voltage V_1 should vary linearly with the deflection of the FMD. For small deflections, the FMD deflection is proportional to the applied stress. Thus the output voltage V_1 should be proportional to the force on the FMD as well. To characterize the response and the perfor-

mance of our force measurements, we conducted two types of calibration: first, by applying a known force to the FMD and measuring the output signal, and second, by mounting the FMD on the shear cell and shearing a sample of known viscosity.

We first calibrated the FMD by applying a known force to it and measuring the output signal. We mounted the FMD sideways, so its measurement axis is aligned vertically instead of horizontally. Then, we hung small weights from the end of the FMD and measured the voltage V_1 across the Wheatstone bridge. The raw voltages from the device were amplified using a signal conditioning amplifier and logged digitally using LabVIEW. Flipping the device over and repeating this procedure, we obtain the voltage response V_1 for forces applied in the opposite direction. The data in both directions, with a range of different weights varying from $f = 10^{-2}$ to 10^{1} N, are plotted in Fig. 3.7. A linear fit to the data, with the slope as the only free parameter, produces the line shown in the Figure. Note that data obtained from both orientations of the device fall onto the same line. The slope of this line, $V_1/f = 0.506 \pm 0.002$ V/N, provides a calibration factor with which we can convert measured voltages into forces. By dividing the forces by the known area of the silicon wafer, we can obtain the average stress on the FMD in the direction of the measurement axis, defined by the cantilevers. Thus our device provides quantitative access to stresses in the sample. The rotation stage on the upper mounting plate allows us to rotate the FMD and to align its measurement axis with any desired in-plane direction.

For steady uniaxial shear, the sensitivity of the device is limited by noise in the measurement system. With excitation voltages V_0 on the order of 5V, our signal conditioning amplifier introduces noise levels on the order of a few mV. This makes shear forces of less than roughly 10 mN difficult to measure precisely.

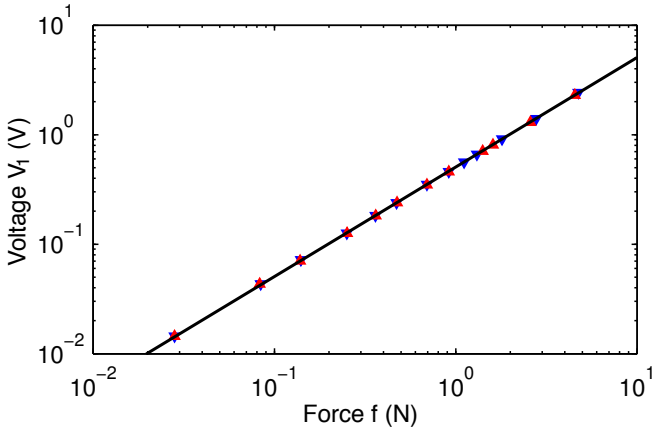

Figure 3.7: Calibration data establishing that voltages obtained from a uniaxial force measurement device are proportional to lateral forces applied to the end of the device. Data obtained for two opposite orientations (blue and red triangles) fall onto the same line: the device is both linear and symmetric. The slope of this line is 0.506 ± 0.002 V/N.

For oscillatory shear, however, we can use Fourier analysis to detect much smaller force signals buried in the noise. The Fourier transform of the force signal shows a definite peak at the oscillation frequency, which can be converted to a force amplitude. This approach, which is the motivating principle behind the lock-in amplifier, is limited by the noise floor in the signal's Fourier transform. This spectral analysis typically gives us access to force signal amplitudes as small as 20 μN, *i.e.*, three orders of magnitude beyond the limit associated with the noise floor in real space. In addition, by conducting a spectral analysis we are able to measure higher order harmonics associated with a nonlinear stress response. Thus, oscillatory shear is especially useful for experiments in which we expect very small forces.

To test the FMD using a sample with known viscosity, we characterized the flow curve of glycerol. The results are shown in Fig. 3.8. A small quantity of fluorescein is mixed into the glycerol, enabling us to use the confocal microscope to measure the gap heights. For each of three different heights, we sweep through a range

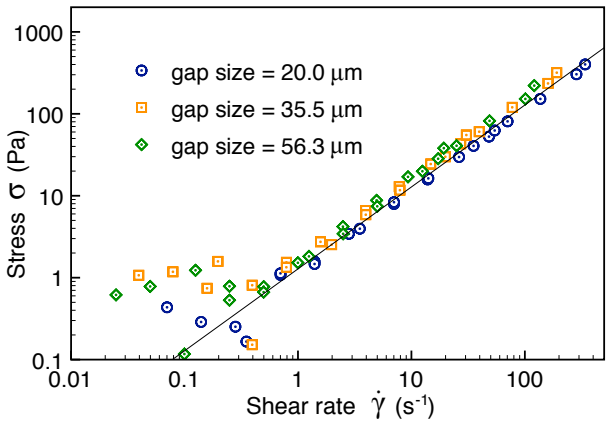

Figure 3.8: Flow curve for glycerol obtained using our apparatus. Six different data sets, taken at a range of gap heights and strain amplitudes, collapse onto a common line of slope $\eta = 1.28 \pm 0.07$ Pa·s. This value falls within the range of accepted values for the viscosity of glycerol.

of frequencies between 0.05 Hz and 100 Hz for two different strain amplitudes γ_0 and measure the force amplitude using Fourier analysis. The sample is allowed to equilibrate with the air environment inside the solvent trap for 30 minutes before beginning shear. Plotting stress amplitude versus strain rate amplitude, the data collapses onto the straight line shown in Fig. 3.8. The slope of this line obtained from a least squares fit to the data, $\eta = 1.28 \pm 0.07$ Pa·s, agrees with accepted viscosity values obtained under similar temperature and humidity conditions. The scatter at the base of the curve reflects a combination of noise in the spectrum and finite resolution of our data acquisition board.

Careful consideration of the conversion process summarized in Fig. 6 helps us better understand which aspects of our design most severely limit the sensitivity of the device. Cantilever design is clearly an important factor, for example. Using finite element calculations and Euler-Bernoulli beam theory, we confirm that under applied shear stresses both of the cantilevers in our device assume the characteristic curved shape shown schematically in Fig. 3.5a. For the weakest stresses resolved in in Fig. 3.8, however, the tip deflection turns out to be extremely small, *i.e.*,

less than the lattice constant of aluminum. At these stress levels, the resulting resistance changes in the four strain gauges are also quite small and subsequent amplification by the Wheatstone bridge circuit and signal conditioning amplifier produces a signal which is buried in the noise. As emphasized above, however, Fourier techniques can be used when dealing with oscillatory shear flows and these techniques extend the device's sensitivity considerably. Even for an oscillating shear stress amplitude of only 3 Pa, there is an unambiguous peak at the oscillation frequency in the measured signal's Fourier spectrum. Thus the noise floor is not the strongest limitation. Moreover, additional gain amplifies both the signal peak and the noise, without improving their ratio. Therefore, additional amplification will not increase our sensitivity either. Likewise, the finite bit depth of the analog-to-digital conversion process is not a major limitation when smaller signals are expected and the range of the data acquisition card is adjusted accordingly. Apart from the noise floor in the Fourier spectrum, cantilever and strain gauge design emerge as the most significant factors limiting sensitivity.

In summary, our current uniaxial device is capable of resolving surprisingly small deflections and is sufficient for rheological studies like those described in the Applications section. Access to even smaller shear stresses, however, requires thinner cantilevers and more sensitive strain gauges. These insights motivated the design of our biaxial force measurement devices, described in the next section.

3.4.3 Biaxial force measurement devices

To construct a biaxial Force Measurement Device, our design combines two independently functioning uniaxial FMDs. However, combining the two FMDs into one device introduces two new major design challenges. The first challenge is to

combine the FMDs in a geometry that can measure the same region of the sample, while still fitting into the sample testing chamber. Moreover, the implementation of this design geometry must not decrease the sensitivity of either axis of the FMD. The second major design challenge is to eliminate the coupling between the signals from the two different axes. For instance, while the sample is being sheared along one axis, the other axis of the FMD should have zero signal output.

We thus place the second FMD in series with (*i.e.*, vertically on top of) the first, orienting the uniaxial FMDs at 90° relative to each other as shown in Fig. 3.10. By including a solid block between the two, the boundaries of each cantilever remain clamped, as in the uniaxial version of our FMD. When a shear force is applied on the biaxial FMD, the identical boundary conditions ensure that the mechanical response of the double cantilevers is the same as that of the uniaxial device. The vertical arrangement of the uniaxial FMD designs allows the force measurements to be taken at the same location in the sample. Moreover, since the overall width of the biaxial and uniaxial FMD are similar, the new biaxial FMD still fits into the sample testing chamber. The dimensions of the biaxial FMD are provided in Fig. 3.9.

To convert the deflection of the cantilevers into an electrical signal, we mount eight strain gauges – four for each of the two axes – on the biaxial FMD. For ease of mounting, we place all the strain gauges on one side of the cantilever; our symmetric design ensures that this single-sided arrangement does not cause a decrease in the FMD's performance. We then wire these strain gauges into two independent Wheatstone bridges, one for each axis. The wiring for each axis is the same as the wiring for the uniaxial FMD. To minimize the number of wires we let the two Wheatstone bridges share the same excitation voltage V_0. The

signal voltages, V_{1x} and V_{1z}, are then passed via one digital acquisition card to a computer. By using two separate Wheatstone bridges, we can convert the stress response along each axis of the FMD into a separate electrical signal.

In general, a force on the bottom plate will deflect both the upper and lower sets of cantilevers in our biaxial FMD. The cantilevers are thin rectangular plates, and deflect most easily along the thin axis. However, exerting a force along the *thick* axis – orthogonal to the thin axis – will still deflect the cantilever parallel to the force, albeit by a much smaller amount. The ratio of these two deflections will be the quotient of the corresponding bending moments. The bending moments along the thin and thick axes are $\propto h^3 b$ and $\propto b^3 h$, respectively [45]. Thus their quotient is the square of the cantilever aspect ratio, $(h/b)^2$. To minimize the mechanical coupling between the FMD's two axes, we design the cantilever with the smallest possible value of h/b. For our design, the ratio of the bending moments $I_x/I_z = (h/b)^2 = 2.5 \times 10^{-3}$, where h= 0.5 mm and b= 10 mm. Thus our design has an extremely small coupling. To understand the coupling in more detail, we performed a finite element analysis, displayed in Fig. 3.10. As expected, we find a small but nonzero mechanical coupling between the two sets of cantilevers. While our design significantly reduces the mechanical coupling between the axes, the coupling is still nonzero and must be accounted for.

There is a secondary source of coupling in the FMD, due to the electronic data acquisition and signal amplification circuits. If the signal amplifier impedance is high (*e.g.*, resulting from a low-pass electronic filter), the response time of the digital acquisition card can be dramatically increased. Thus, when the digital acquisition card switches from reading out one axis to the other, the residual signal from the previous measurement dominates the new measurement. These residuals

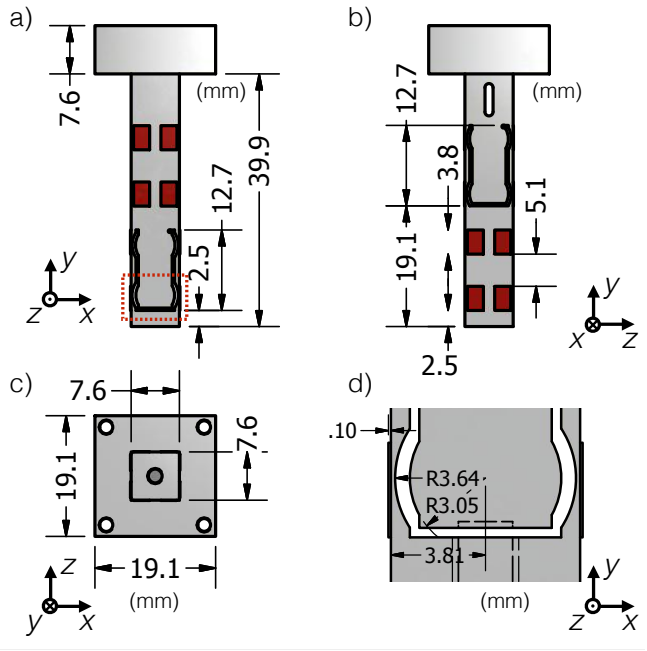

Figure 3.9: Schematic representation showing the dimensions of the biaxial force measurement device from (a) side (b) back and (c) top views. The dimensions of the cantilevers and foil gauges (red box in (a)) are labeled in (d).

cause an additional electronic coupling between the two force measurement axes [77]. To avoid this issue, we use two separate signal amplifiers with extremely low impedance and avoid filtering the signal. As with the single axis FMD post-processing of data from an oscillatory force measurements via Fourier transforms can further enhance the measurement sensitivity.

Finally, an additional source of apparent coupling can arise due to misalignment between the FMD's and the piezo's axes. If the force measurement axes are misaligned with the displacement axes, then a motion which is intended to be along one axis of the FMD will actually have components along both of the FMD's axes. This will result in an apparent force perpendicular to the applied flow.

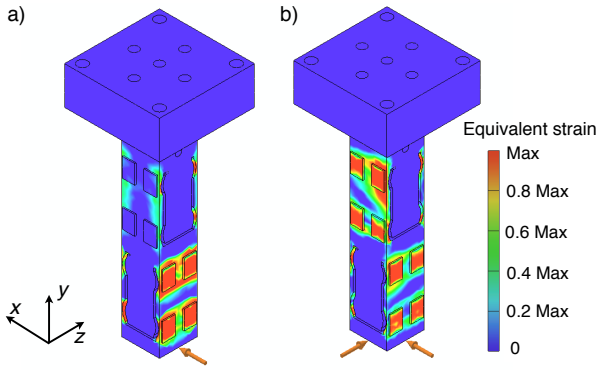

Figure 3.10: Finite element analysis of the biaxial force measurement device with forces (a) perfectly aligned along the bottom cantilever's axis, and (b) at 45° to both cantilevers' axes. The color bar illustrates the value of equivalent strain, which is the magnitude of the stain tensor. As the shear force is applied along the x-axis, most of the strain is focused around the strain gauge area of the x-channel (a). Likewise, as the force is applied along both x-axis and z-axis simultaneously, the gauges of both channels sense large strain at the same time. (b)

3.4.4 Biaxial calibration and sensitivity measurements

We first calibrate the alignment of the FMD's axes, relative to the piezo's axes. To do this, we mount the biaxial FMD on the shear apparatus via a rotation stage. We then apply a uniaxial shear flow and finely adjust the angle of the rotation stage, maximizing the signal in one channel and minimizing the signal in the other. We double-check the alignment by switching the direction of the applied flow by 90°. When the force measurement orthogonal to the shear flow is minimized for both flow orientations, then the biaxial FMD is aligned.

To experimentally determine the coupling between the FMD's axes, we performed force measurements on a sheared standard-viscosity liquid (VIS-RT5K-600, Paragon Scientific). Since the fluid viscosity is known, the stress on the FMD is known for a given shear rate. By varying the strain amplitude at a fixed shear oscillation frequency $f = 10$ Hz, we measured the performance of the FMD over

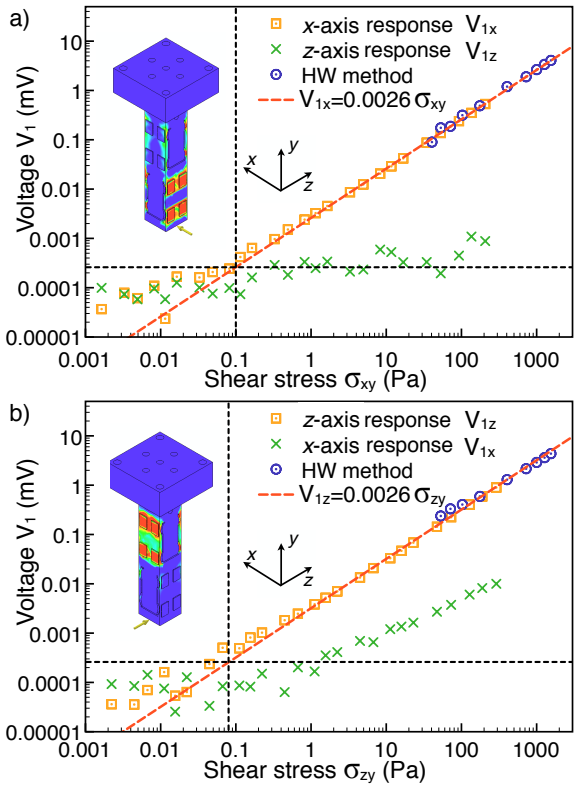

Figure 3.11: The shear stress calibration with shear cell experiment and hanging weight method for x-axis (a) and z-axis (b). The orange data represent the response of the axis that is along the shear direction, and the green data represent the response of another axis. The blue data are the voltage response measured with the hanging weight method. The red curves are the linear fit to the data. The schematics of the strained force measurement device are generated by the finite element analysis. [N. Lin *et al.*, *Soft Matter*, 2014, 10 (12), 1969][51] – Reproduced by permission of The Royal Society of Chemistry

six orders of magnitude in stress, ranging from 1×10^{-3} to 2×10^{3} Pa. Figure 3.11 shows the resulting shear stress versus FMD output voltage, for shear flows oriented along both the x-axis (a) and z-axis (b) of the biaxial FMD. While there is little signal along the z-axis when the flow is along x (Fig. 3.11a), we do find a measurable force signal along the x-direction when the flow is strictly along z (Fig. 3.11b). The calibration shows that this xz-coupling is around $\sim 1\%$. Finally, by using semiconductor strain gauges and reducing the thickness of the cantilevers

by factor of three in the design of biaxial FMD, the stress resolution of this new device is approximately ten times higher than the previous uniaxial design.

What is the source of this coupling? Our signal amplification and digital acquisition circuit designs have eliminated the possibility of electronic coupling between the two axes. Figure 3.11a shows that the system has been aligned as best as possible; thus this coupling cannot result from the misalignment of the FMD with respect to the piezoelectric stage. A clue to the origins of the residual coupling lies in the fact that the zx-coupling is zero while the xz-coupling is finite. This implies that the coupling matrix is not symmetric, and therefore that its principle axes are not orthogonal. Thus, we speculate that the residual coupling arises from imperfect installation of the strain gauges. Any asymmetry in the strain gauge installation will couple with the cantilever's transverse mechanical deflection. In practice this results in a residual coupling and a non-symmetric coupling matrix. It is a testament to the quality of the strain gauge installation that the coupling is only at the 1% level.

Although the coupling between the two axes of the FMD is extremely small, ideally we would like to avoid it altogether. To further eliminate the coupling, we can proceed in two ways. First, we can use the coupling matrix's inverse to convert the measured voltage signal into actual forces. Alternatively, we can apply shear flows in two orthogonal directions with different frequencies. Then, Fourier analysis can be used to pick up the response only at the applied frequencies. This allows for easy disentanglement of the stress responses from the different applied flows.

Shearing the viscosity standard liquid also provides us with measurements of the FMD's sensitivity. The data in Fig. 3.11 demonstrate that both channels of

the biaxial FMD have similar force sensitivity and response. The voltage signals respond linearly with the applied stress over the entire measured range. The biaxial FMD is sensitive to stresses down to ≈ 0.1 Pa, at which point noise starts to dominate the signal. At force values higher than the range accessible with the viscosity standard liquid, we verify the calibration by hanging weights off the FMD. We find that the viscosity standard calibration and the hanging weight calibration are in excellent agreement over the overlapping range. Thus the FMD is linear and accurate over at least four decades in applied stress. Moreover, our FMD was also tested during the strain gauge installation and was shown to behave linearly with the same constant we measure for forces up to 15 N. This force would correspond to 6×10^5 Pa. Thus, our FMD functions linearly and accurately over a range of more than six decades.

3.5 Visualization and Flow Characterization

For over a decade, confocal microscopy has been recognized as ideally suited to the quantitative study of soft materials [63, 27, 40, 11]. Our central purpose in designing a shear apparatus and force measurement device is to use them in conjunction with a high-speed confocal microscope. This allows us to correlate the real-time evolution of the sample's three-dimensional microscopic structure with its rheology and mechanical response. In particular, much of our work involves studying colloidal suspensions under shear. However, special care must be exercised to usefully implement confocal microscopy in conjunction with our shear apparatus and FMD. First, to study colloidal suspensions, we must choose a suspension that allows for imaging with a confocal microscope and that provides strong stress signals for the FMD. Second, confocal images are always partially distorted due

to the confocal's optics. To accurately resolve the sample's microstructure, then, we must understand this distortion and account for it if necessary. Finally, to quantitatively measure the sample microstructure and its dynamics, the confocal image data must be characterized with computational image analysis methods. After discussing the details of these three issues, we illustrate the performance of our shear apparatus in conjunction with confocal microscopy by examining the possibility of wall-slip and non-affine motion in a colloidal suspension, both of which are difficult to check in a conventional rheometer.

3.5.1 Choosing a suspension for rheoscopic measurements: index and density matching

Our shear apparatus is designed to mount onto the stage of a confocal microscope (Zeiss LSM 5 Live inverted confocal microscope). The basic principles of the technique are described in detail elsewhere [26]. In short, a confocal uses a pinhole to control optical sectioning of a fluorescent sample. Focusing light of the appropriate wavelength at one point in the sample causes the sample to fluoresce. The pinhole is placed at a focal point conjugate to the illuminated point, which blocks all out-of-focus light from reaching the detector. Thus, in principle, only a single point is imaged at a time. Scanning this point throughout the sample provides a three-dimensional map of sample regions containing fluorescence dye. To speed up data acquisition the Zeiss LSM 5 Live instrument scans an entire line at once, instead of a point, but the basic principles remain the same.

Since confocal microscopy relies on fluorescence rather than transmitted or reflected light, either the particles or the solvent must be dyed. If the parti-

cles are dyed, confocal images show bright spots on a dark background, whereas if the solvent is dyed instead, the spaces occupied by the particles appear dark and the background bright. As long as the refractive index of the solvent closely matches that of the particles, the interior structure of even dense suspensions can be mapped with precision. However, if the particles' refractive index differs from the solvent, then due to Mie scattering the particles will scatter the illuminating light, in turn creating a turbid sample and severely degrading the image quality. This requirement of matched particle-solvent refractive indices strongly constrains one's choices when selecting a suspension for quantitative experiments using confocal microscopy. One of the most popular choices is poly-(methyl methacrylate) (PMMA) spheres suspended in a mixture of hydrocarbons such as decalin (decahydronaphthalene) and bromocyclohexane (CXB). PMMA spheres can be synthesized, stabilized, and dyed using standardized recipes [2, 16, 43]. Hydrocarbon solvent mixtures can be designed to nearly match both the density and the refractive index of the PMMA spheres. Moreover, PMMA suspensions provide an excellent approximation of hard-sphere interaction dynamics [65, 16].

For stress measurements, however, one also requires the solvent viscosity to be high enough to produce measurable stresses. The calibration curves shown in Section III suggest that, despite the sensitivity of the double cantilever design, it is difficult to access shear stresses below roughly 1 Pa using our apparatus. Thus, shear rates on the order of 10^3 s^{-1} are needed to produce measurable stresses when the suspension viscosity is similar to that of water, *e.g.*, on the order of a few mPa·s. At low and intermediate volume fractions many suspensions, including the PMMA standard described above, have viscosities close to this range. Thus a more viscous solvent-particle system is therefore required if our rheoscopic experiments are to explore broad ranges of shear rates.

Silica particles suspended in glycerol and water provides a useful alternative to PMMA suspensions. A roughly 4:1 mixture of glycerol and water can match the refractive index of silica. Moreover, this mixture has a viscosity of 60 mPa $\cdot$ s, nearly two orders of magnitude larger than that of water and many oils, including decalin, tetralin, and CXB. This silica-based suspension makes it possible to obtain measurable stresses across many orders of magnitude in shear rate using our apparatus. The silica particles are not density matched with the solvent, however, and thus sedimentation effects need to be considered. The gravitational Péclet number,

$$\mathrm{Pe}_g = \frac{aU}{D},$$

provides a comparison between sedimentation and diffusion [66, 64]. Here, the diffusion constant D for a sphere is given by the Stokes-Einstein relation,

$$D = \frac{kT}{6\pi a\eta},$$

where a is the sphere radius and η is the viscosity of the surrounding fluid. The sedimentation velocity U for a falling sphere is set by a balance between gravity, buoyancy, and drag:

$$U = \frac{2(\rho - \rho_f)a^2 g}{9\eta},$$

where ρ and ρ_f are, respectively, the densities of the sphere and the surrounding fluid. Combining these expressions, we find that 1.0 μm diameter silica spheres in an index-matching suspension of glycerol and water have a $\mathrm{Pe}_g \approx 0.5$. Although the effect of sedimentation on our system is not negligible, we observe considerable shear-induced viscous resuspension of our colloidal particles [49]. Furthermore, since the gravitational Péclet number $Pe_g \propto a^4$, its value quickly reduces to $\sim$ 0.1 when particles that have a slightly smaller diameter $2a = 0.7$ μm are used. Thus, the micron-sized silica-based suspensions are fairly well-suited to rheoscopic measurements.

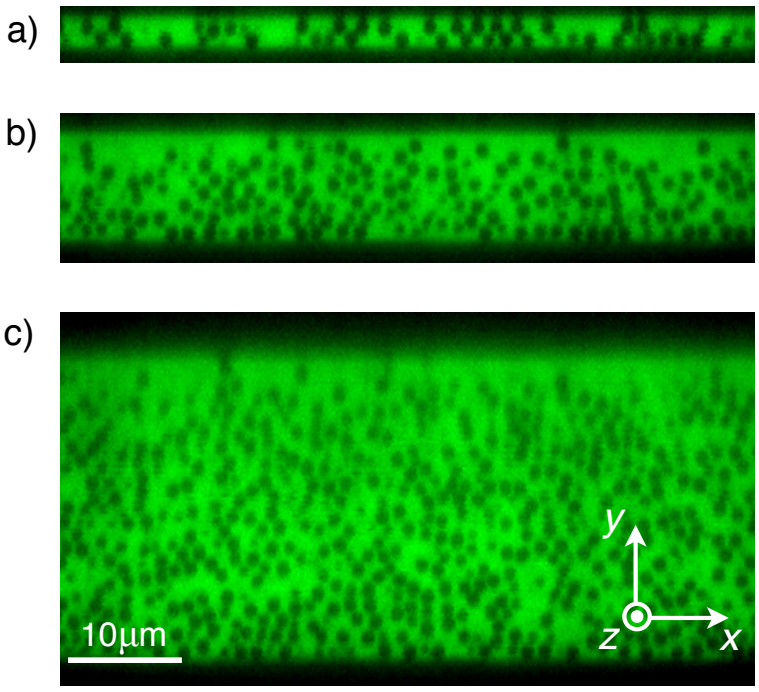

Figure 3.12: Images of quiescent colloidal silica suspensions at different gap sizes (a-c). The flow-gradient cross-section is shown (gravity points down in the figure). The dyed solvent appears bright in the image. Since the dye does not penetrate the silica spheres, they appear dark. The glass plate (bottom of cross-sections) and the silicon wafer (top of cross-sections) appear as the dark horizontal regions. Our shear cell allows us to tune the gap size from 3.1 μm (a) to explore strongly confined systems, to 10.1 or 27.4 μm (b,c) to explore systems that approach bulk suspensions. However, as is visible in (c), poor image quality and significant aberrations appear when imaging deep into the sample, due to inherent limitations in confocal optical imaging [38].

3.5.2 Quantifying the confocal's optical response

Before analyzing the suspension's microstructure and rheology, we must first explore the limitations and responses of our confocal microscope. Our lab uses a Zeiss LSM 5-Live system with a lens stage that is driven by a stepper motor. The calibration procedure described below was conducted for a 100× objective model number 9900. However many of the considerations described below apply broadly. Fig. 3.12 shows vertical xy slices through three-dimensional images of one of our

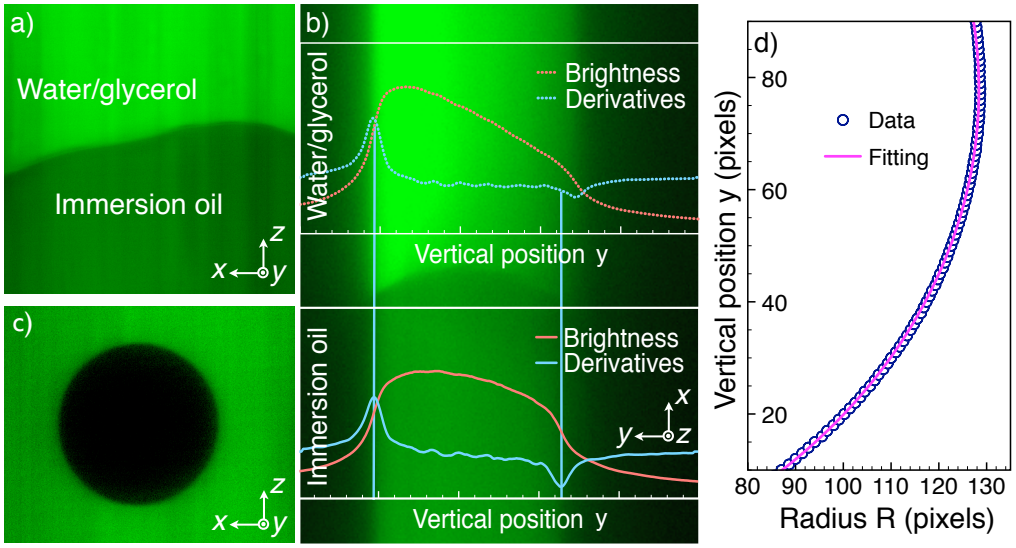

Figure 3.13: Measuring the optical distortion along the y-direction. (a) xz-cross section of the immersion oil: water glycerol image. (b) xy-cross section of the same image. Plotted at right is the intensity profile of the image as a function of y. In both images, the oil phase is located at the top of the image. At left is the derivative of the above intensity profile. (c) Cross-section of the 30 μm polystyrene sphere used to find the y-voxel size. (d) Blue circles: The apparent sphere radius R in (c) as a function of the apparent y-pixel. By fitting the data to an ellipse (red line), we can extract the y-voxel height from the known xz-pixel values.

silica-based suspensions, obtained for gap heights of 3.1 μm, 10.1 μm, and 27.4 μm. The dark dots are 1μm silica colloidal spheres and the bright background is the glycerol-water solvent containing fluorescein sodium salt. The black regions at the top and bottom of each slice represent regions where the focal plane is chosen beyond the upper or lower boundaries of the shear cell, *i.e.*, outside the sample volume. These slices clearly showcase the instrument's ability to create highly confined samples with upper and lower boundaries that can be brought within a few particle diameters of one another. Two imaging artifacts are conspicuous in Fig. 3.12, however. First, the spherical particles appear to be stretched along the

y-direction. Second, the image quality noticeably worsens deeper into the sample. Careful consideration of these effects is important, especially for experiments requiring analysis of scans taken at different depths in the sample. Note that in the microscopy literature what we call the y-axis is often referred to as the optical z-axis.

The imaging artifacts visible in Fig. 3.12 arise from two separate issues. First, due to mechanical and software limitations, the actual y-direction step size differs from its nominal value. Second, as shown in the previous works [38, 40], there are inherent imaging distortions in confocal microscopy, especially if there is an index mismatch between the sample and the microscope lens. The mismatch between the sample and optics is significantly worse for silica in glycerol and water than for PMMA suspensions. These issues have two major consequences. First, the center of the microscope's point-spread function, or the confocal's imaging response to a point source, does not move with the lens but instead lags behind. This lagging results in an apparent volumetric pixel (voxel) height that is less than would be expected from the motion of the lens. Second, the confocal's point-spread function in the y-direction significantly worsens as images are taken deeper into the sample. Without correcting for these biases, one cannot be confident about particle positions in the y-direction. In addition, the anisotropy in the point spread function and an incorrect y-positioning will make a spherical particle appear stretched and can affect featuring of non-spherical particles.

We calibrated the distortion in the y-direction using two independent methods. Following Ref. [38], we first made a sample cell consisting of two pieces of glass in a wedge configuration. One half was filled lengthwise with a mixture of 80:20 water glycerol with fluorescein dye added (used for experiments with silica particles), and

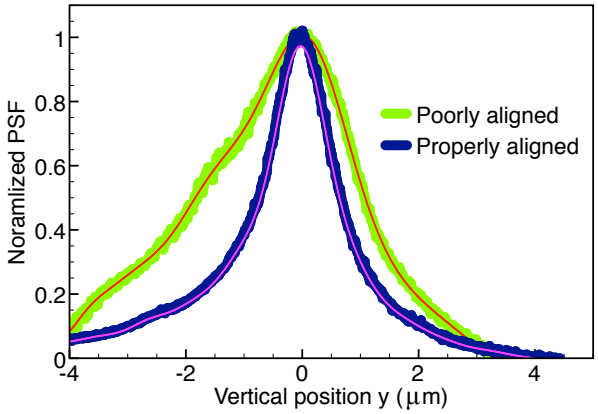

Figure 3.14: Point-spread function when the confocal is aligned (purple) and when the confocal is misaligned (green). Misalignment of the confocal's internal optics can significantly affect image quality, as visible from the figure. For both curves, the thick lines are clouds of individual data points. The solid thin lines in the foreground are a Legendre polynomial approximation to the measured points, which reduces the noise in the measured PSF.

the other half with immersion oil with Nile Red dye added. Since the immersion oil has the same index of refraction as the coverslip and the microscope lens, there is minimal optical distortion in the immersion oil region. We took three-dimensional images of the entire gap in each section simultaneously and found the apparent top and bottom of the sample cell in each region. Due to effects of index mismatch, there appears to be a "jump" in height across the oil/water interface [38], cf. Fig. 3.13a & b. The difference in heights gives the effect of y-distortion due to the index mismatch alone. Moreover, by taking slow image stacks with high slice fidelity, we measured systematic differences between the confocal's scanning stage nominal step size at fast frame rates and the actual y-displacement of the lens. By combining the effects of optical distortion and incorrect mechanical step size, we find that when the confocal is programmed to use 0.2 μm step sizes, the final apparent step size is only 0.166(5) μm in a water-glycerol solvent, or $\approx$83% of the input value. Of this, the optical distortion causes a $\approx$ 8% decrease in the

voxel Y-size, and the incorrect mechanical step size causes a $\approx 10\%$ decrease in the voxel size.

Our second method for measuring optical distortion consisted of using large beads. We obtained highly monodisperse 20.85 $\pm$0.04 μm and 30.39$\pm$0.05 μm polystyrene spheres from Bangs Laboratories (NIST-traceable grade). For each sphere size, we made a dilute suspension of these spheres in the same 80:20 glycerol-water mixture used for imaging silica spheres, and we mounted this suspension on a microscope sample slide. Since polystyrene is slightly buoyant in the water-glycerol mixture, we placed the coverslip directly onto the sample to keep the polystyrene particles near the interface. We then repeatedly imaged the bottom halves of several spheres. From these images, we used an image edge finding technique to find the radius ρ of the sphere as a function of the apparent y height. Any distortion or incorrect mechanical step sizes will stretch the image along the y-direction, making the spherical particle appear as an ellipsoid of revolution. We then fit $\rho(y)$ to an ellipse and extracted the semimajor and semiminor axes of the ellipse. From the ratio of the semimajor to semiminor axes and the known xz-pixel value, we can calculate the apparent y-pixel value. This method allows us to include effects from both incorrect y-positioning of the confocal and from index mismatch of the solvent in one measurement. We repeated this measurement with multiple spheres at each of the two different sphere sizes. From these images, we measure the apparent y-pixel ratio to be 0.169(3) μm with an input 0.2 μm y-step size. Through a simple rescaling of the positions along the gradient direction, these calibrations allow us to accurately measure both the gap size of our shear cell – crucial for knowing the applied shear rate – and the microstructure of the colloidal suspension.

Calibrating the effects of the confocal's point-spread function (PSF) is more difficult. Hell [38] has shown that the PSF varies with the optical depth into the sample, and that the PSF changes significantly for samples of different refractive indices. Rather than measuring the full PSF in a different medium than our sample [21], we opted to measure an xz-averaged PSF in the same medium as our sample. To do this, we approximated the PSF as translationally invariant near the cover slip. We then imaged a flat interface between a glass slide and the same fluorescein-dyed glycerol-water solution used in our experiments. The resulting image can be expressed as

$$\begin{aligned} I(x,y,z) &\propto \int_{-\infty}^{\infty} H(y-y')p(x',y',z')dx'dy'dz' \\ &\propto \int_{-\infty}^{\infty} H(y-y')\tilde{p}(y')dy' \end{aligned} \tag{3.3}$$

where $p(x,y,z)$ is the confocal's point-spread function, and $\tilde{p}$ is the $xz-$averaged PSF. $H(y)$, the Heaviside step function, describes the true intensity profile near the interface. Taking a derivative in y recovers $\tilde{p}(y)$, the xz-averaged PSF. This formulation has the additional advantage of averaging over a large field of view to reduce noise in the PSF. To increase our accuracy in the measurement of the PSF, we averaged our measurements over 600 images. By setting the location of the interface as the value of y such that the measured intensity reaches a fixed fraction of its maximum, we can account for variations in the confocal's y-positioning. The resulting xz-averaged PSF is shown in Fig. 3.14. Fig. 3.14 also displays a PSF measured for poor alignment of the confocals internal optics. We find that the PSF is significantly worse when the internal optics are not precisely aligned, as mentioned in previous work [21]. Therefore, proper optical alignment of the confocals internal optics is critical for precision measurements of 3-dimensional particle structure.

3.5.3 Quantifying suspension structure and dynamics with confocal microscopy

The confocal microscope's three-dimensional scanning ability allows us to check the entire shear zone for dust, bubbles, silicon wafer fragments, and other sample contaminants before beginning an experiment. Under shear, we typically observe uniform behavior throughout the sample but often use only the central region of the cell for quantitative measurements. Our Zeiss LSM 5 Live instrument captures a single 512-pixel row of data at a time. This line, which is oriented in the x-direction, is scanned in the z-direction to complete a full 512 pixel $\times$ 512 pixel image. For a 100$\times$ microscope objective, this corresponds to a 61.4 μm $\times$ 61.4 μm sample slice oriented parallel to the cell boundaries, *i.e.*, parallel to the velocity-vorticity plane. At this resolution, a maximum of 60 frames per second can be collected at a fixed height y. When the field of view is reduced to 512 pixels $\times$ 128 pixels, the maximum frame rate increases to 216 frames per second. Frames can be collected at different heights to probe three-dimensional structure. Using standard center-finding algorithms, particle positions can be estimated to sub-pixel accuracy [22]. These particles positions can be used to calculate a number of important physical quantities, including flow profiles and correlation functions, as discussed below and elsewhere [22, 11].

Strictly speaking, confocal microscopy does not provide an instantaneous snapshot of particle positions in the imaging plane. Data is collected from different parts of the sample at slightly different times. For static samples, this has little quantitative impact. For suspensions under shear, however, the sample is moving while being scanned and the detector may record distortions associated with these motions. At the maximum frame rate, the instrument can scan across a 512 pixel $\times$

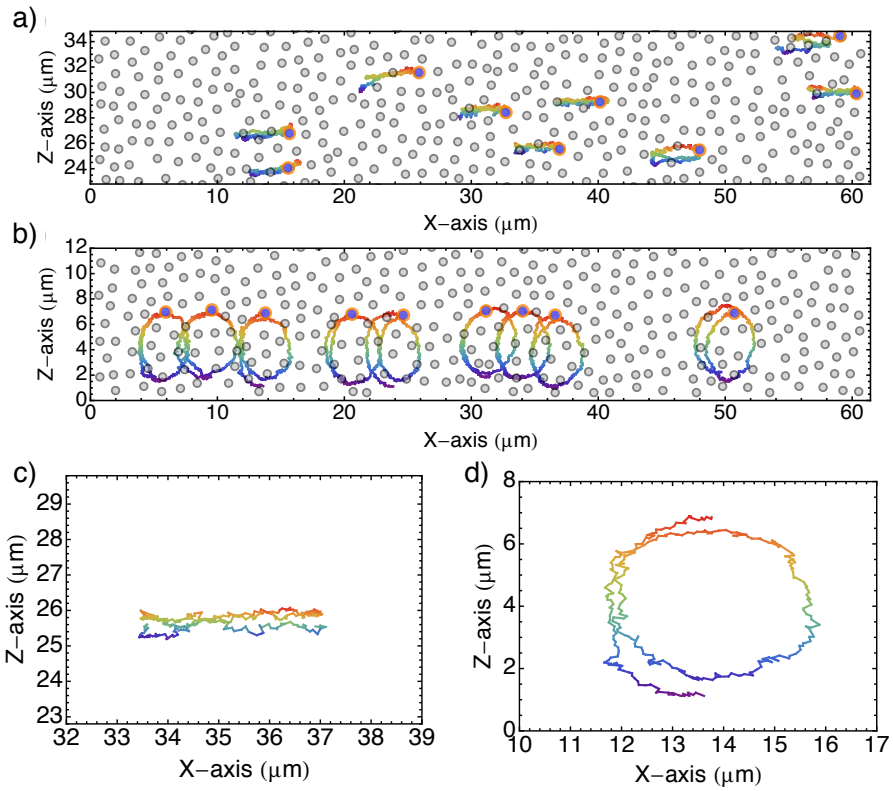

Figure 3.15: Particle trajectories under linearly polarized (a) and circularly polarized (b) shear, color coded in time over one shear cycle. Particle positions at the start of the cycle are shown in gray filled circles. By tracking individual particles we can not only find the collective motion of the suspension but we can also examine individual particle trajectories. (c,d) A close-up view of the tracked trajectories from (a) and (b), respectively. The trajectories clearly show both the shear-induced motion of the particle as well as a random Brownian component.

512 frame in roughly 0.01 seconds, *i.e.*, at a scan speed on the order of 6000 μm/s. As a comparison, the maximum velocity $v_{\max}$ of a colloidal particle subjected to sinusoidal shear is given by $v_{\max} = 2\pi f A$, where A is the displacement amplitude and f is the oscillation frequency. Using the amplitude $A \approx 22$ μm, we find that $v_{\max}$ is much smaller than 6000 μm/s for oscillation frequencies on the order of a few Hz or less. In a sample with a gap height of 5 μm, for example, shear rates of up to 100 can be reached with these frequencies. Thus, for slow to moderate shear

flows in narrow gap samples, the instrument can be regarded as imaging particle configurations in two dimensions nearly instantaneously. This range includes, for example, the entire shear thinning regime and much of the Newtonian plateau probed in Ref. [13].

As an illustration of the usefulness of this approach for direct visualization of suspension dynamics, Fig. 3.15 compares two-dimensional particle motions observed under different shear conditions. The particles are tracked individually using standard techniques [22, 11]. Imposing oscillatory shear flow in the x-direction, we see that particle trajectories are horizontal on average (Fig. 3.15a). A close up view of a single particle trajectory is shown in Fig.3.15c. The fluctuations, which are due to Brownian motion, are dominated by the imposed flow when the shear rate is much larger than a characteristic relaxation rate. A circular shear flow can be generated by imposing oscillatory shear flows along x-axis and z-axes simultaneously with a phase difference of $\pi/2$. This generates circular particle trajectories like those shown in Fig. 3.15b. A close up view of one of these trajectories is shown in Fig. 3.15d. In other situations, real-time access to particle-scale dynamics is useful in other ways. In crystalline samples, for example, point and line defects can be tracked along with individual particles.

Due to the symmetries of shear flow between parallel plates, all colloidal particles at the same height move with the same velocity on average. Moreover, these coarse-grained velocities are parallel to the microscope's horizontal imaging plane. Thus, the bulk velocity field can be extracted by averaging over different in-frame velocity measurements. In practice, for simple oscillatory shear flows, we image a 512 pixel $\times$ 512 pixel window and subdivide it into 31 different overlapping windows, each at 512 $\times$ 32 pixels. Using particle imaging velocimetry (PIV) in

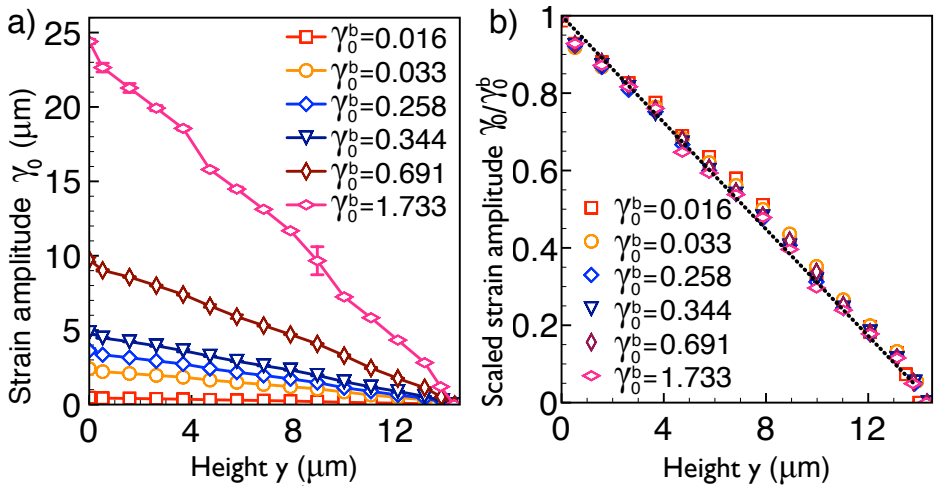

Figure 3.16: (a) Average particle displacement amplitude as a function of height, for six different strain amplitudes ranging from $\gamma = 0.016$ (red squares) to $\gamma = 1.733$ (magenta diamonds), with an intermediate volume fraction $\phi = 0.48$. All the profiles are linear, and show no shear banding or wall slip. (b) The average particle displacement from (a), normalized to the maximal displacement γ_0^{bottom} which is observed at the bottom of the shear cell. The curves fall on a constant line, as expected for a simple shear flow.

each window, we then average over all 31 overlapping windows to find the mean oscillation amplitude and speed of the full 512 × 512 pixel frame. Repeating this procedure at a series of different heights y builds up an estimate of the flow profile. Fig. 3.16 shows profiles obtained for oscillatory shear at a range of different shear rates $\dot{\gamma}_0$. The profiles collapse when normalized by $\dot{\gamma}_0$ or, equivalently, by the maximum displacement imposed by the piezoelectric device. The lack of inertial effects in our strongly confined samples (Reynolds number $\text{Re} \sim 10^{-6}$) ensures that the instantaneous particle velocities give the instantaneous flow field. Moreover, our samples are homogeneous apart from slight sedimentation. We do not observe shear banding in low to intermediate volume fraction suspensions, as one can see in the linear profiles of Fig. 3.16. Together, these properties ensure that the entire sample oscillates in phase to an excellent approximation. Thus, the amplitudes calculated using PIV are indeed a portrait of the instantaneous bulk flow.

For sufficiently fast shear, the in-plane structure is distorted by the finite lateral scan-rate. Since this distortion is linear with y position, simply shifting different lines backwards by different amounts is sufficient to correct the distortion. To obtain an estimate of the instantaneous structure in three dimensions, the vertical scan rate must be taken into account as well. For a reduced field of view of 512 pixels $\times$ 128 pixels, the maximum scan rate in the y-direction is roughly 31 μm/s. For a gap size of 5 μm, then, it takes roughly 0.16 seconds to complete a full stack of images from the bottom boundary of the sample to the top. Under these conditions, a three-dimensional scan is essentially equivalent to an instantaneous snapshot of the suspension structure only for slow oscillation frequencies of 20-30 mHz or less. For larger frequencies, however, there will be a noticeable mismatch between adjacent image slices, due to the finite vertical scanning speed of the confocal. This distortion can be corrected by linearly shifting the vertical image slices using the PIV data, similar to the method for fixing distortions from the lateral scan rate. A three-dimensional correction scheme is not necessary for flow profiling, since individual frames can be scanned one by one and their contributions to the profile are independent. The ability to correct distortions in three-dimensions is critical, however, for a statistical analysis of suspension structure. In particular, a three-dimensional map of particle positions provides access to the pair correlation function, $g(\vec{r})$, the probability of finding a particle at a position $\vec{r}$ relative to another particle's center. As discussed in the next section, $g(\vec{r})$ provides useful information concerning the relationship between suspension microstructure and bulk rheology.

3.6 Applications

In the previous sections, we have demonstrated that our confocal rheoscope accurately measures the structural and stress responses of a complex fluid in a precisely-controlled shear flow. Similar to other confocal rheometers [24, 25, 3, 9, 4, 70, 67, 36, 37, 60, 20, 19, 74, 10, 73, 88, 89] this instrument allows us to investigate the interplay between a suspension's structure and its rheology. However, our device also allows for biaxial rheological measurements and the study of confined systems. For example, using this device we have studied shear thinning and thickening of suspensions, the interplay between novel string structures and rheology in confined suspensions, and the rotational as well as translational diffusion of anisotropic particles. Moreover, our device can easily incorporate additional instrumentation or be combined with other imaging techniques such as polarization microscopy to enable and even wider range of studies.

3.6.1 Shear thinning and thickening of colloidal suspensions

One generic flow behavior of complex fluids is shear thinning or thickening – the viscosity either decreasing or increasing, respectively, with increasing shear rate [13, 37]. Colloidal suspensions show both shear thinning and shear thickening behavior. The structural origins of these behaviors have been extensively studied with Stokesian dynamics simulations [30, 5] and more recently with experiments combining rheometry with light- or neutron-scattering [8]. Stokesian dynamics simulations can probe single particle dynamics with unprecedented accuracy in small systems of typically $\sim 10^3$ particles, given the current limits on computational

power. The scattering techniques, on the other hand, measure average behavior of systems consisting of a very large number ($\sim 10^9$) of particles. The huge gap in system size between these two regimes demands a new bridging technique, which can assess not only the average properties of a suspension, such as its viscosity and normal stress differences, but also the dynamics of individual particles. Using the uniaxial version of this confocal rheoscope we studied the non-Newtonian rheology of suspensions [13]. In a typical experiment, our system consisted of 10^7 to 10^8 particles between two shear plates, which allowed us to obtain accurate average behavior of sheared suspensions. Meanwhile, with the help of fast confocal microscopy, we resolved the motion of single particles over a long period of time. Statistical errors were reduced significantly by averaging over the $\sim 10^4$ particles within the imaging field of view.

Using our confocal rheoscope, we investigated the configuration of particles under oscillatory shear in the shear thinning regime (around $\mathrm{Pe}_s \equiv \dot{\gamma} d^2/D_s \sim 1$, where $\dot{\gamma}$ is the shear rate, $d = 2a$ the particle diameter, and D_s is the particle self-diffusion constant) [18]. Using the real-time particle positions measured by our confocal microscope, we examined the pair correlation function of particles in the plane of shear, $g(x, y)$, under a full cycle of oscillatory shear. The fore-and-aft asymmetry developed near the maximum shear rate within the cycle is consistent with previous theories and experiments for suspensions under steady shear flow [14, 31, 81, 90]. The temporal resolution of high-speed confocal microscopy allows us to track the configurations of particles *in situ*. We can further relate the pair correlation function $g(\vec{r})$ to the Brownian stress by[14]:

$$\tau_B \approx -n^2 k_\mathrm{B} T a \int_{r=2a} \hat{r}\hat{r} g(\vec{r}) \mathrm{d}S \tag{3.4}$$

where n is the number density of particles, $k_\mathrm{B}T$ is the thermal energy, a is the

particle radius, and $\hat{r}$ is the unit vector in r-direction. Due to resolution limitations in the experiments the integral is evaluated over a small range of radii centered at $r = 2a$ and a prefactor is introduced to compensate for the adjusted integral range in the stress calculation. The total stress can then be calculated by adding the hydrodynamic stress to the Brownian stress [13]. Comparison between the total calculated stress determined from the particle positions and the direct measurement with our Force Measurement Device show quantitative agreement.

Furthermore, we also probed the linear viscoelastic behavior of the Brownian stress under oscillatory shear. We fit the real and imaginary parts of the complex Brownian viscosity, as calculated from Brownian stress (Eq. 3.4), to a linear viscoelastic response [13]. Fitting these curves indicates a relaxation time on order of 30 s, consistent with the Brownian diffusion time-scale of a dilute suspension.

More recently, we also investigated the large amplitude oscillatory shear response of suspensions[52]. By varying the shear amplitude and frequency separately, large amplitude oscillatory shear is able to disentangle the underlying dynamics that are usually convolved in far-from-equilibrium systems. In contrast to the response in the linear regime, the suspension structure response under large amplitude oscillatory shear demonstrates a nonlinear saturation that arises from shear-induced advection. We also showed that in spite of the distinct underlying mechanisms giving rise to the linear and nonlinear responses, all data can be scaled onto a master curve that links small-amplitude oscillatory shear with continuous shear [52].

Finally, we also studied the configurations of particles for large Pe $\geq$ 4,000 in the weak shear thickening regime. Reconstructed images show that the suspended particles form a clustered structure [13]. This structure is preferentially aligned

along the compression axis of the shear. The result is consistent with the prediction on the emergence of hydro-clusters during shear thickening [50, 48, 54]. Future investigations of hydro-cluster dynamics should elucidate the mechanisms linking hydro-cluster formation and interactions with shear thickening.

3.6.2 String structure of confined colloidal suspensions

Our confocal rheoscope also allows us to investigate suspension structure and rheology in a confined geometry [18]. When we shear a confined suspension, one with less than 10 layers of particles, we observe a strong vorticity-aligned string structure at intermediate volume fractions 0.34 to 0.4 with $80 \leq \mathrm{Pe} \leq 4,000$. This vorticity-aligned string structure contrasts with previous simulation studies, where *flow*-aligned string phase have been observed instead. The vorticity-aligned string structure can be attributed to the combination of strong interparticle hydrodynamic couplings and the interlayer momentum exchange in the confined sample [18, 91].

Employing our biaxial shear cell, we examined this far-from-equilibrium string structure under two-dimensional oscillatory shear[51]. Using biaxial shear we have unprecedented control over the suspension behavior. For example, we imposed two orthogonal shear flows at the same frequency with different phases δ. If the shear flows are in-phase ($\delta = 0$) the resulting shear flow is a uniaxial oscillatory shear and the string structure is very pronounced. If the shear flows are out-of-phase ($\delta = \pi/2$) the resulting shear flow is a circularly polarized shear. We find that the particle alignment into strings decreases gradually with increasing δ and eventually becomes isotropic when $\delta = \pi/2$.

We also investigated the effect of the particle string configuration on the suspension rheology, using our biaxial FMD[51]. Surprisingly, as the suspension morphology progresses from string structures to an isotropic state, we see no corresponding change in the suspension rheology. To clarify the lack of the string structure's rheological signature, we performed an "oscillatory superposition spectroscopy" measurement on the suspension. While the suspension was under a uniaxial oscillatory shear flow, with particles assembled into strings, we applied a second, high-frequency oscillatory shear flow. From this second flow, we probed the stress response of the sample both parallel and orthogonal to the primary flow. We found that the stress response is isotropic at the frequencies probed, despite the highly anisotropic suspension string structure. Moreover, the flow behavior is Newtonian both along and orthogonal to the applied flow[51]. These observations highlight our device's capability to investigate novel structures of highly confined samples and test their anisotropic rheological properties.

3.6.3 Particle diffusion under shear

Our shear apparatus can also be used to study particle dynamics including the translational and rotational diffusion of colloidal particles under shear. Due to Taylor dispersion [76, 6] particles undergo faster translational diffusion along the flow direction during shear. By using our confocal microscope in conjunction with our shear apparatus, we were able to measure two additional types of enhanced diffusion under shear [47]. Whereas enhanced translational diffusion relies on Brownian motion and an inhomogeneous flow field, enhanced rotational diffusion relies of the inhomogeneous orientation flow field due to the Jeffrey orbits exhibited by the particles. This enhancement of rotational diffusion may allow for interesting

self-assembly or rheological applications. Similarly, by looking at dense suspensions of spherical particles, we can use our confocal rheoscope to measure that colloidal particles' diffusion is also enhanced *perpendicular* to the flow direction [18]. This enhancement arises from hydrodynamic interactions between particles giving diffusive behavior.

3.6.4 Other applications

While we have only discussed applications of our shear apparatus for simple colloidal liquids, this device is designed to be easily customized for additional applications. For example, with our current design, we can use our shear apparatus in conjunction with a holographic optical tweezers to locally control suspension structure [84]. In principle, this allows us to manipulate the suspension structure down to the single particle scale in a sheared sample. Our three-axis piezoelectric stage additionally allows us to investigate compressional or extensional flows in complex fluids [28, 35], simply by taking advantage of the y-positioning capabilities of the piezo to move the plates perpendicular to the sample boundaries. Moreover, by mis-aligning the top and bottom plates, we can use our shear apparatus to investigate shear or compressional lubrication flows in complex fluids. Our biaxial FMD also allows for probing the anisotropic viscosities of a variety of other complex fluids ranging from colloidal crystals to collagen fiber networks. Moreover, we can access a vast array of additional experimental approaches with only minor modifications to our shear or imaging apparatus. By substituting a transparent cover slip for the opaque FMD, we can use cross-polarized microscopy to investigate the structural dynamics of sheared liquid crystals. Alternatively, we can introduce polarizers and use epifluorescence to conduct fluorescence confocal

polarizing microscopy (FCPM) [72] and measure the 3D director orientation of sheared liquid crystals. To investigate the effects of different boundary structures on the rheology of confined suspensions, we can replace the silicon wafers and glass cover slips with patterned surfaces [41, 1, 50]. Our shear apparatus can be easily modified for use in conjunction with Dynamic Light Scattering, by using a FMD with a small window for a laser beam to pass through. Moreover, due to our modular design of our FMD, in the future it will be easy to substitute an FMD that additionally measures normal stresses. The capabilities of our shear apparatus and its flexibility for a wide range of applications promise that similar confocal rheoscopes will find important uses in future experiments in rheology and soft matter.

3.7 Acknowledgements

The authors would like to acknowledge J. Mergo, T. Beatus, and Y.-W. Lin for technical help and useful discussions on apparatus design. Because this technique took years to develop many individuals contributed to its design. The original prototype was developed by I.C. in collaboration with T. G. Mason and D. A. Weitz. The current version of the multiaxis piezo actuator and uniaxial FMD were developed by J.H.M., J.N.I., and I.C., the biaxial shear protocols and FMD were developed by N.L., J.N.I, and I.C. In addition, the arduous work of developing mechanical and optical calibrations, method development, and developing operating procedures were worked on by N.L., X.C., B.L., and J.H.M.. This publication was based on work supported by Award No. KUS-C1-018-02, made by King Abdullah University of Science and Technology (KAUST), the National Science Foundation under Grant No. (DMR 1056662); the US Department of Energy, Office of Ba-

sic Energy Sciences, Division of Materials Sciences and Engineering under Award No. ER46517, and in part under National Science Foundation CBET-PMP Award No. 1232666. J.H.M. was funded in part by Colby College, B.L. acknowledges the DoD, Air Force Office of Scientific Research, National Defense Science and Engineering Graduate (NDSEG) Fellowship 32 CFR 168a. J.N.I was supported by the Department of Energy, Office of Basic Energy Sciences, Division of Materials Sciences and Engineering, under Award DE-FG02-87ER-45331, and by the National Science Foundation NSF grant CHE-1059108.

REFERENCES

[1] Joanna Aizenberg, Paul V Braun, and Pierre Wiltzius. Patterned colloidal deposition controlled by electrostatic and capillary forces. *Physical review letters*, 84(13):2997, 2000.

[2] L. Antl, J. W. Goodwin, R. D. Hill, R. H. Ottewill, S. M. Owens, and S. Papworth. The preparation of poly(methyl methacrylate) latices in non-aqueous media. *Colloids and Surfaces*, 17:67, 1986.

[3] P. Ballesta, R. Besseling, L. Isa, G. Petekidis, and W. C. K. Poon. Slip and flow of hard-sphere colloidal glasses. *Phys. Rev. Lett.*, 101:258301, 2008.

[4] P. Ballesta, R. Besseling, L. Isa, G. Petekidis, and W. C. K. Poon. Shear banding and flow-concentration coupling in colloidal glasses. *Phys. Rev. Lett.*, 105:268301, 2010.

[5] Adolfo J Banchio and John F Brady. Accelerated stokesian dynamics: Brownian motion. *The Journal of chemical physics*, 118:10323, 2003.

[6] Evan M Beckman, Steven A Porcelli, Craig T Morita, Samuel M Behar, Stephen T Furlong, and Michael B Brenner. Recognition of a lipid antigen by gdi-restricted $\alpha\beta+$ t cells. *Nature*, 372:691, 1994.

[7] Jonathan Bender and Norman J Wagner. Reversible shear thickening in monodisperse and bidisperse colloidal dispersions. *Journal of Rheology*, 40:899, 1996.

[8] Jonathan W Bender and Norman J Wagner. Optical measurement of the contributions of colloidal forces to the rheology of concentrated suspensions. *Journal of colloid and interface science*, 172(1):171–184, 1995.

[9] R. Besseling, L. Isa, E. R. Weeks, and W. C. K. Poon. Quantitative imaging of colloidal flows. *Adv. Colloid Interfac.*, 146:1, 2009.

[10] R. Besseling, Eric Weeks, A. Schofield, and W. Poon. Three-Dimensional Imaging of Colloidal Glasses under Steady Shear. *Phys. Rev. Lett.*, 99(2):028301, July 2007.

[11] Rut Besseling, Lucio Isa, Eric R Weeks, and Wilson CK Poon. Quantitative imaging of colloidal flows. *Advances in colloid and interface science*, 146(1):1–17, 2009.

[12] GVR Born and MoJ Cross. The aggregation of blood platelets. *The Journal of physiology*, 168(1):178–195, 1963.

[13] Joseph M Brader. Nonlinear rheology of colloidal dispersions. *Journal of Physics: Condensed Matter*, 22(36):363101, 2010.

[14] John F Brady. The rheological behavior of concentrated colloidal dispersions. *The Journal of chemical physics*, 99(1):567–581, 1993.

[15] Carl Branan. *Rules of Thumb for Chemical Engineers [: A Manual of Quick, Accurate Solutions to Everyday Process Engineering Problems*. Butterworth-Heinemann, Oxford, 5th ed. edition, 2012.

[16] A. Campbell and P. Bartlett. Fluorescent hard-sphere polymer colloids for confocal microscopy. *J. Colloid and Interface Science*, 256:325, 2002.

[17] Xiang Cheng, Jonathan H. McCoy, Jacob N. Israelachvili, and Itai Cohen. Imaging the Microscopic Structure of Shear Thinning and Thickening Colloidal Suspensions. *Science*, 333(6047):1276–1279, February 2011.

[18] Xiang Cheng, Xinliang Xu, Stuart A Rice, Aaron R Dinner, and Itai Cohen. Assembly of vorticity-aligned hard-sphere colloidal strings in a simple shear flow. *Proceedings of the National Academy of Sciences*, 109(1):63–67, 2012.

[19] I. Cohen, B. Davidovich, A. B. Schofield, M. P. Brenner, and D. A. Weitz. Slip, yield, and bands in colloidal crystals under oscillatory shear. *Phys. Rev. Lett.*, 97:215502, 2006.

[20] I. Cohen, T. G. Mason, and D. A. Weitz. Shear-induced configurations of confined colloidal suspensions. *Phys. Rev. Lett.*, 93:046001, 2004.

[21] R. Cole, T. Jinadasa, and C. M. Brown. Measuring and interpreting point spread functions to determine confocal micrsocope resolution and ensure quality control. *Nature Protocols*, 6:1929, 2011.

[22] J. C. Crocker and D. G. Grier. Methods of digital video microscopy for colloidal studies. *J. Colloid and Interface Science*, 179:298, 1995.

[23] Pierre Gilles De Gennes. *Scaling concepts in polymer physics*. Cornell university press, Ithaca, 1979.

[24] D. Derks, H. Wisman, A. van Blaaderen, and A. Imhof. Confocal microscopy of colloidal dispersions in shear flow using a counter-rotating coneplate shear cell. *J. Phys.: Condens. Matter*, 16:S3917, 2004.

[25] D. Derks, Y. L. Wu, A. van Blaaderen, and A. Imhof. Dynamics of colloidal crystals in shear flow. *Soft Matter*, 5:1060, 2009.

[26] A. Diaspro. *Confocal and two-photon microscopy: Foundations, applications, and advances*. Wiley-Liss, Hoboken, New Jersey, 2002.

[27] A. D. Dinsmore, E. R. Weeks, V. Prasad, A. C. Levitt, and D. A Weitz. Three-dimensional confocal microscopy of colloids. *Appl. Optics*, 40:4152, 2001.

[28] Patrick S Doyle, Eric SG Shaqfeh, Gareth H McKinley, and Stephen H Spiegelberg. Relaxation of dilute polymer solutions following extensional flow. *Journal of non-newtonian fluid mechanics*, 76(1):79–110, 1998.

[29] Thomas FF Farage and Joseph M Brader. Three-dimensional flow of colloidal glasses. *Journal of Rheology*, 56:259, 2012.

[30] David R Foss and John F Brady. Structure, diffusion and rheology of brownian suspensions by stokesian dynamics simulation. *Journal of Fluid Mechanics*, 407:167–200, 2000.

[31] C Gao, SD Kulkarni, JF Morris, and JF Gilchrist. Direct investigation of anisotropic suspension structure in pressure-driven flow. *Physical Review E*, 81(4):041403, 2010.

[32] Jean-Luc Gennisson, Thomas Deffieux, Emilie Macé, Gabriel Montaldo, Mathias Fink, and Mickaël Tanter. Viscoelastic and anisotropic mechanical properties of in vivo muscle tissue assessed by supersonic shear imaging. *Ultrasound in medicine & biology*, 36(5):789–801, 2010.

[33] Steve Granick. Motions and relaxations of confined liquids. *Science*, 253:1374–9, 1991.

[34] X Guo and M Ballauff. Spatial dimensions of colloidal polyelectrolyte brushes as determined by dynamic light scattering. *Langmuir*, 16(23):8719–8726, 2000.

[35] Rahul K Gupta, DA Nguyen, and T Sridhar. Extensional viscosity of dilute polystyrene solutions: Effect of concentration and molecular weight. *Physics of Fluids*, 12:1296, 2000.

[36] M. D. Haw, W. C. K. Poon, and P. N. Pusey. Direct observation of oscillatory-shear-induced order in colloidal suspensions. *Phys. Rev. E*, 57:6859, 1998.

[37] M. D. Haw, W. C. K. Poon, P. N. Pusey, P. Hebraud, and F. Lequeux. Colloidal glasses under shear strain. *Phys. Rev. E*, 58:4673, 1998.

[38] S. Hell, G. Reiner, C. Cremer, and E. H. K. Stelzer. Aberrations in confocal fluorescence microscopy induced by mismatches in refractive index. *J. Microsc.*, 169:391, 1992.

[39] Jacob N Israelachvili. *Intermolecular and surface forces: revised third edition*. Academic press, 2011.

[40] Matthew C Jenkins and Stefan U Egelhaaf. Confocal microscopy of colloidal particles: towards reliable, optimum coordinates. *Advances in colloid and interface science*, 136(1):65–92, 2008.

[41] Peng Jiang and Michael J McFarland. Large-scale fabrication of wafer-size colloidal crystals, macroporous polymers and nanocomposites by spin-coating. *Journal of the American Chemical Society*, 126(42):13778–13786, 2004.

[42] Willem K Kegel, Alfons van Blaaderen, et al. Direct observation of dynamical heterogeneities in colloidal hard-sphere suspensions. *Science*, 287(5451):290–293, 2000.

[43] S. Klein, V. Manoharan, D. Pine, and F. Lange. Preparation of monodisperse pmma microspheres in nonpolar solvents by dispersion polymerization with a macromonomeric stabilizer. *Colloid Polym. Sci.*, 282:7, 2003.

[44] Mark Kroon, Gerard H Wegdam, and Rudolf Sprik. Dynamic light scattering studies on the sol-gel transition of a suspension of anisotropic colloidal particles. *Physical Review E*, 54(6):6541, 1996.

[45] L. Landau and L. M. Lifshitz. *Theory of Elasticity*. Pergamon, NY, 3rd ed. edition, 1986.

[46] Ronald G. Larson. *The Structure and Rheology of Complex Fluids*. Oxford University Press, New York, 1998.

[47] Brian D Leahy, Xiang Cheng, Desmond C Ong, Chekesha Liddell-Watson, and Itai Cohen. Enhancing rotational diffusion using oscillatory shear. *Physical Review Letters*, 110(22):228301, 2013.

[48] Young Sil Lee and Norman J Wagner. Dynamic properties of shear thickening colloidal suspensions. *Rheologica Acta*, 42(3):199–208, 2003.

[49] D. Leighton and A. Acrivos. Viscous resuspension. *Chem. Eng. Sci.*, 41:1377, 1986.

[50] Keng-hui Lin, John C Crocker, Vikram Prasad, Andrew Schofield, David A Weitz, TC Lubensky, and AG Yodh. Entropically driven colloidal crystallization on patterned surfaces. *Physical review letters*, 85(8):1770, 2000.

[51] Neil YC Lin, Xiang Cheng, and Itai Cohen. Biaxial shear of confined colloidal hard spheres: the structure and rheology of the vorticity-aligned string phase. *Soft Matter*, 10(12):1969, 2014.

[52] Neil YC Lin, Sushmit Goyal, Xiang Cheng, Roseanna N Zia, Fernando A Escobedo, and Itai Cohen. Far-from-equilibrium sheared colloidal liquids: Disentangling relaxation, advection, and shear-induced diffusion. *Physical Review E*, 88(6):062309, 2013.

[53] C. W. Macosko. *Rheology: Principles, Measurements, and Applications*. Wiley-VCH, New York, 1994.

[54] Brent J Maranzano and Norman J Wagner. The effects of interparticle interactions and particle size on reversible shear thickening: Hard-sphere colloidal dispersions. *Journal of Rheology*, 45:1205, 2001.

[55] Jan Mewis and Norman J Wagner. *Colloidal suspension rheology*. Cambridge University Press, 2012.

[56] PCF Møller, Stéphane Rodts, MAJ Michels, and Daniel Bonn. Shear banding and yield stress in soft glassy materials. *Physical Review E*, 77(4):041507, 2008.

[57] K Hima Nagamanasa, Shreyas Gokhale, Rajesh Ganapathy, and AK Sood. Confined glassy dynamics at grain boundaries in colloidal crystals. *Proceedings of the National Academy of Sciences*, 108(28):11323–11326, 2011.

[58] Chinedum O Osuji and David A Weitz. Highly anisotropic vorticity aligned structures in a shear thickening attractive colloidal system. *Soft Matter*, 4(7):1388–1392, 2008.

[59] Jia Ou, Blair Perot, and Jonathan P Rothstein. Laminar drag reduction in

microchannels using ultrahydrophobic surfaces. *Physics of fluids*, 16:4635, 2004.

[60] G. Petekidis, A. Moussa id, and P. N. Pusey. Rearrangements in hard-sphere glasses under oscillatory shear strain. *Phys. Rev. E*, 66:051402, 2002.

[61] MP Pileni. Reverse micelles as microreactors. *The Journal of physical chemistry*, 97(27):6961–6973, 1993.

[62] Natalia V Pogodina, Victor P Lavrenko, Srivatsan Srinivas, and H Henning Winter. Rheology and structure of isotactic polypropylene near the gel point: quiescent and shear-induced crystallization. *Polymer*, 42(21):9031–9043, 2001.

[63] V. Praad, D. Semwogerere, and E. R. Weeks. Confocal microscopy of colloids. *J. Phys.: Condens. Matter*, 19:113102, 2007.

[64] C Patrick Royall, Joachim Dzubiella, Matthias Schmidt, and Alfons van Blaaderen. Nonequilibrium sedimentation of colloids on the particle scale. *Physical review letters*, 98(18):188304, 2007.

[65] C. Patrick Royall, W. C. K. Poon, and E. R. Weeks. In search of colloidal hard spheres. *Soft Matter*, 9:17, 2013.

[66] W. B. Russel, D. A. Saville, and W. R. Schowalter. *Colloidal Dispersions*. Cambridge University Press, Cambridge, UK, 1989.

[67] R. C. Arevalo S. K. Dutta, A. Mbi and D. L. Blair. Development of a confocal rheometer for soft and biological materials. *Review of Scientific Instruments*, 84(6825), 2013.

[68] Peter Schall, Itai Cohen, David A Weitz, and Frans Spaepen. Visualization of dislocation dynamics in colloidal crystals. *Science*, 305(5692):1944–1948, 2004.

[69] Peter Schall, Itai Cohen, David A Weitz, and Frans Spaepen. Visualizing dislocation nucleation by indenting colloidal crystals. *Nature*, 440(7082):319–323, 2006.

[70] K. M. Schmoller, P. Fernández, R. C. Arevalo, D. L. Blair, and A. R. Bausch. Cyclic hardening in bundled actin networks. *Nature Comm.*, 1:134, 2010.

[71] JM Schultz, BS Hsiao, and JM Samon. Structural development during the early stages of polymer melt spinning by in-situ synchrotron x-ray techniques. *Polymer*, 41(25):8887–8895, 2000.

[72] Ivan I Smalyukh, SV Shiyanovskii, and OD Lavrentovich. Three-dimensional imaging of orientational order by fluorescence confocal polarizing microscopy. *Chemical Physics Letters*, 336(1):88–96, 2001.

[73] P. A. SMith, G. Petekidis, S. U. Egelhaaf, and W. C. K. Poon. Yielding and crystallization of colloidal gels under oscillatory shear. *Phys. Rev. E*, 99:041402, 2007.

[74] T. Solomon and M. J. Solomon. Stacking fault structure in shear-induced colloidal crystallization. *J. Chem. Phys.*, 124:134905, 2006.

[75] Rajesh H Somani, Ling Yang, Benjamin S Hsiao, Pawan K Agarwal, Hitesh A Fruitwala, and Andy H Tsou. Shear-induced precursor structures in isotactic polypropylene melt by in-situ rheo-saxs and rheo-waxd studies. *Macromolecules*, 35(24):9096–9104, 2002.

[76] G. Taylor. Dispersion of soluble matter in solvent flowing slowly through a tube. *Proc. R. Soc. Lond. A*, 219:186, 1953.

[77] H Rosemary Taylor. *Data acquisition for sensor systems*, volume 5. Springer, New York, 1997.

[78] W Van Megen and PN Pusey. Dynamic light-scattering study of the glass transition in a colloidal suspension. *Physical Review A*, 43(10):5429, 1991.

[79] W Van Megen and SM Underwood. Dynamic-light-scattering study of glasses of hard colloidal spheres. *Physical Review E*, 47(1):248, 1993.

[80] J. Vermant, P. Moldenaers, J. Mewis, M. Ellis, and R. Garritano. Orthogonal superposition measurements using a rheometer equipped with a force rebalanced transducer. *Rev. Sci. Instrum.*, 68:4090, 1997.

[81] Jan Vermant and MJ Solomon. Flow-induced structure in colloidal suspensions. *Journal of Physics: Condensed Matter*, 17(4):R187, 2005.

[82] Jan Vermant, L Walker, Paula Moldenaers, and Joannes Mewis. Orthogonal versus parallel superposition measurements. *Journal of Non-Newtonian Fluid Mechanics*, 79(2):173–189, 1998.

[83] VS Volkov and VG Kulichikhin. Anisotropic viscoelasticity of liquid crystalline polymers. *Journal of Rheology*, 34:281, 1990.

[84] Dirk LJ Vossen, Astrid van der Horst, Marileen Dogterom, and Alfons van Blaaderen. Optical tweezers and confocal microscopy for simultaneous three-dimensional manipulation and imaging in concentrated colloidal dispersions. *Review of Scientific Instruments*, 75(9):2960–2970, 2004.

[85] Norman J Wagner and John F Brady. Shear thickening in colloidal dispersions. *Physics Today*, 62(10):27–32, 2009.

[86] Lynn M Walker, Jan Vermant, Paula Moldenaers, and Jan Mewis. Orthogonal and parallel superposition measurements on lyotropic liquid crystalline polymers. *Rheologica acta*, 39(1):26–37, 2000.

[87] Thomas A Witten and Philip A Pincus. *Structured fluids: polymers, colloids, surfactants*. Oxford University Press, Oxford, 3rd ed. edition, 2004.

[88] Y. L. Wu, J. H. J. Brand, J. L. A. van Gemert, J. Verkerk, H. Wisman, A. Van Blaaderen, and A. Imhof. A new parallel plate shear cell for in situ real-space measurements of complex fluids under shear flow. *Rev. Sci. Instrum.*, 78:103902, 2007.

[89] Y. L. Wu, D. Derks, A. Van Blaaderen, and A. Imhof. Melting and crystallization of colloidal hard-sphere suspensions under shear. 106:10564, 2009.

[90] Roseanna N Zia and John F Brady. Single-particle motion in colloids: force-induced diffusion. *Journal of Fluid Mechanics*, 658(1):188–210, 2010.

[91] M Zurita-Gotor, J Bławzdziewicz, and E Wajnryb. Layering instability in a confined suspension flow. *Physical review letters*, 108(6):068301, 2012.

CHAPTER 4

FAR-FROM-EQUILIBRIUM SHEARED COLLOIDAL LIQUIDS: DISENTANGLING RELAXATION, ADVECTION, AND SHEAR-INDUCED DIFFUSION[1]

4.1 Abstract

Using high-speed confocal microscopy, we measure the particle positions in a colloidal suspension under large amplitude oscillatory shear. Using the particle positions we quantify the *in situ* anisotropy of the pair-correlation function – a measure of the Brownian stress. From these data, we find two distinct types of responses as the system crosses over from equilibrium to far-from-equilibrium states. The first is a nonlinear amplitude saturation that arises from shear-induced advection, while the second is a linear frequency saturation due to competition between suspension relaxation and shear rate. In spite of their different underlying mechanisms, we show that all the data can be scaled onto a master curve that spans the equilibrium and far-from-equilibrium regimes, linking small amplitude oscillatory to continuous shear. This observation illustrates a colloidal analog of the Cox-Merz rule and its microscopic underpinning. Brownian Dynamics simulations show that interparticle interactions are sufficient for generating both experimentally observed saturations.

[1]Neil Y.C. Lin, Sushmit Goyal, Xiang Cheng, Roseanna N. Zia, Fernando A. Escobedo, and Itai Cohen. "Far-from-equilibrium sheared colloidal liquids: Disentangling relaxation, advection, and shear-induced diffusion." Physical Review E 88, no. 6 (2013): 062309.

4.2 Introduction

While ubiquitous across many time and length scales, far-from-equilibrium behavior is still largely uncharted territory[1]. To understand such systems, the crossover from nearly equilibrium to far-from-equilibrium regimes provides crucial insights that bridge distinct concepts developed in either limit. Furthermore, this poorly explored crossover is important for understanding natural phenomena such as nonlinear elasticity[2], flow-induced rejuvenation[3, 4], and shear thinning[42, 6, 42], which all occur in industrial settings. A particularly fascinating and relevant example is the nonlinear stress response of fluids under large amplitude oscillatory shear (LAOS)[8, 9]. By varying the amplitude and frequency separately, LAOS disentangles the underlying dynamics that are usually convolved in such far-from-equilibrium systems. Despite great efforts, conventional flow measurement techniques[11, 12, 10, 14, 13] have had difficulties elucidating the origins of these nonlinear behaviors without information about the fluid microstructure.

Because of their experimentally accessible time and length scales, hard-sphere colloids are an ideal model system to study nonlinear behaviors in far-from-equilibrium systems[15, 16, 17]. Here, by mounting a custom shear cell on a confocal microscope, we directly image colloidal liquids and quantify the suspension structure using the pair correlation function $g(\vec{r})$. As the suspension is sheared, distortions of $g(\vec{r})$ increase and lead to the Brownian stresses that arise from the thermal motion of particles[18, 19]. We quantify this $g(\vec{r})$ change to capture the *suspension structure response* in the crossover regime bounded by lightly perturbed states (nearly-equilibrium) and strongly driven states (far-from-equilibrium). This approach circumvents many difficulties encountered by conventional flow characterization techniques because it identifies the microscopic origin of the stress response.

In contrast to the previously explored linear response regime[13], in this report we focus on the nonlinear response by performing LAOS measurements. Our data shows two distinct structure responses that collapse onto a master curve revealing the interplay between thermal relaxation, advection, and shear induced diffusion in the crossover regime.

4.3 Experiment

In our experiments we use silica particles with radius $a = 490$ nm and 2% polydispersity, suspended in an index matching water-glycerine mixture whose viscosity $\eta_0 = 0.06$ Pa·s. We add 1.25 mg/ml of fluorescein sodium salt to dye the solvent for imaging[13]. The electrostatic screening length is ∼10 nm, hence particle interactions are nearly hard-sphere, see Appendix A. Experiments are conducted on six samples with volume fractions $0.17 \leq \phi \leq 0.44$.

To image the suspension structure during shear, we mount a piezoelectrically driven parallel plate shear cell on a fast scanning confocal microscope. The cell consists of a moveable cover slip as the bottom plate and a silicon wafer as the top plate (Fig. 4.1 (a)). We fix the separation along the gradient or $\hat{Y}$ direction to be 6.5 ± 0.2 μm with both plates aligned to within 0.0075° of one another by adjusting set screws. A solvent trap is used to prevent evaporation of the solvent. We sinusoidally shear the suspension over a range of amplitudes $0.06 \leq \gamma_0 \leq 3.34$ and angular frequencies $0.006\ \text{s}^{-1} \leq \omega \leq 0.628\ \text{s}^{-1}$, where γ_0 is the shear strain amplitude that characterizes the ratio of the shear plate displacement to gap size. Capturing 216 frames per second, we acquire stacks of 40 images in less than 0.2 s. This scan rate is one hundred times faster than the highest shear frequency used

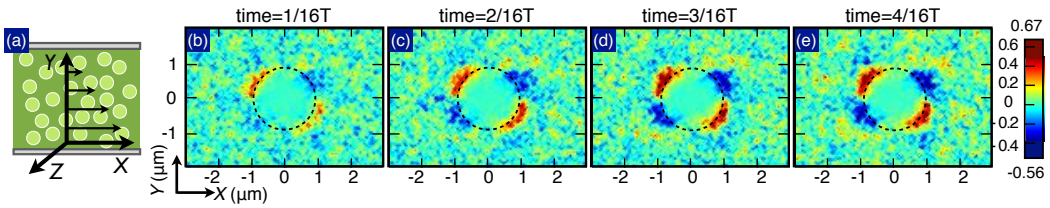

Figure 4.1: Shear configuration and coordinates (a), and $\hat{X}-\hat{Y}$ projection of $\Delta g(\vec{r})$ (b)-(e). The sheared suspension has volume fraction $\phi = 0.28$. The values of ω and γ_0 are 0.13s^{-1} and 3.34. Plots (b)-(e) show $\Delta g(\vec{r})$ for a quarter cycle of shear. (b)-(c), Anisotropy of $\Delta g(\vec{r})$ increases. (d)-(e), With increased displacement we find very little additional change in structure.

and hence avoids distortion or mismatch between images. Prior to measurement, the sample is sheared at $\gamma_0 = 3.34$ with ω=12.56 s^{-1} to generate consistent initial conditions and then sheared with the target γ_0 and ω for five minutes, or 10 times the system relaxation time, 30 s. No hysteresis is observed throughout the measurements. Since the relaxation time for the suspension to diffuse back from the reservoir surrounding the shear zone is on the order of hours, the conducted experiments do not last long enough for shear induced migration effects to be substantial. We also find that the shear velocity profile is linear. Finally, we do not observe any driven assembly and structure organization under shear.

4.4 Results

To measure the three dimensional structure, we image the suspension, determine the particle positions[21], and construct the three dimensional pair correlation function $g(\vec{r})$. This function is proportional to the probability of finding a particle at position $\vec{r}$ with respect to each particle center.

We exclude the particles that are aligned by the shearing surfaces by re-

ducing the measurement window in the $g(\vec{r})$ calculation. This exclusion allows for accurately calculating the suspension structure from the bulk of the sample. The three dimensional $g(\vec{r})$ is used to quantify the anisotropy in the shear induced structure. Under shear, particles accumulate along the maximal compression axis (MCA) – oriented at 45° to the flow direction $\hat{X}$ – resulting in a distorted $g(\vec{r})$ [18, 19, 42, 29, 22, 23, 25]. We illustrate this effect by plotting $\Delta g = g_{xy}(t) - g_{xy}(t = 0)$ over a quarter of an oscillation cycle, characterized by a large strain amplitude $\gamma_0 = 3.34$ and high frequency $\omega = 0.126$ s^{-1}. Here, g_{xy} is a two dimensional cross section of $g(\vec{r})$ centered at $z = 0$ with a width of 1.4 μm, and the response cycle starts at time $t = 0$ where g_{xy} is isotropic (Fig. 4.1 (b)-(e)). At this large strain amplitude and frequency, Δg strongly saturates after the first eighth of the period T, as indicated by the negligible difference between Fig. 4.1(d) and (e). In addition, we find that at large strains, particle accumulation tends to be broad and extends to angles below 45°. The unsubtracted $g_{xy}(t)$ is shown in Appendix B.

To quantify these observations, the structure signature

$$\Psi(t) = \left\langle \oint g(\vec{r}, t)\hat{X}\hat{Y}d\Omega \right\rangle, \tag{4.1}$$

is defined, where $\hat{X}$ and $\hat{Y}$ are the unit vectors defined in Fig. 4.1(a), $d\Omega$ is the solid angle, and the bracket denotes averaging over the interval $1.84a \leq r \leq 2.35a$. Ψ is zero when the particle configuration is isotropic, and increases in value as particles line up along the MCA. Imaging artifacts associated with particle featuring errors broaden the first peak of $g(\vec{r})$. To account for this effect, the lower bound of the averaging interval is chosen to be 80 nm smaller than $2a$, while the upper bound is chosen to be at the first peak of $g(\vec{r})$ where $r = 2.35a$ (See Appendix C).

We explore the structural saturation (Fig. 4.1 (d) and (e)) by comparing $\Psi(t)$ at four strain amplitudes (Fig. 4.2 (a) and (b)). The dimensionless frequency, or Deborah number is $\mathrm{De} = 6\pi a^3 \omega \eta_0 / k_B T$, and fixed at $\mathrm{De} = 3.78$. Physically, De is the ratio of oscillation frequency to suspension relaxation rate, while $\gamma_0 \mathrm{De}$ defines the Péclet number – the ratio of advective forcing to entropic restoring force. We explore the saturation at high frequencies by measuring $\Psi(t)$ at fixed strain amplitude $\gamma_0 = 0.67$, and at four values of De (Fig. 4.2(c) and (d)). Remarkably, the observed saturation of $\Psi(t)$ is qualitatively different depending on whether we increase γ_0 or De.

For the constant-De data, at low strain amplitudes the structure response of the suspension is linear and well described by a sinusoid (dashed black line Fig. 4.2 (a)). At a strain of $\gamma_0 \geq 1.33$ we find that $\Psi(t)$ begins to saturate at its maximal values. This saturation is more pronounced at even higher strain amplitudes as illustrated by the $\gamma_0 = 2.00$ and 3.34 data. Thus, we find that $\Psi(t)$ deviates from a linear sinusoidal response at large γ_0. To demonstrate the phase relationship between $\Psi(t)$ and the instantaneous strain, we plot the corresponding Lissajous-Bowditch (L-B) curves in Fig. 4.2 (b). In this representation, a linear viscoelastic response is depicted by an ellipse whose orientation and enclosed area correspond to the material elasticity and viscous dissipation, respectively. For large γ_0 at fixed De, the elliptical linear response saturates at a γ_0-independent plateau. We plot the Pipkin diagram in Appendix D.

$\Psi(t)$ shows strikingly different behavior when we hold γ_0 at 0.67 and sweep over De. At small De we find the response is sinusoidal and purely viscous as illustrated by the horizontal orientation of the $\mathrm{De} = 0.39$ L-B curve (Fig. 4.2 (d)). As De increases to 1.89, the L-B curve remains elliptical but acquires a significant tilt –

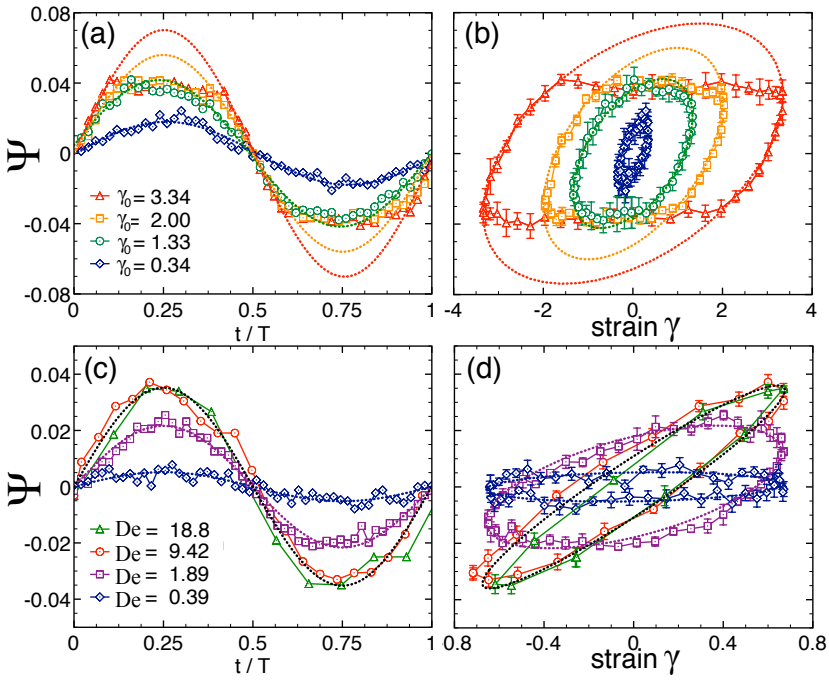

Figure 4.2: Structure response versus normalized time and Lissajous-Bowditch curves. (a), Four $\Psi(t)$ curves averaged over five measurements for De $= 3.78$ and $0.34 \leq \gamma_0 \leq 3.34$. Dashed lines are the sinusoidal fit to the data in the linear regime where $|\Psi(t)| < 0.03$. (b), The L-B curves for the panel (a) dataset. (c), Four different curves for $\gamma_0 = 0.67$ and $0.39 <$ De < 18.8 versus the normalized time. The black dashed line is the best fit to the combined data for De $= 9.42$ and 18.8. (d), The L-B curves of the data set from panel (c). Error bars correspond to the standard error of $\Psi(t)$.

indicating a harmonic response with increased elasticity. As De increases further, the L-B curves overlap indicating a De-independent harmonic response (Fig. 4.2(c) and (d)).

To understand the saturation of $\Psi(t)$ with increasing γ_0 and De, we track its maximum value per cycle, $\Psi_0(\gamma_0, \text{De})$. We plot $\Psi_0(\gamma_0, \text{De})$ versus De for four representative values of γ_0 in Fig. 4.3(a). For $\gamma_0 = 0.06$ we find $\Psi_0(\gamma_0, \text{De})$ increases linearly below De ≈ 3 and saturates to a plateau value $\Psi_0(\gamma_0, \infty)$ at large De. Similar trends are observed in all datasets but with different plateau values depending only on γ_0. To quantify changes in these plateau values, we plot $\Psi_0(\gamma_0, \infty)$ versus

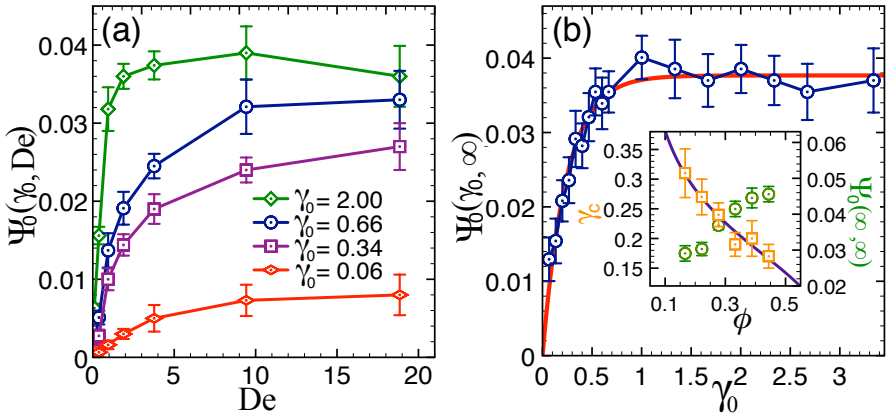

Figure 4.3: Structure response saturations. (a), Peak value of structure response in each cycle, $\Psi_0(\gamma_0, \mathrm{De})$ versus De with four representative amplitudes. Error bars depict the standard error of $\Psi_0(\gamma_0, \mathrm{De})$ over five cycles. (b), The saturation value $\Psi_0(\gamma_0, \infty)$, measured at De = 18.8, is plotted versus γ_0. The red curve is a fit of $\Psi_0(\infty, \infty)(1 - e^{-\gamma_0/\gamma_c})$ to the data. The inset illustrates the volume fraction dependence of γ_c and $\Psi_0(\infty, \infty)$. The solid line in the inset has the form $\gamma_c \propto (\frac{0.64-\phi}{\phi})^{1/3}$. Data points are averaged over ten measurements and error bars depict standard errors.

γ_0 in Fig. 4.3 (b). We find that the data are well fit by an exponential saturation, $\Psi_0(\gamma_0, \infty) = \Psi_0(\infty, \infty)(1 - e^{-\gamma_0/\gamma_c})$ (red curve) indicating a linear growth at low γ_0 and saturation to $\Psi_0(\infty, \infty)$ beyond a cutoff strain amplitude γ_c.

These saturation behaviors can be understood by considering the microscopic particle dynamics. In the experiments, $\Psi_0(\gamma_0, \mathrm{De})$ reflects the maximum degree to which particles accumulate along the MCA due to shear. The data trends for small strain amplitudes can be understood as resulting from competition between Brownian relaxation of particles to their equilibrium configuration and advection resulting from the suspending fluid as described by the advection-diffusion equation[26]. Hydrodynamic intereactions can also affect details of the suspension microsctructure. However, in the low De regime these effects are weaker than those played by Browninan motion [27], and in the high De regime their effect on the shape of the distorted microstructure still results in only a weak quantitative difference in

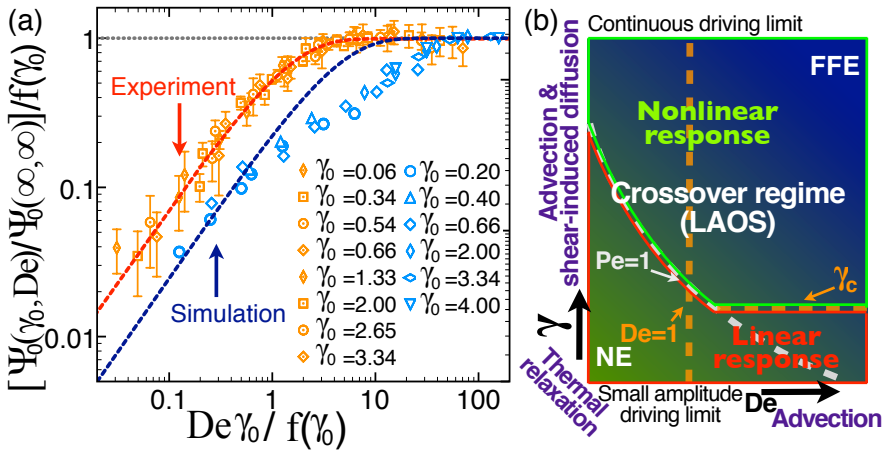

Figure 4.4: $\Psi_0(\gamma_0, \mathrm{De})$ collapse (a), and phase diagram of LAOS crossover (b). (a), $[\Psi_0(\gamma_0, \mathrm{De})/\Psi_0(\infty,\infty)]/f(\gamma_0)$ versus the dimensionless scaling parameter De $\gamma_0/f(\gamma_0)$, where $f(\gamma_0) = 1 - e^{-\gamma_0/\gamma_c}$. Each symbol denotes one strain amplitude for seven different De in the range $0.39 < \mathrm{De} < 18.8$. All 56 data points collapse on a master curve and can be fit by an exponential saturation (upper red line) $1 - e^{-\beta\gamma_0 De/f(\gamma_0)}$, where $\beta = 0.72$ is a fitting parameter. Error bars correspond to standard errors of the data averaged over five runs. (b) Three entangled dynamics (bold purple fonts) result in two types of response saturations. In the crossover regime bounded by nearly equilibrium (NE) and far-from-equilibrium states (FFE), nonlinear response emerges when Pe>1 and $\dot{\gamma} > \gamma_c$.

the $g(\vec{r})$ at contact [28]. Thus we focus on the interplay between Brownian motion and advection.

In the low De regime, Brownian diffusion dominates but becomes less effective at homogenizing particles with increasing De. Consequently, $\Psi_0(\gamma_0, \mathrm{De})$ increases linearly with De as particles accumulate along the MCA. In the high De regime, oscillatory flow dominates and thermal relaxations are negligibly weak: particles are simply advected by the flow. Thus, the plateau value $\Psi_0(\gamma_0, \infty)$ is set by the extent to which particles can accumulate along the MCA for a given strain amplitude. Lastly, the crossover between these limiting behaviors occurs at De ≈ 1.

The initial linear increase in $\Psi_0(\gamma_0, \infty)$ (Fig. 4.3 (b)) reflects the fact that for

small γ_0, where there are very few collisions with neighboring particles, particle accumulation along the MCA increases with γ_0. As γ_0 approaches γ_c, particles collide more frequently thereby randomizing particles accumulated along the MCA. The saturation of $\Psi_0(\gamma_0, \infty)$ for $\gamma_0 > \gamma_c$ indicates there exists a limit to which particles can be driven to accumulate along the MCA. This limit results from a competition between collision-induced randomization [29, 30, 31, 32, 33] and advection. Thus, γ_c corresponds to the average strain needed to induce collisions between neighboring particles.

This argument suggests that for higher volume fractions where interparticle distances are smaller, γ_c should be smaller. Specifically, we expect that at $\gamma_0 = \gamma_c$, the relative distance traveled by particles separated by a diameter along the gradient direction, $2a\gamma_0$, will equal the mean distance between neighboring particles. From geometrical considerations this distance scales as $a(\frac{\phi_c - \phi}{\phi})^{1/3}$, where $\phi_c = 0.64$ is the random close packed volume fraction. Thus, $\gamma_c \propto (\frac{0.64-\phi}{\phi})^{1/3}$ up to a constant.

To test this prediction we measure $\Psi_0(\gamma_0, \infty)$ for six different volume fractions ranging between 0.15 to 0.44. For each curve we extract both γ_c and $\Psi_0(\infty, \infty)$ and plot these values as a function of ϕ (Fig. 4.3(b) inset) along with the fit from our model (solid curve). We find excellent agreement between the γ_c data and the model fit. We also find that for the range of ϕ values measured, $\Psi_0(\infty, \infty)$ increases monotonically with ϕ. Finally, we find the data from eight different runs where $0.06 \leq \gamma_0 \leq 3.34$ and $0.09 \leq \mathrm{De} \leq 18.8$ collapses onto a curve of the form:

$$\frac{\Psi_0(\gamma_0, \mathrm{De})}{\Psi_0(\infty, \infty)} = f(\gamma_0)\left[1 - e^{-\gamma_0 \mathrm{De}\beta / f(\gamma_0)}\right] \tag{4.2}$$

where $f(\gamma_0) = 1 - e^{-\gamma_0/\gamma_c}$ and β is a fitting parameter (Fig. 4.4(a) red curve). This functional form recovers the linear regime, where the normalized structure response $\tilde{\Psi} = \Psi_0(\gamma_0, \mathrm{De})/\Psi_0(\infty, \infty)$ is equal to $\gamma_0 \mathrm{De}$, when either De or $\gamma_0 \to 0$; the

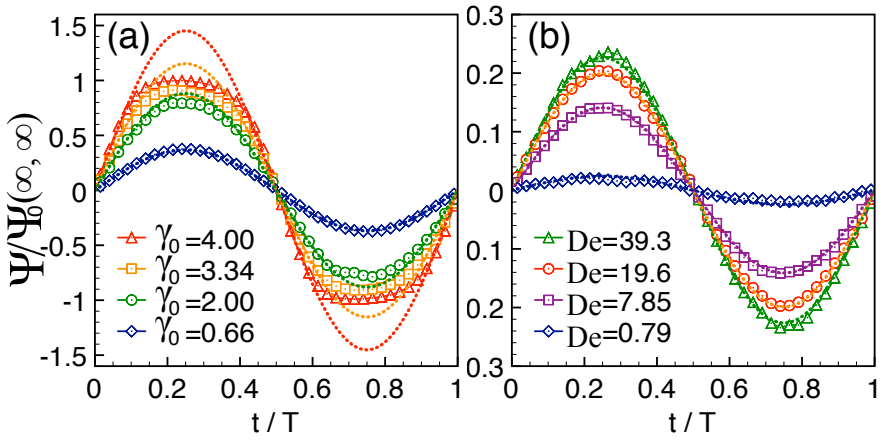

Figure 4.5: $\Psi_0(\gamma_0, \mathrm{De})$ in Brownian dynamics simulations. (a), Amplitude saturation. $\Psi_0(\gamma_0, \mathrm{De})$ is plotted for four different γ_0 at De = 15.7. (b), Frequency saturation. $\Psi_0(\gamma_0, \mathrm{De})$ is plotted for four different De at γ_0 = 0.20.

high-frequency regime $\tilde{\Psi} = f(\gamma_0)$, when De $\to \infty$; and the high-strain amplitude limit $\tilde{\Psi} = 1$, when $\gamma_0 \to \infty$. More broadly, these results are summarized by the phase diagram in Fig. 4.4(b) that shows the crossover between near-equilibrium linear response and far-from-equilibrium nonlinear response.

4.5 Simulation

The interactions between hard sphere colloids leading to the observed saturations can be mediated either by collisions or hydrodynamics. To determine whether particle collisions are sufficient to generate such saturations, we conduct dynamic simulations using the LAMMPS package (Sandia National Laboratory). We implement Brownian Dynamics simulation by applying a Langevin thermostat to the streaming velocity of simulated particles to maintain a constant temperature of T*=1. The interparticle potential is taken to be $U/(k_BT) = r^{-c}$. We found that the stress response for $c = 50$ agrees well with reported results for hard spheres.

The simulation setup contains 10,000 particles with $\phi = 0.28$. We apply oscillatory shear to the system with the Lees-Edwards boundary condition. Since the inter-particle potential is very steep, the time step is carefully chosen to avoid unphysical particle overlaps. This model provides insights into the limiting physical behavior that ensues when pair- and higher-level hydrodynamic interactions are neglected. We run 100 oscillatory cycles for each De and γ_0, and discard data obtained from the first 10 cycles as transient. In direct analogy with the experiments, we calculate $\Psi(t)$ using Eq. 4.3 with a radial integral that extends up to the first peak of $g(\vec{r})$ (see Appendix G).

We perform an amplitude sweep at De = 15.7 for six different amplitudes, and plot $\Psi(t)/\Psi_0(\infty,\infty)$ for four different γ_0 in Fig. 4.5 (a). As with the experiments (Fig. 4.2 (a)), this model system also demonstrates an amplitude saturation at large γ_0, where $\Psi(t)/\Psi_0(\infty,\infty)$ deviates from the linear response. We also perform a frequency sweep for $0.20 \leq \gamma_0 \leq 4.00$ and plot the results for four of the six amplitudes in Fig. 4.5(b). We find that the model system exhibits a similar saturation to that found in experiments (Fig. 4.2(b)). To determine whether similar data scaling can be applied to the numerical results, we plot the normalized value $\tilde{\Psi}/f(\gamma_0)$ versus $\gamma_0 \mathrm{De}/f(\gamma_0)$ in Fig. 4.4(a). We find that the simulation data also collapses, but the curve's form deviates from the experimental curve at intermediate shear rates. Nevertheless, the collapse is qualitatively similar to the experimental results showing a linear response at low shear rates and saturation at high shear rates. These results demonstrate that the interplay between Brownian relaxation, advection and shear induced diffusion is sufficient to produce the observed saturations.

4.6 Conclusion

Measuring suspension structure is a noninvasive and explicit method to quantify each contribution of the macroscopic stress response[13]. Specifically, direct imaging allows one to measure the contribution due to Brownian motion of the microscopic constituents, which is a vital component to the response of any thermal system. Previous theoretical work showed that the surface integral of $\hat{r}\hat{r}g(\vec{r})$ at $r = 2a$ is proportional to the pairwise Brownian stress[19, 18]. In experiments, optical resolution limits require that a radially averaged quantity is used instead (Eq. 4.3). This modified calculation has been shown to agree with macroscopic force measurements in the nearly equilibrium regime[13]. While it remains to be shown that this modified expression is a valid measure of the Brownian stress in the far-from-equilibrium regime, our results on the saturations of Ψ_0 are consistent with bulk rheological measurements reported previously[13, 10], suggesting a very strong link between Ψ_0 and the Brownian stress.

Since the shear separation in the experiment is approximately seven particle diameters, the confinement effect may be significant in the reported system. Even though the particles that are near boundaries are excluded in analysis, the long-ranged hydrodynamic interactions between wall and particles may still play an important role in determining the dynamics and configuration of particles. Furthermore, the interparticle hydrodynamic interactions are left out in the Brownian dynamics simulation for identifying the origin of the structure response saturation. The fact that the Brownian dynamics simulations do not perfectly reproduce the experimental data indicate that HI do have some effect on the particle distributions. However, this effect is not large enough to qualitatively alter the trends. Namely we still observe linear scaling at low Pe and a saturation with higher

frequency or strain amplitude, see Fig. 4.4(a) and the Appendix. Nevertheless, conducting full hydrodynamic simulation that accurately take into account the boundary conditions at the surface is necessary for having a more rigorous and quantitative comparison with our experimental results.

Many different complex systems such as emulsions[34], plasmas[35], and polymers[8] exhibit saturation behaviors when driven away from equilibrium. For example, polymer blends have the same measured viscosity whether driven by continuous shear ($\mathrm{De} \ll 1, \gamma_0 \to \infty$) or perturbed with small amplitudes at high frequency ($\mathrm{De} \to \infty$, $\gamma \ll 1$). Understanding the underpinnings of this well known but poorly understood empirical observation, known as the Cox-Merz rule[36, 6], has remained a long standing theoretical challenge [38, 39]. By combining direct imaging with LAOS, we find an analogous behavior in the double saturation of the suspension structure response. Here, we show this double saturation can be collapsed on a master curve (Eq. 4.2), which identifies the roles of Brownian relaxation, affine motion, and shear induced diffusion. In part, this finding is made possible by combining direct imaging with LAOS, a shear protocol that disentangles these dynamics (Fig 4.4(b)). Brownian dynamics simulations show that the interplay between these three elements is sufficient to generate the Cox-Merz rule, analogous to other driven far-from-equilibrium systems. Further experiments with these techniques should elucidate additional mechanisms in the crossover regimes between nearly equilibrium and far-from-equilibrium states, and shed light on the highly nonlinear dynamics found in many other far-from-equilibrium systems.

4.7 Acknowledgments

We thank D. Koch, L. Archer, I. Procaccia, G. Henchel, E. Bochbinder, B. Leahy, and J. L. Silverberg for helpful conversations. This work was supported in part by Award No. KUS-C1-018-02 made by King Abdullah University of Science and Technology (KAUST), the U.S. Department of Energy, Office of Basic Energy Sciences, Division of Materials Sciences and Engineering under Award No. ER46517 (X. C.) and the National Science Foundation CBET-PMP award No. 1232666. FAE is grateful to computer cycles supplied by the Extreme Science and Engineering Discovery Environment (XSEDE) which is supported by National Science Foundation grant number OCI-1053575.

4.8 Supplementary Information

4.8.1 Sample characterization and imaging resolution

To measure the size distribution of our silica particles, we acquired a series of SEM images (Leica 440 SEM) of the particles (Fig. 4.6 (a)). We measured the sphere size from the SEM images. Fig. 4.6 (b) shows the size distribution of the sample in Fig. 4.6 (a) based on the statistics of 200 particles. Because the particles are spherical and the screening length $\sim$ 10nm is short, the hydrodynamic radius and the hard sphere radius are nearly the same in this experiment.

In Fig. 4.6 (b), we find that the distribution of the particle size is well fitted by a Gaussian distribution with a mean value $2a = 980$nm, and a standard deviation $2a \times 2.05\%$.

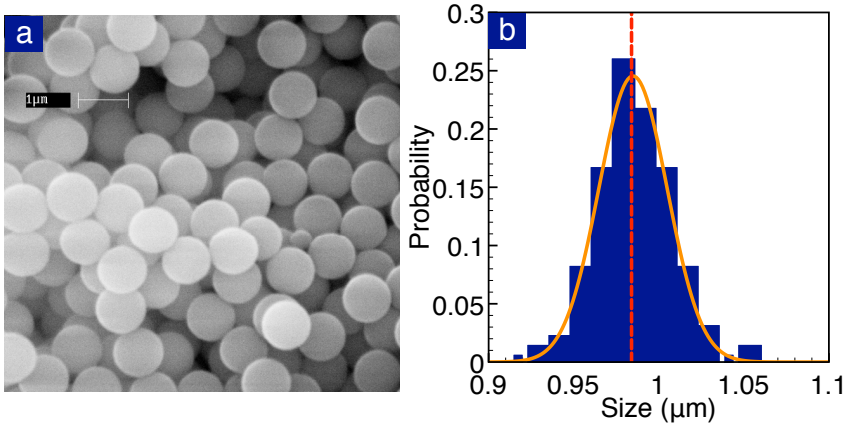

Figure 4.6: (a) SEM image of the silica particles. (b) The probability distribution function of the particle size. The orange solid line is a fit of the Gaussian distribution, and the red vertical dashed line at 0.98μm delineates the mean of the distribution.

Our resolution for locating particles is about 50nm. Since the circumference of a particle is $2\pi(2a) \approx 6,280$ nm, our angular resolution ends up being about three degrees. If all particles were to have neighbors along the maximal compression axis the exact result would give a Ψ of 0.5. We estimate that a 50nm error would lead us to calculate a Ψ of 0.499. Therefore, the measurement error due to our imaging resolution is not significant.

4.8.2 Raw data of g_{xy}

We plot the actual g_{xy} in Fig. 4.7 to illustrate the evolution of the sheared suspension structure. Fig. 4.7 and Fig. 1 of the main report share the same data set. The squared first peak of g_{xy} indicates that the system has layering due to the confinement effect. It is important to point out that the layer structure does not have any contribution to the value of Ψ due to the mirror symmetry of g_{xy} at $t = 0$.

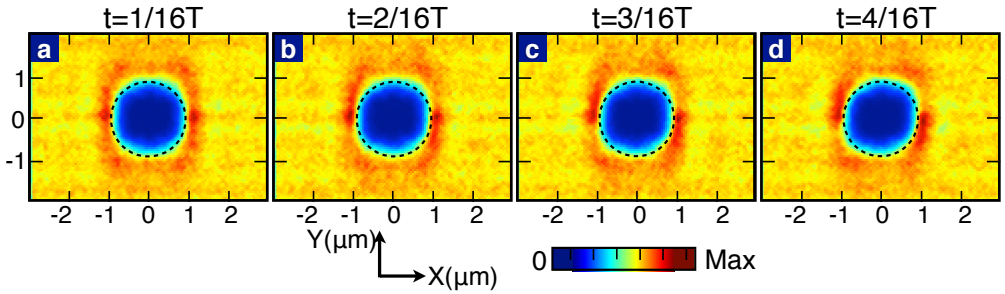

Figure 4.7: g_{xy} without subtraction. The corresponding experimental parameters are the same as the ones of Fig. 1 in the main report.

4.8.3 The radial integral range

Many methods have been used to quantify the structure response of systems under shear. For instance, the ellipticity has been used to illustrate the distortion of $g(\vec{r})$ in dusty plasmas[35], the bond order parameter Ψ_6 has been employed in colloidal crystal under shear[41, 40], and the alignment factor ΔA has been employed to determine the orientation of the assembly of particle strings[22, 43]. Here, we specifically calculate the angular probability distribution of neighboring particles to characterize the anisotropy of $g(\vec{r})$. This anisotropy of $g(\vec{r})$, which is closely related to the stress response, quantifies the response of the microstructure to the external shear flow[18]. To quantify the structural response, we integrate $g(\vec{r})$ up to its first peak to account for particle contacts. We find that in our experiments the first peak of $g(\vec{r})$ is at $r = 2.35a$. Thus we define the shear or XY component of our structural signature as:

$$\Psi_B = [\frac{1}{0.51a}\int_{1.84a}^{2.35a} dr \oint \hat{r}\hat{r}g(\vec{r})d\Omega]_{XY}. \tag{4.3}$$

Imaging artifacts associated with particle tracking errors are removed by introducing a lower bound to the radial integral at $1.84a$. We find that narrowing this

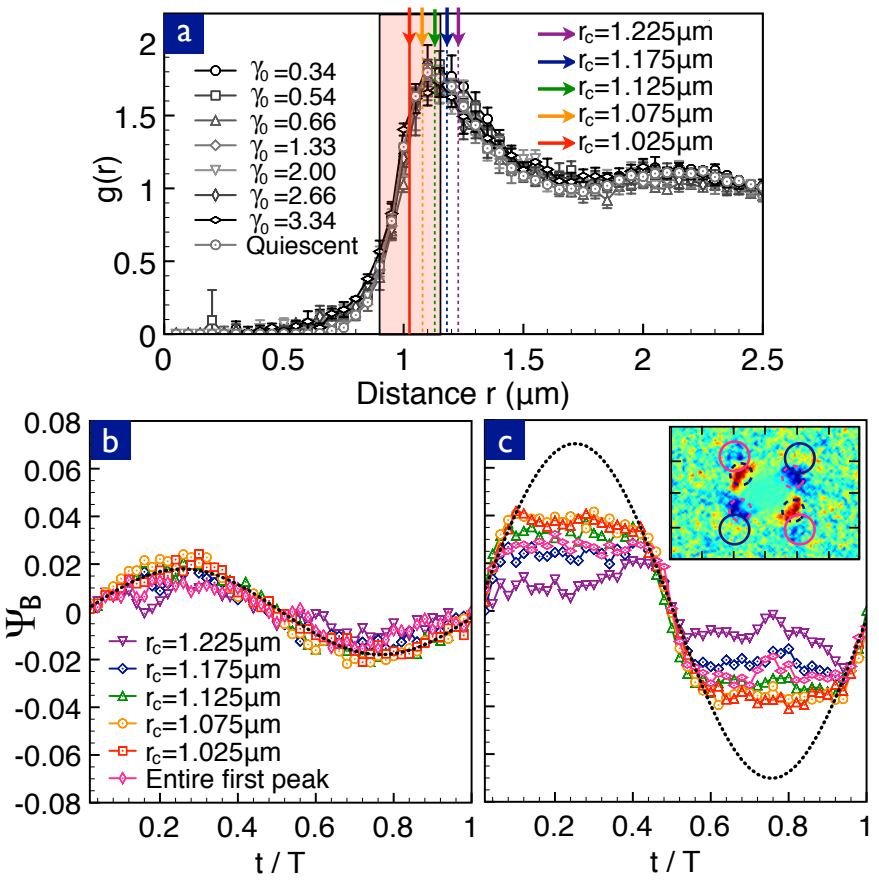

Figure 4.8: Radial distribution functions $g(r)$ (a) and Ψ_B for different integral bounds at $(\gamma_0 = 0.34, \omega = 0.126s^{-1})$ (b) and $(\gamma_0 = 3.34, \omega = 0.126s^{-1})$ (c). (a) 1D radial distribution functions of the suspension for seven different γ_0 at $\omega = 0.126s^{-1}$ and the quiescent sample are plotted versus distance. The five arrows indicate the centers of the integral bounds that are tested for the calculation of Ψ_B. The red shaded area illustrates the integral bound of r_c=1.025μm. The vertical arrows from left to right correspond to the integral centers at $r_c(\mu\text{m})$=1.025, 1.075, 1.125, 1.175 and 1.225, respectively. (b) The raw oscillatory data of Ψ_B at $(\gamma_0 = 0.34, \omega = 0.126s^{-1})$ is plotted versus t/T for five different r_c and the integral bound 0.90μm$< r <$1.50μm. (c)Ψ_B at $(\gamma_0 = 3.34, \omega = 0.126s^{-1})$ is plotted versus t/T for five different r_c and the integral bound 0.90μm$< r <$1.50μm. Both dashed lines in (b) and (c) are the linear fit from Fig. 2(a) of the main paper. In the inset to (c), the solid circles highlight the wake structure of the $\Delta g(\vec{r})$ measurement taken from Fig 2(d) of the main paper.

integral width in order to have a stricter criteria for the contacting particles does not alter the qualitative trend of Ψ_B but only introduces more noise due to poorer statistics.

Furthermore, we have studied the dependence of the structural signature Ψ_B on the radial integral center r_c. We show angular averaged $g(\vec{r})$ for eight strain amplitudes γ_0 with a fixed shear frequency $\omega = 0.126\text{s}^{-1}$ in Fig. 4.8 a. All radial distribution functions overlap on a single curve within the error bars. This overlap indicates that using a single fixed integral bound for all the experiments presented in this paper produces consistent calculation results. The short tail at $r < 2\text{a} = 0.98\mu\text{m}$ is mainly due to the finite resolution and the point spread functions along the vertical-axis (the Y-axis) of the confocal microscope, as well as the particle polydispersity. This relatively poorer resolution results in an uncertainty in the particle featuring process and introduce a small portion of unphysical particle overlaps. We set the lower bound of the integral at $0.92\mu\text{m}$ to exclude those overlapping particles. With this lower bound, which is about four standard deviations from the mean, at least 94% of the particle population is included.

We calculate Ψ_B with five different integral centers for the two data sets that have $(\gamma_0 = 0.34, \omega = 0.126s^{-1})$ (Fig. 4.8b) and $(\gamma_0 = 3.34, \omega = 0.126s^{-1})$ (Fig. 4.8c). These data sets correspond to the linear high frequency response and the high amplitude nonlinear response of Ψ_B. The corresponding positions of r_c are labeled as vertical lines in Fig. 4.8a and cover the range $1.025\mu\text{m} \leq r_c \leq 1.225\mu\text{m}$ which encompasses the first peak of $g(r)$. We find that the qualitative trends in Ψ_B are not sensitive to the choice of r_c (Fig. 4.8b,c). We have also verified that increasing the integral range to $0.90\mu\text{m} < r < 1.50\mu\text{m}$ does not alter the qualitative trends in Ψ_B (entire first peak data).

The particular choice of r_c and the integral range do however, have a quantitative effect. For example, the deviation from the sinusoidal fit in Fig. 4.8b increases with increasing r_c. For the nonlinear response, we find that as r_c increases, the magnitude of Ψ_B decreases. These smaller magnitudes result from the angular inhomogeneity in $\Delta g(\vec{r})$. As shown in the inset of Fig. 4.8c, positive and negative regions are paired so that a larger integral range in r leads to cancellations that result in smaller values of Ψ_B. This collision induced wake structure has also been reported in previous simulations [44]. In conclusion, we find that the value of Ψ_B is qualitatively insensitive to the radial integral bound, and captures the anisotropy of the angular distribution of contacting particles in both the high frequency linear and high amplitude nonlinear regimes.

4.8.4 Pipkin diagram

For suspensions that are driven into their nonlinear response regime, the resulting stress response can depend on multiple experimental parameters. Pipkin diagrams in which a matrix of Lissajous-Bowditch (L-B) curves are organized into one figure have been widely used to aid in elucidating the dependence on multiple parameters [45, 46, 48, 47]. For the problem of colloids under shear the two relevant dimensionless parameters are γ_0 and De. As such we plot 16 Ψ_B versus strain L-B curves in a Pipkin diagram in Fig. 4.9.

At low shear rates (small De and small γ_0), the suspension structure demonstrates a viscous response, where Ψ_B peaks as γ passes through zero. As De increases with a fixed small strain amplitude $\gamma_0 = 0.33$ (the first column of Fig. 4.9), the L-B curves become increasingly oblique indicating that the suspension structure response is more elastic. This viscous to elastic transition is reminiscent of the

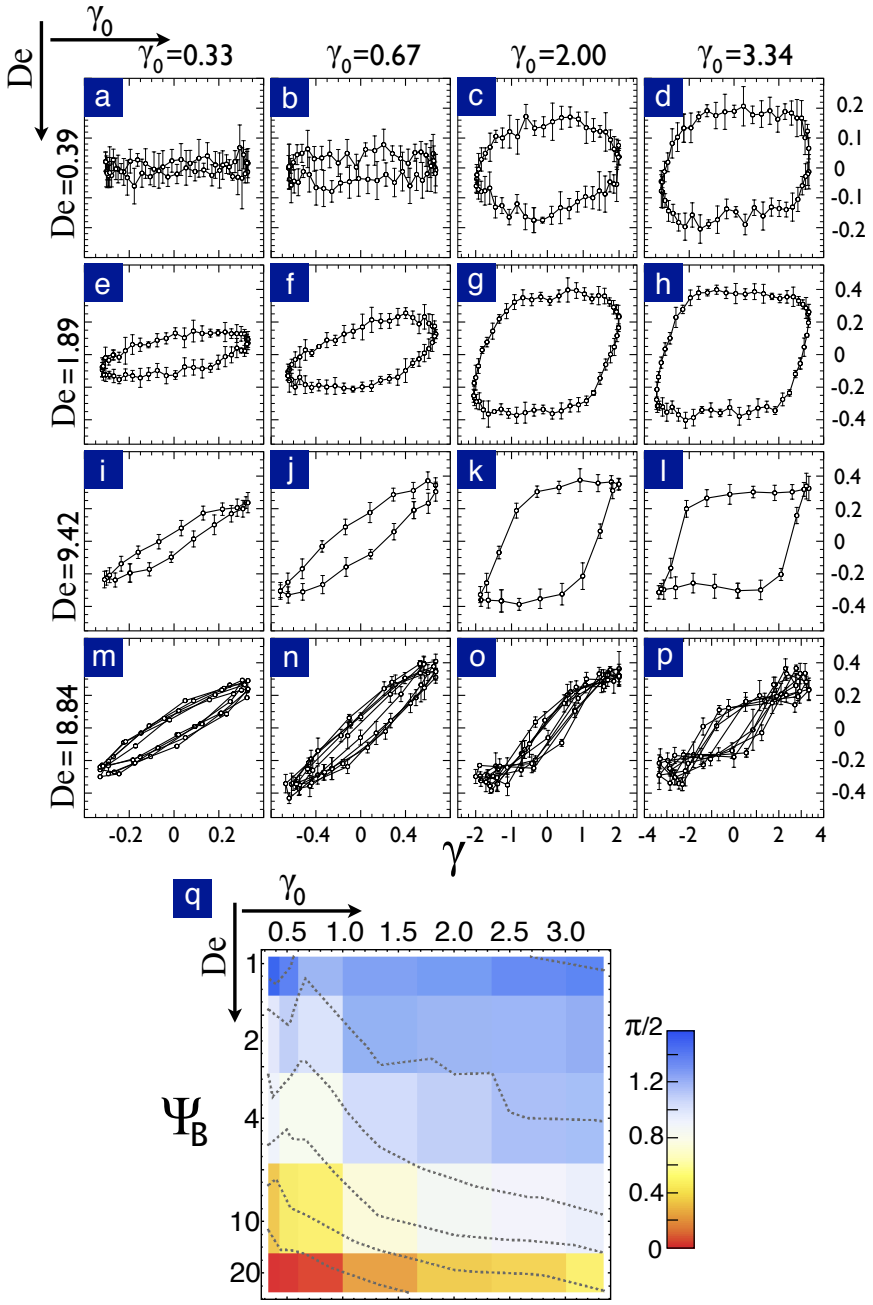

Figure 4.9: (a) to (p) L-B curves of Ψ_B versus γ for 4×4 different γ_0 and De on a Pipkin diagram. Each curve is averaged over five cycles of shear and the error bars denote the standard deviations. In the fourth row of plots ((m) to (p)), the data are averaged over 20 cycles of shear and five curves are displayed for clarity. (q) Phase angle between strain and stress is plotted versus De and γ_0. The color scale represents the value of the phase angle. The dashed lines depict the equal phase angel contours. The centers of the squares are the positions of the data points.

linear viscoelasticity observed in macroscopic rheological measurements [13, 49, 50], and the elastic plateau observed in simulations [18]. With increasing γ the L-B curves become more hysteric indicating a larger degree of viscous dissipation. These trends are summarized by a plot of the phase difference between the applied strain and Ψ_B (Fig. 4.9 (q). For the highest De measured we find that the L-B curves exhibit an overshooting behavior which is illustrated by the figure-eight curves in Fig. 4.9 (l), (o) and (p). Similar overshoots have been found in the rheological measurements with much denser suspensions. In colloidal glasses, the overshoot is associated with the cage breaking[51, 52, 53] while in colloidal crystals the overshoot is suggested to be related to the zig-zag relative motion between two layers of lattices[54, 55, 56, 57]. Whether similar mechanisms can explain the overshoots in our data for low volume fraction $\phi = 0.28$ suspensions under LAOS remains unknown. Overall, these trends are very different from those exhibited by Maxwell materials where an increase in strain produces a more elastic response and highlight the unique properties of suspensions under LAOS.

4.8.5 Quiescent $g(r)$ in experiments and simulations

We compare the pair correlation functions $g(r)$ of static samples from the Brownian Dynamics simulation, analytical calculation, and the experiment in Fig. 4.10. We find that all the curves are qualitatively similar and that the simulation and analytical results agree quantitatively. The analytical result is calculated from Percus-Yevick Integral Equation[60, 61, 62]. The good agreement between the simulation curve and the theoretical prediction indicates that the steep potential used in the simulations is a good approximation to the hard sphere potential. The experimental $g(r)$ has a longer extension into the overlapping region ($r < 1\mu m$)

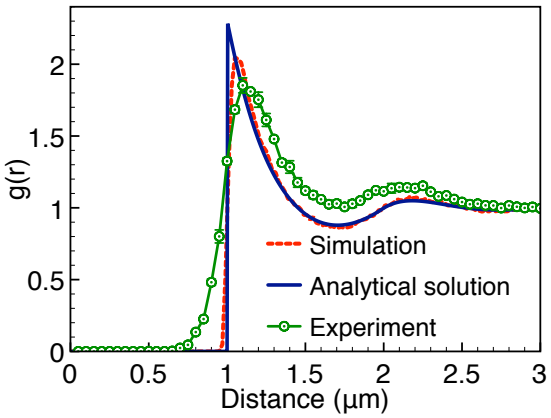

Figure 4.10: Comparison between the experimental (joined points), simulation (dashed line), and theoretical (solid line) $g(r)$ curves for quiescent samples of hard-sphere suspensions for a volume fraction of 0.28.

while the $g(r)$ from the simulation has a sharp drop at $r = 1\mu$m. To understand this discrepancy, we also simulate the $g(r)$ with the polydispersity of our sample (2%). We find that the $g(r)$ with 2% polydispersity is indistinguishable from the curve for perfectly monodisperse spheres (not shown). This comparison implies that the tail extended in the overlapping region is due to the particle featuring errors. The magnitude of the particle featuring errors is set by limitations in imaging resolution, mismatched index of refraction, and shape of the point spread function.

4.8.6 Quantification of the nonlinearity

In addition to reporting on the peak value of Ψ_B we further analyze the data to quantify the saturation at large γ_0 and De. There are a number of generic methods currently being used to quantify nonlinearities in the stress response of materials under LAOS [58, 8]. However, these methods require a large amount of data to perform an accurate measurement of the higher order harmonics. In direct imaging experiments however, each experiment run only acquires data for five oscillation

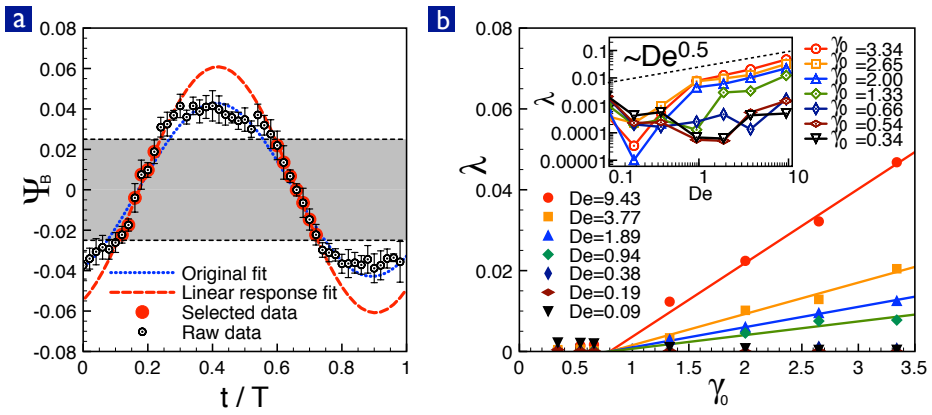

Figure 4.11: Definition of the degree of nonlinearity λ (a), and λ as a function of γ_0 for different De, (b). (a) The raw Ψ_B data is plotted along with the best sinusoid fit to the raw data (blue dotted line), and the recovered linear response fit (red dashed line). The selected data ($\Psi_B \leq 0.25$, gray shaded area) for the linear response fitting are highlighted by red circles. (b) λ is plotted as a function of γ_0 for seven different De. The solid lines are the linear fits to the data for $\gamma_0 > 0.75$. The inset shows λ versus De for different γ_0, and the dashed line that illustrates the power law $\lambda \sim \mathrm{De}^{0.5}$.

cycles since each data point entails scanning the sample in 3D, tracking the particles positions, and calculating the variations in the pair correlation function. As such the data yield is not sufficient for running a harmonic analysis. Nevertheless, since the majority of the nonlinear response is associated with saturation plateaus, we can calculate the deviation of Ψ_B from the linear response [59] by defining the degree of nonlinearity λ as:

$$\lambda = \frac{1}{T}\left\{\int_{t_0}^{t_0+T/2}\left[\Psi_l(t) - \Psi_B(t)\right]dt + \int_{t_0+T/2}^{t_0+T}\left[\Psi_B(t) - \Psi_l(t)\right]dt\right\} \quad (4.4)$$

where T is the period of one shear cycle, t_0 corresponds to the time where $\Psi_B = 0$ and $\Psi'_B > 0$, and $\Psi_l(t)$ is the recovered linear response. Ψ_l is determined by fitting a sine wave to linear portion of the data where $\Psi_B \leq 0.025$. Eq. 4.4

measures the deviation of the actual response, $\Psi_B(t)$, from the ideal linear response $\Psi_l(t)$. Integrating $|\Psi_l(t) - \Psi_B(t)|$ would produce integration artifacts due to noise. Instead, we divide the integral into two terms each of which integrates over a half cycle of the oscillation. This modified analysis significantly reduces the unbiased error by canceling random fluctuations. To illustrate the difference between the recovered linear response and the original fit, we plot Ψ_l (red dashed line) and the best fit to the raw data (blue dashed line) in Fig. 4.11a.

We calculate λ and plot it as a function of strain amplitude γ_0 for seven different De in Fig. 4.11 b. We find that for $\gamma_0 \leq 0.75$, the structure response Ψ_B is linear at all De. This strain value is close to $\gamma_c = 0.24$ the cutoff strain obtained by fitting Ψ_{De_∞} to an exponential saturation $\Psi^{\gamma_\infty}_{\omega_\infty}(1 - e^{-\gamma_0/\gamma_c})$. While we do not expect these two values to be identical, we do expect that the saturation behavior is closely tied to the nonlinearity and as such expect that γ_0 should be on the same order as γ_c.

At large γ_0 and De, λ increases linearly with γ_0. To study the De-dependence, λ is plotted versus De for seven different γ_0 values in the inset of Fig. 4.11 b. We find that $\lambda < 0.001$ and independent of De at small γ_0. At large γ_0 and De, we find that λ is consistent with the form $\mathrm{De}^{0.5}$. Whether this functional dependence extends to larger γ_0 and De, and what implications this functional form suggests are not known.

4.9 The effect of the interparticle potential on simulations

To examine whether the interparticle potential in Brownian dynamics simulations effectively mimics the hard sphere potential, we calculate the shear stress Σ_{XY} for three different potentials, which are Lennard-Jones potential, $U \propto r^{-36}$ and

$U \propto r^{-50}$. The results of all three different potentials are plotted along with the data reproduced from previous simulations results [19] in Fig. 4.12. For the reproduced data, we determine the corresponding stresses by multiplying the η value plotted in the reference by $\mathrm{Pe}/(6\pi r^3)$.

To examine whether the interparticle potential in Brownian dynamics simulations effectively mimics the hard sphere potential, we calculate the shear stress Σ_{XY} for three different potentials, namely, the WCA Lennard-Jones-based (LJ) potential, $U \propto r^{-36}$ and $U \propto r^{-50}$. Fig. 4.12 shows the results of all three different potentials are plotted along with data from previously reported simulations results for hard spheres [19] (for the latter we determine the corresponding stresses by multiplying the reported η value by $\mathrm{Pe}/(6\pi r^3)$).

We find that when the steepness of the repulsive branch of the potential is increased from WCA Lennard-Jones potential ($U \propto r^{-12}$) to $U \propto r^{-36}$, the stress response is quantitatively similar at small $\mathrm{De}\gamma_0$ and deviates very slightly at $\mathrm{De}\gamma_0 > 10$. As the potential steepness is increased from $U \propto r^{-36}$ to $U \propto r^{-50}$, the stress remains quantitatively similar at all $\mathrm{De}\gamma_0$. This shows that the $U \propto r^{-36}$ and $U \propto r^{-50}$ potentials can both be considered very good approximations to the hard sphere potential. The stress outputs from both potentials also nearly match the resulting stress from previous Brownian dynamics simulations, which use a different algorithm to generate the hard sphere potential[19]. Results from Stokesian dynamics simulations for hard sphere suspensions are also available but for a packing fraction of 0.45[19], which is larger than that the 0.30 used in the Brownian dynamics simulations. Under such conditions, the calculated stress from Stokesian dynamics is approximately one order of magnitude larger than that found for the Brownian dynamics simulations at small $\mathrm{De}\gamma_0$. At large $\mathrm{De}\gamma_0$, the stress from

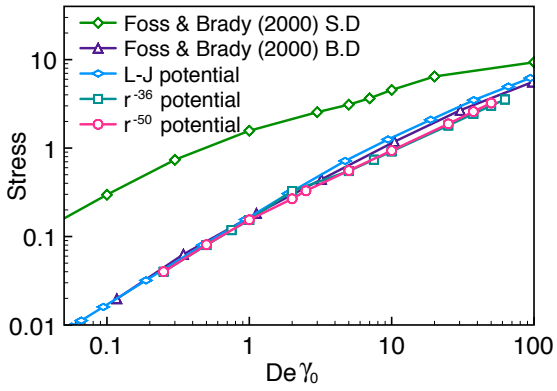

Figure 4.12: Stress responses in different simulations are plotted versus $\mathrm{De}\gamma_0$. The data points of Foss & Brady (2000) S.D and Foss & Brady (2000) B.D are the Stokesian dynamics simulation ($\phi = 0.45$) and Brownian dynamics simulation ($\phi = 0.30$) from [19] respectively.

Stokesian dynamics simulations appears to saturate while the stress in Brownian dynamics simulation keeps increasing with nearly constant rate[19].

4.9.1 Ψ_B versus Σ_{XY} in Brownian dynamics simulation

In previous experimental and theoretical works, it has been shown that as the suspension is sheared, distortions of $g(\vec{r})$ increase and lead to the Brownian stresses that arise from the thermal motion of particles[18, 19, 13]. Although the relative contribution from Brownian stress does decrease with increasing shear rate, it is important to note that this relative decrease arises because the hydrodynamic contribution grows linearly with strain rate while the Brownian contribution grows at a slower rate in this regime.

To examine whether Ψ_0 reproduces the stress response in Brownian dynamics simulations, we directly calculate the stress tensor $\Sigma = \langle \vec{X}\vec{F} \rangle$, where $\vec{X}$ is the center to center position vector and $\vec{F}$ is the interparticle force. We plot Ψ_0 (solid lines) and the XY component of the stress tensor Σ_{XY} (dashed lines) as a function

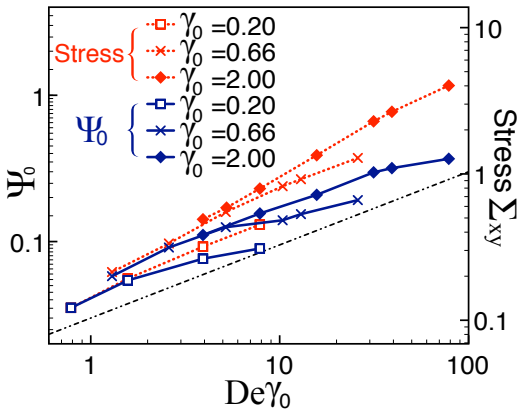

Figure 4.13: Ψ_0 and shear stress Σ_{XY} are plotted versus Deγ_0 for three different γ_0. The black dashed (straight) line illustrates the power-law $(De\gamma_0)^{0.5}$.

of De for three different γ_0 in Fig. 4.13. Here, we find good agreement for Ψ_0 and Σ_{XY} at low shear rates, De$\gamma_0 \leq 5$, which is consistent with the previous experimental finding [13]. The values of the two calculations deviate from one another as Deγ_0 >5. This deviation between $\hat{r}\hat{r}g(\vec{r})$ integral and the stress response may be caused by the extra radial integral in the main manuscript Eq. 1. For example, in the high shear rate regime, the separation between particles becomes really small due to the strong shear flow. This narrow gap along with the divergent nature of the interparticle force may lead to large deviations between Ψ_0 and Σ_{XY}.

We also find that the trend of Σ_{XY} is strikingly distinct from that of the existing rheological measurements [13, 10] and our structure measurements. While Σ_{XY} keeps increasing as Deγ_0 increases, the latter two types of experiments show clear saturations at high Deγ_0. This difference may indicate the increasingly important role of hydrodynamic interactions for colloidal suspensions driven away from equilibrium by LAOS.

In contrast to the interparticle interactions in the Brownian Dynamics simulations, the Brownian stress in colloidal suspensions is transmitted through the sol-

vent between particles. To calculate these hydrodynamically mediated forces, it is necessary to consider the mobility tensors, which require knowledge of the particle positions and velocities. It has been shown that as the separation between particles $\xi \to 0$, the mobility tensors are singular diverging as $1/\xi$. In addition, it was shown that because the singular force between particles is localized to the point of contact the final force calculation can be simplified to $nk_BTa \oint_{r=2a} \hat{r}\hat{r}g(\vec{r})dS$, which has no ξ dependence or particle relative position dependence.

In our experiments, we find that the angular part of the pair correlation function, $g(\theta, \phi)$, has negligible dependence on the distance over the integral range. This observation suggests that one is able to perform a separation of variables on $g(\vec{r}) = g(r)g(\theta, \phi)$. Thus, Eq. 1 of main paper can be rewritten as:

$$\Psi_B = \frac{1}{0.51a}\Big(\int_{1.84a}^{2.35a} g(r)dr\Big)\Big(\oint_{r=2a} \hat{r}\hat{r}g(\theta, \phi)d\Omega\Big). \tag{4.5}$$

The value of the first radial integral $\int g(r)dr$ is nearly constant at all shear rates as shown in Fig. 6a of main paper. The second integral, which only accounts for the contacting particles, is mathematically proportional to the Brownian stress $nk_BTa \oint_{r=2a} \hat{r}\hat{r}g(\vec{r})dS$. Taken together, these results suggest Ψ_B is proportional to the Brownian stress response of colloidal suspensions under LAOS.

To further examine whether Ψ_B reports on the stresses it will be necessary to elucidate the role played by hydrodynamically mediated particle interactions. As such full hydrodynamic simulations will be necessary to more rigorously investigate the effect from the extra radial integral in Eq. 1 of main paper and the accuracy of estimating the total Brownian stress by only considering the pairwise term. Experimental confirmation of the ability to use Ψ_B to report on the stress, will

require precision force measurements that will allow for such comparisons.

REFERENCES

[1] H. Jaeger and A. J. Liu, What Happens Far from Equilibrium and Why?, *Condensed-matter and materials physics: the science of the world around us (2007)* (pp. 91-110) (The National Academies Press, Washington, D. C. 2013)

[2] C. Storm, J. J. Pastore, F. C. MacKintosh, T. C. Lubensky, and P. A. Janmey, Nature, **435**, 191 (2005).

[3] D. Bonn, S. Tanase, B. Abou, H. Tanaka, and J. Meunier, Phys. Rev. Lett., **89**, 015701 (2002)

[4] C. Derec, G. Ducouret, A. Ajdari, and F. Lequeux, Phys. Rev. E **67**, 061403 (2003)

[5] N. J. Wagner and J. F. Brady, Phys. Today **62**, 27 (2009).

[6] D. J. Evans and G. P. Morriss, *Statistical mechanics of nonequilibrium liquids* (ANU E Press, Canberra, 2007).

[7] J. M. Brader, J. Phys. Condens. Matter **22**, 363101 (2010).

[8] K. Hyun,, M. Wilhelm, C. O. Klein, K. S. Cho, J. G. Nam, K. Ahn, S. J. Lee, R. H. Ewoldt, G. H. McKinley, Progress in Polymer Science **36**, 1697 (2011).

[9] C. R. López-Barrón, L. Porcar, A. P. R. Eberle, and N. J. Wagner, Phys. Rev. Lett. **108**, 258301 (2012).

[10] J. M. Brader, M. Siebenbrger, M. Ballauff, K. Reinheimer, M. Wilhelm, S. J. Frey, F. Weysser, and M. Fuchs, Phys. Rev. E Stat. Nonlin. Soft Matter Phys. **82**, 061401 (2010).

[11] T. Narumi, A. Suzuki, T. Hasegawa, and H. See, J. Rheol., **49**, 71 (2005).

[12] K. Hyun, S. H. Kim, K. H. Ahn, and S. J. Lee, J. of Non-Newtonian Fluid Mech., **107**, 51 (2002).

[13] E. D. Giuseppe, A. D., E. Mittelstaedt, M. Francois, Rheol. Acta. **51**, 451 (2012).

[14] R. H. Ewoldt, A. E. Hosoi, G. H. McKinley, Integr. Comp. Biol., **49**, 40 (2009).

[15] E. R. Weeks, J. C. Crocker, A. C. Levitt, A. Schofield, D. A. Weitz, Science **287**, 627 (2000).

[16] W. K. Kegel and A. van Blaaderen, Science **287**, 290 (2000).

[17] S. Toyabe, T. Sagawa, M. Ueda, E. Muneyuki, M. Sano, Experimental demonstration of information-to-energy conversion and validation of the generalized Jarzynski equality, Nature Phys. **6**, 988 (2010)

[18] J. F. Brady, Journal of Chemical Physics, **99** 567 (1993).

[19] D. R. Foss and J. F. Brady, J. Fluid Mech **407**, 167 (2000).

[20] X. Cheng, J. H. McCoy, J. N. Israelachvili, and I. Cohen, Science **333**, 1276 (2011).

[21] J. C. Crocker and D. G. Grier, J. Colloid Interface Sci. **179**, 298 (1996).

[22] R. N. Zia and J. F. Brady, J. Fluid Mech. **658**, 188 (2010).

[23] N. Koumakis, M. Laurati, S. U. Egelhaaf, J. F. Brady, and G. Petekidis, Phys. Rev. Lett. **108**, 098303 (2012).

[24] C. Gao, S. D. Kulkarni, J. F. Morris, J. F. Gilchrist, Phys. Rev. E Stat. Nonlin. Soft Matter Phys. **81**, 041403 (2010).

[25] J. Vermant and M. J. Solomon, J. Phys.: Condens. Matter **17**, 187 (2005).

[26] R. B. Bird, W. E. Stewart, E. N. Lightfoot, *Transport Phenomena, 2nd Edition* (Wiley, Hoboken, 2006).

[27] J. Bergenholtz, J. F. Brady, and M. Vicic, The non-Newtonian rheology of dilute colloidal suspension, J. Fluid Mech. **456**, 239-275 (2002).

[28] J. F. Brady, and J. F. Morris, J. Fluid Mech. **348** 103-139 (1997).

[29] Laurent Corté, P. M. Chaikin, J. P. Gollub, and D. J. Pine, Nature Phys. **4**, 420 (2008).

[30] L. Corté, S. J. Gerbode, W. Man, and D. J. Pine, Phys. Rev. Lett. **103**, 248301 (2009).

[31] D. R. Foss and J. F. Brady, J. Fluid Mech **401**, 243 (1999).

[32] A, Sierou and J. F. Brady, J. Fluid Mech **506**, 285 (2004).

[33] D. Leighton and A. Acrivos, J. Fluid Mech **177**, 109 (1987).

[34] W. Yu, M. Bousmina, C. Zhou, J. Non-Newtonian Fluid Mech., **133**, 57 (2006).

[35] V. Nosenko, A. V. Ivlev, and G. E. Morfill, Phys. Rev. Lett., **108**, 135005 (2012).

[36] W. P. Cox and E. H. Merz, Journal of Polymer Science, **28**, 619 (1958).

[37] R. G. Larson, *The Structure and Rheology of Complex Fluids* (Oxford University, Press, Cary 1998).

[38] D. Doraiswamy, A. N. Mujumdar, I. Tsao, A. N. Beris, S. C. Danforth, and A. B. Metzner, J. Rheol. **35**, 647 (1991).

[39] T. S. R. Al-Hadithi, H. A. Barnes, K. Walters, Colloid and Polymer Science, **270**, 40 (1992).

[40] J. Hernández-Guzmán and E. R. Weeks, Natl. Acad. Sci. U. S. A. **106**, 15198 (2009)

[41] Y. Peng, Z. Wang, A. M. Alsayed, A. G. Yodh and Y. Han, Phys. Rev. Lett. **104**, 205703 (2010).

[42] R. Pasquino, F. Snijkers, N. Grizzuti, J. Vermant, Rheologica Acta **49**, 993-1001 (2010).

[43] B. J. Maranzano and N. J. Wagner, J. Chem. Phys. **117** 10291 (2002).

[44] R. N. Zia and J. F. Brady, J. Rheol. **57** 457 (2013).

[45] M. E. Helgeson, N. J. Wagner, and D. Vlassopoulos, J. Rheol. **51**, 297 (2007).

[46] J. M. Adams and P. D. Olmsted, Phys. Rev. Lett. **102** 067801 (2009).

[47] R. H. Ewoldt, P. Winter, J. Maxey, and G. H. McKinley, Rheol. Acta, **49**, 191 (2010).

[48] S. A. Rogers, B. M. Erwin, D. Vlassopoulos, M. Cloitre, J. Rheol. **55** 733 (2011).

[49] R. A. Lionberger and W. B. Russel, J. Rheol., **38**, 1885 (1994)

[50] T. Shikata, D. S. Pearson, J. Rheol., **38**, 601 (1994).

[51] N. Koumakis, M. Laurati, S. U. Egelhaaf, J. F. Brady, and G. Petekidis, Phys. Rev. Lett. **108**, 098303 (2012).

[52] N. Koumakis, A. Pamvouxoglou, A. S. Poulos, G. Petekidis, Soft Matter **8** 4271 (2012).

[53] P. Agarwal, S. Srivastava, and L. A. Archer, Phys. Rev. Lett. **107** 268302 (2011).

[54] L. B. Chen, B. J. Ackerson, C. F. Zukoski, J. Rheol. **38**, 193 (1994).

[55] M. S. Elliot, B. T. F. Bristol, W. C. K. Poon, Physica A: Statistical Mechanics and its Applications **235** 216 (1997).

[56] B. J. Ackerson, J. B. Hayter, N. A. Clark, and L. Cotter, J. Chem. Phys. **84** 2344 (1986).

[57] C. R. López-Barrón, L. Porcar, A. P. R. Eberle, and N. J. Wagner, Phys. Rev. Lett. **108** 258301 (2012).

[58] Randy H. Ewoldt, A. E. Hosoi, and Gareth H. McKinley, J. Rheol. **52** 1427 (2008).

[59] K. Emancipator, M. H. Kroll, Clinical chemistry **39**, 766 (1993)

[60] A. Trokhymchuk, I. Nezbeda, J. Jirsók, and D. Henderson "Hard-sphere radial distribution function again", The Journal of Chemical Physics, **123** 024501 (2005)

[61] M. S. Wertheim, Exact Solution of the Percus-Yevick Integral Equation for Hard Spheres, Phys. Rev. Lett. **10** 321 (1963).

[62] S. B. Yuste and A. Santos, Radial distribution function for hard spheres, Phys. Rev. A **43** 5418 (1991).

CHAPTER 5

BIAXIAL SHEAR OF CONFINED COLLOIDAL HARD SPHERES: THE STRUCTURE AND RHEOLOGY OF THE VORTICITY-ALIGNED STRING PHASE[1]

5.1 Abstract

Using a novel biaxial confocal rheoscope, we investigate the flow of the shear induced vorticity aligned string phase [X. Cheng *et al., Proc. Natl. Acad. Sci. U. S. A.*, 2011, **109**, 63], which has a highly anisotropic microstructure. Using biaxial shear protocols we show that we have excellent control of the string phase anisotropic morphology. We choose a shear protocol that drives the system into the string phase. Subsequently, a biaxial force measurement device is used to determine the suspension rheology along both the flow and vorticity directions flows. We find no measurable dependence of the suspension stress response along the shear and vorticity directions due to the hydrodynamically induced string morphology. In particular, we find that the suspension's high frequency stress response is nearly identical along the two orthogonal directions. While we do observe an anisotropic stress response at lower shear frequencies associated with shear thinning, we show that this anisotropy is independent of the shear induced string structure. These results suggest that for the range of flows explored, Brownian and hydrodynamic contributions to the stress arising from the anisotropic suspension microstructure are sufficiently weak that they do not significantly contribute to the rheology. Collectively, this study presents a general and powerful approach for using biax-

[1]Neil Y.C. Lin, Xiang Cheng, and Itai Cohen. "Biaxial shear of confined colloidal hard spheres: the structure and rheology of the vorticity-aligned string phase." Soft Matter 10.12 (2014): 1969-1976.

ial confocal rheometry to elucidate the relationship between microstructure and rheology in complex fluids driven far-from-equilibrium.

5.2 Introduction

Anisotropic materials are ubiquitous in nature - examples include wood, bone[1], anisotropic crystals[2, 3], and plasmas[4]. Furthermore, many soft materials, which are important for industrial and biological applications, form anisotropic structures in response to external fields[5, 6] and demonstrate highly anisotropic viscosities. Representative examples include nematic liquid crystals[7, 8], magnetic fluids[9], and muscle tissues[10], all of which exhibit different viscosities along different directions. In many of these systems, anisotropic microstructures give rise to the anisotropic mechanical properties.

A particularly striking example of anisotropic microstructures are the various vorticity-aligned assemblies found in many complex fluids, including thixotropic clay gels[11], attractive colloids[12] and emulsion droplets[13], nanotube suspensions[14, 15, 16], fiber suspensions [17], and hard sphere colloids [18]. Such phases are of technological interest since they have potential applications in the areas of nano-fabrication and bio-analysis [20, 19, 21]. Despite extensive study of these shear induced anisotropic structures and their rheology under uniaxial shear [18, 12, 13, 14, 15, 16, 17], the relation between the structures they form and their corresponding direction-dependent viscosities is still poorly explored. One of the technical hurdles for relating anisotropic structure to the material's anisotropic rheology is the inability to simultaneously image the sample microstructure while measuring its anisotropic rheology.

Here, we use a newly developed technique to simultaneously investigate the structure and biaxial rheology of the vorticity-aligned string phase in sheared colloidal suspension under confinement. This phase demonstrates string-like particle assemblies aligning along the vorticity direction, and has a one-dimensional translational symmetry [22, 25, 23, 24, 26, 18, 12]. In many systems it has been suggested that the vorticity-aligned structures arise from interparticle attractions[12, 13, 14, 16]. In contrast, the string assemblies in the hard sphere colloid system investigated here, result from the unique interactions that arise from geometric constraint and hydrodynamic particle-particle and particle-wall couplings all of which are enhanced by confinement [18].

To measure suspension rheology we construct a biaxial confocal rheoscope by combining a dual-directional shear cell with a biaxial force measurement device. This apparatus allows for manipulating the formation and the orientation of shear-induced structures while simultaneously measuring their anisotropic mechanical response, and imaging their structure [30, 31, 28, 29, 27]. We first demonstrate direct control over the isotropic-to-string phase transition using biaxial shear flows. With this technique in conjunction with *oscillatory superposition spectroscopy*, we then directly measure the rheology of the string phase along different directions. Surprisingly, we find that the anisotropic structure has a negligible effect on the corresponding rheological properties of the suspension.

5.3 Experiment

The schematic of the biaxial shear cell is illustrated in Fig. 5.1. For each experimental run, $10\mu l$ of suspension are loaded in a gap consisting of a coverslip and

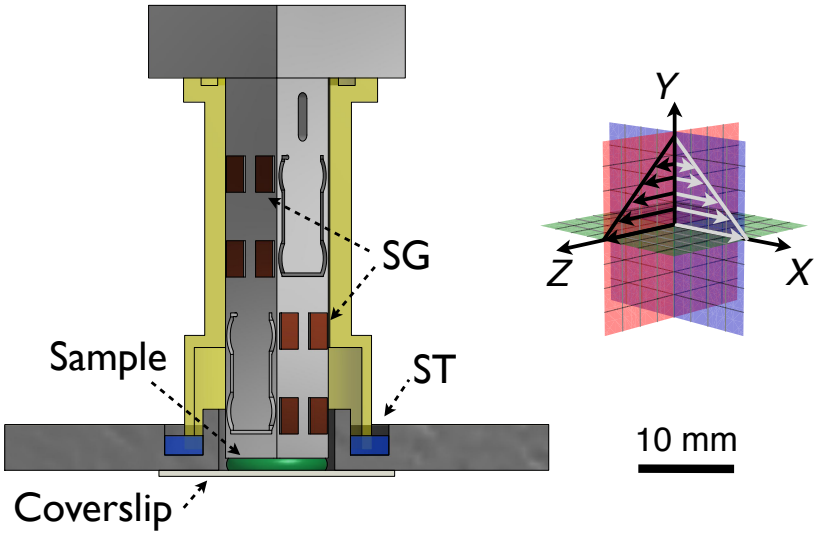

Figure 5.1: Three dimensional schematic of the biaxial force measurement device (left) and coordinate definition (right). The abbreviations SG and ST stand for strain gauges and the solvent trap, respectively. The lower strain gauges measure the stress response along the X-axis, σ_{xy}, and the upper ones measure the response along the Z-axis, σ_{zy}. The gap between the top plate (silicone wafer) and the bottom plate (coverslip) is exaggerated for clarity. The gap separation in the experiments is 9.0μm. The shear flow is separately imposed along the X and Z axes by moving the bottom plate using a multi-axis piezoelectric actuator.

a 4mm$\times$4mm silicon wafer with a 9μm separation between them. Both plates are adjusted to be parallel within 0.0075° by turning three set screws. The coverslip is coupled to a multi-axis piezo (PI P-733) that can generate movements along all directions to apply biaxial shear flows. The silicon wafer is attached to a biaxial force measurement device (FMD) so that the shear stresses σ_{xy} and σ_{zy} are measured simultaneously. Here, X, Y, and Z correspond to the flow, gradient, and vorticity axes of the first shear flow.

In the FMD, eight foil gauges - four for each direction - are wired as two independent Wheatstone bridges that enable stress measurement. All signals measured by the FMD are amplified by signal conditioning amplifiers (Vishay 2310B) then

digitized for Fourier analysis. By mounting this biaxial shear cell on a fast confocal microscope (Zeiss LSM 5 Live), we also image the microstructure while the suspension is sheared and the stress response is measured. The calibration details of the shear cell alignment and the FMD performance are in the Appendix.

Our sample is comprised of silica particles with diameter $a = 1.3\mu$m suspended in a 1:4 water-glycerin mixture. The solvent has a viscosity $\eta = 0.06$Pa·s and a refractive index of 1.442 that matches that of the particles. The suspension volume fractions we work with are $\phi = 0.37$ and 0.47. We add 1.25mg/ml of fluorescein sodium salt to dye the solvent for confocal imaging. The electrostatic screening length is $\sim$10nm, so that the interparticle interactions are nearly hard-sphere.

The biaxial shear flow imposed can be divided into two oscillatory shear flows

$$\bar{\bar{\gamma}}(t) = \bar{\bar{\gamma}}_1 \sin(\omega_1 t) + \bar{\bar{\gamma}}_2 \sin(\omega_2 t + \delta_\gamma). \tag{5.1}$$

Here, $\bar{\bar{\gamma}}$ corresponds to the strain amplitude tensor, ω corresponds to the shear frequency, and δ_γ corresponds to the phase angle difference between the first flow, indicated by the subscript 1 and the second flow, indicated by the subscript 2. When both the first and the second flows are parallel, the strains $\bar{\bar{\gamma}}_1$ and $\bar{\bar{\gamma}}_2$ are aligned and the stress response is probed along the flow direction. When the first and the second flows are perpendicular, the strain $\bar{\bar{\gamma}}_2$ probes the response orthogonal to the direction of the first flow.

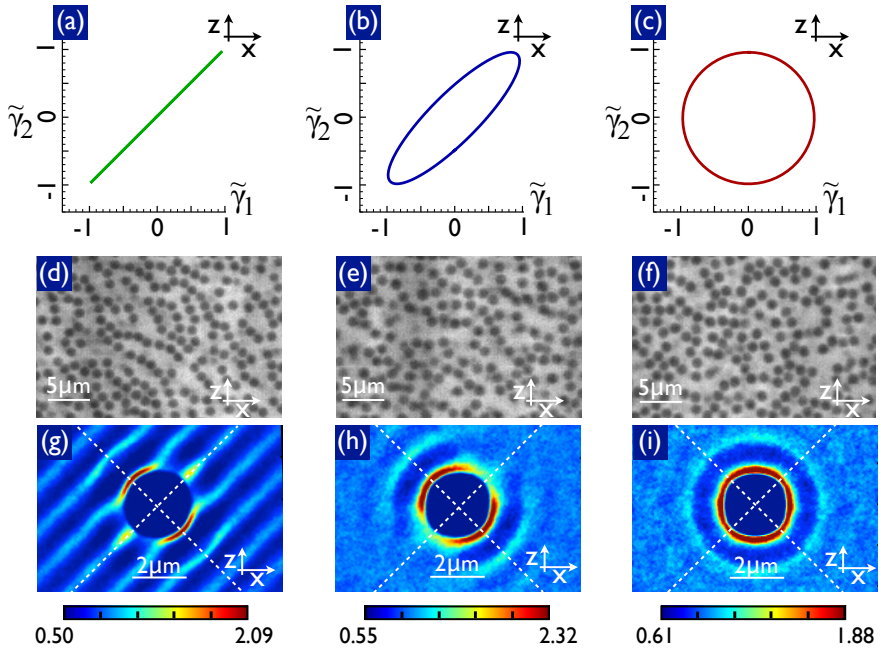

Figure 5.2: Suspension microstructure for three phase angles $\delta_\gamma = 0, \pi/6$ and $\pi/2$. Lissajous curves for the normalized shear strains $\tilde{\gamma}_y$ versus $\tilde{\gamma}_x$ are plotted in (a)-(c), where (a) (b) and (c) correspond to $\delta_\gamma = 0, \pi/6$ and $\pi/2$ respectively. The 2D confocal images of the suspension with $\delta_\gamma = 0, \pi/6$ and $\pi/2$ are shown in (d), (e), and (f) respectively. The corresponding pair correlation functions $g(\vec{r})$ of the particle distribution are shown in (g), (h) and (i). Each $g(\vec{r})$ image represents a measurement averaged over 20 shear cycles. The dashed lines are guides for the eye and denote the 45° and the 135° orientations. The color ranges in the density plots are chosen to emphasize the structural features.

5.4 Results

5.4.1 2D-Oscillatory Shear: Phase Angle Dependence of Structure and Rheology

In the phase angle experiment, we set the first flow $\bar{\bar{\gamma}}_1 = 2.50\hat{X}\hat{Y}$ and the second flow $\bar{\bar{\gamma}}_2 = 2.50\hat{Z}\hat{Y}$ perpendicular. Here, while the flows characterized by γ_1 and γ_2 are along X-axis and Z-axis respectively, both γ_1 and γ_2 share the same gradient

axis (Y-axis). We fix the shear frequency at $\omega_1 = \omega_2 = 31.4$ s^{-1} and vary the phase angle δ_γ over the range $0 \leq \delta_\gamma \leq \pi$. Thus the maximum shear rate along each axis is 78.5 s^{-1}, which corresponds to Pe= 4.73×10^3. Here, the Péclet number is defined as Pe=$6\pi\eta_0\dot{\gamma}a^3/(8k_BT)$ and characterizes the ratio of the shear rate $\dot{\gamma}$ to the relaxation rate $1/\tau_s$ of the sample. This method has been introduced as 2D-SAOS (small amplitude oscillatory shear) when the strain amplitude ($\leq 5 \times 10^{-2}$) is small [32].

Fig. 5.2(a), (b) and (c) show the normalized magnitude $\tilde{\gamma}_1$ versus $\tilde{\gamma}_2$ Lissajous-Bowditch curves for the imposed flows where $\delta_\gamma = 0, \pi/6$ and $\pi/2$ respectively. For $\delta_\gamma = 0$, the shear strain trajectory is linear and aligned at 45° to the X-axis. This linearly polarized shear flow is the same as the uniaxial shear flow with a different orientation (Fig. 5.2(a)). In Fig. 5.2(b) and (c), $\bar{\bar{\gamma}}(t)$ is elliptically polarized with $\delta_\gamma = \pi/6$ and circularly polarized with $\delta_\gamma = \pi/2$.

Previous measurements have shown that the string structures are most pronounced near the boundaries [18]. Thus, for each phase angle, we image the colloidal particles in the second layer 2.5μm below the top stationary plate. We find that as δ_γ changes from 0 to $\pi/2$ the suspension structure transitions from a string morphology to one that is isotropic (Fig. 5.2(d-f)). To illustrate this transition we calculate the pair correlation functions $g(\vec{r})$ and average them individually over 20 cycles of shear (Fig. 5.2(g), (h) and (i)). Here $g(\vec{r})$ is the normalized probability of finding a particle at vector $\vec{r}$ with respect to another particle in the X-Z plane. In Fig. 5.2(d), we find that when the suspension is subjected to a linearly polarized shear flow, $g(\vec{r})$ demonstrates a highly anisotropic distribution at its first peak and exhibits stripes at larger $\vec{r}$. These stripes along with the anisotropic distribution of particle densities confirm that particles align along the vorticity direction and

form string structures under uniaxial shear (Fig. 5.2(g)). This finding is consistent with previous results [18]. As δ_γ increases to $\pi/6$, the first peak of $g(\vec{r})$ maintains a similar shape but with a broader peak width. Most stripes disappear and the anisotropy of the second and the third peaks of $g(\vec{r})$ significantly decreases (Fig. 5.2(h)). Finally, for $\delta_\gamma = \pi/2$, $g(\vec{r})$ is isotropic indicating that the suspension is characterized by liquid-like order Fig. 5.2(i).

Additional structural characterization of the string phase including the alignment order parameter, layering, and time dependence can be found in Supplementary Information (SI). Here we simply point out that by imposing different phase angles we are able to control the suspension structure while keeping the Pe for the flows along both axes constant. This protocol allows for excluding effects from other contributions, including Brownian stresses and hydrodynamic coupling, that can arise when comparing the rheology of the sample at different shear rates.

Using this protocol we study the relation between the rheology and the anisotropic microstructure by measuring the stress responses along the X-axis, σ_{xy}, and the Z-axis, σ_{zy}, simultaneously for different phase angles δ_γ. We find that the first harmonic term for the stress response accounts for over 90% of the force amplitude and dominates the higher order terms [33], which are often buried in the noise. We therefore report the first harmonic response amplitude as the measured stress peak within one shear cycle. We plot σ_{xy} and σ_{zy} versus δ_γ in Fig. 5.3 (a). Despite the dramatic change in microstructure, we find that both σ_{xy} and σ_{zy} are independent of δ_γ. To measure the Pe-dependence of stress responses we perform an amplitude sweep over the range $5.70 \times 10^{-3} \leq |\bar{\bar{\gamma}}| \leq 3.00$ while keeping the frequencies fixed at $31.4s^{-1}$. We plot σ_{xy} versus Péclet number for both $\delta_\gamma = 0$ (linear) and $\delta_\gamma = \pi/2$ (circular) polarizations in Fig. 5.3 (b). We find quantita-

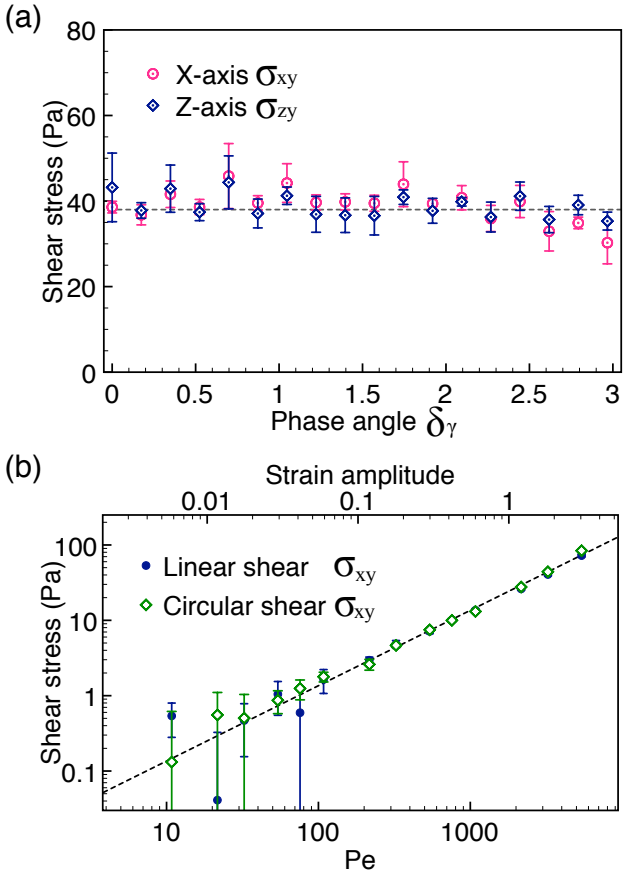

Figure 5.3: Suspension stress response versus δ_γ (a) and Pe (b). (a) The stress responses along the X-axis, σ_{xy}, and the Z-axis, σ_{zy}, are plotted versus δ_γ with $\gamma_{1,2} = 2.50$ and $\omega_{1,2} = 31.4$ s^{-1}. The dashed horizontal line indicates the mean value of the data. Each data point is averaged over five independent measurement runs with each run consisting of 500 cycles. (b) The stress response is plotted as a function of Pe for linearly polarized and circularly polarized shear flows. The data are consistent with a Newtonian response as indicated by the linear fit (dashed line). We note that the smallest measureable stress difference would correspond to approximately twice the error bar value or ∼10 Pa

tively similar dependencies for both polarizations. These data indicate that for $\omega = 31.4$ s^{-1} the shear induced in-plane structure does not alter the suspension rheology for $11 <$ Pe$< 5.7 \times 10^3$.

5.4.2 Oscillatory Superposition Spectroscopy

To probe the anisotropic rheological properties of the suspensions, we perform an *oscillatory superposition spectroscopy* measurement [34, 35]. Similar methods have recently gained traction for determining the shear thinning behavior of polymer solutions[34, 35] and colloidal glasses [37, 36], as well as slow relaxations in granular systems[38]. To investigate the string phase we choose the first shear flow along the X-axis that generates the most pronounced strings ($|\bar{\dot{\gamma}}_1| = 2.50$ and $\omega_1 = 31.4$ s^{-1}), and use the second flow to probe the suspension response. It is important to note that in such biaxial flow experiments, technically there are no well defined vorticity and flow axes for the overall flow, as shear is being applied in both the $X-Y$ and $Z-Y$ planes. Nevertheless, it is still useful to think of the system as being driven by the first flow and being probed by the second flow. These labels do however lose their meaning as the shear rate due to the second flow becomes comparable to that of the first flow.

Because the rheological phase space that can be explored is vast and because the measurements are time intensive, we use the second flow to conduct an amplitude and a frequency sweep. These measurements are able to investigate the string phase rheology over a range of flow rates that separately capture the hydrodynamic and Brownian contributions to the stress response. The regime of the string structure rheology that these measurements access is illustrated in the Pipkin diagram in Fig. 5.4.

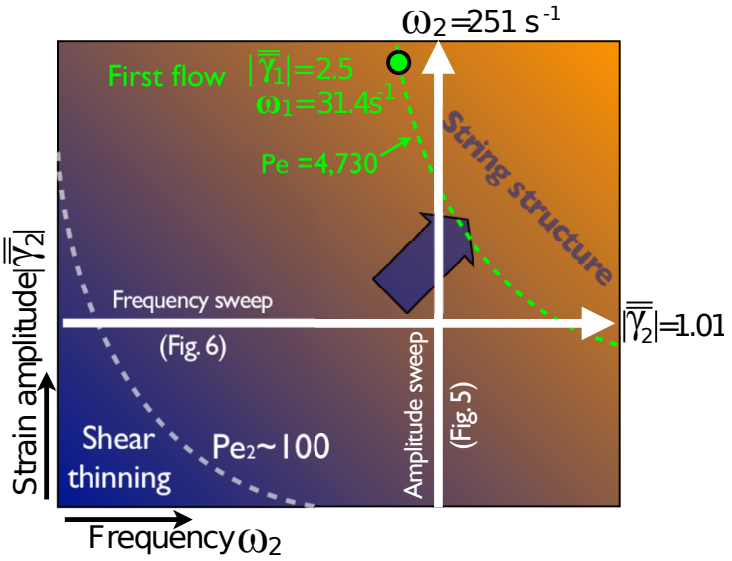

Figure 5.4: Pipkin diagram of the explored regime in this experiment. The green dashed curve denotes the constant Pe of the first flow. The gray dashed curve indicates the shear thinning regime. Two long arrows illustrate the amplitude (vertical) and frequency (horizontal) sweep measurements performed.

5.4.3 Amplitude Sweep: Hydrodynamic Contributions

In the amplitude sweep measurements, we conduct experiments using parallel and orthogonal modulations of the first shear flow. In both orthogonal and parallel cases we record the total stress for 500 cycles and then take a Fourier transform of the measurement to read out the response - σ_{zy}, or σ_{xy} at the frequency ω_2. The regime examined by this measurement is depicted by the vertical white arrow in Fig. 5.4. We plot $\sigma_{zy}(\omega_2)$ for the orthogonal modulation (green diamonds) and $\sigma_{xy}(\omega_2)$ for the parallel modulation (blue squares) versus Pe_2 (bottom axis) and $|\bar{\bar{\gamma}}_2|$ (upper axis) in Fig. 5.5(a). We find that the measurements for both modulations are quantitatively similar. In both cases we find a linear dependence of stress on Pe_2 indicating a Newtonian response. Thus, we find no measurable effect of the string structure on the suspension oscillatory shear rheology. To further probe the

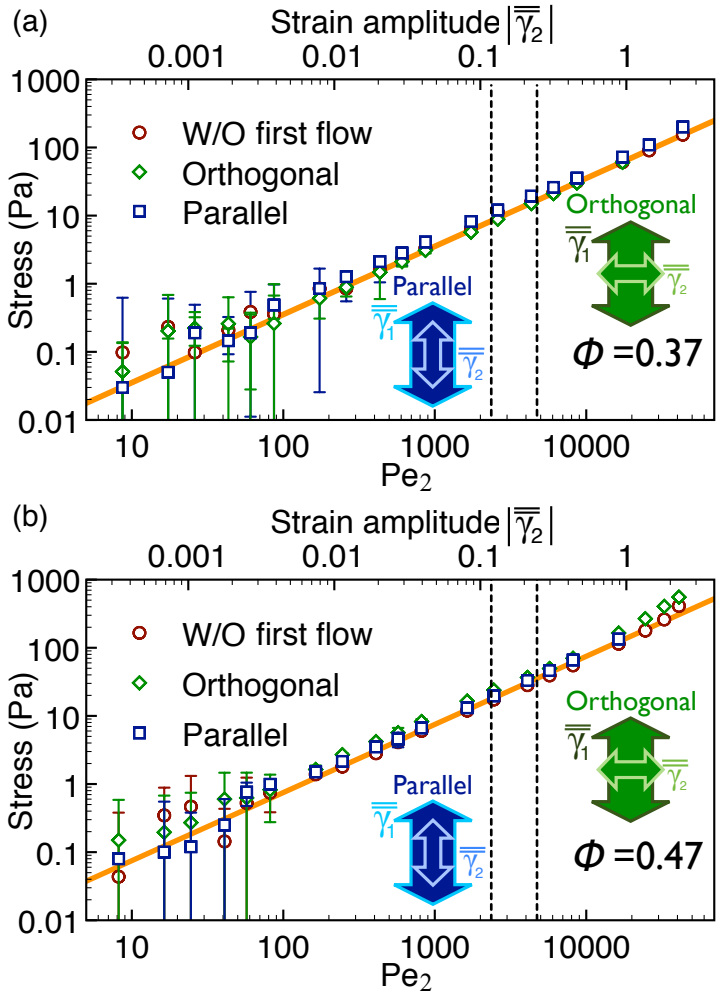

Figure 5.5: Stress responses measured using oscillatory superposition spectroscopy for orthogonal (green diamonds) and parallel modulations (blue squares). (a) Stresses measured in the modulation experiments are plotted as a function of Pe_2 for $\phi = 0.37$. The stress response without the first flow is also shown in the plot for comparison (red circles). The dashed vertical lines are the first flow Péclet numbers for orthogonal (right) and parallel (left). The oblique dashed line is the theoretical calculation of the hydrodynamic stress response[39]. In the parallel modulation experiment, Pe_1 is smaller than that of orthogonal modulation due to the limitation of the piezo travel distance. (b) Stress measurements with the same shear protocols conducted for a denser suspension with $\phi = 0.47$. This suspension demonstrates a slight shear thickening behavior when $\mathrm{Pe}_2 \geq 10^4$. The orange lines in both figures are the theoretical values for the hydrodynamic stress response calculated using Eq. 2 [39]. The smallest measureable stress difference in the amplitude sweep measurements would correspond to approximately twice the error bar value or ~ 1 Pa.

dependence of rheology on the shear induced string structure we conduct additional experiments in which the first flow is absent (red circles). We find that the stress measurements for these flows are quantitatively similar to those in which the first flow is applied. Collectively these results demonstrate that despite the formation of string structures, the suspension response remains isotropic. In addition, we calculate the hydrodynamically dominated high frequency stress response for an isotropic bulk suspension [39] with $\phi = 0.37$ using

$$\eta_H = \frac{1 + \frac{3}{2}\phi[1 + \phi(1 + \phi - 2.3\phi^2)]}{1 - \phi[1 + \phi(1 + \phi - 2.3\phi^2)]}. \tag{5.2}$$

We find that the predicted viscosity $\eta_H = 240$mPa·s gives a stress response (orange lines in Fig. 5.5) that is in excellent agreement with the data. We also find that the suspension stress response remains linear in the applied strain amplitude at low Pe≤ 100 and small amplitudes $|\bar{\bar{\gamma}}_2| \leq 2.00 \times 10^{-3}$. This linear stress response results in an amplitude-independent complex viscosity magnitude[40], which is consistent with active microrheology measurements on quiescent suspensions where the applied oscillation frequency of the probe particle exceeds the relaxation rate of the suspension [41].

The overlap between the data and the relation from Eq. 5.2 suggests that the tested confined suspension demonstrates a bulk stress response. We do however note that the gap height corresponds to approximately seven particle layers. Here, our goal was to maximize the portion of the suspension forming the string phase. At larger gaps strings no longer form while at smaller gaps the rheology is dominated by the suspension structures arising from interactions with the shearing plates. Thus it is difficult to test the explicit effects of confinement on the rheology of the string phase. More broadly, whether the rheology exhibits significant dependence on gap height for confined suspensions remains an interesting open question that

we hope to address in future work.

To test whether these results also apply in higher volume fraction suspensions, we conduct an identical amplitude sweep measurement with a denser suspension ($\phi = 0.47$), and plot the stress responses in Fig. 5.5(b). The rheological properties of the denser suspension are qualitatively similar to that of the sample with an intermediate volume fraction $\phi = 0.37$ (Fig. 5.5(a)). In addition, no wall slip is observed at either volume fraction [28]. Overall, these results imply that for the range of Pe_2 explored, the shear stress response of the string phase is dominated by a hydrodynamic contribution that is independent of the shear induced suspension structure.

5.4.4 Frequency Sweep: Brownian Contributions

Shear thinning in suspensions results from the decreased relative contribution of the Brownian stresses to the total stress[42, 28, 43, 42]. To probe whether the string structure alters the response in the shear thinning regime we conduct a frequency sweep measurement. To confirm that we are probing the shear thinning regime we first characterize the flow behavior of quiescent suspensions where no first flows are imposed. We plot the stress response versus Pe_2 for $\phi = 0.37$ and 0.47 in Fig 5.6. Consistent with prior literature results, we find very weak shear thinning for the $\phi = 0.37$ sample (red squares) and a pronounced thinning behavior for the $\phi = 0.47$ sample (red circles) [42, 45].

Next, we impose a first shear flow with $|\bar{\bar{\gamma}}_1| = 2.50$ at $\mathrm{Pe}_1 = 4.73 \times 10^3$ that is strong enough to generate the string phase and conduct oscillatory superposition spectroscopy measurements using parallel and orthogonal modulations. For both

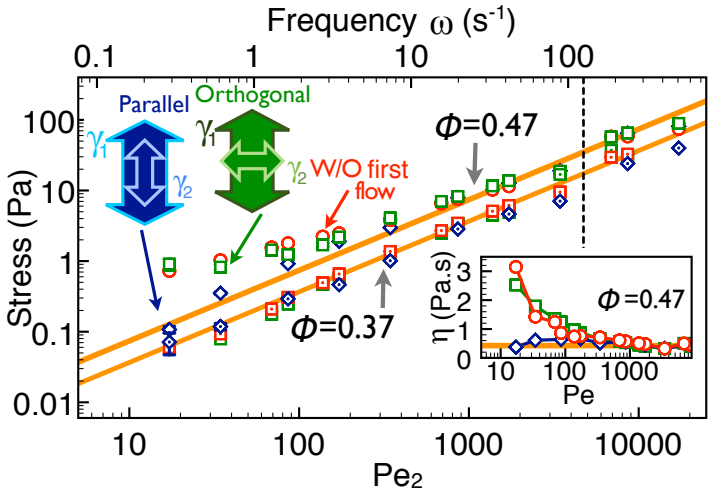

Figure 5.6: Stress responses measured using frequency sweep protocols for $\phi = 0.37$ (dotted symbols) and $\phi = 0.47$ (open symbols). The data for both volume fractions share the same color code. The orange lines are the high frequency responses calculated from Eq. 5.2. The inset shows the corresponding complex viscosity magnitudes of the suspension with $\phi = 0.47$. The error bars illustrate the standard errors of the data averaged over five runs of measurements. The dashed vertical line is the Pe of the first flow. The smallest measureable stress difference in the frequency sweep measurements would correspond to approximately twice the error bar value or ~ 0.1 Pa.

the orthogonal and parallel modulations, we set $|\bar{\bar{\gamma}}_2| = 1.01$ and vary the frequency so that $17.2 \leq \mathrm{Pe}_2 \leq 1.72 \times 10^4$. The regime explored by this frequency sweep measurement is depicted by the horizontal white arrow in Fig. 5.4.

We plot $\sigma_{zy}(\omega_2)$ for the orthogonal modulation (green squares) and $\sigma_{xy}(\omega_2)$ for the parallel modulation (blue diamonds) versus Pe_2 (bottom axis) and ω_2 (upper axis) in Fig. 5.6. The data for the intermediate ($\phi = 0.37$) and high ($\phi = 0.47$) volume fractions are denoted by the dotted and open symbols respectively. Because the shear thinning behavior is weak ($\sim 30\%$) for $\phi = 0.37$[42, 45], the change of the flow behavior at low Pe is barely measurable with our force measurement device. For the high volume fraction suspension ($\phi = 0.47$), we find that the stress response along the orthogonal direction (green squares) demonstrates pronounced

shear thinning behavior for $Pe_2 < 200$. In contrast, we find that the stress response along the parallel direction (blue diamonds) linearly increases with Pe_2 indicating that the suspension has already been shear thinned by the first flow. We highlight this anisotropic responses by plotting the corresponding complex viscosity magnitudes $|\sigma/\dot{\gamma}|$ in the inset of Fig. 5.6.

At first glance these results suggest that there is a significant anisotropic response due to the shear induced string structure. However, close examination of the stress amplitude response curves shows that the response along the orthogonal direction displays the same Pe_2 dependence as the quiescent sample where no first flow was applied. These results demonstrate that the significantly denser packing fraction along the orthogonal direction due to the string structure (Fig. 5.2(g)) dose not enhance the suspension stress response during the orthogonal modulation. Furthermore, the data for the parallel modulation (blue diamonds) are well fit by the Eq. 5.2 for an isotropic suspension indicating that the string structure does not further affect the rheology. In fact, the suspension's response to parallel modulation appears to be dominated by hydrodynamic contributions that are relatively insensitive to the suspension structure (Fig 5.5). Finally, if the difference between the parallel and orthogonal stress responses was related to the string structure, we would have expected that it would have persisted until the second flow was strong enough to alter the string structure. However, the data for both modulations begin to overlap at $Pe_2 \approx 200$, which is still an order of magnitude smaller than Pe_1. Thus we are forced to conclude that while the rheology of the string structure is anisotropic, this anisotropy does not result from the shear induced string structure.

5.5 Discussion and conclusion

Using a novel biaxial confocal rheoscope, we measured the rheological response of the vorticity-aligned string phase along the flow and vorticity directions. This apparatus enabled us to control the orientation and morphology of the sheared colloidal suspension under confinement. We showed that by varying the phase between the two shear directions the sample transitions from a string phase to an isotropic phase. By employing various biaxial shear protocols, we found that despite its anisotropic structure, the string phase rheology is quantitatively similar to that of the isotropic suspension for the range of frequencies and strain amplitudes explored. These result are in agreement with previous work that shows hydrodynamic interactions play a crucial role in the formation of the string phase and dominate its rheological response [18]. In addition, the measurements presented here demonstrate that for the tested volume fractions ($\phi = 0.37$ and 0.47) and degree of confinement, the hydrodynamic contribution to the shear stress is not significantly altered by the suspension microstructure. This structure-independent hydrodynamic response is reminiscent of the weak correlation between the structure and rheology in other complex fluids [46, 43]. For instance, it was recently shown that layering in sheared suspensions of hard-sphere colloids does not correlate with any rheological signature [43]. As another example, the strong viscoelasticity of the synthetic clay Laponite does not depend on the fractal nature of its structure [46]. It is important to note that the viscosity under steady state conditions can be different from the reported amplitude of the complex viscosity under oscillatory shear. Therefore, it would be useful to conduct further experiments to investigate the rheological anisotropy using a superposition of continuous and oscillatory shear.

In the frequency sweep measurements, we do find that suspensions demonstrate an anisotropic shear thinning behavior due to the applied first flow. This anisotropic shear thinning behavior in hard-sphere suspensions is remarkably different from the isotropic shear thinning observed in polymer solutions[34] and is an important result in itself. This thinning behavior is consistent with previous results that have demonstrated that as the system is driven towards high Pe or at a shear frequency above its relaxation rate, the Brownian stresses saturate and the overall viscosity decreases. The observed anisotropy in the stress response indicates that saturation of the Brownian stresses only occurs along the first flow direction. Our data show that such effects are sufficient to account for the measured anisotropic thinning behavior and that the added effect of the string structure is negligible.

In conclusion, by using oscillatory superposition spectroscopy, we find no measurable difference in the stress response between the isotropic and string phases. This finding implies that the hydrodynamically dominated high-frequency stress response model for the isotropic suspension can be applied to the confined anisotropic shear-induced structure reported here. Many studies conducted on other systems that also display vorticity-aligned strings suggest pronounced changes in the normal stress difference. It is interesting to ask whether such normal stress differences arise for the hard sphere system we study. Unfortunately, measurements of normal stress difference can not be performed with our current setup. Thus, this question remains unanswered. Nevertheless, the results presented here show that anisotropic structure does not always lead to a measurable anisotropic stress response at the frequency explored. Moreover, they illustrate a powerful approach for elucidating the underlying relationship between anisotropic structure and anisotropic rheology in systems driven far-from-equilibrium.

5.6 Supplementary Information: Plate Alignment and Force Measurement Device Calibration

To align the silicon wafer (top plate) and coverslip (bottom plate), after the sample is loaded in the shear cell we first use the confocal microscope to measure the gap height at the four corners and the center of the gap. Then, we finely adjust three differential screws on the shear cell to minimize the tilt of the top plate. After the differential screws are adjusted, we measure the gap height at the four corners and the center again to examine how parallel the plates are. We continuously perform this alignment process until two plates are aligned with less than 0.0075°. Using the confocal microscope to measure the gap variation during alignment, we find the gap height variation across the plate to be less than 0.5μm, which is close to the optical uncertainty along the vertical-axis (Y-axis) of the confocal microscope. We find that when there is a significant tilt between the two plates, or if one corner is lower than the others, we observe inhomogeneous shear flows. No such flows were observed in the experiments reported here.

To characterize the Force measurement device (FMD) performance, we measure the flow curve of a viscosity standard (VIS-RT5K-600, Paragon Scientific). With the given value of the fluid viscosity and the controlled shear rate, we are able to calculate the corresponding shear stress σ exerted on the FMD. We find linear relations between the applied shear stress and the FMD output signal over the range 0.05 Pa$< \sigma <$2000 Pa for both axes, which determine the sensitivity (0.05 Pa) of the device Fig. 5.7. We also verify this calibration result by hanging weights off the FMD. This weight hanging method enables us to obtain the direct relation between the output signal of FMD and the applied force. We find that both calibrations are in excellent agreement with one another.

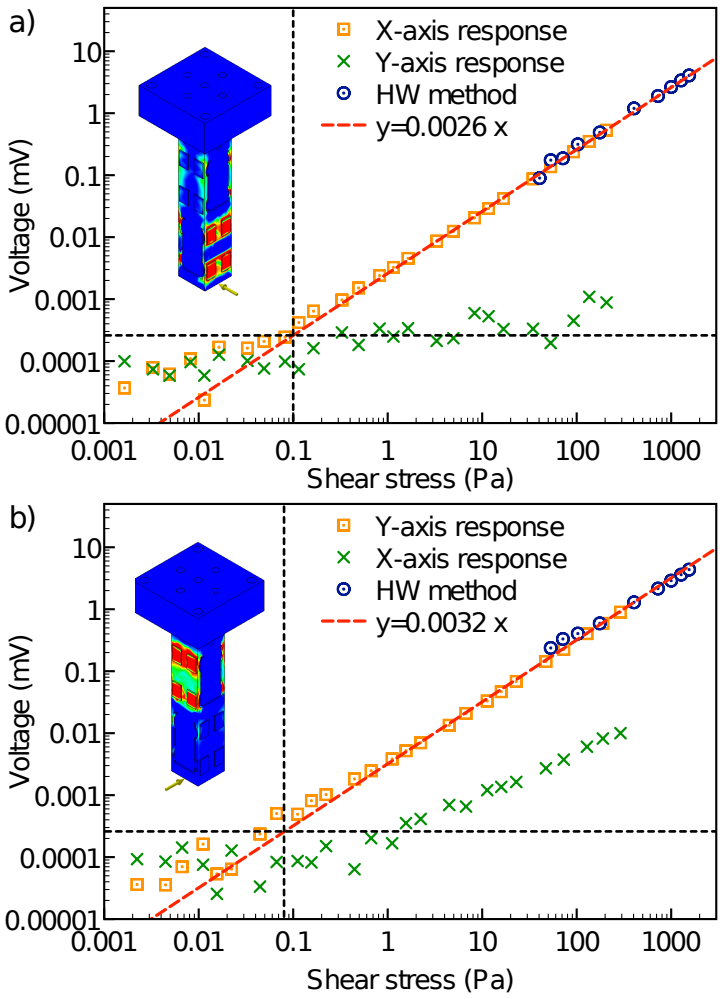

Figure 5.7: The shear stress calibration with shear cell experiment and hanging weight method for X-axis (a) and Y -axis (b). The orange data are the response of the axis that is along the shear flow direction, and the green data represent the response of another axis. The blue data are the voltage response measured with the hanging weight method. The red curves are the linear fit to the data. The schematics of the strained force measurement device are generated by the finite element analysis.

It is important to rule out the possibility that the measured shear stress is affected by other sources of force related to the capillary forces and deformation of the cover slip. To minimize the contribution of the capillary stress we overfill the sample so that the region within the shearzone is in contact with a suspension reservoir. Since the change in fluid boundary length in the reservoir is negligible during shear this force becomes small relative to the shear stress. By measuring the viscosity of simple fluids at various gap heights showing that they are purely viscous and indepenent of gap height, we are able to further rule out the effect of such capillary forces [28]. To determine the deformation of the coverslip we monitored the gap during our shear experiments. We find that the gaps remain constant to within our experimental resolution. We believe that this stability results from the high viscosity of the suspension solvent and the fact that our confocal imaging is conducted for a single height rather than a continuous 3D scan which may tug at the cover slip. Overall, we find that the biaxial FMD, our apparatus, and our experimental procedure allow for accurate measurement of the shear stress response of the suspension.

REFERENCES

[1] G. Yang, J. Kabel, B. Van Rietbergen, A. Odgaard, R. Huiskes, and S. C. Cown, Journal of Elasticity, 1998, **53**, 125-146.

[2] J. J. Hopfdeld, J. Phys. Chem. Solids, 1960, **15**, 97-107.

[3] G. deWit and J. S. Koehler, Phys. Rev., 1959, **116**, 11131120.

[4] A. Rebhan and D. Steineder, Phys. Rev. Lett., 2012, **108**, 021601.

[5] J. Vermant and M. J. Solomon, J. Phys. Condens. Matter, 2005, **17**, 187-216.

[6] R. G. Larson, The Structure and Rheology of Complex Fluids, Oxford University Press, Oxford.

[7] S. Hess, J. F. Schwarzl and D. Baalss, J. Phys.: Condens. Matter, 1990, **2**, SA279.

[8] K. A. Kemp and S. V. Letcher, Phys. Rev. Lett., 1971, **27**, 16341636.

[9] A. Mertelj, A. Re?eti?, S. Gyergyek, D. Makoveca and M. ?opi?ab, Soft Matter, 2011, **7**, 125-131.

[10] J. Gennisson, T. Deffieux, E. Mace, G. Montaldo, M. Fink, and M. Tanter, Ultrasound in Medicine and Biology, 2010, **36**, 789801.

[11] F. Pignon, A. Magnin and J. M. Piau, Phys. Rev. Lett., 1997, **79**, 4689.

[12] C. O. Osuji, D. A. Weitz, Soft Matter, 2008, **4**, 1388-1392.

[13] A. Montesi, A. A. Pea, and M. Pasquali, Phys. Rev. Lett., 2004, **92**, 058303.

[14] E. K. Hobbie, S. Lin-Gibson, H. Wang, J. A. Pathak and H. Kim, Phys. Rev. E, 2004, **69**, 061503.

[15] V. Grenard, N. Taberlet and S. Manneville, Soft Matter, 2011, **7**, 3920-3928.

[16] S. Lin-Gibson, J. A. Pathak, E. A. Grulke, H. Wang, and E. K. Hobbie, Phys. Rev. Lett., 2004, **92**, 048302.

[17] B. Snook, E. Guazzelli, and J. E. Butler, Phys. Fluids, 2012, **24**, 121702.

[18] X. Cheng, X. Xu, S. A. Rice, A. R. Dinner, and I. Cohen, Proc. Natl. Acad. Sci. U. S. A., 2011, **109**, 63-67.

[19] M. Grzelczak, J. Vermant, E. M. Furst, and L. M. Liz-Marzán, ACS nano, 2010, **4**, 3591-3605.

[20] P. Jiang, M. J. McFarland, J. Am. Chem. Soc. 2004, **126**, 13778-13786.

[21] J. Baudry, C. Rouzeau, C. Goubault, C. Robic, L. Cohen-Tannoudji, A. Koenig, E. Bertrand, and J. Bibette, Proc. Natl. Acad. Sci. U. S. A., 2006, **103**, 16076-16078.

[22] R. Pasquino, F. Snijkers, N. Grizzuti, J. Vermant, Rheologica Acta, 2010, **49**, 993-1001.

[23] L. B. Chen, B. J. Ackerson and C. F. Zukoski, J. Rheol., 1994, **38**, 193-216.

[24] B. J. Ackerson, J. Rheol., 1990, **34**, 553-590.

[25] R. Pasquino, F. Snijkers, N. Grizzuti, and J. Vermant, Langmuir, 2010, **26**, 3016-3019.

[26] H. M. Laun, R. Bung, K. Hahn, E. Hädicke, R. Hingmann, F. Schmidt, S. Hess, W. Loose, O. Hess, and P. Lindner, J. Rheol., 1992, **36**, 743-787.

[27] K. M. Schmoller, P. Fernandez, R. C. Arevalo, D. L. Blair, and A. R. Bausch, Nature Communications, 2010, **1**, 134.

[28] X. Cheng, J. H. McCoy, J. N. Israelachvili and I. Cohen, Science, 2011, **333** 1276-1279.

[29] C. Gao, S. D. Kulkarni, J. F. Morris, J. F. Gilchrist, Phys. Rev. E Stat. Nonlin. Soft Matter Phys., (2010), **81**, 041403.

[30] R. Besseling, E. R. Weeks, A. B. Schofield, and W. C. K. Poon, Phys. Rev. Lett., 2007, **99**, 028301.

[31] R. Besseling, L. Isa, P. Ballesta, G. Petekidis, M. E. Cates, and W. C. K. Poon, Phys. Rev. Lett. 2010, **105**, 268301.

[32] C. Mobuchon, P. J. Carreau, M. Heuzey, N. K. Reddy, and J. Vermant, J. Rheol., 2009, **53**, 517.

[33] J. W. Swan, R. Zia, and J. F. Brady, J. Rheol., 2014, **58**, 1.

[34] J. Vermant, L. Walker, P. Moldenaers, J. Mewis, J. Non-Newtonian Fluid Mech., 1998, **79** 173-189.

[35] J. Vermant, P. Moldenaers, J. Mewis, M. Ellis and R. Garritano, Rev. Sci. Instrum., 1997, **68**, 4090-4096.

[36] T. F. F. Farage and J. M. Brader, J. Rheol., 2012, **56**, 259-278.

[37] G. Ovarlez, Q. Barral and P. Coussot, Nat. Materials, 2010 **9** 115119.

[38] L. Zou, Phys. Rev. E, 2010, **81** 031302.

[39] Z. Cheng, J. Zhu, P. M. Chaikin, S. Phan and W. B. Russel, Phys. Rev. E, 2002, **65**, 041405.

[40] C. W. Macosko, Rheology: Principles, Measurements, and Applications (Advances in Interfacial Engineering), Wiley-VCH, New York.

[41] I. Sriram, E. M. Furst, R. J. DePuit, T. M. Squires, J. Rheol., 2009, **53**, 357.

[42] J. M. Brader, J. Phys. Condens. Matter, 2010, **22**, 363101.

[43] X. Xu, S. A. Rice, A. R. Dinner, Proc. Natl. Acad. Sci. U. S. A., 2012, **110**, 3771-3776.

[44] N. J. Wagner and J. F. Brady, Phys. Today, 2009, **62**, 27.

[45] H. M. Laun, Die Angewandte Makromolekulare Chemie, 1984, **123**, 335.

[46] D. Bonn, H. Kellay, H. Tanaka, G. Wegdam, J. Meunier, Langmuir, 1999, **15**, 75347536.

CHAPTER 6

HYDRODYNAMIC AND CONTACT CONTRIBUTIONS TO CONTINUOUS SHEAR THICKENING IN COLLOIDAL SUSPENSIONS[1]

6.1 Abstract

Shear thickening is a widespread phenomenon in suspension flow that, despite sustained study, is still the subject of much debate. The longstanding view that shear thickening is due to hydrodynamic clusters has been challenged by recent theory and simulations suggesting that contact forces dominate, not only in discontinuous, but also in continuous shear thickening. Here, we settle this dispute using shear reversal experiments on micron-sized silica and latex particles to measure directly the hydrodynamic and contact force contributions to shear thickening. We find that contact forces dominate even continuous shear thickening. Computer simulations show that these forces most likely arise from frictional interactions.

6.2 Introduction

Shear thickening, the increase of viscosity with shear rate, is ubiquitous in complex fluids [13, 42, 37, 11]. In particular, it plays a controlling role in the flow of concentrated suspensions of micron-sized particles [24]. Such suspensions occur widely in applications, from ceramics and bullet-proof armor, through cement and

[1]Neil Y.C. Lin, Ben M. Guy, Michiel Hermes, Chris Ness, Jin Sun, Wilson CK Poon, and Itai Cohen. "Hydrodynamic and contact contributions to continuous shear thickening in colloidal suspensions." Physical review letters 115.22 (2015): 228304.

even chocolate. Shear thickening has also become a mainstay of popular science, in the form of running on a pool of corn starch solution.

Despite sustained study, the mechanism of suspension shear thickening is still disputed. A longstanding view is that thickening, especially if it is continuous with shear rate, is predominantly driven by hydrodynamic interactions [5, 8, 42, 37]. In some theories, the increase in viscosity arises directly from enhanced dissipation in the narrow lubrication films between particles [8, 36]; in others, it is caused by the formation of transient particle clusters ("hydroclusters") [40, 5, 42, 37, 5]. In support, experiments have identified putative hydroclusters [13, 25, 32] and found an increase in hydrodynamic stresses during thickening [4, 23, 44].

Recently, contact forces have been shown to mediate a discontinuous jump in viscosity with shear rate in dense suspensions of non-Brownian particles at volume fractions greater than random loose packing $\phi \geq 0.58$ [11, 20, 17, 17, 10, 9]. More controversially, simulations [44, 33] and theories [3, 43] suggest that direct frictional contact can also lead to continuous shear thickening in moderately dense suspensions with $\phi \leq 0.58$. This proposal has not yet gained wide acceptance: conceptually, it seems harder to find a role for such forces without the formation of system-spanning contact networks [11].

6.3 Experiment

Experiments that can dissect the relative contributions of hydrodynamics and contact stresses can settle this issue definitively. Here, we demonstrate that shear reversal techniques, pioneered by Gadala-Maria *et al.* [22, 28], can distinguish the relative contributions of these stresses in non-inertial shear thickening systems.

The basic idea is simple but powerful: immediately upon shear reversal, instantaneous contact stresses vanish, but hydrodynamic stresses remain because of Stokes flow reversibility. Thus, monitoring time-dependent stresses after reversal will reveal the relative roles of these two interactions in thickening.

We do so in two canonical shear thickening systems: charge-stabilized silica (Seikisui Chemical) with diameter 2.0 μm suspended in a mixture of glycerol and water (viscosity $\eta_0 = 0.98$ Pa.s at 20°C) at volume fraction $\phi = 0.49$, and polymethylmethacrylate (PMMA) particles with diameter 1.4 μm sterically stabilized with poly-dimethyl-diphenyl siloxane (PDV-2335, Gelest) with chain length ≈ 50 nm [27] suspended in PDV-2331 (Gelest, viscosity $\eta_0 = 1.78$ Pa.s at 20°C) at $\phi = 0.51$. The high solvent viscosities ensure that particle inertia is negligible at the shear rates we study (see Supplemental Information [2]).

Shear reversal measurements were performed in an ARES strain-controlled rheometer (Rheometric Scientific) with roughened cone-plate geometry (25 mm, 0.1 rad) modified with a DAQ directly connected to the analogue output of the stress and strain sensors [16]. Directly measuring the output of these sensors bypasses signal processing that hinders the instantaneous measurement of the system's short-time response.

6.4 Results

In our protocol, figure 6.1(a), a positive shear rate $\dot{\gamma}$ is imposed until the accumulated strain γ reaches 10, after which the shear is reversed and a negative shear rate is imposed to accumulate the same amount of strain. Just before shear rever-

[2]See Supplemental Material [url], which includes Refs. [35-43]

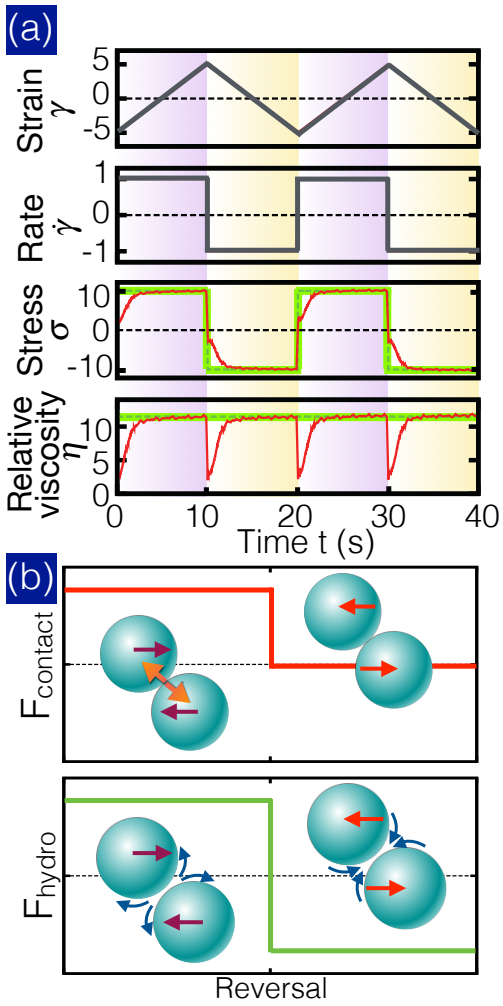

Figure 6.1: (a) Schematic of our shear reversal protocol. The applied strain γ is a triangle wave with peak-to-peak amplitude of 10. The applied strain rate $\dot{\gamma}(t)$ is a square wave whose amplitude we vary in our experiments. The instantaneous stress response, σ, of a viscous fluid and a contact-dominated fluid are shown in the green and red, respectively. (The same color scheme applies throughout all parts of this figure.) The instantaneous relative viscosity $\eta(t) = \sigma(t)/(\dot{\gamma}(t)\eta_0)$. (b) Schematic illustrating the difference between hydrodynamic forces, which stay the same in magnitude immediately upon reversal, and contact forces, which drop to zero immediately upon reversal.

sal, the suspension is in a steady state. Immediately upon reversal, the structure is unchanged, so that hydrodynamic forces will remain identical in magnitude but reversed in direction. In contrast, contact forces in hard-sphere systems will drop

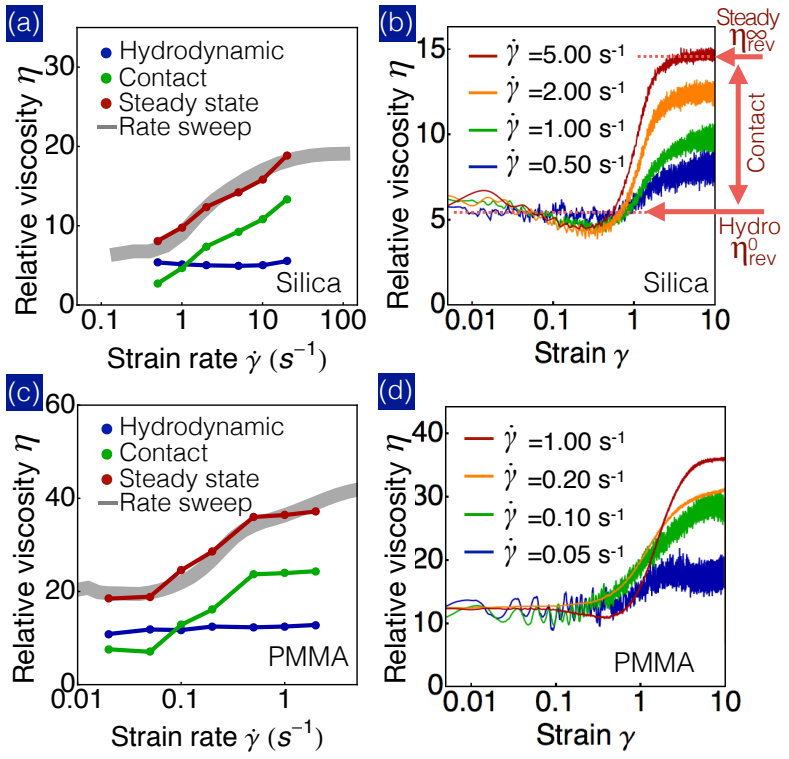

Figure 6.2: Relative viscosity, η, *vs* strain rate, $\dot{\gamma}$, for the (a) silica and (b) PMMA suspensions. Shown are rate sweep measurements (thick grey line), steady state relative viscosities from flow reversal (red) decomposed into contributions from hydrodynamic (blue) and contact (green) interactions. (b) and (d): Instantaneous relative viscosity after shear reversal, $\eta_{rev}(\gamma) = \sigma(\gamma)/(\dot{\gamma}\eta_0)$, *vs* strain, γ, at different applied $\dot{\gamma}$. The hydrodynamic component of the relative viscosity, η^0_{rev}, is taken to be the average of the relative viscosity over the range $0.01 < \gamma < 0.2$. The contact component is taken to be the difference between the steady state value at $\gamma = 10$, η^{∞}_{rev}, and η^0_{rev}.

to zero immediately after reversal, figure 6.1(b). This qualitative difference between these two forces allows us to disentangle their separate contributions by measuring the transient stress upon reversal. Figure 6.1(a) illustrates schematically the instantaneous relative viscosity $\eta(t) = \sigma(t)/(\dot{\gamma}(t)\eta_0)$ as a function of time (or, equivalently, accumulated strain) of a purely Newtonian fluid (green line) and the response where contact forces contribute to the total stress (red line). (See Supplemental Information for calibration [**?**].)

A rate-sweep measurement of the charge-stabilized silica suspension gives its flow curve, $\eta(\dot{\gamma})$, figure 6.2(a) (thick grey line), which shows shear thickening at $\dot{\gamma} \geq 0.3$ s^{-1}. Next, we monitor the viscosity after shear reversal, $\eta_{\rm rev}$, as a function of accumulated strain after reversal, γ, at four representative shear rates $\dot{\gamma} = 0.50, 1.00, 2.00$ and 5.00 s^{-1}, in the shear thickening regime, figure 6.2(b). Immediately before reversal, η has a value (not shown) equal to that measured in the steady state ($\gamma = 10$). The viscosity immediately after reversal drops to a value, $\eta^0_{\rm rev}$, that remains constant, to within experimental error, until $\gamma \geq 0.1$. We take $\eta^0_{\rm rev}$ to be the hydrodynamic contribution to the total steady-state viscosity. From $\gamma \approx 0.3$, $\eta_{\rm rev}$ rises, reaching a steady-state value, $\eta^\infty_{\rm rev}$, that is the same as the steady-state viscosity before reversal. We take $\eta^\infty_{\rm rev} - \eta^0_{\rm rev}$ to be the contact contribution.

The hydrodynamic and contact contributions to the total viscosity so obtained are plotted as a function of $\dot{\gamma}$ in figure 6.2(a). Strikingly, while the contact contribution increases with $\dot{\gamma}$, the hydrodynamic contribution remains constant as the suspension shear thickens. This demonstrates the essential role played by contact forces in the continuous shear thickening of this silica suspension.

Contact forces depend sensitively on the nature of particle surfaces. We therefore repeated our experiments using a PMMA suspension. In contrast to our silica particles, which are charge stabilized, these PMMA particles are stabilized by (neutral) surface 'hairs'. Our $\phi = 0.51$ PMMA suspension shear thickens more readily, at $\dot{\gamma} \approx 0.05$ s^{-1}, figure 6.2(c). Again using shear-reversal to measure $\eta_{\rm rev}$, figure 6.2(d), and analyzing the data in the same way to obtain the hydrodynamic and contact contributions, figure 6.2(c), we find essentially the same pattern of behavior already uncovered for the $\phi = 0.49$ silica suspension. Thus, contact forces

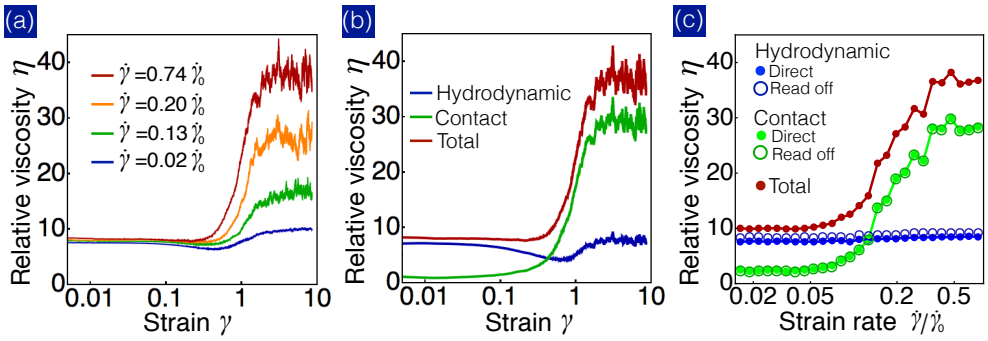

Figure 6.3: Critical load model simulations of particles with hydrodynamic and frictional interactions. (a) Relative viscosity $\eta(\gamma)$ versus strain γ at four different shear rates (given in the legend, see text for the definition of $\dot{\gamma}_0$); compare experimental results in figure 6.2(b) and (d). (b) Directly-calculated hydrodynamic and contact contributions to the total viscosity as functions of the accumulated strain after reversal for the case of $\dot{\gamma} = 0.74\dot{\gamma}_0$. (c) The total viscosity as a function of shear rate, and its decomposition into hydrodynamic and contact contributions done in two ways: directly calculated from simulations, and 'read off' the data shown in part (a) in the same way as the experimental data is analyzed into these contributions, for which see figure 6.2(b).

also dominate the continuous shear thickening in this sterically-stabilized system.

To validate this interpretation, and to probe the nature of these contact forces, we conducted computer simulations of repulsive spheres (radius a) in which the short-range lubrication and repulsive contact forces were mimicked using a previously-established critical load model [44], implemented in a classical discrete element method code (details of which are identical to those in [32]; also, see Supplemental Information [**?**]). In this model, frictional interactions appear beyond a critical normal force between particles, F^{CL}, which also sets a shear rate scale, $\dot{\gamma}_0 = F^{CL}/(6\pi\eta_0 a^2)$. We explored shear reversal at $\phi = 0.51$.

The observed evolution of the viscosity with accumulated strain after reversal, figure 6.3(a), is qualitatively similar to experiments. In the simulations, however, we can follow the hydrodynamic and contact contributions as a function of accu-

mulated reversed strain by direct evaluation; figure 6.3(b) shows the results for $\dot{\gamma} = 0.74\dot{\gamma}_0$. Consistent with the interpretation we have offered for our experimental data, the contact contribution drops essentially to zero immediately after reversal, and only increases back to its steady-state magnitude after an accumulated stain of order unity. By contrast, the hydrodynamic contribution remains more or less constant.

We cannot access directly the hydrodynamic and contact stresses in our experiments. Instead, we have to 'read off' these contributions to the reversed viscosity from the data as η^0_{rev} and $\eta^\infty_{\text{rev}} - \eta^0_{\text{rev}}$, respectively, figure 6.2(b). We validate this procedure using simulations. First, we 'read off' the hydrodynamic and contact contributions to the reversed viscosity data, figure 6.3(a), in exactly the same way as in experiments, giving results, figure 6.3(c), analogous to the experimental data shown in figure 6.2(a) and (c). Secondly, we evaluated these contributions directly from the raw simulation data, and overlaid the results in the same graph, figure 6.3(c). The near identity of the two sets of results validates our identification of η^0_{rev} and $\eta^\infty_{\text{rev}} - \eta^0_{\text{rev}}$ with the hydrodynamic and contact contributions, respectively. Thus, simulations confirm the key role played by contact forces in continuous shear thickening.

Traditionally, shear thickening is supposed to occur beyond a critical onset strain rate [2]. Recent theories, simulations and experiments [44, 33, 36, 43, 24] suggest that, instead, the phenomenon appears at a critical onset shear stress. Indeed, this assumption has been built into the critical load model used in our simulations. To explore the role of stress in the onset of shear thickening, we performed rate sweep measurements in our two systems at different temperatures, T, to change the solvent viscosity, $\eta_0(T)$, over an order of magnitude.

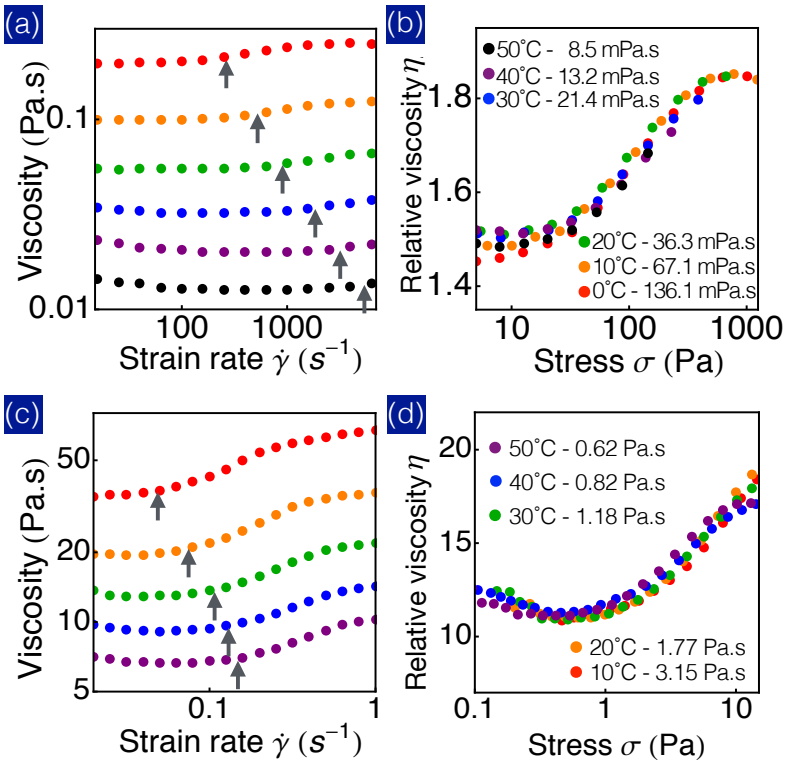

Figure 6.4: Scaling of the relative viscosity with shear stress. (a) and (c): Viscosity versus shear rate for silica ($\phi = 0.43$) and PMMA ($\phi = 0.46$) suspensions at different temperatures. Solvent viscosities and temperatures are as labeled in (b) and (d) (for silica, we used a different solvent composition to figure 6.1; see Supplementary Information [**?**]). Due to the temperature dependence of the solvent viscosity the initial suspension viscosity and onset strain rate (arrows) of the thickening are substantially altered. (b,d) Relative viscosity *vs* stress showing collapse of the thickening data onto a master curve.

We find that as the solvent viscosity varies, the onset of thickening (dashed lines in figure 6.4(a) and (c)) occurs at different strain rates for both of our suspensions. Thus, in the silica suspension, figure 6.4(a), the highest solvent viscosity (lowest temperature) data set shows shear thickening at $\dot{\gamma} \geq 200$ s^{-1}, but this onset progressively moves to higher rates as we lower the solvent viscosity, until in the lowest viscosity data set, we barely see thickening over our range of shear rates, but observe a small degree of shear thinning instead. Similarly, in the PMMA suspension, figure 6.4(c), we see the onset of thickening at around 0.05 s^{-1} in the

highest viscosity data set; this onset also moves to higher shear rates as the solvent viscosity decreases.

Each of these two data sets, however, can be scaled onto a master curve if we plot the relative viscosity $\eta(\dot{\gamma}) = \sigma/(\dot{\gamma}\eta_0(T))$ against the shear stress σ [3]. The master curve for the silica particles, figure 6.4(b), indeed shows a single onset stress at ≈ 10 Pa, while that for the PMMA system, figure 6.4(d), shows an onset stress at ≈ 1 Pa. Thus, in both systems, our experiments show that shear thickening occurs above a critical stress. The difference in the magnitude of the onset stress of the two suspensions is consistent with the expectation that the load needed to press particles into contact should be sensitive to details of the stabilization mechanism [20].

6.5 Discussion and conclusion

So far, we have not considered the effect of Brownian motion in our systems – it has been suggested that residual Brownian motion influences the flow behavior even at the high Peclet numbers ($\sim 10^3$ at the onset of shear thickening) investigated here[8]. However, recent simulations [35] that further incorporate the Brownian motion have shown that shear thickening is still predominantly driven by an increase in contact forces. The quantitative agreement between our experiments and simulations, in which there is strictly no Brownian motion, suggests that thermal motion of the particles does not play a large role in suspension thickening.

Our observation of contact-driven shear thickening contradicts the conclusions

[3] This is in contrast to confined, sedimenting granular systems under oscillatory shear, where the severity of shear thickening is found to vary with η_0; Q. Xu, S. Majumdar, E. Brown, and H. M. Jaeger, Euro. Phys. Lett. **107**, 680004 (2014).

drawn from rheo-SANS [23] and scattering dichroism measurements [4] data on other colloidal systems. The rheo-SANS data provides an approximation of the hydrodynamic stresses through a non-trivial analysis of the structural anisotropy in the suspension. However, even the latest rheo-SANS measurements show thickening that is only a small fraction of that observed in rheometry [23]. In the scattering dichroism measurements, the total suspension viscosity, η, and the viscosity contribution from Brownian stresses, η_B, can be measured independently. The authors found that the contribution to the viscosity from other stresses, $\eta - \eta_B$, increased upon shear thickening, and attributed this to an increase in hydrodynamic stresses [4]. However, the remaining viscosity may in fact be dominated by contact contributions, an interpretation that is in alignment with results from dense non-Brownian suspensions [30] as well as the data presented in the current work.

To conclude, we have used shear reversal to show that, for two canonical colloidal suspensions, continuous shear thickening does not originate from hydrodynamic interactions but from the formation of particle contacts. The onset of contact formation, and thus shear thickening, is found to occur above a critical stress whose value is sensitive to whether the particles are charge- or sterically-stabilized. Further work is needed to establish whether shear thickening of nanoparticles, for which Brownian stresses are not negligible, is also driven by contact formation; this should be possible with shear reversal.

While shear reversal alone provides no *a priori* information about the nature of the interactions between contacting particles, the quantitative agreement between the experimental and simulation viscosity response after reversal, figure 2(b), (d) and 3(a), strongly suggests that static friction is present. Indeed, evidence for

frictional contacts was recently found in a similar model system [24]. A careful study of the effect of particle surface properties – specifically surface roughness – on suspension rheology would be required to validate this claim, which in turn motivates the need for robust measurements of particle friction.

6.6 Acknowledgements

The data in this article are available online at http://dx.doi.org/10.7488/ds/324. We thank Gareth McKinley for use of his modified ARES rheometer, John Brady and Mike Cates for fruitful discussions of the shear reversal method, the Cohen group for helpful inputs and Andy Schofield for synthesizing PMMA particles. The Cornell work was supported by NSF CBET-PMP Award No. 1232666 and continued support from NSF CBET-PMP Award No. 1509308. BMG and CN held EPSRC CASE studentships with Johnson Matthey. MH and WCKP were funded by EPSRC grant EP/J007404/1.

6.7 Supplementary Information

6.7.1 Instrumentation characterization

It is challenging to resolve the instantaneous stress response of a shear thickened sample during reversal. The reason is that shear thickening usually occurs at high shear rates, and we are interested in the behaviour immediately (preferably $\gamma < 0.01$) after reversal. For example, if the onset shear rate is $\sim 10\,\mathrm{s}^{-1}$, which is typical for the most colloidal samples studied in the literature, a temporal resolution of

1 ms is required to resolve the stress response with 0.01 shear strain resolution. There are two reasons that it is difficult to measure the stress 1 ms after reversal. The first one is that the instantaneous jump in rate often results in vibrations (inertial ringing) of the geometry, this needs to be damped out before the stress measurements can be made. The second problem is that the stress at the reversal point discontinuously jumps as it changes sign, so to measure something after this jump we need to ensure that the response time is short and that no (high frequency) filtering takes place, since this would smooth out the jump and affect our measurement. For these two reasons, as well as the signal to noise ratio of the transducers, it is difficult to measure the stress less then ~ 10 ms after reversal. We get around these problems by lowering the onset shear rate of shear thickening. To do this we disperse our micron-sized silica and latex particles in solvents that have high viscosities. This works because the onset shear stress of shear thickening is determined by the stabilization mechanism and the particle size and does not depend on the solvent viscosity. These highly viscous base fluids allow particles to exert large interparticle stresses at a much lower and experimentally-accessible shear rates. For example, for the silica dispersed in a viscous mixture of glycerol and water the onset rate $\dot{\gamma}_{\text{onset}} = 1\ \text{s}^{-1}$ this allows us to access a minimum strain of ~ 0.01. Furthermore by using relatively small particles we ensure that the onset stress is high so that we have a relatively high stress and thus a good signal to noise ratio. An additional advantage is that sedimentation is much slower due to both the viscous solvents and the small particles.

To confirm that the rheometers measure an accurate stress after reversal we test two representative models of true strain-controlled rheometers and report their performances for the reversal rheology of a Newtonian liquid. Fig. 6.5a and b show the measured viscosities of a viscosity standard (CANNON N350) for ARES-G2

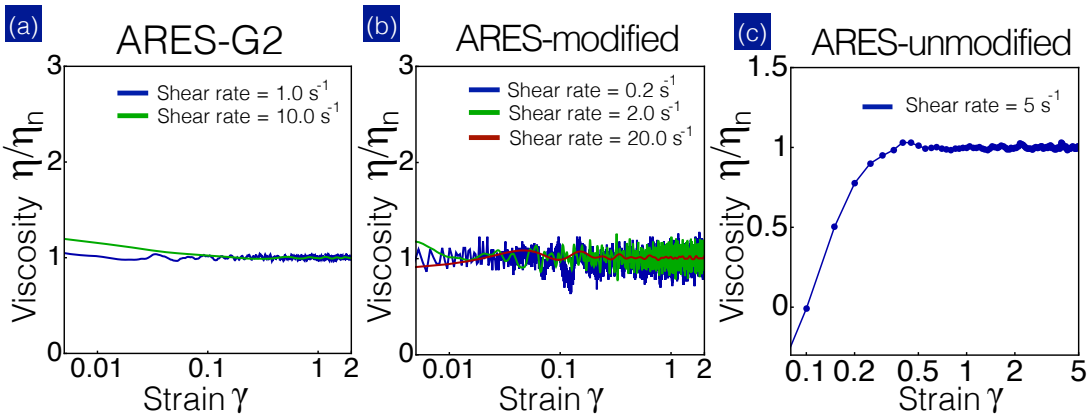

Figure 6.5: **Reversal curves for different instruments of a Newtonian viscosity standard.** The viscosity measured after reversal (at $t = 0$) of a Newtonian fluid (CANNON N350) with a viscosity of 1 Pa $\cdot$ s. We normalize the apparent viscosity η by the nominal viscosity η_n of the tested sample for better comparison. We show (a) data from TA Instrument ARES-G2; (b) raw data from our modified Rheometric Scientific ARES and (c) filtered data from the ARES.

and ARES, respectively. Overall, both strain-controlled rheometers demonstrate consistent calibration results, where the viscosity immediately after the reversal closely reproduces the steady state value. In the current work, we perform the shear reversal experiments on the modified ARES. Specifically, we collect the data by directly wiring the stress and strain analog outputs to a Data Acquisition Device (DAQ). By doing so we bypass all electronic and digital filters and directly record the unfiltered stress and strain responses, preventing any time delay or alteration of data arising from the filtering procedures. We also show the filtered data to illustrate the instrumental time delay in Fig. 6.5c. The time delay is ~ 0.1 s for all $\dot{\gamma}$; here we only show the response for $\dot{\gamma} = 5$ s^{-1}. A comprehensive discussion of the effect of filtering on the measured transient stress during rapid changes in $\dot{\gamma}$ can be found in ref. [15, 31].

To further characterize the response time of our modified ARES, we measure the instantaneous stress response of a silica suspension during shear reversal at

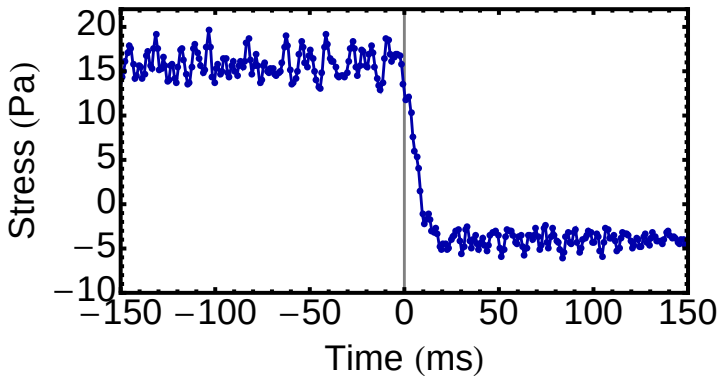

Figure 6.6: Shear stress versus time t for the silica suspension during shear reversal at $\dot{\gamma} = 0.5$ s^{-1} measured using the modified ARES; the direction of shear is reversed at $t = 0$. The response time of the instrument is ≈ 20 ms. The difference between the magnitude of the stress before reversal (+15 Pa) and after reversal (-5 Pa) arises from the contact force between particles.

$\dot{\gamma} = 0.5$ s^{-1}, and plot the stress value versus time t (reversal occurs at $t = 0$) In Fig. 6.6. The minimum time we can reliably access after reversal is ≈ 20 ms, which is independent of shear rate up to $\dot{\gamma} = 20$ s^{-1}, higher than the maximum $\dot{\gamma}$ probed in this work.

6.7.2 Sample preparation and characterization

Silica suspension – shear reversal

The volume fraction of the silica suspension is controlled by calculating the corresponding weight ratio between particles and glycerol. The colloidal silica density 2.15 g/cm^3 is determined by the manufacturer using the multi-volume method. For a $\phi = 0.48$ suspension that contains 2.00 g silica particles, we add 1.22 g of glycerol to the sample to reach the desired volume fraction. We also add approximately 0.1 g of ethanol to thin the sample and make dispersing particles easier. The sample

is then rigorously vortexed and sonicated to avoid any agglomeration. Since the particles have a high density and low porosity, they contain a negligible amount of water at room temperature. Therefore, the measured weight of the dry powder is very close to the its true net weight. After the particles are fully dispersed, the sample is left in a vacuum oven (temperature at 25 °C) overnight to evaporate all water and ethanol. To understand the details of this evaporation process, we also test the evaporation rates of ethanol, water and glycerol in the same sample vials. We found that while the evaporation rate of ethanol and water are 162, and 88 mg/hr, respectively under the pressure of 25 torr, glycerol's evaporation rate is < 1 mg/hr (below the precision scale resolution). The large evaporation rate ratio between ethanol and glycerol confirms that our vacuum pumping procedure is able to effectively eliminate the ethanol and water content in the sample while preserving the suspension's volume fraction.

After the ethanol and water are pumped out, the sample is then placed and stored at standard temperature and pressure for a week prior to any experiments, so the hygroscopic glycerol is able to reach a steady state. In addition, we place a freshly opened glycerol sample in a similar environment for the same amount of time, and measure its final glycerol/water ratio and viscosity. The glycerol/water ratio is 98.5% (by refractometer), and the viscosity is 980 mPa.s. During the experiments, since the sample is already stable, we do not observe any rheological change over time. Finally, we find a good agreement between our silica sample's flow curve (Fig. 2(a) of main manuscript) and previous measurements [29]. This good agreement implies that we are able to accurately control the volume fraction using this method.

Silica suspension – temperature dependence

While it is possible to maintain the low water/glycerol ratio and viscosity of our nearly-pure glycerol solvent (98.5%) at a fixed temperature, it is known that the glycerol's water absorption is highly dependent on the temperature. Therefore, in the temperature dependence experiment we use a 20/80 (by weight) water/glycerol mixture for the suspension solvent to avoid any effect from hygroscopicity. By using this solvent we do not need to apply any mineral oil to hermetically seal the sample during the experiment. In addition, the refractive index of this water/glycerol mixture matches the silica spheres, and enables us to directly examine the sample's volume fraction under our confocal microscope.

PMMA suspension

The PMMA particles were synthesised with the method described in [27]. After the synthesis the particles are washed (at least 4 times) in hexane. The particles are then dispersed in vinyl terminated poly(22-25% diphenylsiloxane)(75-78% dimethylsiloxane) copolymer (Gelest, PDV-2331, density 1.05 g/ml) by adding this solvent to the particles dispersed in hexane. The hexane is then evaporated by leaving the sample in the fume cupboard for several weeks. The mass fraction is determined by drying a small fraction of the sample from hexane before dispersing in PDV-2331. The mass fraction is then converted to a volume fraction by assuming a particle density of 1.18 g/ml.

It has been shown that that non-Newtonian nature of some solvents can affect the interactions between particles [37]. In the case of a non Newtonian solvent, the local flow around the particles can be much more complicated than expected.

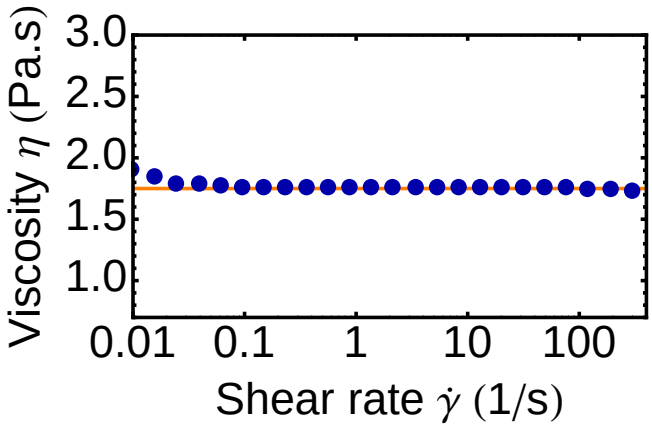

Figure 6.7: **Rate sweep of PDV-2331** The viscosity of PDV-2331 is plotted versus shear rate at temperature 20°C. The slight shear thinning behavior at small share rates might be because the stress signal reaches the instrumentation sensitivity. The horizontal orange line indicates a viscosity = 1.75 Pa.s.

Therefore, it is important to characterize the flow behavior of the suspending medium. The water-glycerol mixtures are Newtonian at the shear rates used. To prove that the solvent for the PMMA particles is also Newtonian at the shear rates we use, we plot the viscosity of the PDV-2331 polymer as a function of shear rate in Fig. 6.7. We find a nearly perfect Newtonian behavior over almost five decades of shear rate, including the rates used in the reversal experiments. The solvent viscosity remains approximately 1.76 Pa·s except for a very weak shear thinning at either end of the regime $\dot{\gamma} < 10^{-1}$ s^{-1} and $\dot{\gamma} > 10^{2}$ s^{-1}. We expect this weak rate-dependence will not influence the behaviour of our system at the shear rates probed.

6.7.3 Surface roughness of silica particles

We use a Scanning electron microscope (LEO 1550 FESEM) to image our particle surface, and show the micrographs in Fig. 6.8 (a) and (b). These micrographs

clearly show fluctuations in height that were determined, through Atomic force microscopy (Veeco Dimension 3100 Ambient AFM STM), to be approximately 2 nm in height, which is about 10^{-3} particle diameter Fig. 6.8 (c).

6.7.4 Effects of particle inertia

We emphasize that the shear thickening we observe in figure 1a and c of the main text is distinct from the inertial thickening reported for particles with diameter ≥ 10 μm in low-viscosity solvents [20, 18]. Evidence that our system behaves non-inertially comes from the viscous scaling of the suspension viscosity in the shear thickening regime in figure 4 of the main text, i.e., the suspension viscosity is proportional to the solvent viscosity η_0. This in turn implies that the shear stress scales as $\sigma \sim \eta_0 \dot{\gamma}$, which is consistent with the flow of hard, non-Brownian particles at low Reynolds number [30, 10]. If the shear thickening regime corresponded to fully-established inertial flow then the shear stress would scale as $\sigma \sim \rho_p d^2 \dot{\gamma}^2$, where ρ_p is the particle density and d is the diameter, which does not depend on η_0. In that case, dividing by η_0 would not collapse data for different solvent viscosities.

6.7.5 Simulation method

We assume that long range hydrodynamic interactions are negligible in very dense suspensions, and resolve only the leading terms of the fluid resistance matrix [4, 1]. For an interaction between neighboring particles i and j, the force and torque on

particle i are obtained from lubrication theory and can be expressed as

$$\begin{aligned}\mathbf{F}^l_{ij} = &-a_{sq}6\pi\eta_f(\mathbf{v}_i - \mathbf{v}_j)\cdot\mathbf{n}_{ij}\mathbf{n}_{ij} \\ &-a_{sh}6\pi\eta_f(\mathbf{v}_i - \mathbf{v}_j) \cdot (\mathbf{I} - \mathbf{n}_{ij}\mathbf{n}_{ij}),\end{aligned} \tag{6.1}$$

$$\begin{aligned}\mathbf{\Gamma}^l_{ij} = -a_{pu}\pi\eta_f d_i^3(\boldsymbol{\omega}_i - \boldsymbol{\omega}_j)\cdot(\mathbf{I} &- \mathbf{n}_{ij}\mathbf{n}_{ij}) \\ &- \frac{d_i}{2}\left(\mathbf{n}_{ij}\times\mathbf{F}^l_{ij}\right).\end{aligned} \tag{6.2}$$

for particle diameter d_i, fluid viscosity η_f, particle translational and rotational velocity vectors $\mathbf{v}_i$ and $\boldsymbol{\omega}_i$ respectively, centre-to-centre unit vector $\mathbf{n}_{ij}$ and identity tensor $\mathbf{I}$, with the squeeze a_{sq}, shear a_{sh} and pump a_{pu} resistance terms as derived by [24], for $\beta = r_j/r_i$, as:

$$a_{sq} = \frac{\beta^2}{(1+\beta)^2}\frac{d_i}{2h} + \frac{1+7\beta+\beta^2}{5(1+\beta)^3}\frac{d_i}{2}\ln\left(\frac{d_i}{2h}\right) + \frac{1+18\beta-29\beta^2+18\beta^3+\beta^4}{21(1+\beta)^4}\frac{d_i^2}{4h}\ln\left(\frac{d_i}{2h}\right),$$

$$a_{sh} = 4\beta\frac{2+\beta+2\beta^2}{15(1+\beta)^3}\frac{d_i}{2}\ln\left(\frac{d_i}{2h}\right) + 4\frac{16-45\beta+58\beta^2-45\beta^3+16\beta^4}{375(1+\beta)^4}\frac{d_i^2}{4h}\ln\left(\frac{d_i}{2h}\right),$$

$$a_{pu} = \beta\frac{4+\beta}{10(1+\beta)^2}\ln\left(\frac{d_i}{2h}\right)\frac{32-33\beta+83\beta^2+43\beta^3}{250\beta^3}\frac{d_i}{2h}\ln\left(\frac{d_i}{2h}\right).$$

A linear spring model [12] is used to capture direct particle-particle contacts. Each pairwise contact is characterised by an overlap length δ (typically of the order 10^{-5} particle diameters) and a tangential displacement vector $\mathbf{u}_{\mathrm{ij}}$, which are used to calculate the normal ($\mathbf{F}^{c,n}$) and tangential ($\mathbf{F}^{c,t}$) force and torque $\mathbf{\Gamma}^c$

$$\mathbf{F}^{c,n}_{ij} = k_{\mathrm{n}}\delta\mathbf{n}_{\mathrm{ij}}, \tag{6.3a}$$

$$\mathbf{F}^{c,t}_{ij} = -k_{\mathrm{t}}\mathbf{u}_{\mathrm{ij}}, \tag{6.3b}$$

$$\mathbf{\Gamma}^c_{ij} = -\frac{d_i}{2}(\mathbf{n}_{ij}\times\mathbf{F}^{c,t}_{ij}), \tag{6.3c}$$

for a collision between particles i and j with normal and tangential spring stiffnesses k_n and k_t respectively.

A further length scale is incorporated into the model to account for a repulsive potential that inhibits direct particle contacts. In this case, we employ the Critical Load Model proposed by [44, 30]. We regulate the tangential force that may be exerted during a direct particle-particle collision using a Coulomb friction coefficient μ_p, defined according to $|\mathbf{F}_{i,j}^{c,t}| \leq \mu_p |\mathbf{F}_{i,j}^{c,n}|$. For each collision, μ_p is dependent upon the normal force and a critical normal force F^{CL} such that

$$\mu_p = \begin{cases} 1 & \text{for } |\mathbf{F}_{i,j}^{c,n}| > F^{CL} \\ 0 & \text{otherwise.} \end{cases} \tag{6.4}$$

Contacts for which the normal force is small are frictionless, while those for which the normal force is large are frictional. Particle velocities and positions are updated each timestep using a Velocity-Verlet algorithm implemented in the discrete element method solver LAMMPS [40].

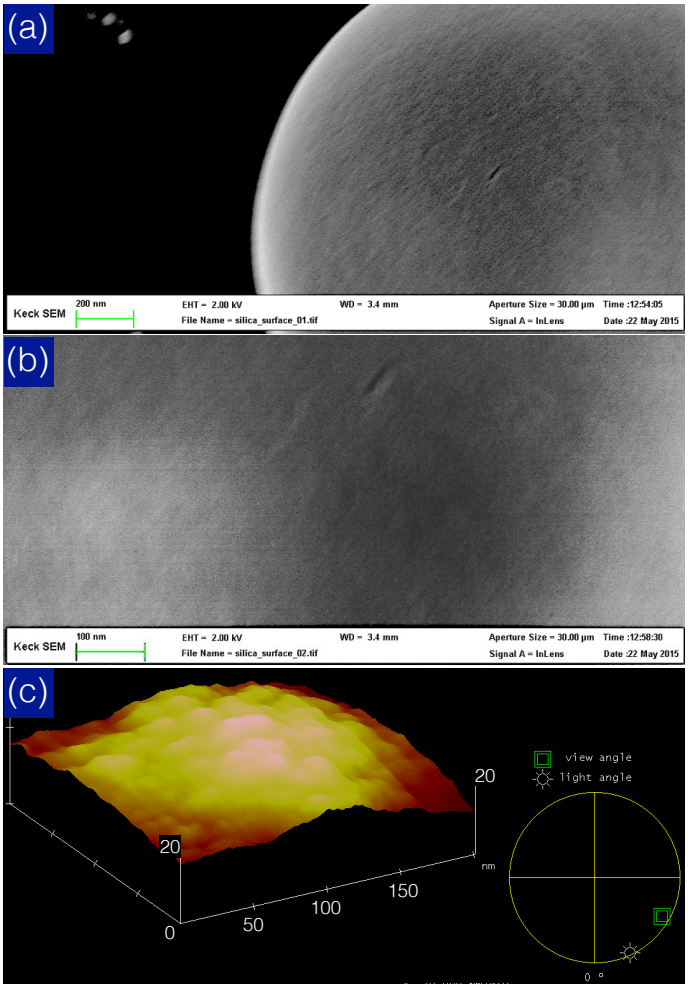

Figure 6.8: **SEM and AFM images of silica sphere surface** (a,b) SEM micrographs of the 2 μm-sized silica surfaces. These SEM images show that the silica spheres have uneven surfaces. To confirm the textures observed are not artifacts due to electron beam noise or surface charge accumulation, we rotate the beam 90° and observe the same features but oriented 90°. (c) We use an AFM to map the surface topography of the same silica sample. The scanning field is 200 nm $\times$ 200 nm, which corresponds to a $\sim$ 5 nm height difference between the positions at the image center and corners. We find that the surface roughness is $\sim$ 2 nm. A larger field scan is prohibited by the unreasonable tapping amplitude of the probe due to the sudden height drop near the particle edge.

REFERENCES

[1] R C Ball and John R Melrose. A simulation technique for many spheres in quasi-static motion under frame-invariant pair drag and Brownian forces. *Physica A Statistical and Theoretical Physics*, 247(1-4):444–472, 1997.

[2] H. A.. Barnes. Shear thickening (dilatancy) in suspensions of nonaggregating solid particles dispersed in newtonian liquids. *J. Rheol.*, 33:329–366, 1989.

[3] I. a. Bashkirtseva, a. Yu. Zubarev, L. Yu. Iskakova, and L. B. Ryashko. On rheophysics of high-concentrated suspensions. *Colloid Journal*, 71(4):446–454, August 2009.

[4] Jonathan Bender and Norman J. Wagner. Reversible shear thickening in monodisperse and bidisperse colloidal dispersions. *Journal of Rheology*, 40(5):899–916, September 1996.

[5] G. Bossis and J. F. Brady. The rheology of Brownian suspensions. *J. Chem. Phys.*, 91(3):1866, 1989.

[6] J F Brady and G Bossis. Stokesian Dynamics. *Annual Review of Fluid Mechanics*, 20(1):111–157, January 1988.

[7] John F Brady and Georges Bossis. The rheology of concentrated suspensions of spheres in simple shear flow by numerical simulation. *Journal of Fluid Mechanics*, 155:105–129, 1985.

[8] John F. Brady and Jeffrey F. Morris. Microstructure of strongly sheared suspensions and its impact on rheology and diffusion. *Journal of Fluid Mechanics*, 348:103–139, October 1997.

[9] Eric Brown, Nicole A Forman, Carlos S Orellana, Hanjun Zhang, Benjamin W Maynor, Douglas E Betts, Joseph M DeSimone, and Heinrich M Jaeger. Generality of shear thickening in dense suspensions. *Nature materials*, 9(3):220–224, 2010.

[10] Eric Brown and Heinrich M Jaeger. Dynamic jamming point for shear thickening suspensions. *Physical Review Letters*, 103(8):086001, 2009.

[11] Eric Brown and Heinrich M. Jaeger. Shear thickening in concentrated suspensions: phenomenology, mechanisms and relations to jamming. *Reports on Progress in Physics*, 77(4):046602, April 2014.

[12] Michael E. Cates and Matthieu Wyart. Granulation and bistability in non-brownian suspensions. *Rheologica Acta*, 53(10):755–764, 2014.

[13] Xiang Cheng, Jonathan H. McCoy, Jacob N. Israelachvili, and Itai Cohen. Imaging the Microscopic Structure of Shear Thinning and Thickening Colloidal Suspensions. *Science*, 333(6047):1276–1279, February 2011.

[14] P A Cundall and O D L Strack. A discrete numerical model for granular assemblies. *Géotechnique*, 29(1):47–65, 1979.

[15] K Dullaert and J Mewis. Stress jumps on weakly flocculated dispersions: steady state and transient results. *J. Colloid Interface Sci.*, 287(2):542–51, July 2005.

[16] Konraad Dullaert and Jan Mewis. Thixotropy: Build-up and breakdown curves during flow. *Journal of Rheology (1978-present)*, 49(6):1213–1230, 2005.

[17] A Fall, F Bertrand, D Hautemayou, C Mezière, P Moucheront, A Lemaître, and G Ovarlez. Macroscopic discontinuous shear thickening versus local shear jamming in cornstarch. *Physical review letters*, 114(9):098301, 2015.

[18] Abdoulaye Fall, N Huang, François Bertrand, G Ovarlez, and Daniel Bonn. Shear thickening of cornstarch suspensions as a reentrant jamming transition. *Physical Review Letters*, 100(1):018301, 2008.

[19] Abdoulaye Fall, Anael Lemaitre, François Bertrand, Daniel Bonn, and Guillaume Ovarlez. Shear thickening and migration in granular suspensions. *Physical review letters*, 105(26):268303, 2010.

[20] Nicolas Fernandez, Roman Mani, David Rinaldi, Dirk Kadau, Martin Mosquet, Hélène Lombois-Burger, Juliette Cayer-Barrioz, Hans J Herrmann, Nicholas D Spencer, and Lucio Isa. Microscopic mechanism for shear thickening of non-brownian suspensions. *Physical review letters*, 111(10):108301, 2013.

[21] Nicolas Fernandez, Roman Mani, David Rinaldi, Dirk Kadau, Martin Mosquet, Hélène Lombois-Burger, Juliette Cayer-Barrioz, Hans J. Herrmann, Nicholas D. Spencer, and Lucio Isa. Microscopic mechanism for shear thickening of non-brownian suspensions. *Phys. Rev. Lett.*, 111:108301, Sep 2013.

[22] F. Gadala-Maria and Andreas Acrivos. ShearInduced Structure in a Con-

centrated Suspension of Solid Spheres. *Journal of Rheology*, 24(6):799–814, December 1980.

[23] A. Kate Gurnon and Norman J. Wagner. Microstructure and rheology relationships for shear thickening colloidal dispersions. *Journal of Fluid Mechanics*, 769:242–276, April 2015.

[24] B. M. Guy, M. Hermes, and W. C. K. Poon. Towards a unified description of the rheology of hard-particle suspensions. *Phys. Rev. Lett.*, 115(8):088304, 2015.

[25] Dennis P. Kalman and Norman J. Wagner. Microstructure of shear-thickening concentrated suspensions determined by flow-USANS. *Rheol. Acta.*, 48(8):897–908, March 2009.

[26] Sangtae Kim and Seppo Karrila. *Microhydrodynamics: Principles and selected applications*. Dover publications, 1991.

[27] Michael Kogan, Clare J. Dibble, Reginald E. Rogers, and Michael J. Solomon. Viscous solvent colloidal system for direct visualization of suspension structure, dynamics and rheology. *J. Colloid Interface Sci.*, 318(2):252–263, February 2008.

[28] Venkata Giri Kolli, Emily J. Pollauf, and Francis Gadala-Maria. Transient normal stress response in a concentrated suspension of spherical particles. *Journal of Rheology*, 46(1):321, 2002.

[29] Hans Martin Laun. Rheological properties of aqueous polymer dispersions. *Die Angewandte Makromolekulare Chemie*, 123(1):335–359, 1984.

[30] Anaël Lemaître, Jean-Noël Roux, and François Chevoir. What do dry granular flows tell us about dense non-brownian suspension rheology? *Rheol. Acta.*, 48(8):925–942, 2009.

[31] M E Mackay, C Liang, and P J Halley. Instrument effects on stress jump measurements. *Rheol. Acta.*, 489:481–489, 1992.

[32] Brent J Maranzano and Norman J Wagner. Flow-small angle neutron scattering measurements of colloidal dispersion microstructure evolution through the shear thickening transition. *The Journal of chemical physics*, 117(22):10291–10302, 2002.

[33] Romain Mari, Ryohei Seto, Jeffrey F. Morris, and Morton M. Denn. Shear thickening, frictionless and frictional rheologies in non-Brownian suspensions. *Journal of Rheology*, 58(6):1693–1724, November 2014.

[34] Romain Mari, Ryohei Seto, Jeffrey F. Morris, and Morton M. Denn. Shear thickening, frictionless and frictional rheologies in non-Brownian suspensions. *Journal of Rheology*, 58(6):1693–1724, November 2014.

[35] Romain Mari, Ryohei Seto, Jeffrey F Morris, and Morton M Denn. Discontinuous shear thickening in brownian suspensions by dynamic simulation. *arXiv preprint arXiv:1508.01243*, 2015.

[36] JR Melrose, JH Van Vliet, and RC Ball. Continuous shear thickening and colloid surfaces. *Physical review letters*, 77(22):4660, 1996.

[37] Jan Mewis and Norman J Wagner. *Colloidal suspension rheology*. Cambridge University Press, 2012.

[38] Christopher Ness and Jin Sun. Flow regime transitions in dense non-brownian suspensions: Rheology, microstructural characterization, and constitutive modeling. *Phys. Rev. E*, 91:012201, Jan 2015.

[39] Steve Plimpton. Fast Parallel Algorithms for Short Range Molecular Dynamics. *J. Comput. Phys.*, 117(June 1994):1–42, 1995.

[40] Srinivasa R Raghavan and Saad A Khan. Shear-thickening response of fumed silica suspensions under steady and oscillatory shear. *Journal of colloid and interface science*, 185(1):57–67, 1997.

[41] Ryohei Seto, Romain Mari, Jeffrey F. Morris, and Morton M. Denn. Discontinuous Shear Thickening of Frictional Hard-Sphere Suspensions. *Physical Review Letters*, 111:218301, 2013.

[42] Norman J Wagner and John F Brady. Shear thickening in colloidal dispersions. *Physics Today*, 62(10):27–32, October 2009.

[43] M. Wyart and M. E. Cates. Discontinuous Shear Thickening without Inertia in Dense Non-Brownian Suspensions. *Phys. Rev. Lett.*, 112(9):098302, March 2014.

[44] Bu Xu and James F Gilchrist. Microstructure of sheared monosized colloidal

suspensions resulting from hydrodynamic and electrostatic interactions. *The Journal of chemical physics*, 140(20):204903, 2014.

CHAPTER 7

ACTIVE CONTROL OF SHEAR THICKENING IN SUSPENSIONS[1]

7.1 Abstract

Shear thickening, an increase of viscosity with shear rate, is a ubiquitous phenomena in suspended materials that has implications for broad technological applications. Controlling this thickening behavior remains a major challenge and has led to empirical strategies ranging from altering the particle surfaces and shape to modifying the solvent properties. However, none of these methods allow for active control of flow properties during shear itself. Here, we demonstrate that by strategic imposition of a high-frequency and low-amplitude shear perturbation orthogonal to the primary shearing flow, we can largely eradicate shear thickening. The orthogonal shear effectively becomes a regulator for controlling thickening in the suspension, allowing the viscosity to be reduced by up to two decades on demand. In a separate setup, we show that such effects can be induced by simply agitating the sample transversely to the primary shear direction. Overall, the ability of in situ manipulation of shear thickening paves a route towards creating materials whose mechanical properties can be actively controlled.

7.2 Introduction

The viscosity of a densely packed suspension of particles can increase radically when sheared beyond a critical stress [50, 22]. This thickening behavior has been

[1] Neil Y.C. Lin, Christopher Ness, Michael E. Cates, Jin Sun, and Itai Cohen. "Active Control of Shear Thickening in Suspensions." PNAS in review (2016).

exploited in technological applications ranging from vehicle traction control to flexible spacesuits that protect astronauts from micrometeorite impacts [51, 25, 13]. It may also lead to flow problems such as pipe blockage during industrial extrusion processes [8]. Shear thickening has generally been considered an inherent material property [6], rather than as a response that can be actively controlled. As a consequence, suspension process design is often constrained within tight bounds to avoid thickening [2], while the applications of such flow behavior are limited by a lack of tunability.

To design our control method, we take advantage of the underlying shear thickening mechanisms that have been revealed recently. Experiments and simulations have shown that when the stress applied to a suspension of micron-sized particles exceeds a critical value, the particle-particle interaction switches from lubricated to frictional, enhancing resistance to flow [20, 43, 52, 26, 8, 7]. The stress is transmitted through shear-induced force chains, which arise from frictional particle contacts [3, 29, 8, 7], aligned along the compressive axis. Such chains are fragile [9, 28] and are constantly broken and rebuilt during steady shear.

This fragility paradigm asserts that these stress-transmitting chains are themselves a product of the stress, with a finite chain-assembly time required following startup or perturbations to the flow direction [21, 34]. These insights suggest a strategy for controlling thickening. For perturbations slower than chain assembly, contact rearrangement is sufficiently fast that force chains remain aligned with the instantaneous net compressive axis. Conversely, for perturbations faster than the assembly time, chains cannot reach compatibility with the instantaneous net compressive axis, but occupy a partially-assembled transient state, illustrated in Fig. 7.1(a). The alignment of the perturbed or tilted chain deviates from the net

compressive axis and it no longer transmits stresses effectively. Thus it should be possible to precisely regulate the thickening behavior by applying appropriate lateral perturbations.

To that end we design a *biaxial* shear protocol that uses an orthogonal flow perturbation to interfere with force chains induced by a primary shearing flow. Our strategy is to maximize the perturbation influence so the force chains usually responsible for thickening cannot establish fully. We conduct biaxial rheometry experimentally and numerically, mapping the response of a hard-sphere suspension as the perturbation rate and amplitude are systematically varied. By integrating our knowledge of the force chain alignment, mechanical instability and direct link to the viscosity, we show how this strategy can be optimized. We focus on *discontinuous* shear thickening suspensions, as their vast viscosity variations make them most problematic to the engineer [52, 43, 17]. Our results show that through suitable regulation, the suspension viscosity at a fixed flow rate may be reduced by up to two decades in an active and controlled manner. We finally demonstrate the wide utility of the technique using a simpler flow regulation set up.

7.3 Experiment

The biaxial rheometry experiment is performed using a double-wall Couette geometry that has an outer cup driven continuously by an underneath motor, and an inner bob attached to an oscillating shaft [49, 48, 23]. A simplified schematic and coordinate definition are shown in Fig. 7.1(b). The continuous primary flow in the $\hat{r}\hat{\theta}$ plane along the $\hat{\theta}$ direction, at controlled rate $\dot{\gamma}_0$, constantly induces force chains, sets the initial shear thickening state, and probes the parallel viscos-

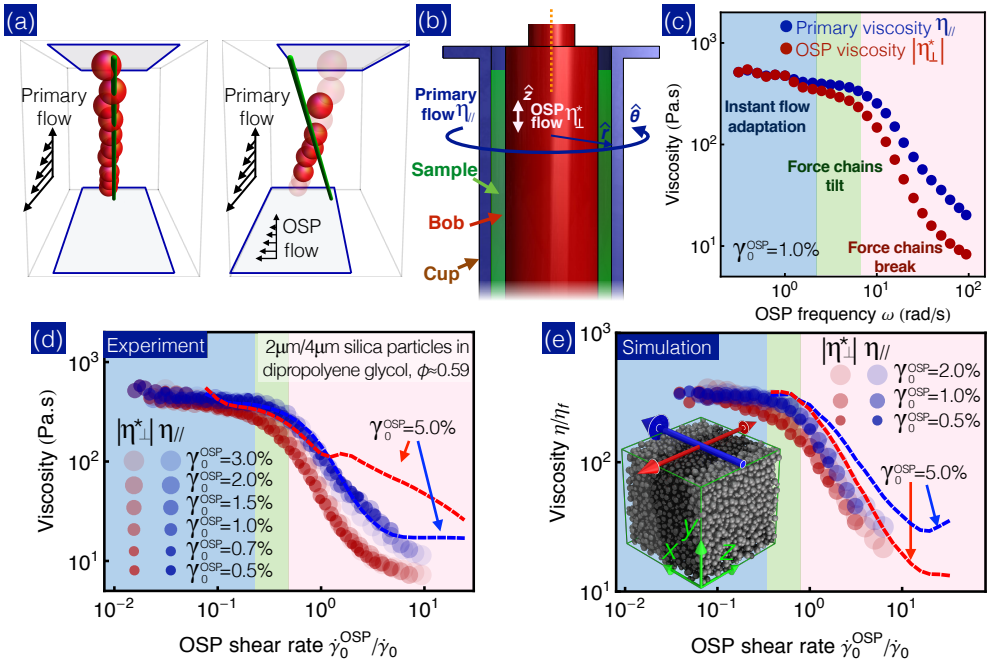

Figure 7.1: Perturbing the frictional force chains that govern shear thickening by imposing orthogonal shear can reduce the suspension viscosity by nearly two decades. (a) Schematic showing force chain alignment during flow. Left panel: Under simple, uniaxial shear, particles (red spheres) naturally align along the compressive axis (green line); Right panel: Under rapid biaxial shear, with transverse flow indicated by the shifted upper plate, the orthogonal perturbations may tilt or break the chains, so that they deviate from the combined compressive axis. (b) Schematic of experimental apparatus showing the continuous primary flow that drives shear thickening and the inner oscillatory module that perturbs the force chains; (c) Frequency sweep experimental data for γ_0^{OSP}=1%. Shown are the primary viscosity ($\eta_{\|}$, blue dots) and orthogonal complex viscosity ($|\eta^*_\perp|$, red dots); (d) Experimental and (e) simulation viscosity data collapse as function of the relative OSP shear rate ($\dot{\gamma}_0^{\mathrm{OSP}}/\dot{\gamma}_0$), for several γ_0^{OSP}. Dashed lines indicate reentrant thickening when the OSP strain becomes large enough to induce new force chains; Inset (e), snapshot of simulation configuration, indicating the coordinate definitions with respect to the primary (blue arrow) and OSP (red arrows) flow directions. Further details and characterisation of experimental sample can be found in Method and SI.

ity, $\eta_{\parallel}$. Concurrently, an orthogonal superimposed perturbation (OSP) comprising oscillatory flow in the $\hat{r}\hat{z}$ plane along the $\pm\hat{z}$ direction perturbs the suspension by imposing a deformation $\gamma^{\mathrm{OSP}} = \gamma_0^{\mathrm{OSP}} \sin(\omega t)$ with rate $\dot{\gamma}^{\mathrm{OSP}} = \omega\gamma_0^{\mathrm{OSP}} \cos(\omega t)$, and simultaneously probes its orthogonal complex viscosity, $|\eta_{\perp}^*|$. Given the employed Couette cell dimension, we approximate the primary flow as a uniaxial shear in parallel plate geometry. Further details about the geometry and OSP calibration can be found in Method and SI.

Following the above reasoning, we take the primary shear timescale $1/\dot{\gamma}_0$ and the OSP period $1/\omega$ as proxies for chain-assembly and perturbation times, respectively. We fix the primary shear rate at $\dot{\gamma}_0 = 0.2$ s^{-1}, where the suspension is normally strongly thickened (see SI), and conduct an OSP frequency sweep at a fixed strain amplitude $\gamma_0^{\mathrm{OSP}} = 1\%$. The evolutions of $\eta_{\parallel}$ and $|\eta_{\perp}^*|$ are given in Fig. 7.1(c).

7.4 Results

7.4.1 Rheometry and simulations

At low frequencies $\omega \leq 2$ rad/s (blue area, Fig. 7.1(c)), $\eta_{\parallel}$ and $|\eta_{\perp}^*|$ exhibit plateaus that match the original thickening viscosity ~ 500 Pa.s, for $\gamma_0^{\mathrm{OSP}} = 0$ (see SI). In this regime, the primary flow renews the force chains rapidly so that they are always compatible with the net compressive axis, and their alignment appears to adapt instantly to the OSP flow. This instantaneous adaptation gives rise to an isotropic and unaffected thickening behaviour (see SI for an analytical derivation). As the frequency increases to 2 rad/s $< \omega \leq 8$ rad/s (green area), we find that the OSP viscosity $|\eta_{\perp}^*|$ decays slightly, while the primary value $\eta_{\parallel}$ remains relatively

constant (within 7%). The decay in $|\eta_\perp^*|$ suggests that the OSP flow deforms or tilts existing force chains more quickly than they are replaced by new ones, while the unchanged $\eta_\parallel$ suggests the tilted chains remain largely intact. Finally, we observe a substantial drop in both $\eta_\parallel$ and $|\eta_\perp^*|$ at even higher frequencies $\omega > 8$ rad/s implying significant breakage of force chains and dissolution of the flow induced contact network. Qualitatively, this result is consistent with our above interpretation of the fragile, marginally stable nature of the force chain network, and reaffirms the link between the stress bearing capability of the chains, and the viscosity of the suspension [52].

To further elucidate the roles being played by the primary and OSP flows, we repeat the frequency sweep measurement at six different γ_0^{OSP}, Fig. 7.1(d). We normalize the OSP shear rate magnitude by the primary rate $\dot{\gamma}_0^{\mathrm{OSP}}/\dot{\gamma}_0 (= \omega\gamma_0^{\mathrm{OSP}}/\dot{\gamma}_0)$, and find that all $\eta_\parallel$ and $|\eta_\perp^*|$ data, for $\gamma_0^{\mathrm{OSP}} < 5\%$, collapse onto two master curves (blue and red dots, respectively). Furthermore, the onset of the chain breaking regime occurs at $\dot{\gamma}_0^{\mathrm{OSP}}/\dot{\gamma}_0 \approx 1$. This scaling suggests that the force chain response, whether they instantly adapt to the OSP flow, tilt, or break, is determined by the competition between $\dot{\gamma}_0^{\mathrm{OSP}}$ and $\dot{\gamma}_0$. While $\dot{\gamma}_0$ indicates how frequently force chains reform, $\dot{\gamma}_0^{\mathrm{OSP}}$ dictates how rapidly the OSP flow perturbs these structures. In other words, the ratio $\dot{\gamma}_0^{\mathrm{OSP}}/\dot{\gamma}_0$ directly governs the viscosity reduction of a biaxially sheared sample. For large γ_0^{OSP} (>5%), we observe a deviation from the master curves, suggesting a possible reentrant thickening arising when chains induced by the OSP flow emerge. We conclude, therefore, that for sufficiently large $\dot{\gamma}_0{}^{\mathrm{OSP}}/\dot{\gamma}_0$ and sufficiently small γ_0^{OSP}, our orthogonal flow perturbation disrupts the conventional shear-induced contact network, inhibiting friction-mediated force chains and mitigating shear thickening. The extent of this mitigation may be set using $\dot{\gamma}_0^{\mathrm{OSP}}/\dot{\gamma}_0$ as a control parameter, allowing precise *regulation* of the viscosity

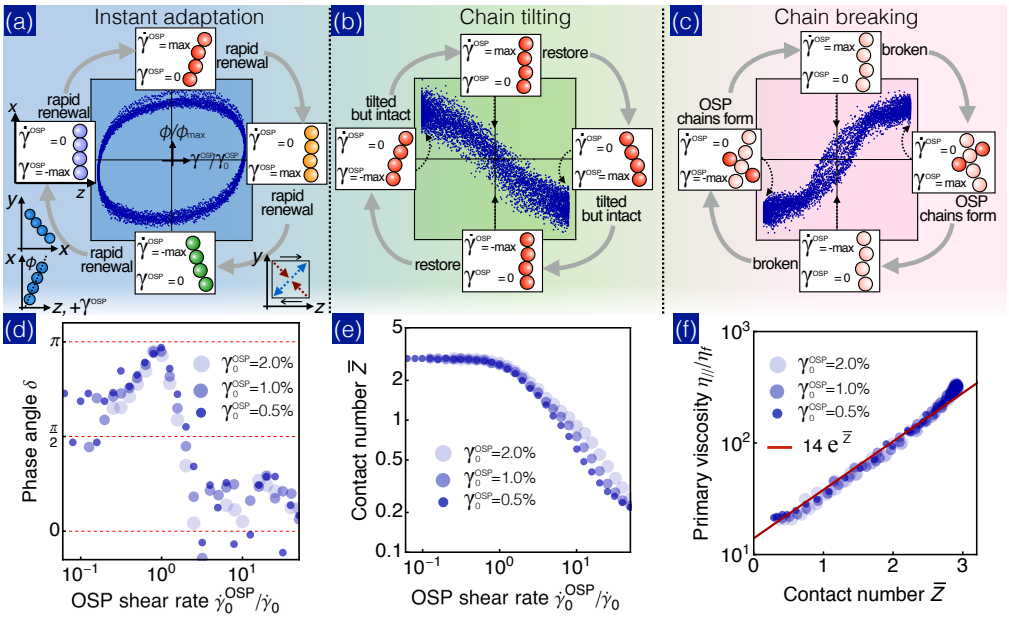

Figure 7.2: Microstructural information from simulations to illustrate the mechanism behind the viscosity reduction with increased OSP flow, for $\gamma_0^{\mathrm{OSP}} = 1\%$. Shown are Lissajous curves for microstructural force chain alignment for the (a) instant adaptation, (b) chain tilting and (c) chain breaking regimes, with ϕ and γ^{OSP} normalized by their maximal values, where $\phi_{\max} \sim \mathcal{O}(10^{-2})$. ϕ and the sign of γ^{OSP} are defined in the Left Inset of (a), and definitions of compression (red) and extension (blue) quadrants of the OSP flow in Right Inset of (a), for positive $\dot{\gamma}^{\mathrm{OSP}}$. Force chain diagrams in (a), (b), (c) illustrate alignment projected to $\hat{x}\hat{z}$ at each stage of the oscillatory cycle, while alignment in $\hat{x}\hat{y}$ remains along the compressive axis of the primary flow throughout (Left Inset of (a)); (d) Evolution of phase angle δ between ϕ and γ^{OSP} with OSP shear rate, where $\delta = 0$ and $\delta = \pi/2$ respresent elastic and viscous responses respectively; (e) Evolution of time-averaged contact number $\bar{Z}$ with OSP shear rate; (f) Direct dependence of primary flow viscosity on time-averaged contact number $\bar{Z}$.

of dense suspensions.

To clarify the detailed microstructural rearrangements leading to the observed measurements we use numerical simulations, explicitly resolving the trajectories and interactions of suspended, bidisperse spheres (diameter ratio 1:1.4) using a classical discrete element code [12, 39] enhanced with the recently established

Critical Load Model [29, 33]. Hydrodynamic forces are approximated as pairwise lubrication interactions (viscosity η_f) between neighboring particles, while particle contacts are treated as linear springs with friction appearing above a critical normal force. The fixed-volume fraction (55%), periodic, Cartesian simulation cell can be deformed to simulate steady shear in a primary direction with a small amplitude oscillation in the orthogonal direction. With respect to the illustration in Fig 7.1(e), primary flow (blue arrow) is in the $\hat{x}\hat{y}$ plane, along the $\hat{x}$ direction, and OSP flow (red arrows) is in the $\hat{y}\hat{z}$ plane, along the $\pm\hat{z}$ direction. Full details and discussion of model assumptions are given in SI.

The experimental flow measurements are repeated computationally with consistent results, shown in Fig. 7.1(e). The force chain alignment is interrogated in the three identified regimes, instant adaptation, chain tilting, and chain breaking. In all regimes, the chains lie mainly along the compressive axis of the primary shear flow, but are subtly shifted out of the $\hat{x}\hat{y}$ plane by the OSP flow. To quantify these deviations, we calculate a fabric tensor $\langle \hat{r}_i^{\alpha\beta}\hat{r}_j^{\alpha\beta}\rangle$ capturing the particle contact configuration [3], where $r_i^{\alpha\beta}$ ($\alpha \neq \beta$) is the unit vector between particles α and β, while i, j denote the coordinate indices and $\langle \ldots \rangle$ denotes the average over all neighboring particles. We take $\phi = \tan^{-1}(\langle \hat{r}_y\hat{r}_z\rangle / \langle \hat{r}_x\hat{r}_y\rangle)$ as the angle between the force chains and x-axis, when projected to $\hat{x}\hat{z}$, Fig 7.2a (Left Inset), which remains small, $\phi_{\max} \sim \mathcal{O}(10^{-2})$, throughout. Chains inclined towards the compressive quadrant of the OSP flow (see Right Inset, Fig 7.2a) have positive ϕ for positive $\dot{\gamma}^{\mathrm{OSP}}$.

Representative Lissajous curves of $\phi(\gamma^{\mathrm{OSP}})$ for the three regimes are shown in Fig. 7.2(a), (b), and (c), for time-varying OSP strain γ^{OSP}. For low OSP rates $\dot{\gamma}_0^{\mathrm{OSP}}/\dot{\gamma}_0 \ll 1$, newly formed force chains always align with the net compressive

axis dictated by the instantaneous combined flow, so ϕ is in phase with the time-varying OSP *strain rate*, $\phi \propto \dot{\gamma}^{\mathrm{OSP}}$, Fig. 7.2(a), generating isotropic thickening as reported in Fig. 7.1(d) and (e). For $\dot{\gamma}_0^{\mathrm{OSP}}/\dot{\gamma}_0 \approx 1$, the time scales for the OSP and primary flows are comparable, so it is expected that chains are tilted before they can rearrange. Indeed, we find that chain alignment is antiphase to the OSP *strain*, $\phi \propto -\gamma^{\mathrm{OSP}}$, Fig. 7.2(b). This indicates that rather than adapting to the instantaneous flow rate, existing force chains are instead tilted affinely by the transverse deformation (strain) and occupy the extensional quadrant of the OSP flow while $\gamma^{\mathrm{OSP}} \neq 0$, as sketched in Fig 7.1a (right panel). When the OSP rate dominates $\dot{\gamma}_0^{\mathrm{OSP}}/\dot{\gamma}_0 \gg 1$, the affine deformation caused by the transverse flow is fast enough to break these tilted force chains more rapidly than the primary flow is able to sustain or re-establish them. Meanwhile, new contacts may be formed by the OSP flow in its compressive quadrant. Thus, the chain alignment is in phase with the OSP strain $\phi \propto \gamma^{\mathrm{OSP}}$, Fig. 7.2(c). The implication of the final curve is striking. In the chain breaking regime, the thickening becomes solely governed by the strain amplitude of the OSP flow. We summarize the chain alignment behavior by plotting the phase lag δ between ϕ and γ^{OSP} in Fig. 7.2(d).

Since the shear thickened viscosity directly arises from frictional particle contacts [26], we expect that the evolution of the force chain response with increasing $\dot{\gamma}_0^{\mathrm{OSP}}/\dot{\gamma}_0$ is accompanied by a reduction in particle contacts. To verify this, we calculate the time-averaged per-particle coordination number $\bar{Z}$. We find that $\bar{Z}(\gamma_0^{\mathrm{OSP}}, \omega)$ collapses in a similar fashion to the measured viscosity, and starts to decay around $\dot{\gamma}_0^{\mathrm{OSP}}/\dot{\gamma}_0 \approx 1$, Fig. 7.2(e). Indeed, plotting $\eta_{\|}$ versus $\bar{Z}$ we recover a simple relationship $\ln \eta \propto \bar{Z} + \mathrm{const}$, Fig. 7.2(f). When no particle contact is formed, $\eta_{\|}$ corresponds to the viscosity purely arising from the interparticle hydrodynamic interactions [11]. As $\bar{Z}$ increases, $\eta_{\|}$ rises and brings more particles

into contact, which in turn produces a higher viscosity. Overall, these simulations reaffirm the bulk rheological effect of the orthogonal perturbation and reveal the microstructural mechanism by which the OSP flow can manipulate the force chains to ultimately eradicate the frictional contacts responsible for shear thickening.

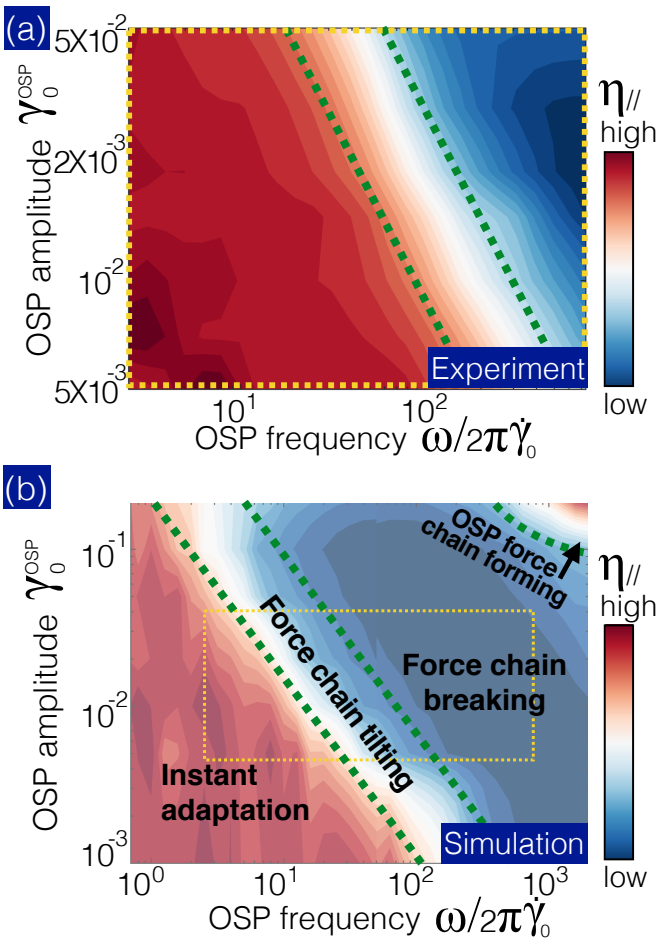

Figure 7.3: Regime maps for strategic suspension viscosity regulation. Data are obtained from (a) experiments and (b) simulations. In (b), we delineate each of the phenomenological shear thickening regimes. Color scale represents primary flow viscosities. The yellow dashed box indicates the regime explored in experiment. In both experiment and simulation, the onset of viscosity reduction occurs at $\dot{\gamma}_0^{\mathrm{OSP}}/\dot{\gamma}_0 \approx 1$. This indicates that the state of the biaxially sheared suspension is determined by the competition between primary and OSP flow rates.

We construct a summary phase diagram recapitulating our strategy for active control of shear thickening, giving experimental and simulated primary viscosities

as functions of γ_0^{OSP} and ω in Fig. 7.3(a) and (b), respectively. When an OSP flow is applied, its shear rate $\gamma_0^{\mathrm{OSP}}\omega$ determines the force chain behavior and the state of thickening in the suspension. The force chain behavior shows a transition from instant adaptation, chain tilting, to chain breaking as the OSP flow rate increases. When the OSP flow rate is even higher, however, the OSP flow may start to induce force chains by itself for sufficiently large γ_0^{OSP}. A reentrant thickening behavior is then observed, as indicated by the curved contours and red region in the upper right corners of Fig. 7.3(a) and (b), respectively.

7.4.2 Speaker experiments

The orthogonal flow induced viscosity reduction allows us to drive the material at a higher speed with the same amount of driving force. In some practical cases, our biaxial protocol or a comparable oscillatory perturbation should be able to 'unblock' the shear jammed suspension flows. We test this prediction in a dense cornstarch suspension [16, 17] using a simple setup consisting of a DC motor and a speaker, as shown by the schematics in Fig. 7.4 (a) and (b). Upon motor startup, the rotating gear on the shaft immediately thickens the cornstarch [38], generating a torque that causes motor stalling. We then use the speaker to apply a high frequency and small amplitude (250Hz, 18 μm) vibration along the vertical direction to break the force chains against the gear. As a result, the motor under the same applied voltage starts to rotate again and shear the material, see Fig. 7.4(c) and SI video. This transition repeats reversibly as we switch the speaker on and off. We also find that the motor rotation speed is maximized when we raise the vibration frequency and lower its amplitude, keeping the induced rate, analogous to $\dot{\gamma}_0^{\mathrm{OSP}}$, fixed Fig. 7.4(d). This finding suggests that the state of the system is in the dark

blue channel in the phase diagram (Fig. 7.3). This channel runs upper left to bottom right indicating larger viscosity reductions at higher frequencies when the shear rate is fixed. This simple demonstration shows that our strategy for using orthogonal flows to control thickening is robust, and can be realized even in less controlled settings.

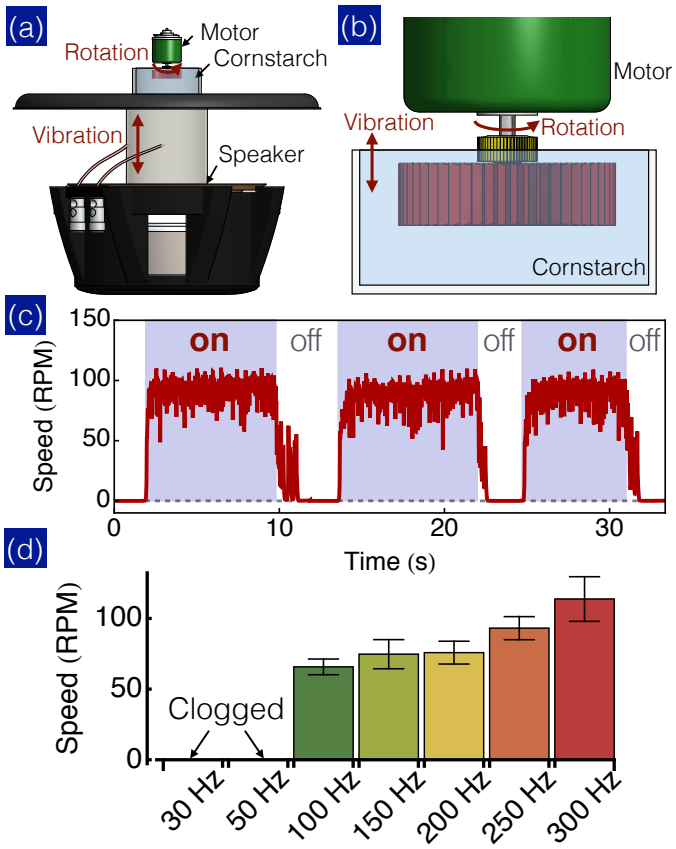

Figure 7.4: A simple flow regulation set up comprising a rotating gear submerged in a cornstarch suspension illustrates the broad utility of our control scheme. Schematic of improvised flow regulator, showing (a) the full setup including driving motor, cornstarch reservoir and speaker and (b) a close-up of the setup. (c) The motor starts to rotate when the vibration (250 Hz) switches on (shaded areas), and stalls when the vibration is off. Shown in (d) is the rotation speed of the motor as a function of vibration frequency at a fixed speed. The motor remains stalled at the frequencies $\leq$ 50 Hz.

7.5 Conclusion

In conclusion, we have, for the first time, employed a biaxial shear protocol to actively control the shear thickening viscosity of a suspension. Active control is achieved by applying a transverse perturbation that regulates the main flow, along the lines of a mechanical transistor. This contrasts with passive control in which the rheological response is set when formulating the suspension and not changed thereafter. By scaling the flow measurement data and numerically investigating the force chain behavior, we elucidate the underlying mechanism of our control method and demonstrate how it can be strategically utilized. This result might inform extension of a three-dimensional continuum description so far limited to the $\dot{\gamma}_0^{\mathrm{OSP}}/\dot{\gamma}_0 \ll 1$ regime [36]. Using a simpler flow regulation set up, we finally demonstrate that the insight obtained here can inform practical strategies, e.g., to unclog blockages caused by thickening during paste extrusion [37], 3D printing suspensions [46], and flow of carbon black in energy storage devices [19], and, more generally, to control bistability in granulation [10] and jamming in hopper flow [14]. In general, active control over a fluid's rheological properties holds the promise for advancing actuation and motion controls [45, 31], which have applications ranging from controllable dampers [45], robotic arms [45, 47], to actuating orthoses [35].

7.6 Acknowledgements

IC and NL were supported by NSF CBET-PMP Award No. 1232666 and continued support from NSF CBET-PMP Award No. 1509308. CN and JS acknowledge funding from the Engineering and Physical Sciences Research Council (EP/N025318/1). MEC is supported by the Royal Society and EPSRC Grant

EP/J007404. IC and NL gratefully acknowledge the Weitz lab at Harvard for generous use of their rheometry facility. The authors would also like to thank Andrea Liu, Romain Mari, John Royer and Wilson Poon for helpful discussions.

7.7 Supplementary Information

7.7.1 Experimental and numerical methods

The experiment is performed using an ARES-G2 rheometer (TA Instrument) in conjunction with an orthogonal superimposed perturbation (OSP) module [48, 49]. During the experiment, the parallel ($\eta_{\parallel}$) and orthogonal ($|\eta^*_{\perp}|$) viscosities of the sample are measured by strain gauges on the upper shaft. The tested suspension comprises silica particles in dipropylene glycol (Sigma-Aldrich). The sample volume fraction $\phi \approx 0.59$ is determined by directly imaging the suspension structure with a confocal microscope. The suspended particles are binary (2μm/4μm diameters) with number ratio roughly 1:1, mitigating crystallization. Our sample shear thickens at a relatively low shear rate due to the high solvent viscosity $\eta_0 = 84$ m.Pa, minimizing the instrumental instability in the biaxial test. For further characterizations of the sample structure and rheological properties, see SI.

The experimental volume fraction of 59% is chosen to represent an upper limit at which steady flow in the shear thickening regime is observed. Numerically, we are able to reproduce the uniaxial experimental rheology at 55% volume fraction. In future work we may address this difference by improving volume fraction measurement [41] and characterising particle friction [20], both of which remain

interesting experimental challenges.

7.7.2 Orthogonal Superposition (OSP) Calibration

To correctly perform the biaxial rheometry, we quantify the coupling between primary and OSP shear stress responses. The major contribution to the coupling arises from the misalignment between instrumental parts. In this section, we report a calibration indicating that the instrumental coupling is negligible.

Instrumental biaxial coupling

The instrumental coupling is closely related to the alignment between the primary and OSP driving motions of the rheometer. Therefore, the parts of the drivers have to be machined and assembled carefully. To quantify the instrumental coupling, we load a suspension into the ARES-G2 rheometer and impose a uniaxial oscillatory shear with a strain amplitude $\gamma_0 = 2$. Meanwhile, we monitor the OSP response that directly arises from the instrumental coupling. We plot the Lissajous-Bowditch (LB) curve of the primary response in Fig. 7.5 (a). The LB curve indicates a viscous response, in which the stress is maximal around zero strain. The stress overshoots around strain $\approx \pm 1.5$ are associated with the formation of particle frictional contacts. In Fig. 7.5 (b), we plot the OSP stress response versus the primary stress. Since we do not impose any OSP shear strain, the measured OSP response solely results from the coupling. We observe a positive correlation between the two stress responses implying that the coupling is finite and measurable. Nevertheless, we find this correlation remarkably small. For example, when the primary stress response is maximal (≈ 10 Pa), the OSP response

is only ≈ 0.15 Pa, about 0.1% of the applied primary stress.

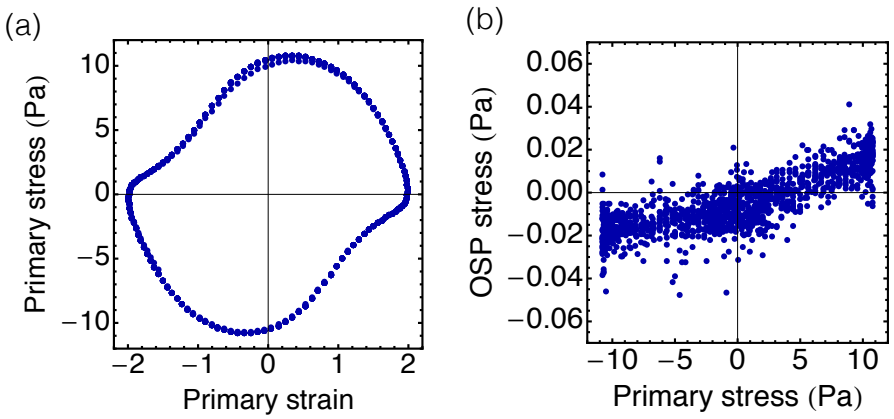

Figure 7.5: (a) Lissajous-Bowditch curve of primary stress versus strain. The stress overshoots at strain $\approx \pm 1.5$ result from the formation of particle contacts within a cycle. (b) Lissajous-Bowditch curve of OSP stress versus primary stress. The positive correlation between these two stresses implies a measurable instrumental coupling. However, the coupling $\approx$ 0.1% is insigficant.

Uniaxial oscillatory shear

In the main draft, we show a reentrant shear thickening at large OSP amplitudes and high frequencies. The reentrant thickening should be related to the frictional contacts formed by the OSP flow when its amplitude is large. This means that under uniaxial shear, the suspension viscosity should start to increase when the applied strain amplitude exceeds a critical value. To confirm this, we repeat the frequency sweep measurement but now in the absence of the primary flow. We plot the OSP viscosity $|\eta_\perp^*|$ as a function of OSP frequency for seven different strain amplitudes $\gamma_\perp$ in Fig. 7.6. We find a slight frequency thinning at low frequencies that might be due to either Brownian motion or the slight attraction between particles. Nevertheless, we do observe thickening behavior at $\gamma_\perp = 5\%$ (black points). This thickening behavior is consistent with the viscosity growth observed in the biaxial case.

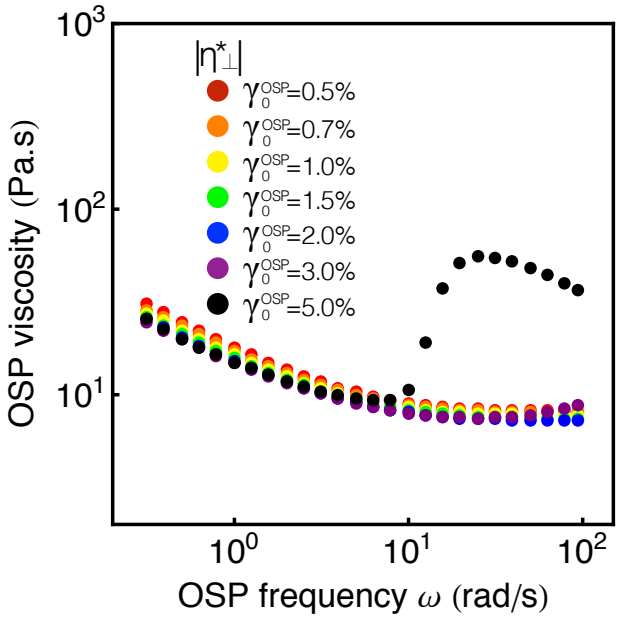

Figure 7.6: OSP viscosity $|\eta^*_\perp|$ as a function of ω for seven different strain amplitudes. We do not observe any shear thickening at $\gamma_0^{OSP} < 5\%$.

Viscosity standard measurement

Finally, we want to further confirm that both primary and OSP measurements of viscosity are accurate and consistent. We load a viscosity standard (CANNON N4000) into the ARES-G2 and repeat the reported biaxial experiment with exactly the same parameters. The tested viscosity standard has a nominal viscosity $\sim$ 12 Pa.s at room temperature, which is similar to our suspension viscosity. For a coupling- and artifact-free measurement, the measured viscosity should be Newtonian, hence independent of the OSP frequency and amplitude. We show the viscosity in Fig. 7.7. Overall both the primary (dashed lines) and OSP (dots) viscosities match each other, and remain constant throughout all frequencies and amplitudes. We observe higher viscosities at low OSP frequencies suggesting that the viscosities are overestimated by the instrument (by $\approx 13\%$). While this small viscosity should be further corrected in future experiments, it is insignificant and

should not alter the main trend of the reported biaxial data.

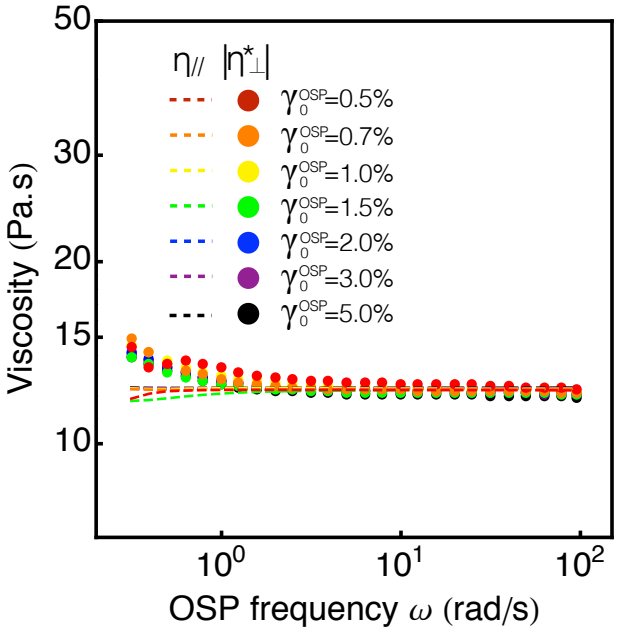

Figure 7.7: Primary $\eta_{\|}$ and OSP $|\eta^*_\perp|$ viscosities versus OSP frequency ω. The primary shear rate is 0.2 s^{-1}.

7.7.3 Sample Characterization and Experimental Details

Structure – confocal images

The solvent (Dipropylene glycol) used in the experiment has a refractive index (1.439) that nearly matches the index of the silica particles (1.435). This index match minimizes the van-der waals force between particles [**?**] and allows us to perform direct imaging of the suspension structure [27, 42, 15]. Furthermore, a small amount of fluorescein salt is added in the sample to dye the solvent and reduce the Debye length of the electrostatic force. We then use a confocal microscope to examine the structure and volume fraction of a quiescent suspension sample. We show the confocal images sliced along three different axes in Fig. 7.8(a). We also

show a 3D reconstruction of the image stack in Fig. 7.8(b). From the images, we do not observe any aggregation of particles over time, implying that the suspension is well stabilized by the electrostatic force. We also find that the suspension structure remains disordered at high volume fractions. Finally, we use the 3D images to estimate the suspension volume fraction by counting particles, and find the volume fraction consistent with that calculated according to the weight ratio.

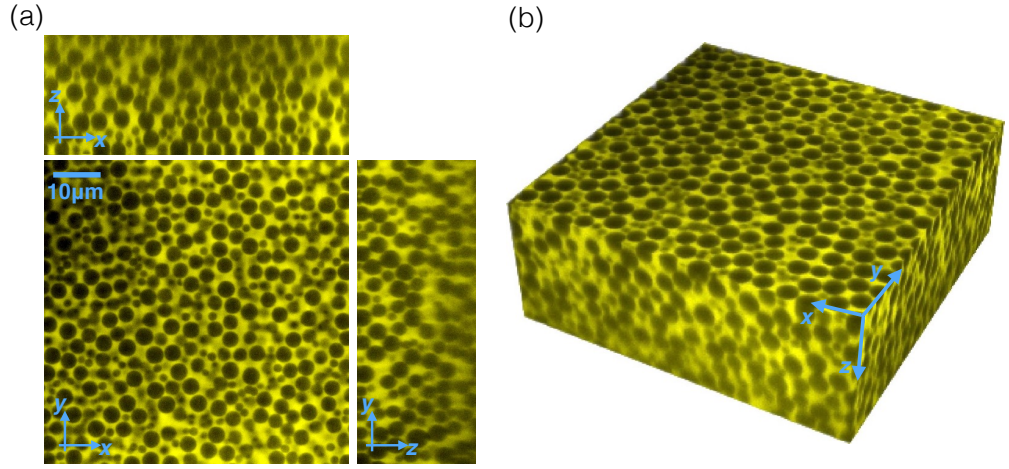

Figure 7.8: (a) Three different slices from a 3D image matrix of the tested binary suspension. The middle, top, and right images correspond to the top ($\hat{x}\hat{y}$), front ($\hat{x}\hat{z}$), and side views ($\hat{y}\hat{z}$), respectively. The solvent is dyed with fluorescein salt, so it appears bright. The silica particles are not fluorescently labeled, so they appear dark. (b) 3D reconstruction of the image stack. The deeper image region (larger z value) gets blurrier due to the spherical aberration and its resulting point-spread-function. We do not observe significant crystallization in the sample.

The used solvent Dipropylene glycol also has a low vapor pressure minimizing the evaporation rate [**?**]. By monitoring the viscosity of the suspension over time, we find that the sample's volume fraction remains constant throughout the entire experiment. Furthermore, we use micron-sized particles to reduce sedimentation effect.

Stress and rate sweep plots

The rheometer used in the biaxial experiment is strain-controlled. The strain-controlled mode ensures the accuracy of the applied OSP strain. In previous literature, however, it has been shown that uniaxial shear thickening is a stress-controlled phenomena [8, **?**, 26]. Many previous works have presented the viscosity data as a function of stress. Therefore, to characterize the uniaxial thickening behavior of our sample, we perform a stress sweep measurement and plot the same dataset in both stress and strain sweep fashions. The measurement is performed using an Anton Paar MCR 301 stress-controlled rheometer. In Fig. 7.9(a) and (b) we show the rate and stress sweep data for our discontinuous thickening sample, respectively. The orange dashed lines in Fig. 7.9(a) indicate the primary shear rate employed in the biaxial experiment and its corresponding shear viscosity. In the stress sweep plot (Fig. 7.9(b)), we find that $\eta_{\parallel} \propto \sigma_0^{0.95}$, depicting a nearly DST behavior [8]. Put differently, $\sigma_0 = \eta_{\parallel}\dot{\gamma}_0$ is almost linear in $\eta_{\parallel}$, signifying that stress takes a range of values at fixed strain rate which is the defining discontinuity property of DST.

OSP phase angle

The oscillatory OSP flow allows us to probe both the overall viscosity magnitude $|\eta^*_\perp|$ and the phase angle δ between the stress and strain. The latter information describes the viscoelasticity of the sample, in which $\delta = \pi/2$ and $\delta = 0$ correspond to viscous and elastic responses, respectively. We report the overall viscosity magnitude $|\eta^*_\perp|$ in the main text. Here, we show the phase angle as a function of OSP strain amplitude and frequency in Fig. 7.10. We find that in the instantaneous adaptation regime, the OSP stress response is mainly viscous. This finding

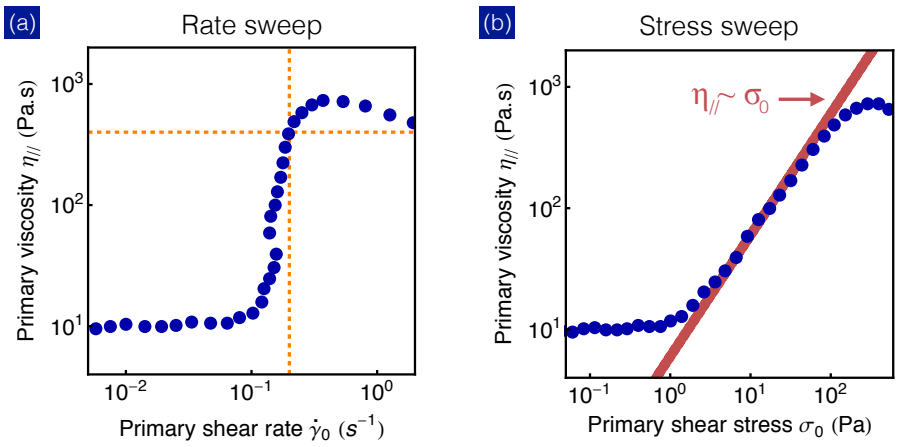

Figure 7.9: (a) Primary viscosity $\eta_{\|}$ as a function of shear rate. We see an abrupt increase in $\eta_{\|}$ at $\dot{\gamma}_0 \approx 0.1$. The dashed lines denote the primary shear rate and its corresponding viscosity in biaxial experiment. (b) Data from (a) but in a stress-sweep fashion. Consistent with previous works [8], we observe a nearly linear increase in viscosity $\eta_{\|} \propto \sigma_0^{0.95}$ in the DST regime. The red line denotes a linear response $\eta_{\|} \propto \sigma_0$.

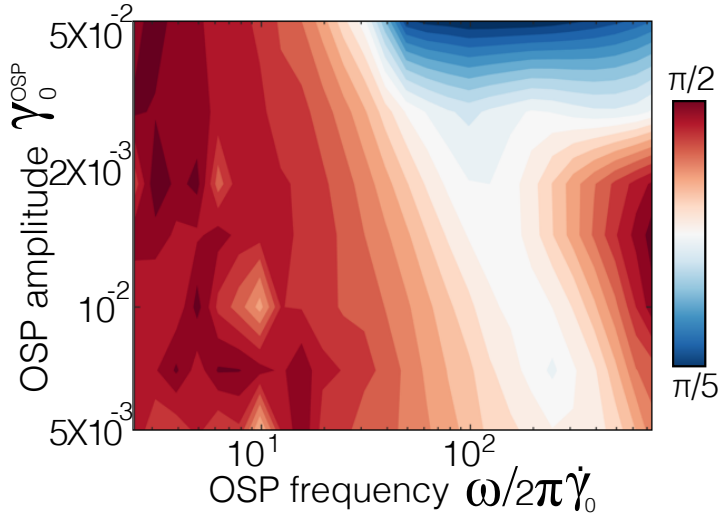

Figure 7.10: Contour plot of phase angle δ between OSP stress and strain. The response at low frequencies and strain amplitudes is viscous ($\delta \approx \pi/2$). The response in the reentrant thickening regime is elastic ($\delta \approx 0$). The trend of $\delta(\omega/2\pi\dot{\gamma}_0)$ at $\gamma_0^{\mathrm{OSP}} \leq 0.002$ is non-monotonic.

suggests that the alignment of the force chain regulated by the ratio $\dot{\gamma}_{OSP}/\dot{\gamma}_0$, consistent with our simulation results reported in the main manuscript Fig. 2. As the OSP frequency increases, δ decays implying a more elastic stress response. The transition from viscous to elastic response characterizes the competition between the primary and OSP shear rates. Surprisingly, this transition trend $\delta(\omega/2\pi\dot{\gamma}_0)$ is non-monotonic, suggesting that the mechanisms of "chain tilting" (OSP rate comparable to primary rate) and "chain breaking" (OSP rate dominates) regimes should be distinct. At large amplitudes and high frequencies, where the reentrant thickening emerges, we observe small $\delta \approx \pi/5$ denoting an elastic response. In this regime, the OSP flow is strong enough to form force chains by itself. Therefore, the stress is largely transmitted through the OSP force chains, and demonstrates a primarily elastic response.

Solvent viscosity

To characterize the viscosity of the used solvent (Dipropylene glycol) we perform rate sweep measurements at ten different temperatures ranging from -1°C to 30°C. The viscosity is plotted as a function of shear rate in Fig. 7.11(a). We find that Dipropylene glycol displays a Newtonian behavior at all shear rates and temperatures. This Newtonian behavior ensures that the interparticle hydrodynamic interaction in our tested shear thickening samples has a conventional form of lubrication force. We further read out the mean viscosity value for each temperature and plot the result in Fig. 7.11(b). We find that the viscosity increases significantly as the temperature drops. In experiment, we set the temperature at 20°C throughout all measurements.

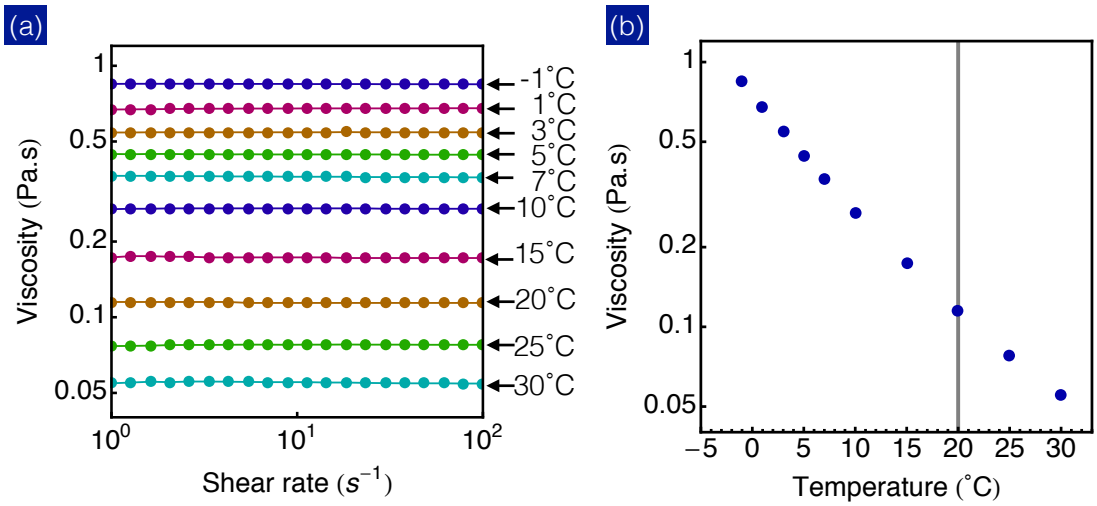

Figure 7.11: Shear rate sweep measurements of Dipropylene glycol viscosity for ten different environmental temperatures. We find the solvent remains Newtonian at all explored shear rates and temperatures. (b) Mean viscosity (averaged over rates) plotted as a function of temperature. The vertical line denotes the temperature 20°C maintained throughout all experiments in the main manuscript.

7.7.4 Speaker Experiment Details

We use a subwoofer to provide vibration orthogonal to the rotation direction of the motor gear. To maintain the vibration speed, $A\omega$ while the frequency ω is ramped up, we monitor the acceleration of the vibration $|a|$, and reduce the amplitude A accordingly. The vibration acceleration $|a| = A\omega^2 \sin(\omega t)$ is measured by a wireless accelerometer (Monnit, g-force max and avg). At ω =250 Hz, the vibration amplitude is approximately 13 μm.

The suspension tested in this experiment is cornstarch in water with a weight concentration $\approx$ 55%. Although the solvent's density does not match the cornstarch density, our experiment time is short ($\approx$ 3 min), so we do not observe any time-dependent behavior associated with sedimentation. We film the gear rotation with a camera at a frame rate 240 fps. This high frame rate allows us to determine

the real-time speed of the motor. To do so, we analyze the local image region of the gear using "Digital Image Correlation" [**?**, **?**] extracting the instantaneous rotation speed.

7.7.5 Instant Adaptation and Isotropic Viscosity

In the instant adaptation regime, force chains always align with the net compressive axis. Therefore, the chain alignment demonstrates a viscous response to the applied OSP flow ($\phi \propto \dot{\gamma}^{\mathrm{OSP}}$) as shown in the main manuscript Fig. 2(a). This instant adaptation directly implies an isotropic viscosity response of the thickening suspension. We provide a simple mathematical argument elucidating this relation.

The magnitude of the overall shear rate can be written as:

$$\dot{\gamma}_{\mathrm{tot}} = \sqrt{\dot{\gamma}_0^2 + (\dot{\gamma}_0^{\mathrm{OSP}} \cos(\omega t))^2} \approx \dot{\gamma}_0 + \mathcal{O}((\dot{\gamma}_0^{\mathrm{OSP}})^2). \tag{7.1}$$

Since the chain angle ϕ remains small, it can be approximated as:

$$\phi = \tan^{-1}\left(\frac{\dot{\gamma}_0^{\mathrm{OSP}} \cos(\omega t)}{\dot{\gamma}_0}\right) \approx \frac{\dot{\gamma}_0^{\mathrm{OSP}} \cos(\omega t)}{\dot{\gamma}_0} \tag{7.2}$$

when the OSP shear rate is small $\dot{\gamma}_0^{\mathrm{OSP}} \cos(\omega t) \ll \dot{\gamma}_0$. The approximately constant strain rate (to leading order) results in a shear stress that is constant in magnitude but of variable orientation. The magnitude of the net shear stress is $\sigma_{uz} = \eta\dot{\gamma}_0$, where $\hat{u}\hat{z}$ is the shear plane of the combined flows, and η is the uniaxial thickening viscosity without orthogonal perturbation. To calculate the primary and OSP stresses measured in experiment, we then project the net stress, which is aligned along $\hat{u}\hat{z}$ axis, back to $\hat{x}\hat{z}$ and $\hat{y}\hat{z}$. The projected stresses $\sigma_{\parallel} = \sigma_{xz}$, and $\sigma_{\perp} = \sigma_{yz}$ are:

$$\sigma_{\parallel} = \sigma_{uz}\cos(\phi) \approx \eta\dot{\gamma}_0 + \mathcal{O}(\phi^2)$$

$$\sigma_{\perp} = \sigma_{uz}\sin(\phi) \approx \eta\dot{\gamma}_0\phi + \mathcal{O}(\phi^3) \quad .$$

From Eq.7.2, $\sigma_\perp$ can be further reduced to $\sigma_\perp \approx \eta\dot{\gamma}_0^{\mathrm{OSP}}\cos(\omega t)$. Collectively, we find that both primary $\eta_\parallel = \sigma_\parallel/\dot{\gamma}_0$ and OSP $\eta_\perp = \sigma_\perp/\left[\dot{\gamma}_0^{\mathrm{OSP}}\cos(\omega t)\right]$ viscosities coincide the original uniaxial viscosity η. The result also suggests a viscous OSP stress response, consistent with the phase angle measurement reported in Sec. 7.7.3.

7.7.6 Simulation Details

Numerical model

The simulation model used in the present work is implemented in the open source molecular dynamics package LAMMPS [40], and has been employed previously in the study of shear thickening suspensions as described in Ref [**?**].

The equations of motion for non-Brownian particles suspended in a fluid can be written simply as [4]

$$m\frac{d}{dt}\begin{pmatrix}\mathbf{v}\\ \boldsymbol{\omega}\end{pmatrix} = \sum\begin{pmatrix}\mathbf{F}\\ \boldsymbol{\Gamma}\end{pmatrix}, \tag{7.3}$$

for particles of mass m with translational and rotational velocity vectors $\mathbf{v}$ and $\boldsymbol{\omega}$ respectively, and subjected to force and torque vectors $\mathbf{F}$ and $\boldsymbol{\Gamma}$ respectively. In this work we limit the forces and torques to those arising due to direct surface contacts between neighbouring particles $(\mathbf{F}^c, \boldsymbol{\Gamma}^c)$ and those arising through short range, pairwise, hydrodynamic lubrication forces $(\mathbf{F}^l, \boldsymbol{\Gamma}^l)$. For an interaction between particles i and j, the force and torque due to hydrodynamics can therefore be expressed as

$$\mathbf{F}^l_{ij} = -a_{sq} 6\pi\eta_f (\mathbf{v}_i - \mathbf{v}_j) \cdot \mathbf{n}_{ij}\mathbf{n}_{ij} \tag{7.4}$$

$$-a_{sh} 6\pi\eta_f (\mathbf{v}_i - \mathbf{v}_j) \cdot (\mathbf{I} - \mathbf{n}_{ij}\mathbf{n}_{ij}), \tag{7.5}$$

$$\mathbf{\Gamma}^l_{ij} = -a_{pu}\pi\eta_f d_i^3 (\boldsymbol{\omega}_i - \boldsymbol{\omega}_j) \cdot (\mathbf{I} - \mathbf{n}_{ij}\mathbf{n}_{ij}) \tag{7.6}$$

$$-\frac{d_i}{2}\left(\mathbf{n}_{ij} \times \mathbf{F}^l_{ij}\right). \tag{7.7}$$

$$\tag{7.8}$$

for a suspending fluid of viscosity η_f, where $\mathbf{n}_{ij}$ is the vector pointing from particle j to particle i, and with squeeze a_{sq}, shear a_{sh} and pump a_{pu} resistance terms as derived by Kim and Karrila [24] and given in Eq 7.12 for particle diameters d_i and d_j, with $\beta = d_j/d_i$:

$$a_{sq} = \frac{\beta^2}{(1+\beta)^2}\frac{d_i^2}{2h_{\text{eff}}} + \frac{1+7\beta+\beta^2}{5(1+\beta)^3}\frac{d_i}{2}\ln\left(\frac{d_i}{2h_{\text{eff}}}\right) \tag{7.9}$$
$$+\frac{1+18\beta-29\beta^2+18\beta^3+\beta^4}{21(1+\beta)^4}\frac{d_i^2}{4h_{\text{eff}}}\ln\left(\frac{d_i}{2h_{\text{eff}}}\right),$$

$$a_{sh} = 4\beta\frac{2+\beta+2\beta^2}{15(1+\beta)^3}\frac{d_i}{2}\ln\left(\frac{d_i}{2h_{\text{eff}}}\right) \tag{7.10}$$
$$+4\frac{16-45\beta+58\beta^2-45\beta^3+16\beta^4}{375(1+\beta)^4}\frac{d_i^2}{4h_{\text{eff}}}\ln\left(\frac{d_i}{2h_{\text{eff}}}\right),$$

$$a_{pu} = \beta\frac{4+\beta}{10(1+\beta)^2}\ln\left(\frac{d_i}{2h_{\text{eff}}}\right) \tag{7.11}$$
$$+\frac{32-33\beta+83\beta^2+43\beta^3}{250\beta^3}\frac{d_i}{2h_{\text{eff}}}\ln\left(\frac{d_i}{2h_{\text{eff}}}\right).$$

For each interaction, the particle pair surface-to-surface distance h is calculated according to $h = |\mathbf{r}_{ij}| - \frac{d_i+d_j}{2}$, for centre-to-centre vector $\mathbf{r}_{ij}$. Recent experimental [**?**] and computational [44] work indicates that direct particle-particle contacts contribute significantly to the suspension viscosity, in addition to hydrodynamics. To

permit such contacts in the present model, we truncate the lubrication divergence at $h_{\min} = 0.001 d_{ij}$ (for weighted average particle diameter $d_{ij} = \frac{d_i d_j}{d_i + d_j}$), i.e., setting $h = h_{\min}$ in the force calculation, when $h < h_{\min}$. The effective interparticle gap used in the force calculation, h_{eff}, is therefore given by

$$h_{\text{eff}} = \begin{cases} h & \text{for } h > h_{\min} \\ h_{\min} & \text{otherwise.} \end{cases} \tag{7.12}$$

For computational efficiency, the lubrication forces are omitted when the interparticle gap h is greater than $h_{\max} = 0.05 d_{ij}$. The volume fraction is sufficiently high that all particles have numerous neighbours within this range, and we verified, therefore, that such an omission is inconsequential to the dynamics. When the lubrication force is overcome and particle surfaces come into contact, their interaction is defined according to a linear spring model [12], with normal ($\mathbf{F}^{c,n}$) and tangential ($\mathbf{F}^{c,t}$) force and torque $\mathbf{\Gamma}^c$ given by

$$\mathbf{F}_{ij}^{c,n} = k_{\text{n}} \delta \mathbf{n}_{\text{ij}}, \tag{7.13a}$$

$$\mathbf{F}_{ij}^{c,t} = -k_{\text{t}} \mathbf{u}_{\text{ij}}, \tag{7.13b}$$

$$\mathbf{\Gamma}_{ij}^{c} = -\frac{d_i}{2} (\mathbf{n}_{ij} \times \mathbf{F}_{ij}^{c,t}), \tag{7.13c}$$

for a collision between particles i and j with normal and tangential spring stiffnesses k_n and k_t respectively, particle overlap δ (equal to $-h$) and tangential displacement $\mathbf{u}_{\text{ij}}$. We note that the damping arising from the hydrodynamics is always sufficient to achieve a steady state without employing a thermostat, and further damping in the particle contact model is omitted for simplicity.

To regulate the particle-particle tangential forces, we employ the Critical Load Model (CLM) for particle-particle friction [44, 30]. This model gives an additional

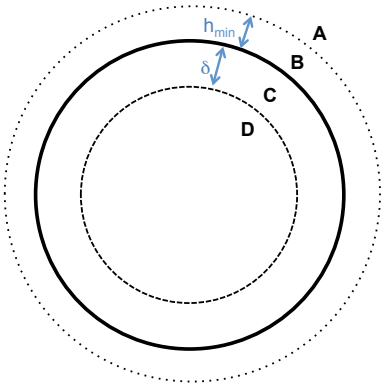

Figure 7.12: Illustration of interaction lengthscales (not to scale). Forces resolved in region A: $\mathbf{F}^l_{ij}(h_{\text{eff}} = h)$; B: $\mathbf{F}^l_{ij}(h_{\text{eff}} = h_{\min})$; C: $\mathbf{F}^l_{ij}(h_{\text{eff}} = h_{\min}) + \mathbf{F}^c_{ij}(\mu_p = 0)$; D: $\mathbf{F}^l_{ij}(h_{\text{eff}} = h_{\min}) + \mathbf{F}^c_{ij}(\mu_p = 1)$.

stress scale for the particle interaction, which, numerically, is the origin of the onset stress for shear thickening σ^* [**?**]. An interparticle static Coulomb friction coefficient μ_p is defined according to $|\mathbf{F}^{c,t}_{i,j}| \leq \mu_p |\mathbf{F}^{c,n}_{i,j}|$, setting a maximum value for the tangential force during a collision. In granular systems, μ_p consequently determines the volume fraction at which flow arrest or jamming will occur [**?**]. For each pairwise collision, the value of μ_p is dependent upon the normal force between the interacting particles and some critical normal force magnitude F^{CL}, such that

$$\mu_p = \begin{cases} 1 & \text{for } |\mathbf{F}^{c,n}_{i,j}| > F^{CL} \\ 0 & \text{otherwise} \end{cases} . \tag{7.14}$$

As a result of the CLM, particles that interact through weak forces, i.e. collisions where $\delta \to 0$, are frictionless, while interactions with large normal forces are frictional. The particle overlaps required to exceed F^{CL} are, at their absolute maximum, of order $10^{-5} d_{ij}$. An overview of the interaction lengthscales is given in Fig 7.12. In principle, $h_{\min}$ and δ might serve as tuning parameters that may be chosen to reflect details of a suspension of interest. For example, particles with particularly long-range repulsion or long stabilising polymer hairs or those

with prominent asperities or complex surface topology might be better captured by large $h_{\min}$. In practice, however, we find that provided $h_{\min} \leq 0.005d$, steady state dynamics are little changed as $h_{\min} \to 0$. Similarly there is little dependence on δ, provided $0 < \delta \ll d$.

Forces calculated according to the above models may then be summed for each particle pair to give the total force and torque $\mathbf{F}_{ij}$ and $\mathbf{\Gamma}_{ij}$, respectively. Particle positions and velocities are then updated according to a time stepping scheme, by summing contributions from all pairwise forces and solving Equation 7.3 numerically.

Isotropic particle assemblies with minimised particle-particle overlaps are generated in a 3-dimensional periodic domain of volume V. It is determined that $\mathrm{O}(10^3)$ spheres are sufficient to capture the bulk rheology and microstructural phenomena independently of system size. Bidispersity at a diameter ratio of $1:1.4$ and volume ratio of $1:1$ is used to minimize crystallization during flow [**?**] (and references therein).

The 3×3 stress tensor is constructed from the particle pair force data, and given by:

$$\boldsymbol{\sigma} = \frac{1}{V} \sum_i \sum_{i \neq j} \mathbf{r}_{ij} \mathbf{F}_{ij}. \tag{7.15}$$

Data from 20 realizations with randomized initial particle positions are used to obtain ensemble-averaged stresses.

Key assumptions of the simulation model and potential sources of discrepancy

1) Full solution of the long and short range hydrodynamic forces, essential for a truly accurate resolution of the fluid effects, has traditionally been achieved using the Stokesian Dynamics algorithm [5], though its great computational expense makes large (or very dense) simulations challenging and time consuming. For highly packed suspensions, where interparticle gap sizes tend to 0, the divergent lubrication forces between extremely close particles dominate the hydrodynamic interaction, so $\mathbf{F}^l$, $\mathbf{\Gamma}^l$ can be approximated by summing pairwise lubrication forces among nearest neighbouring particles. This simplification is becoming a conventional approach for modelling very dense suspended systems [1, **?**, **?**, 44]. A further assumption of the lubrication approximation is that the fluid may permeate the matrix formed by solid particles at infinite rate. For the system size used in the present work, and considering the periodicity of the box, it is assumed that there are no spatial or temporal variations of local volume fraction, so the effects of fluid migration are likely to be negligible.

2) The present simulation model allows particle inertia, but fluid inertia is neglected for simplicity. The flow induced by the primary shearing with rate $\dot{\gamma}_0$ has Stokes number $\rho\dot{\gamma}_0 d_{ij}^2/\eta_f \ll 1$ such that inertia is not relevant. The OSP flow however, has larger Stokes numbers, with $\rho\dot{\gamma}_{\mathrm{OSP}} d_{ij}^2/\eta_f \to 0.1$ for the case where $\gamma_{\mathrm{OSP}} = 5\%$, such that inertia may begin to become important. This may account for the discrepancy between simulation and experiment in this case. Trulsson [**?**] demonstrated that for inertial suspension flows, the dissipation through particle contacts considerably outweighs that due to fluid effects, which we take as justification of the present model. In addition,

the scaling laws predicted by the present simulation model and published elsewhere [32] (specifically $\sigma_{xy} \propto \dot{\gamma}$ and $\sigma_{xy} \propto \dot{\gamma}^2$ for viscous and inertial flows respectively) are consistent with observations from comparable experiments [18, **?**].

3) The employed friction model may be considered to account for roughness on the surface of ideal spheres in model systems, but neglects the resistance to rolling offered by particle asphericity. For less idealised cases, such as cornstarch suspensions, further computational tools such as bonded-sphere complex particle shapes and rolling resistance coefficients are currently being pursued as means of accounting for severe asphericity in addition to surface roughness. It is anticipated that enhanced interlocking in such cases will cause shear thickening to be exaggerated even further.

4) $\mu_p = 1$ is chosen to represent a highly frictional near-upper limiting case. In practice, μ_p can be chosen to represent the roughness of any particles of interest. The primary effect of varying μ_p is to alter the volume fraction at which the viscosity will diverge in the frictional limit. A secondary consequence of this is that at fixed volume fraction, the extent of shear thickening, i.e. the step change in viscosity upon exceeding σ^*, will decrease as $\mu_p \to 0$. Note that σ^* and $\dot{\gamma}_0$ are not functions of μ_p. These properties of μ_p have been reported recently elsewhere [30].

"Uniaxial" shear rheology predicted by the simulation model

Inclusion of the CLM introduces a simulation timescale associated with the shear thickening onset stress σ^*, which can be written as $1/\dot{\gamma}^* = \frac{3}{2}\pi\eta_f d_{ij}^2/F^{CL}$ [30]. An assembly of particles described by the above interaction models is sheared at

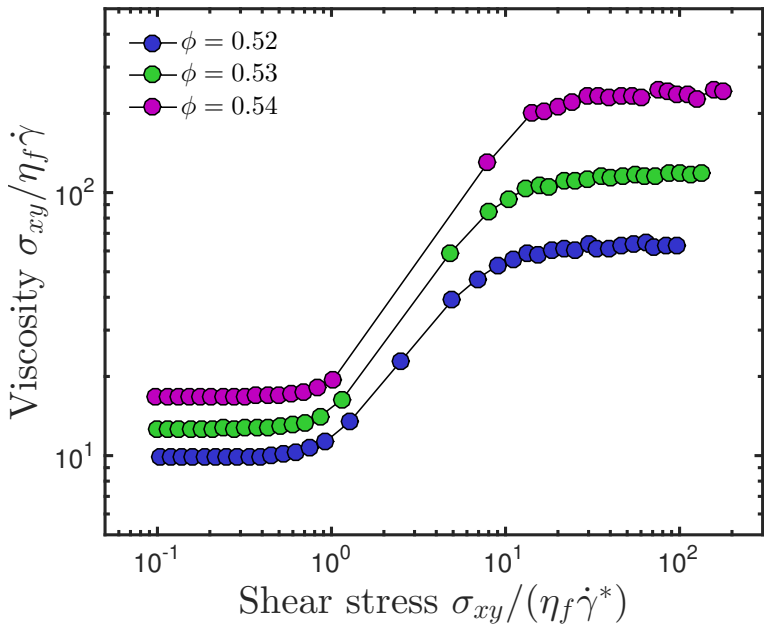

Figure 7.13: Simple shear rheology predicted by the simulation model used in this work. The suspension shear thickens above a critical stress $\sigma_{xy}/(\eta_f\dot{\gamma}^*) \approx 1$.

controlled rate (with flow in x, gradient in y and vorticity in z), with the dimensionless rate $\dot{\gamma}/\dot{\gamma}^*$ varied across orders of magnitude. The rheological flow map is presented in Fig 7.13, where σ_{xy} is the relevant component of $\boldsymbol{\sigma}$ (Equation 7.15) to represent the shear stress. Shear thickening is observed above a critical stress $\sigma_{xy}/(\eta_f\dot{\gamma}^*) \approx 1$. The results in the main part of the present paper are all obtained in the limit of large $\dot{\gamma}/\dot{\gamma}^*$, where $\dot{\gamma}$ is analogous to the *primary* shearing flow, and where the suspension would be expected to flow well within the shear thickened regime.

REFERENCES

[1] R C Ball and John R Melrose. A simulation technique for many spheres in quasi-static motion under frame-invariant pair drag and Brownian forces. *Physica A Statistical and Theoretical Physics*, 247(1-4):444–472, 1997.

[2] J Benbow and J Bridgwater. *Paste flow and extrusion*. Oxford University Press, 1993.

[3] Dapeng Bi, Jie Zhang, Bulbul Chakraborty, and RP Behringer. Jamming by shear. *Nature*, 480(7377):355–358, 2011.

[4] J F Brady and G Bossis. Stokesian Dynamics. *Annual Review of Fluid Mechanics*, 20(1):111–157, January 1988.

[5] John F Brady and Georges Bossis. The rheology of concentrated suspensions of spheres in simple shear flow by numerical simulation. *Journal of Fluid Mechanics*, 155:105–129, 1985.

[6] Eric Brown, Nicole Forman, Carlos Orellana, Hanjun Zhang, Benjamin Maynor, Douglas Betts, Joseph DeSimone, and Heinrich Jaeger. Generality of shear thickening in dense suspensions. *Nature Materials*, 9(3):220–224, 2010.

[7] Eric Brown and Heinrich M Jaeger. The role of dilation and confining stresses in shear thickening of dense suspensions. *Journal of Rheology*, 56(4):875–923, 2012.

[8] Eric Brown and Heinrich M Jaeger. Shear thickening in concentrated suspensions: phenomenology, mechanisms and relations to jamming. *Reports on Progress in Physics*, 77(4):046602, 2014.

[9] ME Cates, JP Wittmer, J-P Bouchaud, and Ph Claudin. Jamming, force chains, and fragile matter. *Physical Review Letters*, 81(9):1841, 1998.

[10] Michael E. Cates and Matthieu Wyart. Granulation and bistability in non-brownian suspensions. *Rheologica Acta*, 53(10):755–764, 2014.

[11] Zhengdong Cheng, Jixiang Zhu, Paul M Chaikin, See-Eng Phan, and William B Russel. Nature of the divergence in low shear viscosity of colloidal hard-sphere dispersions. *Physical Review E*, 65(4):041405, 2002.

[12] P A Cundall and O D L Strack. A discrete numerical model for granular assemblies. *Géotechnique*, 29(1):47–65, 1979.

[13] Colin D Cwalina. *Shear thickening fluids for enhanced protection from micrometeoroids and orbital debris*. PhD thesis, University of Delaware, 2016.

[14] E. Damond. Apparatus for the automatic unclogging of hoppers, September 26 1939. US Patent 2,174,348.

[15] Anthony D Dinsmore, Eric R Weeks, Vikram Prasad, Andrew C Levitt, and David A Weitz. Three-dimensional confocal microscopy of colloids. *Applied Optics*, 40(24):4152–4159, 2001.

[16] Abdoulaye Fall, François Bertrand, Guillaume Ovarlez, and Daniel Bonn. Shear thickening of cornstarch suspensions. *Journal of Rheology*, 56(3):575–591, 2012.

[17] Abdoulaye Fall, N Huang, François Bertrand, G Ovarlez, and Daniel Bonn. Shear thickening of cornstarch suspensions as a reentrant jamming transition. *Physical Review Letters*, 100(1):018301, 2008.

[18] Abdoulaye Fall, Anael Lemaitre, François Bertrand, Daniel Bonn, and Guillaume Ovarlez. Shear thickening and migration in granular suspensions. *Physical review letters*, 105(26):268303, 2010.

[19] Frank Y Fan, William H Woodford, Zheng Li, Nir Baram, Kyle C Smith, Ahmed Helal, Gareth H McKinley, W Craig Carter, and Yet-Ming Chiang. Polysulfide flow batteries enabled by percolating nanoscale conductor networks. *Nano Letters*, 14(4):2210–2218, 2014.

[20] Nicolas Fernandez, Roman Mani, David Rinaldi, Dirk Kadau, Martin Mosquet, Hélène Lombois-Burger, Juliette Cayer-Barrioz, Hans J. Herrmann, Nicholas D. Spencer, and Lucio Isa. Microscopic mechanism for shear thickening of non-brownian suspensions. *Phys. Rev. Lett.*, 111:108301, Sep 2013.

[21] F Gadala-Maria and Andreas Acrivos. Shear-induced structure in a concentrated suspension of solid spheres. *Journal of Rheology*, 24(6):799–814, 1980.

[22] BM Guy, M Hermes, and WCK Poon. Towards a unified description of the rheology of hard-particle suspensions. *Physical Review Letters*, 115(8):088304, 2015.

[23] Alan R Jacob, Andreas S Poulos, Sunhyung Kim, Jan Vermant, and George Petekidis. Convective cage release in model colloidal glasses. *Physical Review Letters*, 115(21):218301, 2015.

[24] Sangtae Kim and Seppo Karrila. *Microhydrodynamics: Principles and selected applications*. Dover publications, 1991.

[25] Young S Lee, Eric D Wetzel, and Norman J Wagner. The ballistic impact characteristics of kevlar® woven fabrics impregnated with a colloidal shear thickening fluid. *Journal of Materials Science*, 38(13):2825–2833, 2003.

[26] Neil YC Lin, Ben M Guy, Michiel Hermes, Chris Ness, Jin Sun, Wilson CK Poon, and Itai Cohen. Hydrodynamic and contact contributions to continuous shear thickening in colloidal suspensions. *Physical Review Letters*, 115(22):228304, 2015.

[27] Neil YC Lin, Jonathan H McCoy, Xiang Cheng, Brian Leahy, Jacob N Israelachvili, and Itai Cohen. A multi-axis confocal rheoscope for studying shear flow of structured fluids. *Review of Scientific Instruments*, 85(3):033905, 2014.

[28] Trushant S Majmudar and Robert P Behringer. Contact force measurements and stress-induced anisotropy in granular materials. *Nature*, 435(7045):1079–1082, 2005.

[29] Romain Mari, Ryohei Seto, Jeffrey F Morris, and Morton M Denn. Shear thickening, frictionless and frictional rheologies in non-brownian suspensions. *Journal of Rheology*, 58(6):1693–1724, 2014.

[30] Romain Mari, Ryohei Seto, Jeffrey F. Morris, and Morton M. Denn. Shear thickening, frictionless and frictional rheologies in non-Brownian suspensions. *Journal of Rheology*, 58(6):1693–1724, November 2014.

[31] Constantinos Mavroidis, Charles Pfeiffer, and Michael Mosley. Conventional actuators, shape memory alloys, and electrorheological fluids. In Y. Bar-Cohen and American Society for Nondestructive Testing, editors, *Automation, Miniature Robotics, and Sensors for Nondestructive Testing and Evaluation*. American Society for Nondestructive Testing, 2000.

[32] Christopher Ness and Jin Sun. Flow regime transitions in dense non-brownian suspensions: Rheology, microstructural characterization, and constitutive modeling. *Phys. Rev. E*, 91:012201, Jan 2015.

[33] Christopher Ness and Jin Sun. Shear thickening regimes of dense non-brownian suspensions. *Soft Matter*, 12(3):914–924, 2016.

[34] Christopher Ness and Jin Sun. Two-scale evolution during shear reversal in dense suspensions. *Physical Review E*, 93(1):012604, 2016.

[35] Jason Nikitczuk, Brian Weinberg, and Constantinos Mavroidis. Rehabilitative knee orthosis driven by electro-rheological fluid based actuators. In *Robotics and Automation, 2005. ICRA 2005. Proceedings of the 2005 IEEE International Conference*, pages 2283–2289. IEEE, 2005.

[36] G Ovarlez, Q Barral, and P Coussot. Three-dimensional jamming and flows of soft glassy materials. *Nature Materials*, 9(2):115–119, 2010.

[37] Pramod D Patil, James J Feng, and Savvas G Hatzikiriakos. Constitutive modeling and flow simulation of polytetrafluoroethylene (ptfe) paste extrusion. *Journal of Non-Newtonian Fluid Mechanics*, 139(1):44–53, 2006.

[38] Ivo R. Peters, Sayantan Majumdar, and Heinrich M. Jaeger. Direct observation of dynamic shear jamming in dense suspensions. *Nature*, 532(7598):214–217, 04 2016.

[39] Steve Plimpton. Fast parallel algorithms for short-range molecular dynamics. *Journal of Computational Physics*, 117(1):1–19, 1995.

[40] Steve Plimpton. Fast Parallel Algorithms for Short Range Molecular Dynamics. *J. Comput. Phys.*, 117(June 1994):1–42, 1995.

[41] Wilson CK Poon, Eric R Weeks, and C Patrick Royall. On measuring colloidal volume fractions. *Soft Matter*, 8(1):21–30, 2012.

[42] V Prasad, D Semwogerere, and Eric R Weeks. Confocal microscopy of colloids. *Journal of Physics: Condensed Matter*, 19(11):113102, 2007.

[43] Ryohei Seto, Romain Mari, Jeffrey F Morris, and Morton M Denn. Discontinuous shear thickening of frictional hard-sphere suspensions. *Physical Review Letters*, 111(21):218301, 2013.

[44] Ryohei Seto, Romain Mari, Jeffrey F. Morris, and Morton M. Denn. Discontinuous Shear Thickening of Frictional Hard-Sphere Suspensions. *Physical Review Letters*, 111:218301, 2013.

[45] R Stanway, JL Sproston, and AK El-Wahed. Applications of electro-rheological fluids in vibration control: a survey. *Smart Materials and Structures*, 5(4):464, 1996.

[46] Ke Sun, Teng-Sing Wei, Bok Yeop Ahn, Jung Yoon Seo, Shen J Dillon, and Jennifer A Lewis. 3d printing of interdigitated li-ion microbattery architectures. *Advanced Materials*, 25(33):4539–4543, 2013.

[47] KP Tan, WA Bullough, Roger Stanway, N Sims, AR Johnson, and RC Tozer. A simple one dimensional robot joint based on the ER linear reversing mechanism. *Journal of Intelligent Material Systems and Structures*, 13(7-8):533–537, 2002.

[48] Jan Vermant, Paula Moldenaers, Joannes Mewis, M Ellis, and R Garritano. Orthogonal superposition measurements using a rheometer equipped with a force rebalanced transducer. *Review of Scientific Instruments*, 68(11):4090–4096, 1997.

[49] Jan Vermant, L Walker, Paula Moldenaers, and Joannes Mewis. Orthogonal versus parallel superposition measurements. *Journal of Non-Newtonian Fluid Mechanics*, 79(2):173–189, 1998.

[50] Norman J Wagner and John F Brady. Shear thickening in colloidal dispersions. *Physics Today*, 62(10):27–32, 2009.

[51] Norman J Wagner and Eric D Wetzel. Advanced body armor utilizing shear thickening fluids, June 5 2007. US Patent 7,226,878.

[52] Matthieu Wyart and ME Cates. Discontinuous shear thickening without inertia in dense non-brownian suspensions. *Physical Review Letters*, 112(9):098302, 2014.

CHAPTER 8

FUTURE WORK

In this chapter, I will discuss future experiments that will further elucidate the particle-scale mechanisms underlying the non-Newtonian flow behaviors of suspensions.

8.1 Nonlinear suspension stress responses

In nature and industrial settings, fluids are commonly driven far-from-equilibrium resulting in highly nonlinear stress responses. The "Large Amplitude Oscillatory Shear" (LAOS) rheometry has been widely employed to characterize how these nonlinear responses and their corresponding viscoelasticities evolve. However, the mechanism that underlies such nonlinear stress responses remains poorly understood, since these responses have multiple components including the Brownian, hydrodynamic, and contact contributions. While numerical simulations can record these contributions individually, conventional LAOS rheometry can only measure their sum. To overcome this technical hurdle, we can perform cessation-LAOS and reversal-LAOS measurements determining individual stress contributions. In these experiments, we first impose LAOS on a suspension until it reaches a steady state (reproducible responses over cycles). Then in the cessation-LAOS experiment, we cease the shear flow when the applied strain reaches a time-of-interest (e.g. strain phase = ϕ), and immediately record the transient stress decay. For hard spheres, while both the hydrodynamic and contact contributions disappear instantly upon cessation, the Brownian stress decays relatively slowly. By extrapolating this gradual Brownian stress decay, we can approximate its magnitude upon

cessation. Similarly, in the reversal-LAOS experiment where the shear flow's direction is reversed, the contact contribution vanishes upon reversal, the sign of the hydrodynamic component changes, and the Brownian stress remains roughly the same. Therefore, by combining cessation-LAOS, reversal-LAOS, and typical LAOS rheometry, we can separate the three primary stress contributions. Finally, we can repeat this procedure at different strains to trace individual stress contributions within LAOS cycles.

8.2 SALSA measurements in colloidal materials

SALSA can measure the stress of hard-sphere suspensions in liquid, crystal, and glass phases. In quiescent liquids, SALSA can measure the thermal fluctuations of stresses allowing us to determine the suspension viscosity using the Green-Kubo relation. SALSA can also measure the stress in highly-confined or far-from-equilibrium colloidal liquids, where substantial modifications to the Green-Kubo formula are expected. More importantly, SALSA becomes more vital in glassy systems, in which the stress distribution is usually heterogeneous and cannot be inferred from the strain field. The ability to directly measure stresses in a glass opens the door to elucidating many fundamental questions in amorphous materials. For example: how does the stress architecture in colloidal glasses compare to the force network in packed granular systems? This comparison will help us to understand how finite-temperature effects, which dominate in colloidal glasses, versus interparticle friction, which dominates in granular packs, affect the stress distribution in disordered systems. Moreover, by using our confocal rheoscope, we can strain a colloidal glass and simultaneously measure its stress evolution. In doing this, we can identify individual local yielding events, and correlate them

with particle motions and suspension microstructures. While previous experiments have been able to identify the local shear transformations associated with particle swaps (T1 transformation), it remains unclear whether these local rearrangements are necessary for yielding. Finally, it will be fruitful to observe how local rearrangements grow in size and fill the suspension volume as the sample approaches its macroscopic yielding. Such measurements would rigorously test previous theories that predict the suspension yields when these local events percolate throughout the sample, giving rise to a non-equilibrium phase transition.

8.3 Shear thickening

One central industrial motivation to study shear thickening is to solve its resulting slow-extrusion problems. In many extrusion processes, the fluid's shear rate radically increases due to the reduction of the flow channel dimension. In addition, such a narrowed channel can also cause confinement effects on the extruded material. In suspension systems, it has been known that confinement can substantially alter their flow behaviors, including the wall-induced liquid-glass transition and the viscosity reduction arising from the wall-induced particle layering. In confined granular systems, the frictional particles usually form percolating force chains more easily than in bulk systems. This finding suggests that when a suspension is confined, it can demonstrate shear thickening at a lower applied stress with a more radical viscosity growth. Therefore, the shear thickening behavior of a suspension can be tuned by simply confining the fluid. To examine this conjecture, we can either confine a suspension using our confocal rheoscope offering a simple parallel-plate geometry, or a micro-fluidic device that mimics the practical extrusion geometry. In addition, it is also important to understand how the sur-

face property of the confining wall influences the suspension thickening behavior. If the walls are atomically-flat (e.g. silicon wafers used in rheoscope), the bulk stress is transmitted to the wall through the liquid between the boundary particles and walls. By introducing surface roughness or creating lubricating layers, such as those recently developed in the Aizenberg lab, that generate almost-perfect slip, we should be able to substantially modify this particle-wall interaction, ultimately altering the effective viscosities of the system. As a result, we can engineer the extruder inner surface to control the flow of thickening suspensions.